In-gas-cell laser resonance ionization spectroscopy of $^{196\text{-}198}$Ir

Momo Mukai

February 2018

In-gas-cell laser resonance ionization spectroscopy of $^{196\text{-}198}$Ir

Momo Mukai

Doctoral Program in Physics

Submitted to the Graduate School of

Pure and Applied Sciences

in Partial Fulfillment of the Requirements

for the Degree of Doctor of Philosophy in

Science

at the

University of Tsukuba

Contents

Abstract **7**

1 Introduction **8**
1.1 Nucleosynthesis . . . 8
1.2 Blank spot on the r-process path . . . 8
1.3 Half-life predictions and elemental abundances . . . 10
1.4 Systematic study of nuclear structure in the vicinity of $N = 126$ . . . 12
1.5 Outline of the present work . . . 14

2 Experimental methods **16**
2.1 Multi-nucleon transfer reactions for the production of nuclei around $N = 126$ 16
2.1.1 Projectile fragmentation reactions combined with in-flight separation 16
2.1.2 Spallation reaction combined with Isotope Separator On-Line (ISOL) 16
2.1.3 Multi-nucleon transfer reactions: ^{136}Xe + ^{198}Pt . . . 17
2.2 KEK Isotope Separation System . . . 19
2.3 Hyperfine Structure . . . 20
2.3.1 Magnetic dipole moment . . . 21
2.3.2 Electric quadrupole moment . . . 21
2.4 Isotope shift . . . 22
2.4.1 Mass effect . . . 22
2.4.2 Volume effect . . . 25
2.5 Nuclear mean-square charge radius and deformation parameter . . . 27
2.6 HFS measurement by laser ionization spectroscopy . . . 27
2.6.1 Principle . . . 27
2.6.2 In-gas-cell laser ionization spectroscopy . . . 28
2.6.3 Spectral lineshape and width . . . 29
2.6.4 Analyses of broad HFS spectra . . . 32

3 Experimental setup **34**
3.1 Gas cell system at KISS . . . 34
3.1.1 Primary beam transport . . . 35
3.1.2 Radiation shield . . . 36
3.1.3 Rotating energy-degrader and target . . . 36
3.1.4 Doughnut-shaped gas cell . . . 38
3.1.5 Laser ionization . . . 39
3.1.6 Gas purification system . . . 42
3.1.7 Multi-RF ion guide (MRFIG) . . . 43
3.2 KISS beam transport . . . 46
3.3 Detection system . . . 48
3.3.1 Detector setup in the first experiment . . . 49
3.3.2 Detector setup in the second experiment . . . 51

4 Experiments **53**
4.1 Primary beam tuning . . . 53
4.2 Extraction of ^{198,199}Pt$^+$ for system optimization . . . 53
4.2.1 Extraction of ^{199}Pt$^+$ . . . 54
4.3 β-decay half-life measurements of iridium isotopes . . . 55
4.4 HFS measurements of iridium isotopes . . . 56

4.5 Analyses of measured HFS spectra . . . 57
4.5.1 Fitting method . . . 59
4.5.2 Energy shifts by the hyperfine coupling constants A_{HF} and B_{HF} . . . 61
4.5.3 Fitting results of the HFS spectra of stable isotopes . . . 62
4.5.4 Results of the simultaneous fittings including the HFS spectra of ^{197}Ir . . . 65
4.5.5 Results of the simultaneous fittings including the HFS spectrum of ^{196}Ir . . . 68
4.5.6 Results of the simultaneous fittings including the HFS spectrum of ^{198}Ir . . . 73

5 Discussion **76**
5.1 Charge radii and deformation parameters . . . 76
5.2 Theoretical calculation . . . 77
5.2.1 Self-consistent HFB calculation with SkM* interaction . . . 77
5.2.2 Shell model calculation . . . 79
5.3 Systematics of nuclear structure in odd-A iridium isotopes . . . 81
5.4 Semi-empirical magnetic moments of ^{196}Ir and ^{198}Ir . . . 83
5.4.1 Check the validity of the semi-empirical calculations for gold isotopes . . . 84
5.4.2 Estimations of spin values and wave-functions for ^{196,198}Ir . . . 84
5.5 Summary of the discussions . . . 85

6 Summary and outlook **87**
6.1 Summary . . . 87
6.2 Outlook . . . 89

Bibliography **91**

Appendix **96**

A King plot **96**

B Evaluation of nuclear spin value I from the number of hyperfine transitions **98**

C Multi-segmented proportional gas counter **99**
C.1 Details of the MSPGC . . . 99
C.1.1 Design of the MSPGC . . . 99
C.1.2 Operation of the MSPGC . . . 102
C.2 Performance tests of the MSPGC . . . 104
C.2.1 Performance test of one telescope in a small chamber with gas flow . . . 104
C.2.2 Performance test of the fully assembled MSPGC . . . 107
C.2.3 Background event rate . . . 109
C.2.4 On-line experimental results obtained by using the MSPGC . . . 111
C.2.5 Absolute detection efficiency as a function of Q_β . . . 114
C.3 Summary . . . 115

D Magnetic moments on the single-particle model **117**

Acknowledgments **119**

List of Figures

1 Expected r-process path and observed solar r-abundances 9
2 Gamow-Teller and first-forbidden decays in the nuclear region $Z \leq 82$ and $N \leq 126$ 10
3 Predicted half-lives of $N = 126$ nuclei by various theoretical models 11
4 Calculated r-abundances around the third peak 12
5 Previous studies of the electromagnetic moments for the ground state of refractory elements 13
6 The variation of the mean-square charge radii of Ir, Pt, Au, and Hg 13
7 Melting and boiling temperatures for the elements from Xe to Rn 17
8 Schematic view of MNT reactions 17
9 Excitation functions for the production cross-sections of ^{196,197,198}Ir 18
10 Emission angle and energy distributions of ^{196,197,198}Ir 18
11 Schematic view of KISS 20
12 Hyperfine structure of the $J = 9/2, I = 3/2$ state 21
13 HFS measurement by laser spectroscopy 28
14 Spectral lineshape and HFS spectrum 29
15 KISS gas cell system 35
16 Design of the rotating energy degrader and target 37
17 Schematic views of the KISS gas cells 38
18 Two-color two-step laser resonance ionization 40
19 KISS laser system 40
20 Laser power dependences of Ir ion counts 41
21 Schematic view of the argon gas feeding line 42
22 Purification of the argon gas 43
23 Cross-sectional view of a multi-pole RF ion guide and pseudo-potentials . . 44
24 Setup of the MRFIG 45
25 RF circuit for the multi-pole RF ion guides 45
26 Schematic view of the KISS beamline 46
27 Photo of the KISS detector station 48
28 Detector setup in the first experiment 50
29 Detector setup in the second experiment 52
30 Measured extraction yield of $^{199}Pt^+$ as a function of gas cell pressure . . . 54
31 Measured extraction yield of $^{199}Pt^+$ as a function of primary beam intensity 55
32 Measured growth and decay time spectra for ^{196,197,198}Ir 56
33 Measured growth time spectra of ^{196,197,198}Ir 57
34 Schematic view of the HFS spectra of ^{191}Ir and ^{A}Ir. 60
35 Energy shifts of hyperfine levels as a function of $A_{\rm HF}$ and $B_{\rm HF}$ 61
36 Measured HFS spectra of ^{191}Ir and ^{193}Ir 62
37 Measured HFS spectrum of ^{191}Ir with a gas cell pressure of 12 kPa 64
38 Measured pressure broadening and shift of iridium in argon gas 64
39 Expected HFS spectrum of ^{197m}Ir 65
40 Measured HFS spectra of ^{197}Ir and the fitting curves 68
41 The β-decay scheme between ground states of ^{196}Os, ^{196}Ir, and ^{196}Pt 69
42 Measured HFS spectra of ^{196}Ir and the fitting curves 70
43 Measured HFS spectra of ^{198}Ir and the fitting curves 73
44 Plot of $\delta\langle r_c^2\rangle^{191,A}$ and $|\langle\beta_2\rangle|^{1/2}$ 77
45 Systematics of the low-lying states in odd-A iridium isotopes 82

46 Nilsson diagram for single-proton levels of ^{197}Ir 82
47 The μ values of iridium and gold isotopes with $N = 112$–120 83
48 Single-particle orbits with the shell model description 83
49 Schematic view of in-gas-jet laser ionization spectroscopy and the expected HFS spectrum 89
A.1 King plot 96
C.1 Cross-sectional view of the detector setup for β-γ spectroscopy at KISS . . 100
C.2 Cross-sectional view of the MSPGC with the vacuum chamber, SCGe detectors, and CEM 101
C.3 Structure of the gas counter telescope 101
C.4 Schematic view of the high voltage connection and signal amplifications . . 102
C.5 Schematic diagram of the data flow 103
C.6 Schematic view of the hit patterns 104
C.7 Schematic view of the performance test setup 105
C.8 Optimization of the anode voltage 106
C.9 Measured intrinsic detection efficiencies 107
C.10 Schematic view of the performance test setup of the MSPGC 108
C.11 Measured coincidence rate in each telescope 109
C.12 Measured background event rate in each telescope 110
C.13 Measured growth and decay time spectrum of β-rays for ^{198}Ir 111
C.14 Decay scheme and measured spectra for ^{199}Pt 113
C.15 Estimated absolute detection efficiency of the MSPGC 115

List of Tables

1 Dominant configurations for iridium isotopes 15
2 Comparison of the production yields of ^{202}Os by three reaction systems . . 19
3 Measured pressure broadening and pressure shift coefficients 31
4 Energy deposits of ^{136}Xe beam on the foils 37
5 Operation parameters of the MRFIG 46
6 Basic parameters for the ion-optical components and beam diagnostics at the KISS beamline 47
7 Settings and specifications of the germanium detectors 51
8 Fitting results of growth and decay time spectra for ^{196,197,198}Ir 56
9 HFS parameters of iridium isotopes 58
10 μ and Q values of iridium and gold isotopes 60
11 Evaluated parameters from the best fittings to the HFS spectra of ^{191,193}Ir 63
12 μ and Q values of $I^\pi = 11/2^-$ isomeric states of iridium and gold isotopes . 66
13 Fitting results of the HFS spectra of ^{197}Ir 67
13 (continued) 68
14 Fitting results of the HFS spectrum of ^{196}Ir with $I = 0$ 71
15 Fitting results of the HFS spectrum of ^{196}Ir with $I \geq 1$ 72
16 Fitting results of the HFS spectrum of ^{198}Ir with $I = 0$ 74
17 Fitting results of the HFS spectrum of ^{198}Ir with $I \geq 1$ 75
18 The evaluated $\delta\langle r_c^2\rangle^{191,A}$ and $|\langle\beta_2^2\rangle|^{1/2}$ values of ^{193}Ir and $^{196-198}$Ir 77
19 Comparison of experimental and theoretical results by the HFB + SkM* calculations 78
20 Theoretical results for low-lying states of ^{197}Ir by the HFB + SkM* calculations 79
21 Theoretical results for low-lying states of ^{196}Ir by the HFB + SkM* calculations 79
22 Comparison of experimental and theoretical results by the shell model calculations 80
23 Configurations obtained from the shell model calculation for ^{198}Ir 81
24 The $\mu_{\rm exp}$ values of ^{191m}Ir, ^{193}Ir, ^{193}Os, ^{195m}Pt, ^{195}Pt, and ^{199}Pt 84
25 The $\mu_{\rm exp}$ and $\mu_{\rm emp}$ values of ^{194}Au, ^{196}Au, and ^{198}Au 85
26 The $\mu_{\rm exp}$ and $\mu_{\rm exp}$ values of ^{194}Ir, ^{196}Ir, and ^{198}Ir 85
27 Comparison between in-gas-cell and -jet laser ionization spectroscopy . . . 90
B.1 The number of transitions between HFS of two atomic states with $I \leq J_1,\ J_2$ 98
B.2 The number of transitions between HFS of two atomic states with $I \leq J_1$ and $I > J_2$ 98
C.1 Measured background event rates in the MSPGC 110

Abstract

The nuclear properties such as half-life and mass of the nuclei with proton number $Z \sim 70$ and neutron number $N = 126$ are essential to reveal the stellar environment of the r-process for the formation of the third peak. However, these nuclei are too far from the stability line, and it is difficult to access them experimentally. For the drastic improvement of the theoretical prediction for the half-lives and masses in this region, the investigation of nuclear wave-functions of the nuclei around $N = 126$ is effective. The nuclear wave-function can be estimated from a nuclear magnetic dipole moment. The magnetic dipole moment is directly deduced by the hyperfine structures (HFS) measured by in-gas-cell laser ionization spectroscopy. We performed the HFS measurements of $^{196-198}$Ir ($Z = 77$, $N = 119$–121) by laser spectroscopy as the first step of systematic nuclear structure study for neutron-rich nuclei with $Z \sim 77$ at KEK isotope separation system (KISS).

The neutron-rich nuclei of $Z \sim 77$ can be produced by the multi-nucleon transfer (MNT) reactions of ^{136}Xe beam and ^{198}Pt target. The selection of a single nuclide from the reaction products by the MNT reactions and decay spectroscopy are performed at KISS, which consists of a laser ion source combined with an argon gas cell to thermalize the reaction products, an on-line isotope separator (ISOL), and detectors for β-γ spectroscopy. The HFS measurement of an unstable nucleus at KISS is performed by counting the β-rays emitted from the laser-ionized atoms as a function of excitation laser wavelength. Even though the HFS spectrum is observed as one broaden peak mainly due to the pressure broadening in the gas cell with a pressure of 74 kPa, it is feasible to deduce the nuclear magnetic dipole moment and isotope shift which determine the peak width and position of the HFS spectrum, respectively.

The nuclear magnetic dipole moments (μ) and isotope shifts of $^{196-198}$Ir were evaluated from the analyses of the measured HFS spectra. The evaluated magnetic moment of ^{197}Ir ($N = 120$ and spin-parity value $I^\pi = 3/2^+$), $\mu = +0.25 \pm 0.03$ μ_N (μ_N is the nuclear magneton), is in good agreement with the previous studied $\mu = +0.261(2)$ μ_N of ^{199}Au ($Z = 79$, $N = 120$, and $I^\pi = 3/2^+$), which has the same valence proton orbit and the number of neutron. This result is consistent with the systematic trend of μ between the iridium and gold isotopes with smaller odd mass numbers (A). In the cases of ^{196}Ir ($N = 119$ and $I^\pi = (0, 1)^-$) and ^{198}Ir ($N = 121$ and $I^\pi =$ unknown), it is strongly suggested to be $I^\pi \geq 1$ from the smaller reduced χ^2 values for the fittings in the measured HFS spectra than that obtained with the assumption of $I = 0$. The μ values of $+0.23 \pm 0.03$ μ_N for ^{196}Ir and $+0.15^{+0.02}_{-0.03}$ μ_N for ^{198}Ir were obtained with the spin assumption of $I = 1$ as the best fitting results.

The variation of the nuclear mean-square charge radius and absolute value of the quadrapole deformation parameter $|\beta_2|$ were deduced from the isotope shifts evaluated from the measured HFS spectra. The $|\beta_2|$ values were calculated as $|\beta_2| = 0.129 \pm 0.009$, 0.14 ± 0.01, and 0.11 ± 0.01 fm^2 for ^{196,197,198}Ir, respectively, based on the $\beta_2 = +0.155$ of ^{191}Ir calculated by the FRDM model. The systematic trend of evaluated $|\beta_2|$ is consistent with that calculated by the FRDM model which suggests the prolate shape ($\beta_2 > 0$) for $A \leq 196$ isotopes and oblate shape ($\beta_2 < 0$) for $A \geq 197$ isotopes. On the other hand, the systematics of low-lying states in odd-A iridium isotopes with $A =$ 187–197 and previous laser spectroscopy study for $^{187-193}$Ir suggests the prolate shape for ^{197}Ir. It is necessary to measure the sign of β_2 to clarify the deformations and the shape transition in neutron-rich iridium isotopes.

To estimate the most probable I^π values and valence nucleon orbits of ^{196,198}Ir, the evaluated μ values were compared with the semi-empirical μ values calculated by using

the experimental g-factors of the neighboring nuclei, whose valence nucleons would have the same neutron or proton orbit with ^{196,198}Ir. The experimental μ values are reproduced with the assumption of $I^\pi = 1^-$ for both isotopes. The configurations of nuclear wave-functions are suggested to be $I^\pi = 1^-$ [πd3/2 $\otimes$ νp3/2 or νf5/2] for ^{196}Ir and $I^\pi = 1^-$ [πd3/2 $\otimes$ νp3/2] for ^{198}Ir.

1 Introduction

1.1 Nucleosynthesis

Light elements such as hydrogen, helium, and lithium are considered to be produced in Big Bang nucleosynthesis. The heavier elements than lithium are synthesized by the following astrophysical processes. The astrophysical processes and corresponding elemental abundances were considered by Hoyle, Fowler, Burbidge, and Burbidge in Ref. [1].

- Hydrogen burning: ^{4}He is synthesized by the fusion reaction of protons and the CNO cycle in the core of stars [2].
- Helium burning: ^{12}C and ^{16}O are synthesized by the triple-alpha process and alpha-capture process of ^{12}C(α,γ)^{16}O, respectively, after the core hydrogen burning [3]. Subsequent burning processes of sequential alpha-capture reaction and fusion reactions by the heavier elements continue until ^{56}Fe (which has maximum binding energy per nucleon) is synthesized.
- s-process: Neutron-capture process slower than β-decay occurs during helium and carbon burning phases with a temperature of $< 3 \times 10^8$ K and neutron density of $< 10^{11}$ cm^{-3} [4] in low-mass asymptotic giant branch stars and massive stars ($\geq 8M_\odot$. Here, $M_\odot$ is the solar mass.). Half the amounts of the stable and long-lived isotopes below ^{209}Bi can be synthesized along the β-stability line.
- rp-process: The nuclei near the proton drip-line up to ^{100}Sn are synthesized by the rapid proton capture process (rp-process) in explosive hydrogen burning such as novae and X-ray bursts [2].
- r-process: Approximately half of the elements heavier than iron are considered to be originated from a rapid neutron capture process (r-process) which occurs in the explosive astrophysical environments such as the core-collapse supernovae [5] and neutron star merger [6]. The astrophysical condition for the r-process are still not fully understood.

1.2 Blank spot on the r-process path

In the explosive astrophysical environment with a stellar temperature higher than 10^9 K and high neutron density higher than 10^{20} cm^{-3} [7], extremely neutron-rich nuclei are synthesized by sequential neutron capture as shown by the red boxes in Fig. 1. These neutron-rich nuclei on the r-process path eventually decay to the stable nuclei through the β-decays and β-delayed neutron emissions. The candidates of the astrophysical sites are considered to be core-collapse supernovae and neutron star merger. Recently, the gravitational waves from a binary neutron star inspiral were detected by the Advanced LIGO/Virgo detector network [8]. The observed multi-wavelength radiation spectra associated with the neutron star merger suggests the synthesis of heavy elements [9, 10]. However, it was difficult to reproduce the observed spectra due to poor nuclear data in this heavy region around $A = 195$ [9]. Systematic nuclear data is important to specify the astrophysical site and mechanism of the heavy element syntheses.

Observed isotope abundances in the solar-system (solar r-abundances), which are considered to be originated from the r-process, are shown at the upper left figure in Fig. 1. The peaks (labeled as 2nd and 3rd) at mass numbers $A \sim 130$ and 195 in the r-abundances

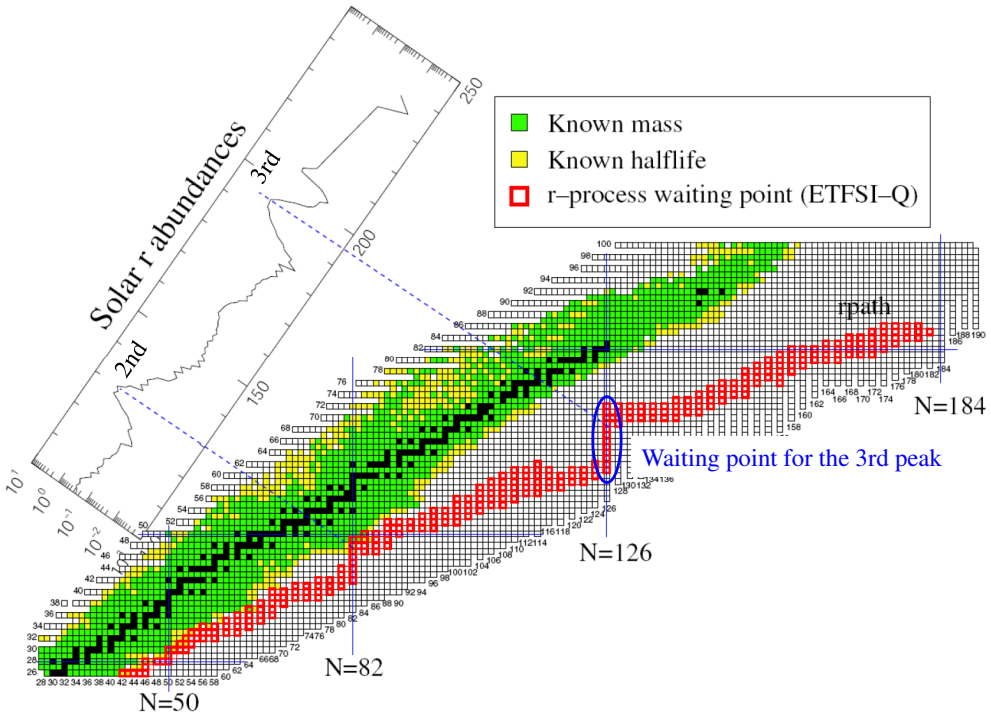

Figure 1: Expected r-process path and observed solar r-abundances (Fig. 18 from Ref. [2]). The r-process path indicated by the red boxes are based on a mass formula with the Extended Tomas Fermi plus Strutinsky Integral (ETFSI) mass model [11].

are originated from the r-process nuclei with neutron magic number $N_{\rm magic} = 82$ and 126. Due to the relatively small neutron separation energy such as a few MeV [11, 12] at $N_{\rm magic} + 1$ nuclei, neutrons are emitted from the nuclei by absorbing γ-rays. Therefore, neutron capture reaction (n, γ) at $N_{\rm magic}$ nuclei and photo-disintegration reaction (γ, n) at $N_{\rm magic} + 1$ nuclei become equilibrium. Consequently, the r-process path is extended to higher atomic (proton) number Z at $N = N_{\rm magic}$ up to break thorough nucleus whose β-decay rate (λ_β) is enough smaller than the (n, γ) reaction rate ($\lambda_{\mathrm{n},\gamma}$), $\lambda_\beta << \lambda_{\mathrm{n},\gamma}$. These nuclear region is called a waiting point. The waiting point for the third peak is the last bottleneck for the synthesis of actinoids in the r-process. The actinoids contribute to the final r-abundances through the fission.

The β-decay half-lives ($T_{1/2}$) of the $N_{\rm magic}$ nuclei are generally longer than those of the other r-process nuclei. Therefore, the time-scale of the r-process is determined by the half-lives of the $N_{\rm magic}$ nuclei. The neutron separation energies at a given stellar temperature and β-delayed neutron emission probabilities affect the location of the r-process path and the final r-abundances, respectively. These nuclear properties are important to reproduce the r-abundances and determine the stellar environment of the r-process.

Recently, the β-decay half-lives of the nuclei $Z = 45$–49 and $N_{\rm magic} = 82$, which are the waiting point nuclei for the second peak, were studied experimentally in Ref. [13]. The calculated r-abundances with newly measured half-lives gave good agreement with the observed solar r-abundances around the second peak and rare-earth region, and the astrophysical environment for the synthesis of the second peak and rare-earth elements were suggested. On the other hand, the waiting nuclei for the third peak such as ^{195}Tm ($Z = 69$) and ^{196}Yb ($Z = 70$) are too far from the β-stability line. It is impossible to access these nuclei experimentally without breakthrough. Therefore, the stellar environments for the formation of the third peak are still unknown.

1.3 Half-life predictions and elemental abundances

For the waiting point nuclei of the third peak, reliable theoretical predictions for the nuclear properties are required because the experimental access to those nuclei are quite difficult. In the nuclei around $N = 126$, Gamow-Teller (GT) and first-forbidden (FF) transitions compete as shown in Fig. 2. The proton orbits of the waiting point nuclei would be $\pi 0h_{11/2}$. The GT transition from the neutron orbit with $N \sim 126$ is only the transition from the $\nu 0h_{9/2}$ orbit.

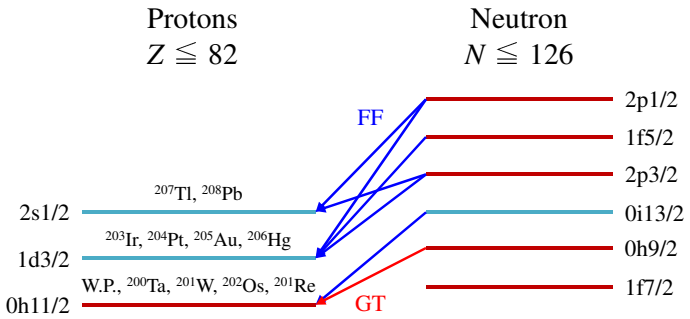

Figure 2: Gamow-Teller and first-forbidden decays in the nuclear region $Z \leq 82$ and $N \leq 126$. The blue and red arrows indicate the Gamow-Teller transition and first-forbidden transitions with the changing of the nuclear spin $\Delta I \leq 1$, respectively. The blue and red lines indicate the odd and even parity state, respectively. The proton orbits of the waiting point nuclei (W.P.) for the third peak are assumed to be $\pi 0h_{11/2}$ by the occupation according to the simple shell model orbits.

The competition between GT and FF transitions makes difficult the precise theoretical prediction of the half-lives as follows. The partial half-life of β-decay is given by

$$t_{1/2} = \frac{1}{f}\frac{\hbar}{m_e c^2}\frac{2\pi^3 \ln(2)}{G^2 |M_{\rm nucl}|^2}, \tag{1}$$

where f is a integrated Fermi function, G is a dimensionless parameter, and $M_{\rm nucl}$ is a nuclear matrix element. The physical constants $\hbar$, m_e, and c are the reduced Planck constant, mass of a stationary electron, and the speed of light, respectively. The dimensionless parameter G includes the coupling constant of weak interaction g as

$$G \sim \frac{m_e^2 c}{\hbar} g. \tag{2}$$

The nuclear matrix element $M_{\rm nucl}$ of GT and FF transitions are approximately expressed as

$$M_{\rm GT} = \int \psi_f^* \sum_k^A \tau_-^k \boldsymbol{\sigma} \psi_i d\tau \sim 1, \tag{3}$$

$$M_{\rm FF} \sim 0.01 M_{\rm GT}. \tag{4}$$

Here, ψ_i and ψ_f are the nuclear wave-functions of initial and final states, and τ_- and $\boldsymbol{\sigma}$ are the isospin and spin operators, respectively. The integrated Fermi function f with ignoring the coulomb interaction is approximately expressed as

$$f \sim \frac{E_{\rm max}^5}{30}, \tag{5}$$

where $E_{\rm max}$ is the total energy of a lepton system. The $E_{\rm max}$ is the sum of the transition energy Q_β and rest energy of an electron $m_{\rm e}c^2$. Therefore, only the change of 100 keV for $E_{\rm max}$ causes more than twice larger contribution of FF transition. The β-decay half-life strongly depends on the competition of the strength distributions of GT and FF transitions, namely, the detail of the nuclear wave-functions of the initial and final states, and Q_β.

Figure 3 shows the half-lives of $N = 126$ nuclei predicted by the theoretical models: KTUY mass model [14, 15], finite-range droplet model (FRDM) [16, 17], shell model (SM) [18], and DF3 + CQRPA model [19, 20]. The FF transitions are included in all the models. The SM results with and without the FF transitions are indicated by the blue open and close circles in Fig. 3. The predicted half-lives including the FF transitions become shorter than those with the pure GT transitions because the transition energies of the FF transitions are higher than those of GT transitions. The predicted half-lives are deviated from a factor of three to more than one order of magnitude between the theoretical models. The experimental results for Pt, Au, and Hg, which are indicated by the black squares in Fig. 3, were well reproduced by the DF3 + CQRPA model. There are no data for the nuclei with $Z \leq 77$.

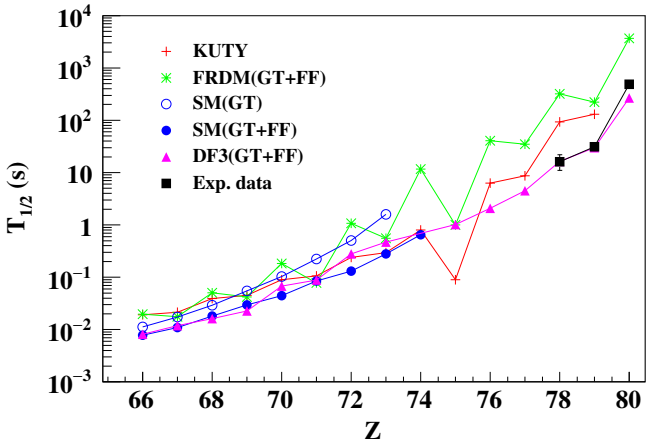

Figure 3: Predicted half-lives of $N = 126$ nuclei by theoretical models. The measured half-lives of Pt, Au, and Hg, which are indicated by the black squares, were taken from National Nuclear Data Center (NNDC) [21].

The half-lives of waiting point nuclei strongly affect the final r-abundances [22]. Figure 4 [23] shows the sensitivity of r-abundances around the third peak to the half-lives of the waiting point nuclei with $N = 126$. The relative amplitude of the r-abundances were calculated with three half-life patterns for the $N = 126$ nuclei: $3 \times \Sigma T_{1/2}$, $\Sigma T_{1/2}$, and $1/3 \times \Sigma T_{1/2}$. The position, width, amplitude of the third peak and the amplitude of heavier nuclei were drastically changed in association with the half-lives of the $N = 126$ nuclei. The longer half-lives cause higher amplitude at lower mass number and wider peak width because the condition of $\lambda_\beta << \lambda_{\rm n,\gamma}$ is achieved at lighter nuclei among the $N = 126$ nuclei. The fraction of heavier nuclei (typically, $A = 209$) relative to the third peak (most intense nuclei) is changed by a factor of ~ 0.5 (green), 0.8 (blue), and 5 (red). This indicates the drastic changing of the amount of fission recycling because the $N = 126$ nuclei are the last bottleneck for the synthesis of actinoids in the r-process. Therefore, for the understanding of astrophysical environment for the formation of the third peak and the contribution of the fission recycling, it is essential to measure the half-life with the accuracy of $< 30\%$ for the nuclei with $N = 126$. However, the waiting point nuclei with $N = 126$ are inaccessible experimentally. Thus, reliable theoretical predictions are

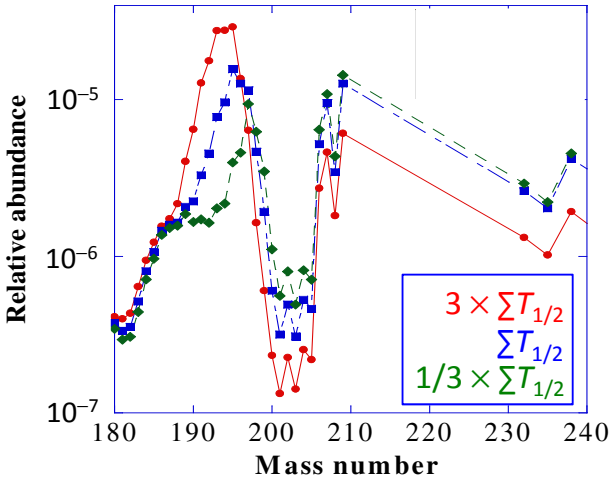

Figure 4: Calculated relative abundances around the third peak with three half-life patterns for the $N = 126$ nuclei [23]. The neutrino driven wind model was used as the element synthesis model.

required for the inaccessible nuclei. The experimental investigation of nuclear property for the nuclei with $71 \leq Z \leq 80$ and $114 \leq N \leq 126$ is quite important for the selection of reliable theoretical model and improvement of theoretical precision.

1.4 Systematic study of nuclear structure in the vicinity of $N = 126$

There are two important parameters of $f(E_{\rm max})$ and $|M_{\rm nucl}|^2$ in Eq. (1) to predict the partial half-life $t_{1/2}$. The $E_{\rm max}$ can be determined from a mass measurement by using multi-reflection time-of-flight mass spectrograph (MR-TOF), penning trap, storage ring devices. Nuclear matrix element $|M_{\rm nucl}|^2$ in Eq. (3) strongly depends on the nuclear wave-functions of initial and final states. The nuclear wave-functions can be investigated through the nuclear electromagnetic moments which are sensitive to the nuclear wave-functions. Therefore, the measurements of nuclear electromagnetic moments are desirable to confirm and improve the accuracy of the theoretical predictions for the nuclear wave-functions and half-lives. The details of the relation between the nuclear wave-function and magnetic dipole moment is explained in Appendix D.

The electromagnetic moments mainly magnetic dipole moment μ and electric quadrupole moment Q of ground and isomeric states are directly deduced from the hyperfine structures measured by laser spectroscopy. Then, it is possible to estimate the wave-function of an initial state in β-decay precisely. (The wave-functions of a final states are also required to determine the half-lives. These can be investigated by β-γ spectroscopy or transfer reactions.) Figure 5 shows the research results [24] of the electromagnetic moments for the ground state of Hf–Pt nuclei which are the heavier nuclei than the waiting point nuclei of the third peak. These studies were performed for the stable isotopes (black colored), long-lived isotopes (green colored), and the neutron-deficient nuclei by using various methods such as atomic beam magnetic resonance, nuclear magnetic resonance, and laser spectroscopy etc. The neutron-rich nuclei of the refractory elements remain unexploited. The strong competition between the allowed GT and FF transitions in this unexploited region are expected. The study of the nuclear wave-functions of the initial state in β-decay through the electromagnetic moments are essential to understand the competition and improve the theoretical models.

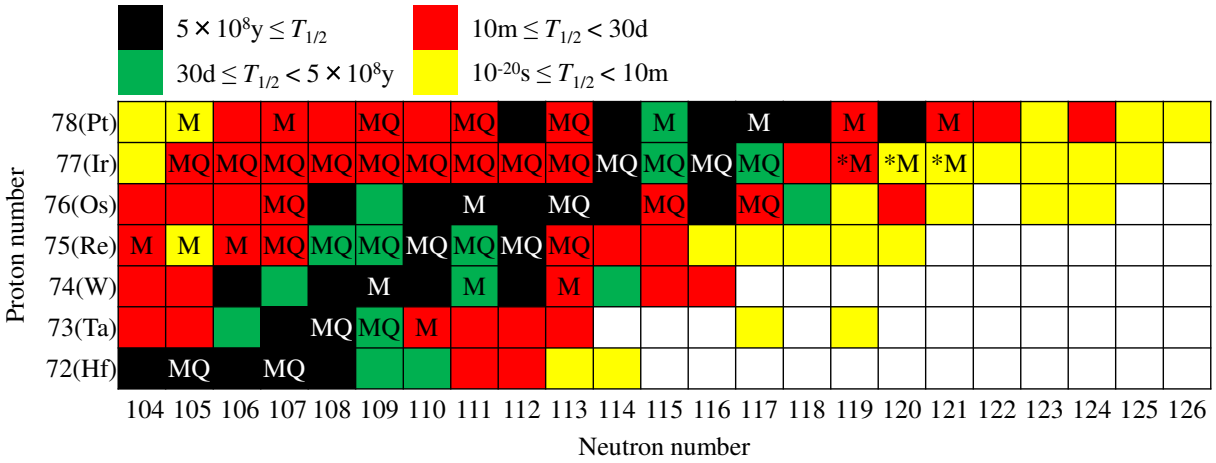

Figure 5: Previous studies of the electromagnetic moments for the ground state of refractory elements. The experimental results of electromagnetic moments are compiled in Ref. [24]. The color code indicates the β-decay half-life. "M" and "Q" indicate that the magnetic dipole moment and electric quadrupole moment have been measured. The nuclei labeled "*M" were studied in the present work.

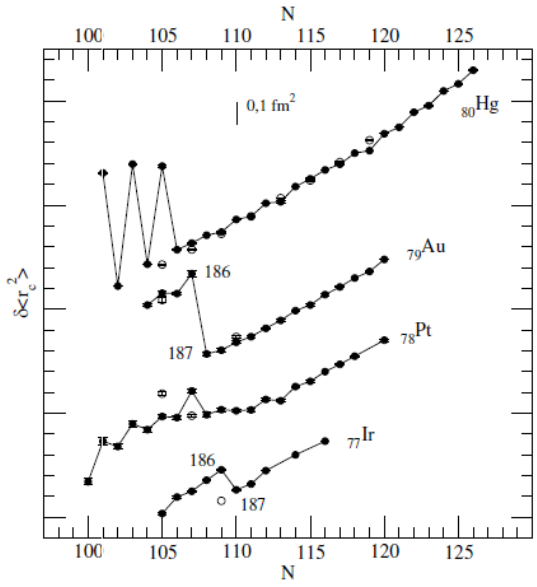

Figure 6: The variation of the mean-square charge radii $\delta\langle r_c^2\rangle$ of Ir, Pt, Au, and Hg obtained by laser spectroscopy (Fig. 14 in Ref. [26]). The open circles indicate the isomeric states.

From the HFS measurement by laser spectroscopy, the variation of the nuclear mean-square charge radius and quadrupole deformation parameter β_2 between isotopes can also be deduced by applying the liquid-drop model [25]. Figure 6 shows the variations of the nuclear mean-square charge radii of iridium ($Z = 77$) [26], platinum ($Z = 78$) [27], gold ($Z = 79$) [28, 29, 30, 31, 32], and mercury ($Z = 80$) [33] isotopes studied by laser spectroscopy. In the neutron-deficient nuclei, the nuclear shape transitions and the change of nucleon orbits were found.

The large deviations of the charge radii in ^{181,183,185}Hg (spin-parity value $I^\pi = 1/2^-$) from the even-A Hg isotopes has been understood by shape staggering from small oblate deformation ($\beta_2 > -0.17$) for even-A Hg isotopes to strong prolate deformation ($\beta_2 > +0.25$) for odd-A Hg isotopes [33]. The most probable candidate of valence neutron orbit

in ^{181,183,185}Hg is $1/2^-[521]$. The shape transition is induced by the smaller loss of pairing energy in the prolate minimum where the valence neutron blocks the state around the Fermi level [34].

The large sudden change of the charge radius was also observed in gold isotopes between ^{186}Au and ^{187}Au, and the shape transition from strong prolate deformation ($A \leq 186$, $\beta_2 \sim +0.25$) to oblate deformation ($A \geq 187$, $\beta_2 > -0.16$) was suggested [30, 31]. The main spherical origins of proton orbit are considered to be intruder $h_{9/2}$ for $A \leq 186$, mixing between $s_{1/2}$ and $d_{3/2}$ for $A = 187$–190, and $d_{3/2}$ for $A \geq 191$. The nuclear electromagnetic moments of gold isotopes with $183 \leq A \leq 197$ were well reproduced by a particle-triaxial-rotor model calculation including the hexadecapole deformation [32]. They suggest the shape transitions as prolate deformation for $A \leq 186$, oblate deformation for $187 \leq A \leq 190$, and triaxial deformation for $191 \leq A \leq 197$.

The relatively smaller change of the charge radius between ^{186}Ir and ^{187}Ir than that between ^{186}Au and ^{187}Au was observed as a sudden increase of $|\beta_2| > 0.2$ for $A \leq 186$ and a decrease of $|\beta_2| < 0.17$ for $A \geq 187$ [26]. The evaluated magnetic dipole moment μ and electric quadrupole moment Q were compared with the theoretical calculations by a rotor core (osmium, $Z = 76$) plus one or two quasi-particles model with a reasonable assumption of the prolate deformation for all the isotopes. As the result, it was found that the change of dominant proton orbit occurs between $1/2^-[541]$ stemmed from the intruder $h_{9/2}$ for $A \leq 186$ and $3/2^+[402]$ for $A \geq 187$. The suggested dominant configurations for iridium isotopes are summarized in Table 1. In the cases of ^{187,189,191,193}Ir ($I^\pi = 3/2^+$), measured μ values were well reproduced by $3/2^+[402]$ proton orbit with effective spin g-factor $g_s^{\rm eff} = 0.6$–$1.0 g_s$, where g_s ($= 5.586$) is spin g-factor of a proton. The electric quadrupole moments of these isotopes suggest the mixture of $K = 1/2$ component with several %, where K is a projection of the nuclear spin to the deformation axis. In the cases of ^{183,185}Ir ($I^\pi = 5/2^-$), the mixed state of $1/2^-[541]$ ($\sim$80%) and $3/2^-[532]$ ($\sim$20%) proton orbits, which are $h_{9/2}$ origin, with $g_s^{\rm eff} = 0.6 g_s$ shows decent agreement for μ, and reproduces the ground state rotational bands. In the cases of odd-odd Ir isotopes, the dominant proton orbit is $3/2^+[402]$ for ^{186m,188}Ir and $1/2^-[541]$ for ^{182,184,186g}Ir. For ^{186m,188}Ir, the good agreement for μ and Q are obtained with the following neutron orbits: $7/2^-[503]$ with $K = 2$ for ^{186m}Ir, and $1/2^-[510]$ and $3/2^-[512]$ with $K = 1$ for ^{188}Ir. For ^{182,184,186g}Ir, the complex configurations including the mixing of different K configurations were suggested, and the measured μ values were well reproduced except for ^{184}Ir.

The shape transition was suggested in unexploited neutron-rich nuclei [12, 35]. It is important to study the nuclear structure and to reveal the deformation for them because the shape transition and sudden change of β_2 indicate the changing of valence proton or neutron orbit as seen in lighter isotopes of Ir–Hg.r As the first onset of the nuclear structure study (investigation of nuclear wave-functions) to improve the nuclear theoretical models in the half-life predictions for the clarification of the astrophysical environments of r-process, we performed the HFS measurements of $^{196-198}$Ir by in-gas-cell laser ionization spectroscopy.

1.5 Outline of the present work

KEK isotope separation system (KISS) is an experimental device which can produce the neutron-rich nuclei of the refractory elements. KISS is an on-line isotope separator (ISOL), which makes use of a laser ion source combined with an argon gas cell to accumulate the target-like fragments of the MNT products. In the present work, in-gas-cell laser ionization spectroscopy of $^{196-198}$Ir were performed by using KISS. These nuclei were produced

Table 1: The suggested dominant (> 10%) configurations for iridium isotopes in Ref. [26]. The configurations of ^{183}Ir is not shown explicitly, but the same conclusion with ^{185}Ir is suggested.

A	I^π	Proton orbit	Neutron orbit	K-value	Fraction
193	$3/2^+$	$3/2^+[402]$ ($d_{3/2}$)	-	3/2	> 90%
191	$3/2^+$	$3/2^+[402]$ ($d_{3/2}$)	-	3/2	> 90%
189	$3/2^+$	$3/2^+[402]$ ($d_{3/2}$)	-	3/2	> 90%
188	1^-	$3/2^+[402]$ ($d_{3/2}$)	$1/2^-[510]$ ($f_{5/2}$)	1	82.6%
187	$3/2^+$	$3/2^+[402]$ ($d_{3/2}$)	-	3/2	> 90%
186m	2^-	$3/2^+[402]$ ($d_{3/2}$)	$7/2^-[503]$ ($h_{9/2}$)	2	99.6%
186g	5^+	$1/2^-[541]$ ($h_{9/2}$)	$1/2^-[510]$ ($f_{5/2}$)	0	24.4%
		$1/2^-[541]$ ($h_{9/2}$)	$1/2^-[510]$ ($f_{5/2}$)	1	13.1%
		$1/2^-[541]$ ($h_{9/2}$)	$3/2^-[512]$ ($p_{3/2}$)	1	19.4%
		$1/2^-[541]$ ($h_{9/2}$)	$3/2^-[512]$ ($p_{3/2}$)	2	18.9%
185	$5/2^-$	$1/2^-[541]$ ($h_{9/2}$)	-	1/2	85.5%
		$3/2^-[532]$ ($h_{9/2}$)	-	1/2	14.5%
184	5^-	$1/2^-[541]$ ($h_{9/2}$)	$9/2^+[624]$ ($i_{13/2}$)	5	50.3%
		$1/2^-[541]$ ($h_{9/2}$)	$9/2^+[624]$ ($i_{13/2}$)	4	44.4%
182	3^+	$1/2^-[541]$ ($h_{9/2}$)	$1/2^-[521]$ ($p_{3/2}$)	0	40.5%
		$1/2^-[541]$ ($h_{9/2}$)	$1/2^-[521]$ ($p_{3/2}$)	1	48.6%

by the multi-nucleon transfer (MNT) reactions of ^{136}Xe beam (9.4 MeV/nucleon) and ^{198}Pt target. The reaction products are collected, neutralized, and laser-ionized element-selectively in the argon gas cell of KISS, and mass separated by the ISOL. The selected nuclei are transported to a detector system for the β-γ spectroscopy. The HFS measurement of unstable nuclei can be performed in KISS by measuring the number of β-rays emitted from the laser-ionized nuclei as a function of the laser wavelength. The principle of experimental methods for the MNT reactions and laser spectroscopy at KISS are explained in section 2. The details of the experimental setup are given in section 3. The experimental results are shown in section 4. The discussion about obtained magnetic moments, nuclear deformations, and comparison with theoretical models are given in section 5.

2 Experimental methods

2.1 Multi-nucleon transfer reactions for the production of nuclei around $N = 126$

There are three methods to produce the nuclei around $N = 126$ and $A = 200$: projectile fragmentation reactions, spallation reactions and multi-nucleon transfer (MNT) reactions. In projectile-fragmentation reactions, the nuclei are produced as projectile-like fragments from the collision between heavy projectile (typically ^{238}U or ^{208}Pb) with relativistic energy higher than 100 MeV/nucleon and light target nucleus (typically ^{9}Be) [36, 37]. In spallation reactions, the nuclei are produced from the spallation of heavy target nuclei (UCx or Ta) by impinging proton beam [38, 39]. In MNT reactions, the nuclei are produced as target-like fragments from multi-nucleon transfer between neutron-rich beam with low energy of 10 MeV/nucleon (^{136}Xe) and neutron-rich heavy target (^{198}Pt or ^{208}Pb) [40, 41, 42]. These production and particle identification are explained in the next subsections. We compared the features of these method and show the advantage of the MNT reaction for the production of nuclei around $N = 126$.

2.1.1 Projectile fragmentation reactions combined with in-flight separation

The projectile-like fragments have nearly the same velocity with that of projectile. The fragments are spatially and temporally separated by using an in-flight separator. Mass number (A) and atomic number (Z) of the projectile are separated by using electromagnetic dipoles and wedge-shaped energy degrader, and the identification of the fragments is achieved by TOF-$B\rho$-ΔE method. Plastic scintillators, multi-sampling ionization chambers and multi-wire proportional chambers are used to measure the time-of-flight (TOF) and energy loss in a detector (ΔE), respectively. This method is applied at the facilities such as BigRIPS at RIKEN and FRS at GSI. Projectile fragmentation reactions of ^{238}U (350 MeV/nucleon) beam and ^{9}Be (5 mm in thickness) target, and ^{208}Pb (1 GeV/nucleon) beam and ^{9}Be (14 mm in thickness) target are used in BigRIPS at RIKEN [36] and FRS at GSI [37], respectively.

The high-energy projectile-like fragments in FRS makes possible to clear Z separation, because all the ions with atomic number up to $Z = 82$ are fully stripped due to the high velocities such as 1 GeV/nucleon, and there is a simple charge state distribution based on the simple relation $A/q \sim A/Z$, where q is a ionic charge. Therefore, the particle identification of A and Z selection is performed accurately. On the other hand, in BigRIPS, the charge state distribution of projectile-like fragments becomes broad because of the relatively low-velocity fragments. Therefore, particle identification is difficult due to the insufficient Z separation.

The features of the reactions for the production of ^{202}Os as an example are listed in Table 2. Transmission efficiency of separators are assumed to be 10% in both facilities. The unknown production cross-section of ^{202}Os in the ^{208}Pb + ^{9}Be system at GSI is assumed less than 1.6 μb from the measured cross-section of ^{200}Os in the same reaction system [43]. Estimated production yields of ^{202}Os at the final focal planes are 0.0068 particles per second (pps) and 0.034 pps in the case of ^{238}U + ^{9}Be and ^{208}Pb + ^{9}Be, respectively.

2.1.2 Spallation reaction combined with Isotope Separator On-Line (ISOL)

The spallation products with the thermal energy (typically 2300 K) are diffused out from the target material, and guided to an ionization region. Surface ionization or hot-cavity

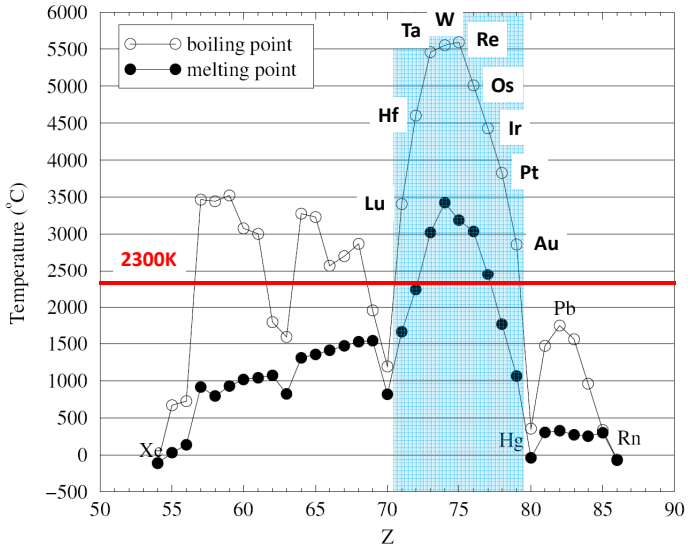

Figure 7: Melting and boiling temperatures for the elements from Xe to Rn [26].

type laser ionization are commonly performed for ionization of the reaction products. After the acceleration of the ions by an electric field of several tens kV, A and Z are separated by an analyzing magnet with high resolving power such as 10,000 at ISOL facilities such as ISOLDE at CERN [44] and ISAC at TRIUMF [45].

Figure 7 shows melting and boiling temperatures for the elements from Xe to Rn [26]. As shown in Fig. 7, the elements with $Z = 72$–77, which have the melting points higher than typical ion-source temperature 2300 K, can not diffuse out from the target. Moreover, it is difficult to produce neutron-rich nuclei in this region ($Z = 72$–77) from the UCx spallation. Therefore, the nuclear and laser spectroscopy for the neutron-rich nuclei in the region have not been performed at the ISOL facilities. In the ISOLDE, the neutron-deficient iridium isotopes were produced from the β^+/EC or α decay of the extracted Hg isotopes [26]. However, neutron-rich isotopes of these refractory elements have not been produced.

2.1.3 Multi-nucleon transfer reactions: ^{136}Xe + ^{198}Pt

The nuclei around $N = 126$ are produced by using a multi-nucleon transfer (MNT) reaction of ^{136}Xe and ^{198}Pt. The MNT reactions are occurred when the beam with an energy of ∼10 MeV/nucleon impinge on a target as shown in Fig. 8. Some neutrons and protons are transfered between beam and target nuclei. Many nuclides are produced by the various patterns of nucleon transfer. The evaluated production cross-sections of the nuclei with $N = 126$ and $Z \leq 78$ are more than 10^3 times higher than those by fragmentation reactions of ^{208}Pb [41].

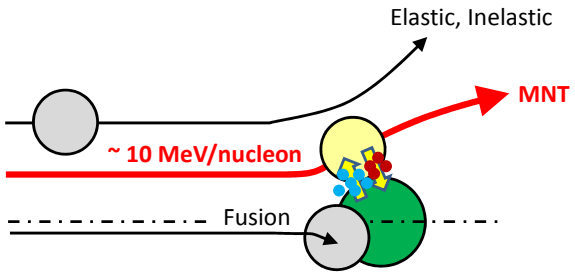

Figure 8: Schematic view of MNT reactions.

Figure 9 shows the excitation function of target-like fragments (TLFs) ^{196,197,198}Ir, which were the nuclei studied in this thesis, via MNT reactions of ^{136}Xe + ^{198}Pt calculated by using a GRAZING code [42]. The reaction energy of $\geq$ 7 MeV/nucleon are required to achieve the almost maximum production cross-section. Figure 10 shows the angular and energy distributions of the ejected TLFs from the target with optimized beam energy of 9.4 MeV/nucleon and target thickness of 12.5 mg/cm^2. The produced TLFs are emitted from the target foil with large azimuthal angles around 65° $\pm$ 10° with respect to the primary beam axis in the laboratory frame due to the reactions around the grazing angles as shown in left panel of Fig. 10. The kinetic energies of TLFs are distributed from zero to 1.5 MeV/nucleon as shown in right panel of Fig. 10. It is because of the broaden recoil energies by energy losses of the beam in the target material and the energy losses of the TLFs in the target material. Therefore, the use of in-flight separator, which typical angular and momentum acceptance are $\leq$ 6° and $\leq$ 6%, respectively, is inadequate for the separation of the TLFs of MNT reactions. KEK isotopes separation system (KISS) has been developed for the extraction and separation of the TLFs by MNT reactions.

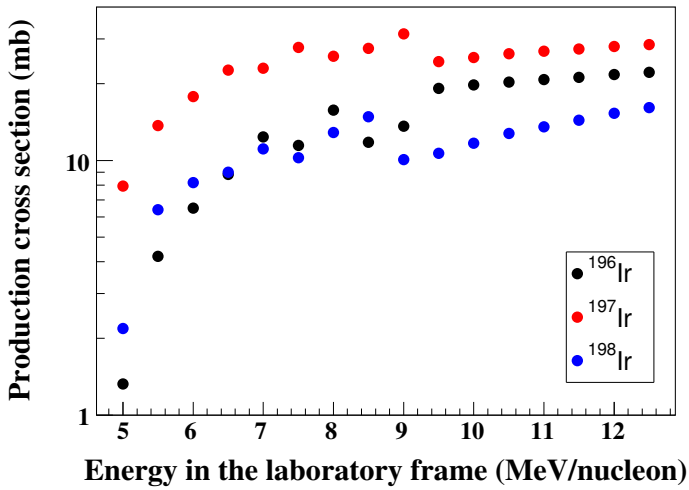

Figure 9: Excitation functions for the production cross-sections of ^{196,197,198}Ir via the MNT reactions of ^{136}Xe + ^{198}Pt calculated by using the GRAZING code.

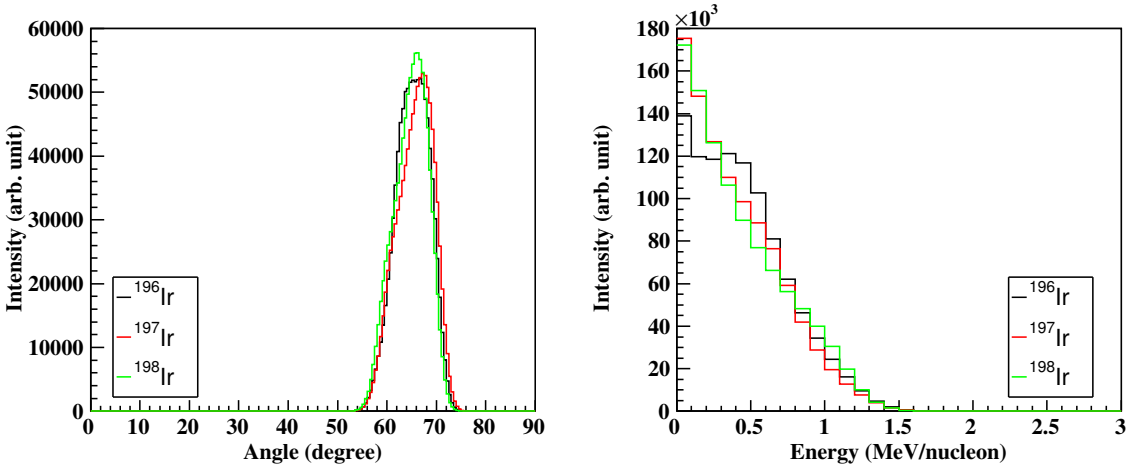

Figure 10: Emission angle distribution (left panel) and energy distribution (right panel) of ^{196,197,198}Ir from the target with optimized beam energy of 9.4 MeV/nucleon and target thickness of 12.5 mg/cm^2.

The production and extraction of ^{202}Os produced by the MNT reaction at KISS is summarized in Table 2. The highest yield is obtained with an effective target thickness of 2 mg/cm^2 at the reaction energy of 8 MeV/nucleon in the case of ^{202}Os. The ^{136}Xe beam with an intensity of 250 pnA and energy of 10.75 MeV/nucleon is available at RIKEN ring cyclotron (RRC) of RIKEN Nishina center (RNC) in RIKEN. As mentioned in later subsection 3.1.3, the primary beam energy is reduced from 10.75 MeV/nucleon to 9.4 MeV/nucleon by passing through the titanium foils with a total thickness of 9 μm. The typical overall efficiency of the system and signal-to-noise ratio (S/N) are 10^{-3} and 300, respectively. Detailed performances of KISS are explained in section 3. The extraction yield of ^{202}Os at KISS is estimated to be more than five times higher than that by fragmentation reactions of ^{208}Pb and ^{238}U combined with in-flight separators.

Table 2: Comparison of the production yields of ^{202}Os by three reaction systems. The rations with respect to the values at KISS are shown.

Production mechanism	KISS MNT	GSI FRS ^{208}Pb Fragmentation	RIKEN BigRIPS ^{238}U Fragmentation
Cross-section (μb)	21	< 0.016 [43]	4.4×10^{-6} [46]
ratio	1	7.6×10^{-4}	2.1×10^{-7}
Target thickness (g/cm^2)	0.002, ^{198}Pt	2.5, ^{9}Be	0.92, ^{9}Be
ratio	1	2.8×10^{4}	10^{4}
Beam intensity (pnA)	200	0.02	40 [47]
ratio	1	10^{-4}	0.2
Efficiency	10^{-3}	10^{-1}	10^{-1}
ratio	1	10^{2}	10^{2}
S/N (Beam purity)	300 (99.7%)	good	Z separation is not good.
Total ratio	1	< 0.2	0.04

2.2 KEK Isotope Separation System

It is essential to accumulate the TLFs and extract one isotope with high efficiency, which has specific atomic number (Z) and mass number (A), to perform the precise nuclear spectroscopy. For the effective collection and separation of TLFs, a gas catcher system combined with mass separator was proposed. The KEK Isotope Separation System (KISS), which was designed according to the above strategy, has been developed at RNC by Wako Nuclear Science Center (WNSC/KEK).

Figure 11 shows schematic view of KISS. ^{136}Xe primary beam (10.75 MeV/nucleon, 250 pnA at maximum) is provided from the RRC with RINAC2 injection. The ^{136}Xe beam is impinged on the ^{198}Pt target for the MNT reactions. The TLFs recoiled out from the target are implanted into the gas cell filled with argon gas of several tens kPa. TLFs are stopped and neutralized in the gas cell, and then are transported to an laser ionization region by argon gas laminar flow. Neutral atoms are ionized by using element-selective laser ionization technique (Z separation) near the gas cell exit. Ions of interest element

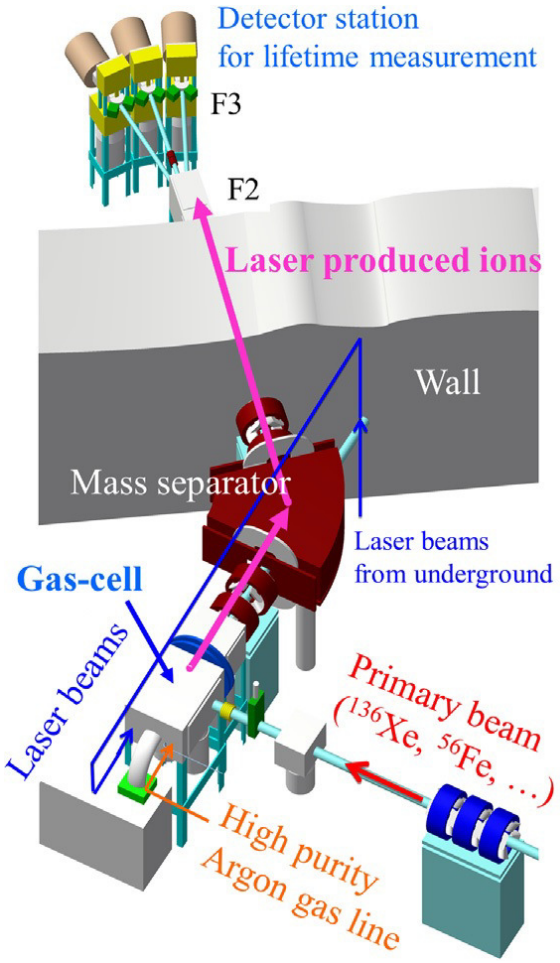

Figure 11: Schematic view of KISS.

are accelerated by an electric field of 20 kV, and then mass number is selected by using the dipole magnet (A separation). The typical mass resolving power of the magnet is $M/\Delta M = 900$, and is enough high to separate an isotope of $A \sim 200$ with a distance larger than 10σ from the neighboring isotopes. Purified radioactive beam is transported to the detector system to perform β-γ spectroscopy. Details of each part in KISS are explained in section 3.

2.3 Hyperfine Structure

Nucleus has electromagnetic moments induced by charge density in the nucleus, orbital motion of proton, and magnetic moment of nucleon. The electromagnetic interaction between electromagnetic field induced by orbital electrons and electromagnetic moment of the nucleus causes hyperfine structure (HFS) in an atomic state. The interaction with magnetic dipole or electric quadrupole moments of nucleus resolve the degeneracy of the atomic energy level and induces large energy shifts for the atomic energy levels as shown in Fig. 12. Here, a new total angular momentum $\boldsymbol{F}$ of an atomic state is defined as a coupling of the angular momenta of the electrons ($\boldsymbol{J}$) and the nucleus ($\boldsymbol{I}$) by the hyperfine interaction. The angular momentum of atom is $\boldsymbol{F} = \boldsymbol{I} + \boldsymbol{J}$. The quantum number of $\boldsymbol{F}$ has the values in the range of $|J - I| \leq F \leq |J + I|$. The number of splittings is $2I + 1$ in the case of $I \leq J$ and is $2J + 1$ in the case of $I > J$. These nuclear electromagnetic moments can be evaluated from the experimental study of HFS.

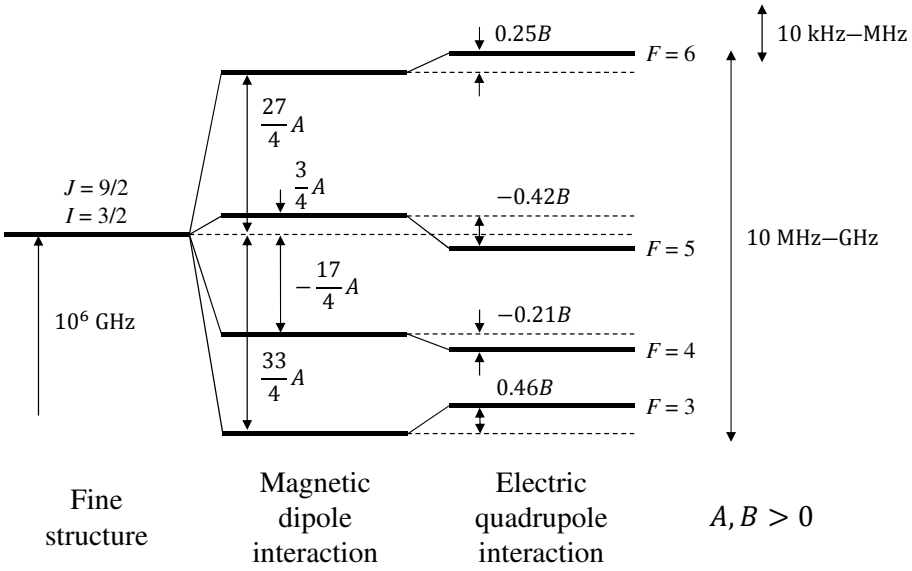

Figure 12: Hyperfine structure in the case of an atomic spin $J = 9/2$ and nuclear spin $I = 3/2$.

2.3.1 Magnetic dipole moment

The interaction energy between a nuclear magnetic dipole moment $\boldsymbol{\mu}$ and the magnetic field $\boldsymbol{H}$ generated by the orbital electrons at the position of nucleus is given by

$$\begin{aligned} W_{\mathrm{M1}} &= -\boldsymbol{\mu} \cdot \boldsymbol{H} \\ &= -\mu H_J(0) \cos(\widehat{\boldsymbol{I}, \boldsymbol{J}}), \end{aligned} \tag{6}$$

where $\widehat{\boldsymbol{I}, \boldsymbol{J}}$ is the angle between $\boldsymbol{I}$ and $\boldsymbol{J}$, and $H_J(0)$ is time averaged magnetic field generated by the orbital electrons at the position of nucleus. The μ is expressed in the unit of nuclear magneton μ_{N}. Eq. (6) can be rewritten by

$$\Delta E_{\mathrm{M1}} = \frac{A_{\mathrm{HF}}}{2} \cdot (F(F+1) - I(I+1) - J(J+1)) \cdot h, \tag{7}$$

$$A_{\mathrm{HF}} = \frac{\mu H_J(0)}{IJ}, \tag{8}$$

where h is the Planck constant and A_{HF} is called as hyperfine coupling constant.

2.3.2 Electric quadrupole moment

Nucleus with $I > 1/2$ and axially symmetric deformation has an electric quadrapole moment. The moment also induces the atomic energy shift due to the HF interaction. The interaction energy between a nuclear electric quadrupole moment and an external electric field is given by

$$W_{\mathrm{E2}} = -\frac{eQ_0\phi(0)}{4} \frac{(3\cos^2(\Theta) - 1)}{2}, \tag{9}$$

where eQ_0 is intrinsic nuclear electric quadrupole moment, $\phi(0)$ is static external electric field gradient at the position of nucleus, and Θ is the angle between space fixed z-axis and deformation axis. Quadrapole interaction energy for an atomic system becomes,

$$W_{\mathrm{E2}} = -\frac{eQ\phi_J(0)}{4} \frac{(3\cos^2(\widehat{\boldsymbol{I}, \boldsymbol{J}}) - 1)}{2}, \tag{10}$$

where eQ is nuclear quadrupole moment to nuclear spin axis and $\phi_J(0)$ is time averaged electric field gradient generated by the orbital electrons at the position of nucleus. The unit of b (barn, 1 b = 10^{-24} cm^2) is used for Q. Eq. (10) can be rewritten by

$$\Delta E_{\mathrm{E2}} = \frac{B_{\mathrm{HF}}}{2} \cdot \frac{3C(C+1) - 2I(I+1)2J(J+1)}{2I(2I-1)2J(2J-1)} \cdot h \quad \left(I, J > \frac{1}{2}\right), \tag{11}$$

$$C = F(F+1) - I(I+1) - J(J+1), \tag{12}$$

$$B_{\mathrm{HF}} = eQ\phi_J(0). \tag{13}$$

where B_{HF} is also called as hyperfine coupling constant.

The total energy shift of an atomic state induced by the dipole magnetic and electric quadrapole interactions is expressed as

$$\Delta\nu_F = \Delta\nu_{\mathrm{M1}} + \Delta\nu_{\mathrm{E2}}. \tag{14}$$

The energy shifts induced in both the ground and excited states are expressed as $\Delta\nu_{F_{\mathrm{gs}}}$ and $\Delta\nu_{F_{\mathrm{ex}}}$, respectively. Finally, the transition frequency between the hyperfine levels in the ground and excited states is given by

$$\nu_i = \Delta\nu_{F_{\mathrm{ex}}} - \Delta\nu_{F_{\mathrm{gs}}} + \nu_0, \tag{15}$$

where ν_0 is the transition frequency between two fine structures (the center of gravity frequency for the transitions).

The electric dipole transition (E1 transition) induced by one photon of the excitation laser with the wavelength λ_1 is governed by the following selection rule:

$$\Delta J = 0, \pm 1 \ (J = 0 \to 0 \text{ is forbidden transition}), \tag{16}$$

namely,

$$\Delta F = 0, \pm 1 \ (F = 0 \to 0 \text{ is forbidden transition}). \tag{17}$$

2.4 Isotope shift

A finite nuclear mass and size affect atomic energy levels by the hyperfine interaction, and induce the energy difference between the isotopes of a certain element. The change of the transition energies between the isotopes is called an isotope shift. The isotope shift consists of the two components included by the following two effects: the change of the reduced mass of a nucleus-electron system (mass effect, $\delta\nu_{\mathrm{MS}}^{AA'}$) and the change of nuclear size (volume effect, $\delta\nu_{\mathrm{FS}}^{AA'}$). Therefore, the isotope shift is expressed as

$$\delta\nu_{\mathrm{IS}}^{AA'} = \delta\nu_{\mathrm{MS}}^{AA'} + \delta\nu_{\mathrm{FS}}^{AA'}. \tag{18}$$

In the following subsections, we discuss the details of the effects.

2.4.1 Mass effect

The change of the reduced mass of a nucleus-electron system affects to the motion of electrons. The shift of transition frequency by the mass effect between the isotopes with mass numbers A and A' is given by

$$\delta\nu_{\mathrm{MS}}^{AA'} = \delta\nu_{\mathrm{NMS}}^{AA'} + \delta\nu_{\mathrm{SMS}}^{AA'}, \tag{19}$$

where the first and second terms are called a normal mass shift and specific mass shift, respectively. The details of these two shifts are explained in the following paragraphs.

The Schrödinger equation for a non-relativistic N_e-electron system with a finite nuclear mass M_A is written in the center of gravity system ([48], page 199–200) as follows:

$$\left[\frac{1}{2\mu_{\rm M}}\sum_i^{N_e} p_i^2 + \frac{1}{M_A}\sum_{i<j}^{N_e} \boldsymbol{p}_i\cdot\boldsymbol{p}_j + \sum_i^{N_e} V_{e\text{-}N}(\boldsymbol{r}_i) + \sum_{i<j}^{N_e} V_{e\text{-}e}(\boldsymbol{r}_i-\boldsymbol{r}_j)\right]\Psi = E_\mu\Psi, \qquad (20)$$

where $\boldsymbol{p}_i$ and $\boldsymbol{r}_i$ are the momentum and coordinate of the ith electron, respectively, and $\mu_{\rm M}$ is the reduced mass between the electron and nucleus. These are given by

$$\begin{aligned} \boldsymbol{p}_i &= \frac{\hbar}{i}\nabla_i, & (21)\\ \boldsymbol{r}_i &= \boldsymbol{R}_i - \boldsymbol{R}_0, & (22)\\ \mu_{\rm M} &= \frac{m_{\rm e}M_A}{m_e+M_A}. & (23) \end{aligned}$$

Here, $\boldsymbol{R}_i$ and $\boldsymbol{R}_0$ are the coordinates of the ith electron and the nucleus in the laboratory coordinate system, respectively. $V_{e\text{-}N}(\boldsymbol{r}_i)$ and $V_{e\text{-}e}(\boldsymbol{r}_i-\boldsymbol{r}_j)$ are the two-body coulomb interaction term between the nucleus and electron and between electrons, respectively. $\boldsymbol{r}_i$ is expressed by using a dimensionless operator $\boldsymbol{\rho}_i$ as

$$\boldsymbol{\rho}_i = \boldsymbol{r}_i/a_\mu, \qquad (24)$$

where a_μ is a scaled Bohr radius defined as

$$\begin{aligned} a_\mu &= \frac{m_{\rm e}}{\mu_{\rm M}}a_0, & (25)\\ \text{Bohr radius } a_0 &= \frac{4\pi\epsilon_0\hbar^2}{m_{\rm e}e^2} = \frac{4\hbar}{\alpha m_{\rm e}c}. \end{aligned}$$

Here, ϵ_0 is the permittivity of vacuum, e is the elementary charge, and α is the fine structure constant. Then, $\boldsymbol{p}_i$ is rewritten by using a dimensionless operator ∇_{ρ_i} as

$$\boldsymbol{p}_i = \frac{\hbar}{i}\frac{1}{a_\mu}\nabla_{\rho_i}. \qquad (26)$$

Therefore, Eq. (20) is rewritten as

$$\frac{\hbar^2}{\mu_{\rm M}a_\mu^2}\left[-\frac{1}{2}\sum_i^{N_e}\nabla_{\rho_i}^2 - \frac{\mu_{\rm M}}{M_A}\sum_{i<j}^{N_e}\nabla_{\rho_i}\cdot\nabla_{\rho_j} + \sum_i^{N_e} V_{e\text{-}N}(\boldsymbol{\rho}_i) + \sum_{i<j}^{N_e} V_{e\text{-}e}(\boldsymbol{\rho}_i-\boldsymbol{\rho}_j)\right]\Psi = E_\mu\Psi. \quad (27)$$

By using Eq. (25), Eq. (27) is modified as follows:

$$\frac{\mu_{\rm M}}{m_{\rm e}}\frac{e^2}{a_0}\left[-\frac{1}{2}\sum_i^{N_e}\nabla_{\rho_i}^2 - \frac{\mu_{\rm M}}{M_A}\sum_{i<j}^{N_e}\nabla_{\rho_i}\cdot\nabla_{\rho_j} + \sum_i^{N_e} V_{e\text{-}N}(\boldsymbol{\rho}_i) + \sum_{i<j}^{N_e} V_{e\text{-}e}(\boldsymbol{\rho}_i-\boldsymbol{\rho}_j)\right]\Psi = E_\mu\Psi, \quad (28)$$

where $e^2/4\pi\epsilon_0$ is replaced by e^2 according to a convention. The dimensionless form of Eq. (28) is given by

$$\left[-\frac{1}{2}\sum_i^{N_e}\nabla_{\rho_i}^2 - \frac{\mu_{\rm M}}{M_A}\sum_{i<j}^{N_e}\nabla_{\rho_i}\cdot\nabla_{\rho_j} + \sum_i^{N_e} V_{e\text{-}N}(\boldsymbol{\rho}_i) + \sum_{i<j}^{N_e} V_{e\text{-}e}(\boldsymbol{\rho}_i-\boldsymbol{\rho}_j)\right]\Psi = \varepsilon\Psi, \qquad (29)$$

where $\varepsilon = E_\mu/(e^2/a_\mu)$ is the dimensionless form of the energy E_μ.

When we consider the infinite nuclear mass with the limit $\mu_{\rm M}/M_A \to 0$, eigenvalue ε_0 and eigenfunction Ψ_0 are obtained and the eigenenergy is given by

$$E_0 = \varepsilon_0 \frac{e^2}{a_0}. \tag{30}$$

In the case of the finite nuclear mass M_A, if the second term in Eq. (20) is treated as a small perturbation, the total energy is expressed as

$$E_\mu = \left[\varepsilon_0 + \frac{\mu_{\rm M}}{M_A}\varepsilon_1 + \left(\frac{\mu_{\rm M}}{M_A}\right)^2 \varepsilon_2 + \cdots\right] \frac{\mu_{\rm M}}{m_{\rm e}} \frac{e^2}{a_0}, \tag{31}$$

where $\varepsilon_1 = -\left\langle \Psi_0 | \nabla_{\rho_i} \cdot \nabla_{\rho_j} | \Psi_0 \right\rangle$ determines the first-order specific mass shift and ε_2 is the second-order coefficient.

Firstly, we consider the first term in Eq. (20), which is correspond to the normal mass shift term. We express the corresponding energy with a finite nuclear mass as E'_μ. From Eqs. (30) and (31), it is apparent that the energy is just scale of the finite nuclear mass value by [49, 50]

$$\frac{\mu_{\rm M}}{m_{\rm e}} = \frac{M_A}{m_{\rm e} + M_A}. \tag{32}$$

Therefore, the energy of atomic level with the finite nuclear mass (E'_μ) is shifted from that with the infinite nuclear mass (E_0) by

$$\delta E_{\rm finite} = E'_\mu - E_0 = \left(\frac{M_A}{M_A + m_{\rm e}} - 1\right) E_0 = -\frac{m_{\rm e}}{M_A + m_{\rm e}} E_0 = -\frac{m_{\rm e}}{M_A} E'_\mu, \tag{33}$$

which depends on the nuclear mass. This shift is related to the normal mass shift. By using Eq. (33), the corresponding energy shift for the isotopes with different mass M_A and $M_{A'}$ is given by

$$\delta E^{AA'}_{\rm finite} = -\frac{M_{A'} - M_A}{M_A M_{A'}} m_{\rm e} E'_\mu. \tag{34}$$

Moreover, by using Eq. (34), the corresponding energy shift $\delta E^{AA'}_{{\rm finite},ab}$ for the atomic transition energy $\delta E'_{\mu,ab} = E'_{\mu,a} - E'_{\mu,b}$ between the states a and b is defined as

$$\delta E^{AA'}_{{\rm finite},ab} = -\frac{M_{A'} - M_A}{M_A M_{A'}} m_{\rm e} \delta E'_{\mu,ab} \equiv \delta E^{AA'}_{\rm NMS}. \tag{35}$$

Here, $\delta E^{AA'}_{\rm NMS}$ is called the normal mass shift. Finally, the frequency expression of Eq. (35) is given by

$$\delta \nu^{AA'}_{\rm NMS} = \frac{M_{A'} - M_A}{M_A M_{A'}} m_{\rm e} \nu_{ab}, \tag{36}$$

where ν_{ab} is the transition frequency between the states a and b ($E'_{\mu,a} < E'_{\mu,b}$).

Next, we consider the effect of the second term in Eq. (20). This term is referred to as a mass polarization term and indicates the change of electron momentum due to the shift of the center of gravity. The corresponding energy shift is given as similar to Eq. (34) by

$$\delta E^{AA'}_{\rm MP} = \frac{M_{A'} - M_A}{M_A M_{A'}} K_{\rm MP}, \tag{37}$$

where $K_{\rm MP} = \sum_{i<j}^{N_e} \langle \boldsymbol{p}_i \cdot \boldsymbol{p}_j \rangle$ is called a mass polarization parameter. The mass polarization contribution to the isotope shift is called the specific mass shift The specific mass shift for a transition energy is given by

$$\delta E_{\rm SMS}^{AA'} = \frac{M_{A'} - M_A}{M_A M_{A'}} \delta K_{\rm MP}, \tag{38}$$

where $\delta K_{\rm MP} = K_{{\rm MP},a} - K_{{\rm MP},b}$ is the difference of the mass polarization parameters for the states a and b. The frequency expression of Eq. (38) is given by

$$\delta \nu_{\rm SMS}^{AA'} = \frac{M_{A'} - M_A}{M_A M_{A'}} \frac{\delta K_{\rm MP}}{h}. \tag{39}$$

$\delta \nu_{\rm MS}^{AA'}$ is inverse proportion to A^2 and is quickly decreased with increasing of nuclear mass. $\delta \nu_{\rm NMS}^{AA'}$ is easily calculated as shown in Eq. (36). On the other hand, $\delta \nu_{\rm SMS}^{AA'}$ contains the change of the electron correlation terms $\boldsymbol{p}_i \cdot \boldsymbol{p}_j$ and is deduced by theoretical calculations.

For a usual alkali-like ns $\rightarrow$ np and alkaline earth-like ns^2 $\rightarrow$ nsnp transition, the specific mass shift is expected to be small. When the specific mass shift is unknown, the assumptions for the specific mass shift as

$$n\mathrm{s} \rightarrow n\mathrm{p} \text{ transition} \;:\; \delta \nu_{\rm SMS}^{AA'} = (0.3 \pm 0.9) \delta \nu_{\rm NMS}^{AA'}, \tag{40}$$

$$n\mathrm{s}^2 \rightarrow ns n\mathrm{p} \text{ transition} \;:\; \delta \nu_{\rm SMS}^{AA'} = (0 \pm 0.5) \delta \nu_{\rm NMS}^{AA'}, \tag{41}$$

are often used [51] in the nuclear region of $Z \geq 20$. For the lighter nuclei ($Z < 20$), the specific mass shift is a dominant component of an isotope shift. Therefore, the specific mass shift for a certain atomic transition of each element was evaluated carefully in each case [50, 52, 53]. The specific mass shit for the transition involving d, f-electron is larger than those of ns $\rightarrow$ np and ns^2 $\rightarrow$ nsnp transitions. Theoretical specific mass shifts are tabulated in Ref. [54] for the atoms of 4d, 4f, 5d, and 5f series using the non-relativistic Hartree-Fock (NRHF) calculation, and in Ref. [55] for the transition in Os I using the multi-configuration Dirac-Hartree-Fock (MCDHF) calculation. The calculated values in these references are close to the experimental values within a factor of two. In the case of heavy elements in the region of Z = 70–80, for example, the calculated specific mass shifts in Os I are $\delta \nu_{\rm SMS}^{190,192} = -125$ MHz for nd $\rightarrow$ $(n+1)$p transition in Ref. [54] and $\delta \nu_{\rm SMS}^{190,192}$ = 100–200 MHz for $(n+1)$s $\rightarrow$ nd transition in Ref. [55]. Although no theoretical calculation has been reported for iridium isotopes, the $\delta \nu_{\rm SMS}$ of the iridium isotopes would be expected to be similar value to those for osmium isotopes.

2.4.2 Volume effect

The charge distribution in a nucleus affects to the electron binding energy since the nucleus has a finite volume. The effect becomes larger in the deformed nucleus such as prolate or oblate shapes than that in a spherical nucleus. The change of the nuclear volume becomes significant with increasing of the atomic number Z. The energy shift by the volume effect is called a field shift and is given by

$$\delta \nu_{\rm FS}^{AA'} = F_{\rm e} \lambda^{AA'}, \tag{42}$$

where $F_{\rm e}$ is called an electronic factor and is proportional to the variation of the electron density $\Delta |\Psi(0)|$ at the nucleus point in the atomic transition and $\lambda^{AA'}$ is related to the variation of the nuclear mean-square charge radius. The $F_{\rm e}$ is defined as [56]

$$F_{\rm e} = \frac{2\pi}{3} \frac{Ze^2}{h} \Delta |\Psi(0)|^2 . \tag{43}$$

$\lambda^{AA'}$ is called a nuclear parameter and is expressed using power series of the variation of the nuclear mean-square charge radius $\delta\langle r_{\rm c}^{2n}\rangle^{AA'}$ as

$$\lambda^{AA'} = \delta\langle r_{\rm c}^2\rangle^{AA'} + \frac{C_2}{C_1}\delta\langle r_{\rm c}^4\rangle^{AA'} + \frac{C_3}{C_1}\delta\langle r_{\rm c}^6\rangle^{AA'}\cdots, \tag{44}$$

where Seltzer coefficients C_i are tabulated for many elements, such as $Z = 70$–80 with our interest, in Refs. [56, 57]. The C_i are originated from the electron density at a nucleus and C_1 is identical with electronic factor $F_{\rm e}$. Therefore, the ratios of C_2/C_1 and C_3/C_1 are independent of the atomic transition [56]. In Ref. [57], the contribution only from $1s^2$ electrons was considered for the estimation of C_i. On the other hand, in Ref. [56], the contribution from not only $1s^2$ electrons but also electrons in the outer orbits was considered for the estimation. The estimated ratios of C_2/C_1 and C_3/C_1 became $> 10\%$ higher than those given in Ref. [57] in the region of $Z \sim 80$. However, the differences of the ratios cause the very small affection to $\lambda^{AA'}$ with $< 0.3\%$. Therefore, the affection to the variation of mean-square charge radius and deformation parameter, which are explained in subsection 2.5, are negligible.

Theoretical electric factors for specific atomic transitions were tabulated in Refs. [55, 58] for Os, and Ref. [56] for various elements. In the previous theoretical studies, the field shift was calculated by using the theoretical $F_{\rm e}$ and experimental charge radius, and the estimated field shift was compared with the experimental one. The estimated field shifts using the theoretical $F_{\rm e}$ by a non-relativistic Hartree-Fock (NRHF) calculation were listed in Ref. [58] for the various transitions $5d^76s \rightarrow 5d^76p$, $5d^66s^2 \rightarrow 5d^66s6p$, $5d^76s \rightarrow 5d^66s6p$, and $5d^66s^2 \rightarrow 5d^76p$ in ^{192}Os with respect to ^{190}Os. The estimated field shifts were in good agreement with the experimental field shifts within the error margin of 20%. Moreover, in Ref. [56], the estimated field shifts using the theoretical $F_{\rm e}$ by a multi-configuration Dirac-Fock (MCDF) calculation were compared with those evaluated from the electronic or muonic X-ray measurements in some elements, and were in good agreement with the experimental values within the margin of two sigma. Thus, the theoretical $F_{\rm e}$ can be predicted with good accuracy, and we can use the theoretical $F_{\rm e}$ to deduce the nuclear parameter $\lambda^{AA'}$. The theoretical $F_{\rm e}$ values evaluated by the MCDF calculation were applied for the laser spectroscopy studies of Ir ($Z = 77$) [26], Pt ($Z = 78$) [27], Au ($Z = 79$) [30], and Hg ($Z = 80$) [33].

If there is no theoretical calculation for the $F_{\rm e}$ value related to a spectroscopic transition, the $F_{\rm e}$ value can be deduced from the experimental values as

$$F_{\rm e} = \frac{\delta\nu_{\rm IS}^{AA'} - \delta\nu_{\rm MS}^{AA'}}{\lambda^{AA'}}. \tag{45}$$

A field shift (typically order of GHz) for heavy elements ($Z > 50$) is more than ten times larger than a mass shift (order of 10–100 MHz), and the effect of the mass shift for the $F_{\rm e}$ evaluation can be negligible. Therefore, the $F_{\rm e}$ value can be evaluated from the measured $\delta\nu_{\rm IS}^{AA'}$ and $\lambda^{AA'}$.

The $\delta K_{\rm mp}$ and $F_{\rm e}$ are determined from a King-plot analysis [59] in the following two cases: (1) isotope shift and nuclear parameter are known for two isotope pairs and (2) isotope shifts of four isotope pairs are known for two transitions. Details of the King-plot are described in Appendix A. In the case of iridium, the King-plot analysis can not be applied because the isotope shift of only one isotope pair was measured for two transitions, which doesn't satisfy the case (2), as mentioned in Appendix A.

2.5 Nuclear mean-square charge radius and deformation parameter

The variation of the nuclear mean-square charge radius of the second-order is expressed as [25]

$$\delta\langle r_{\rm c}^2\rangle^{AA'} = \delta\langle r_{\rm c}^2\rangle_{\rm sph}^{AA'} + \frac{5}{4\pi}\overline{\langle r_{\rm c}^2\rangle}_{\rm sph}^{AA'}\delta\langle\beta_2^2\rangle^{AA'}, \tag{46}$$

where $\delta\langle r_{\rm c}^2\rangle_{\rm sph}^{AA'}$ indicates the variation of the mean-square charge radius of a spherical part and $\overline{\langle r_{\rm c}^2\rangle}_{\rm sph}^{AA'}\delta\langle\beta_2^2\rangle^{AA'}$ indicates the variation of the deformation part using a quadrupole deformation parameter β_2. Nuclear parameter $\lambda^{AA'}$ up to the third term defined in Eq. (44) is rewritten as [25]

$$\lambda^{AA'} = (1+x)\delta\langle r_{\rm c}^2\rangle_{\rm sph}^{AA'} + (1+y)\frac{5}{4\pi}\overline{\langle r_{\rm c}^2\rangle}_{\rm sph}^{AA'}\delta\langle\beta_2^2\rangle^{AA'}, \tag{47}$$

where

$$x = \frac{C_2}{C_1}\frac{10}{7}R^2 + \frac{C_3}{C_1}\frac{5}{3}R^4, \tag{48}$$

$$y = \frac{C_2}{C_1}2R^2 + \frac{C_3}{C_1}3R^4, \tag{49}$$

$$R^2 = \frac{5}{3}\overline{\langle r_{\rm c}^2\rangle}_{\rm sph}^{AA'}, \tag{50}$$

with

$$\overline{\langle r_{\rm c}^2\rangle}_{\rm sph}^{AA'} = \frac{\langle r_{\rm c}^2\rangle_{\rm sph}^{A} + \langle r_{\rm c}^2\rangle_{\rm sph}^{A'}}{2}. \tag{51}$$

$\langle r_{\rm c}^2\rangle_{\rm sph}^{A}$ were calculated by using the droplet model explained in Ref. [60]. We can calculate the $\delta\langle\beta_2^2\rangle^{AA'}$ by using Eq. (47) and experimental $\lambda^{AA'}$. Then, $\delta\langle r_{\rm c}^2\rangle^{AA'}$ considering the contribution of the higher-order is deduced by using Eq. (46) and calculated $\delta\langle\beta_2^2\rangle^{AA'}$.

2.6 HFS measurement by laser ionization spectroscopy

2.6.1 Principle

Laser spectroscopy is a powerful tool for determining nuclear electromagnetic moments and charge radii through the investigation of HFS and isotope shift. Figure 13 shows the principle of HFS measurement by two-color two-step laser resonance ionization technique as used in KISS. The HFS is obtained by measuring the extraction yield of the laser-ionized atoms with changing the laser wavelength λ_1 for the atomic excitation transition. Then, the atoms are ionized by the irradiation of the ionization laser with wavelength λ_2. In the case of a radioisotope, the yield is evaluated from the fitting of the growth curve of β-decay, which is obtained by measuring the β-ray counting rate.

Nuclear electromagnetic moments are deduced from the interval of peaks $(\nu_i - \nu_j)$ in the measured hyperfine spectrum. In the analysis of measured hyperfine spectrum, we assumed that $H_J(0)$ and $\phi_J(0)$ are specific to each atomic state and are common for isotopes. Therefore, the nuclear electromagnetic moments μ and Q can be evaluated from the measured $A_{\rm HF}$ and $B_{\rm HF}$, respectively, by using the known $A_{\rm HF,ref}$, $B_{\rm HF,ref}$, $I_{\rm ref}$, $\mu_{\rm ref}$, and $Q_{\rm ref}$ of a specific (reference) isotope (those of a stable isotopes are generally applied.) as follows:

$$\mu = \frac{I}{I_{\rm ref}}\frac{A_{\rm HF}}{A_{\rm HF,ref}}\mu_{\rm ref}, \tag{52}$$

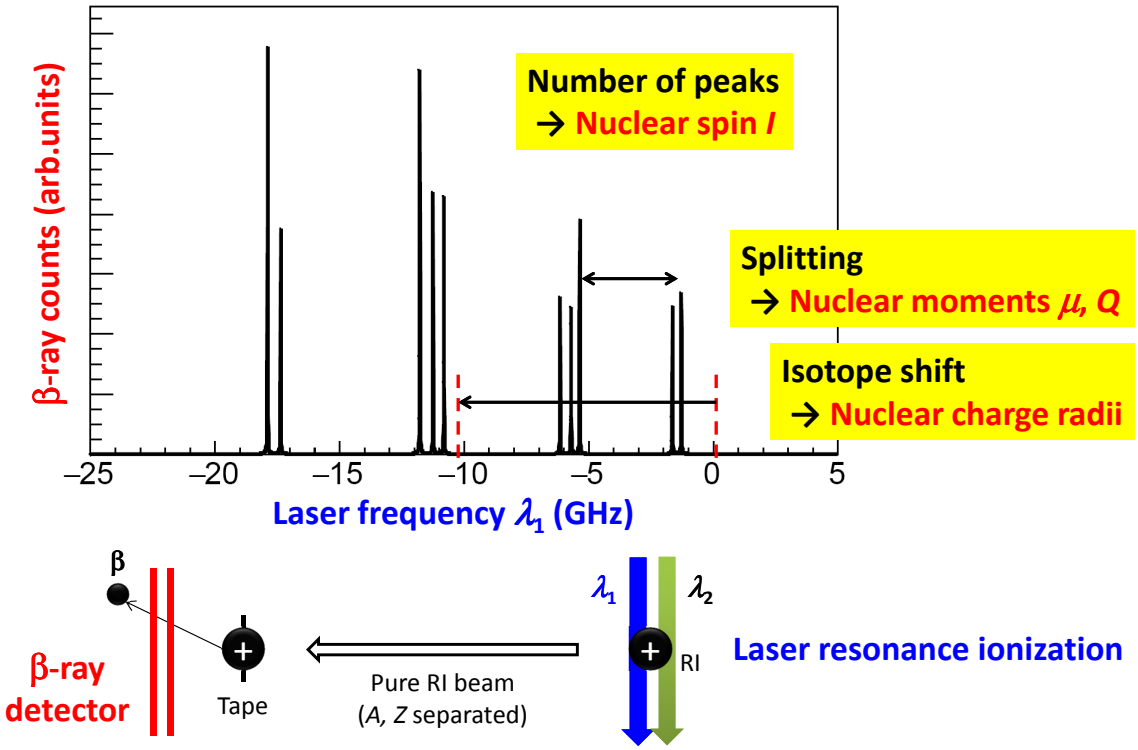

Figure 13: Principle of HFS measurement by laser ionization spectroscopy in the case of $I = 3/2^+$ and $J_{\rm gs} = J_{\rm ex} = 9/2$.

$$Q = \frac{B_{\rm HF}}{B_{\rm HF,ref}} Q_{\rm ref}. \tag{53}$$

In the measurement of HFS, we use the atomic states whose electron configuration, transition energy, and total angular momentum J are known. As mentioned in subsection 2.3, in the case of $I \leq J$, the number $(2I + 1)$ of resonance peaks in the HFS is governed by the nuclear spin I. Therefore, the nuclear spin can be deduced from the number of peaks in the measured HFS spectrum by selecting the initial and final atomic states with atomic spin J_1 and J_2, respectively, which fulfill the condition of $I \leq J_i$ ($i = 1$ and/or 2). The relation of I, J, and the number of hyperfine transitions are summarized in Appendix B.

2.6.2 In-gas-cell laser ionization spectroscopy

In-gas-cell laser ionization spectroscopy has been performed at Leuven Isotope Separator On-line (LISOL) facility [61] by KU Leuven group. The in-gas laser ionization and spectroscopy (IGLIS) technique [62] has been developed at LISOL. The radioactive isotopes produced by nuclear reactions are thermalized and neutralized in a gas cell filled with an argon gas of a few to several ten kPa, and then laser-ionized element-selectively in the gas cell [63, 64]. The mass number of the extracted nuclei with energy of 40 keV is selected by a dipole magnet, and transported to a detector station. Then, the radiations emitted from the laser-ionized unstable nuclei are detected by β- and γ-ray detectors such as Ref. [65]. The in-gas-cell laser ionization spectroscopy has two advantages: (1) refractory element can be extracted and (2) the HFS of rare isotopes can be measured with high sensitivity by detecting the decay radiations. The HFS measurements by in-gas-cell laser ionization spectroscopy were performed for silver isotopes [66], copper isotopes [67], and actinium isotopes [68]. Even through the measured HFS spectra consist of broad one to four peaks

due to various reasons as explained in next subsection, the magnetic moments for these isotopes were deduced successfully with good precision.

2.6.3 Spectral lineshape and width

The HFS spectra measured by laser spectroscopy technique are expressed as a Voigt function, which is a lineshape resulting from the convolution of Gaussian and Lorentzian. In the case of in-gas-cell laser spectroscopy, the linewidth is broadened by the five components described in the following subsections. Therefore, the peak corresponding to each transition between hyperfine levels has the broad width $\delta\nu_{\mathrm{Voigt}}$ as shown in left upper figure of Fig. 14, and this width is common for all the transitions. The peak hight is proportional to a relative transition probability as explained in later paragraphs. When the $\delta\nu_{\mathrm{Voigt}}$ is larger than the energy displacement by the hyperfine interactions, a broad HFS spectrum composed by each peak with broad $\delta\nu_{\mathrm{Voigt}}$ is observed as indicated by the green solid line in Fig. 14. The measured HFS spectra in the present work were analyzed by using the lineshape explained here.

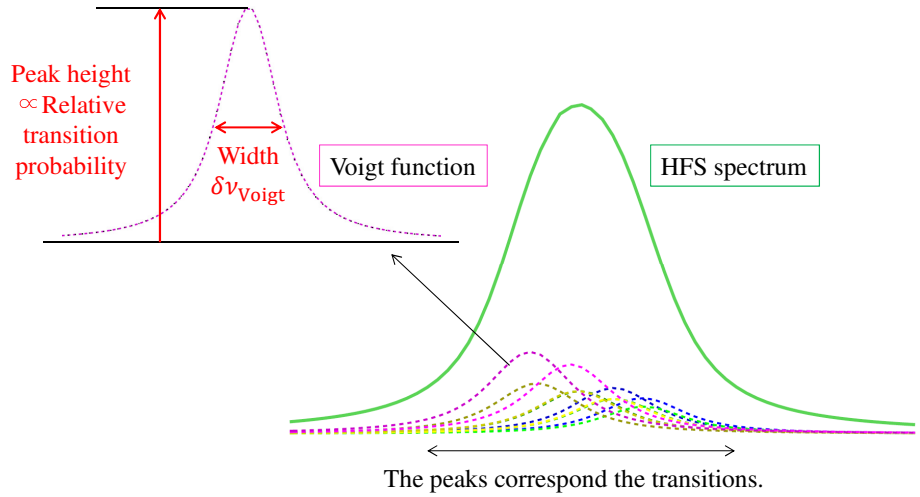

Figure 14: Schematic view of the spectral lineshape and HFS spectrum expected for in-gas-cell laser ionization spectroscopy. The peaks indicated by broken lines correspond to each transition between hyperfine levels. The sum of the peaks forms the HFS spectrum indicated by the green solid line.

The width of a spectral line composes of two Gaussian and three Lorentzian widths as follows: laser linewidth of an excitation laser (Gaussian), Doppler broadened width due to thermal motion of atoms (Gaussian), natural width of an atomic excited state (Lorentzian), pressure broadened width due to interactions with argon gas atoms (Lorentzian), and laser power broadened width due to stimulated emission from an atomic excited state (Lorentzian) [69].

The width of the Voigt function $\delta\nu_{\mathrm{Voigt}}$ in FWHM is expressed by using a Gaussian width $\delta\nu_{\mathrm{Gauss}}$ and Lorentzian width $\delta\nu_{\mathrm{Lorentz}}$, and is given empirically by [70]

$$\delta\nu_{\mathrm{Voigt}} = 0.5346 \cdot \delta\nu_{\mathrm{Lorentz}} + \sqrt{0.2166 \cdot \delta\nu^2_{\mathrm{Lorentz}} + \delta\nu^2_{\mathrm{Gauss}}}. \tag{54}$$

The Gaussian width in FWHM is expressed as

$$\delta\nu_{\mathrm{Gauss}} = \sqrt{\delta\nu^2_{\mathrm{laser}} + \delta\nu^2_{\mathrm{Doppler}}}, \tag{55}$$

where $\delta\nu_{\rm Laser}$ and $\delta\nu_{\rm Doppler}$ are the laser linewidth and Doppler broadened width in FWHM, respectively. The Lorentzian width in FWHM is expressed as

$$\delta\nu_{\rm Lorentz} = \delta\nu_{\rm nat} + \delta\nu_{\rm pressure} + \delta\nu_{\rm power}, \tag{56}$$

where $\delta\nu_{\rm nat}$, $\delta\nu_{\rm pressure}$, and $\delta\nu_{\rm power}$ are the natural width, pressure broadened width, and laser power broadened width in FWHM, respectively. The linewidth of the laser can be given from the measurement using a wavemeter. Generally, the lineshape of dye lasers with broad-band (> 1 GHz) can be expressed by Gaussian shape [66, 71, 72]. Other four widths are discussed in the following paragraphs.

Doppler broadened width

The atoms with thermal equilibrium have kinetic energies obeying Maxwell-Boltzmann distribution at thermal equilibrium temperature. The distributed velocities of atoms cause the broadening of absorption laser frequency. This broadening is called a Doppler broadening. The FWHM of Doppler broadening is given by

$$\delta\nu_{\rm Doppler} = \frac{2\nu_0}{c}\sqrt{\frac{2{\rm ln}2 \cdot k_{\rm B}T}{m}}, \tag{57}$$

where ν_0, k_B, T, and m are the center of gravity frequency for the transition, Boltzmann constant, equilibrium temperature, and mass of an atom, respectively. The Doppler width for the atom with $A = 191$ at a buffer gas (argon gas) temperature of 300 K is calculated to be $\delta\nu_{\rm Doppler} \sim 1.1$ GHz for the transition frequency of $\nu_0 = 1210857$ GHz ($\lambda_1 = 247.587$ nm).

Natural width

Atomic excited state has a finite lifetime with the order of 10-100 ns typically. Therefore, the natural width of the state becomes Lorentz width expressed by the uncertainty principle. The natural width in FWHM is given by

$$\delta\nu_{\rm nat} = \frac{A_{21}}{2\pi}, \tag{58}$$

where A_{21} is an Einstein coefficient. The natural width is evaluated to be $\delta\nu_{\rm nat} = 3.3$ MHz in our transition with $A_{21} = 2.073 \times 10^7$ s^{-1} ($\lambda_1 = 247.587$ nm).

Pressure broadened width

Pressure broadening and shift are stemmed from the energy distribution and shift of an atomic transition, respectively, which are caused by the atomic collisions and interactions with the surrounding buffer gas atoms and/or molecules. The pressure broadening and shift have been studied experimentally because theoretical calculations are complicated. The energy distribution by this effect is a Lorentz distribution. The pressure broadening and shift are proportional to environmental pressure p and given as

$$\delta\nu_{\rm pressure} = \Gamma_{\rm pressure} \times p, \tag{59}$$

$$\delta\nu_{\rm shift} = \Gamma_{\rm shift} \times p, \tag{60}$$

where $\Gamma_{\rm pressure}$ and $\Gamma_{\rm shift}$ are called a pressure broadening and shift coefficients, respectively. These relationship were confirmed experimentally in Refs. [66, 71, 73, 74]. Table 3 shows the measured pressure broadening and shift coefficients for various elements in argon gas. The $\Gamma_{\rm pressure}$ and $\Gamma_{\rm shift}$ for ^{191}Ir were studied in the present work as shown in subsection 4.5.3.

Table 3: Measured pressure broadening and shift coefficients for various elements in argon gas.

Nuclei	$\lambda_{\mathrm{vacuum}}$ [nm]	$\Gamma_{\mathrm{pressure}}$ [MHz/kPa]	$\Delta\lambda_{\mathrm{pressure}}$ [pm/kPa]	Γ_{shift} [MHz/kPa]	$\Delta\lambda_{\mathrm{shift}}$ [pm/kPa]	Ref.
$^{58}_{28}\mathrm{Ni}_{30}$	232.003	113(6)	0.020	-55(3)	-0.0099	[71]
$^{63}_{29}\mathrm{Cu}_{34}$	244.164	54	0.011	-19(1)	-0.0038	[71]
$^{107}_{47}\mathrm{Ag}_{60}$	328.07	120(20)	0.043	-37(4)	-0.013	[66]
$^{120}_{50}\mathrm{Sn}_{70}$	254.731	320(40)	0.069	-40(3)	-0.0087	[73]
$^{190}_{76}\mathrm{Os}_{114}$	247.758	-	-	-51(4)	-0.010	[74]
$^{191}_{77}\mathrm{Ir}_{114}$	247.587	97(8)	- 0.020	-19(7)	-0.0039	present work

Laser power broadened width

The stimulated emission probability from an atomic excited state increases with increasing of the laser power. Consequently, the lifetime of the excited state is shorten and, as a result, the spectral line becomes broader. In the case that a laser pulse width is typically more than five times longer than the lifetime of the excited state considering the exponential decay, absorption and spontaneous emission become equilibrium. Under the equilibrium between two identical states, the spectral line is expressed as [75]

$$f(\delta\nu) = \frac{A_{21}^2}{2} \frac{\frac{I_{\mathrm{p}}}{I_{\mathrm{p,sat}}}}{A_{21}^2 \left(\frac{I_{\mathrm{p}}}{I_{\mathrm{p,sat}}} + 1\right) + 4\delta\nu^2}, \tag{61}$$

where $\delta\nu$ is detuning of applied laser frequency, and I_{p} and $I_{\mathrm{p,sat}}$ are an applied intensity and saturation intensity of the laser, respectively. The saturation intensity is defined as the laser intensity for achieving the half population in the excited state, and is given by

$$I_{\mathrm{p,sat}} = \frac{2hc\pi^2 A_{21}}{3\lambda^3} \ [\mathrm{J/cm^2/s}]. \tag{62}$$

The FWHM of the spectral line by power broadening is expressed as

$$\delta\nu_{\mathrm{power}} = A_{21}\sqrt{\frac{I_{\mathrm{p}}}{I_{\mathrm{p,sat}}} + 1}. \tag{63}$$

The transition we used in the present work was $\lambda_1 = 247.587$ nm and $A_{21} = 2.073\times10^7$ s^{-1} (48 ns). In the case of this transition with typical laser intensity of 100 μJ/pulse, a spot size of 10 mm in diameter ($I_{\mathrm{p}} = 127$ μJ/cm^2/pulse), and laser pulse width of 15 ns, the saturation intensity is $I_{\mathrm{p,sat}} = 180$ mJ/cm^2/s, and power broadening is $\delta\nu_{\mathrm{power}} = 4.5$ GHz. In this case, the laser pulse width is shorter than the lifetime of the excited state, and thus the actual power broadening would become smaller than the calculated value.

Transition intensity

When the broadening of an atomic state is larger than the energy displacements of the HFS, the hyperfine levels are populated according to the number of the magnetic sub states (statistical weight) [76]. The relative transition intensities from the F_{gs} levels are

in proportion to the statistical weights $(2F_{\rm gs}+1)$. The initial population probability of the ith $F_{\rm gs}$ level is given by

$$\frac{2F_{{\rm gs},i}+1}{\Sigma_j(2F_{{\rm gs},j}+1)}, \tag{64}$$

where $\Sigma_j(2F_{{\rm gs},j}+1)$ is the sum of the statistical weights of all the $F_{\rm gs}$ levels in the ground state. In the same manner for the ground state, the relative transition intensities to the $F_{\rm ex}$ levels are in proportion to the statistical weights $(2F_{\rm ex}+1)$. The population probability of the kth $F_{\rm ex}$ level is given by

$$\frac{2F_{{\rm ex},k}+1}{\Sigma_l(2F_{{\rm ex},l}+1)}, \tag{65}$$

where $\Sigma_l(2F_{{\rm ex},l}+1)$ is the sum of the statistical weights of the $F_{\rm ex}$ levels in the excited state which can be populated from a $F_{\rm gs}$ level by accounting for the selection rule of Eq. (17). Finally, the relative transition intensity for the transition from $F_{{\rm gs},i}$ level to $F_{{\rm ex},k}$ level is given by

$$\text{relative transition probability} = \frac{2F_{{\rm gs},i}+1}{\Sigma_j(2F_{{\rm gs},j}+1)}\frac{2F_{{\rm ex},k}+1}{\Sigma_l(2F_{{\rm ex},l}+1)}. \tag{66}$$

2.6.4 Analyses of broad HFS spectra

In the case of in-gas-cell laser ionization spectroscopy, a broad HFS spectrum would be measured as mentioned in the previous sections, and the μ values were deduced from the broad spectra successfully. Here, we introduce another successful experimental results to deduce the μ values from broad HFS spectra by applying χ^2 fitting analyses.

The laser spectroscopy of copper isotopes ($Z = 29$) with large Doppler broadening were performed at ISOLDE/CERN in Refs. [76, 77, 78]. In these studies, copper isotopes were laser-ionized in the hot ionizer cavity (2000°C) and the resulting Doppler width was 3.8 GHz. Two laser lights with the wavelengths of 327.4 and 287.9 nm for the excitation and ionization, respectively, with a band width of 1.2 GHz were used for two-step laser ionization from the ground state $3d^{10}4s\ ^2S_{1/2}$ via the intermediate state $3d^{10}4p\ ^2P_{1/2}$ to the auto-ionizing state $3d^94s5s\ ^2D_{3/2}$. The wavelength of the first step laser were scanned to measure the HFS.

From the HFS spectra with the broad width, the magnetic dipole moments of ^{75,77,78}Cu [76], ^{68,68m,70,70m1,70m2}Cu [77], and ^{58,59}Cu [78] were deduced. In Ref. [76], the spin of ^{75}Cu and ^{77}Cu were confirmed and newly determined, respectively, from the χ^2 values of the fittings in the measured HFS spectra. These HFS spectra clearly show the two broad peaks for both isotopes with the spin assumptions of 1/2, 3/2, 5/2, and 7/2. The minimum χ^2 values were obtained with the spin assumption of 5/2 for both isotopes, and the χ^2 values with other spin assumptions were more than 1.5 times larger than the minimum χ^2. In Ref. [77], one broad peak were observed for ^{68m}Cu ($I^\pi = 6^-$) and ^{70}Cu ($I^\pi = (6)^-$). They deduced the μ values of these isotopes as $\mu(^{68m}{\rm Cu}) = +1.24(4)(6)\ \mu_{\rm N}$ and $\mu(^{70}{\rm Cu}) = (+)1.50(7)(8)\ \mu_{\rm N}$, where the values in the first and second brackets are the statistic and systematic errors, respectively. The absolute value of empirical μ ($= +1.59\ \mu_{\rm N}$) (see subsection 5.4) well reproduces the experimental μ. In Ref. [78], they determined the sign of the μ for ^{58}Cu ($I^\pi = 1^+$) from the χ^2 values ($\chi^2 = 1.1$ and 4.8 with positive and negative μ, respectively) in spite of the measured HFS spectrum was one broad peak due to the Gaussian width (~ 4.5 GHz) and small μ value as $\mu(^{58}{\rm Cu}) = +0.52(8)\ \mu_{\rm N}$.

These previous studies demonstrate that it is possible to determine the μ value from a broad HFS spectrum by comparing the χ^2 values of the fittings. This analysis is applicable to the HFS measurement by in-gas-cell laser ionization spectroscopy at KISS.

3 Experimental setup

The components of KISS and the detector station including the data acquisition system are discussed in this section. The followings are the contents in each subsection: details of the gas cell system which is a laser ion source for the production of the radioactive nuclei at KISS in subsection 3.1; details of the KISS beamline in subsection 3.2; the detector station to perform β-γ spectroscopy in subsection 3.3.

3.1 Gas cell system at KISS

The production and collection of TLFs, laser resonance ionization, and ion beam extraction are performed in the KISS gas cell system. Two experiments were performed as the doctoral theme by using two different gas cell systems in Fig. 15 [79]. The ^{136}Xe primary beam impinged on the energy degrader consisting of three titanium foils with a thickness of 3 μm (9 μm in total) to optimize the MNT reaction energy by reducing the beam energy from 10.75 MeV/nucleon to 9.4 MeV/nucleon. Then, the beam impinged on a ^{198}Pt target (12.5 mg/cm^2 in thickness) for producing the TLFs by using the MNT reactions. Here, the energy degrader and production target were rotating at 1000 rotation per minute (rpm) to reduce a thermal damage induced by the primary beam irradiation of 250 pnA and to avoid the breakup. A doughnut-shaped gas cell was placed at 10 mm downstream of the target and was filled with purified argon gas ($<$ 0.1 ppb) of 88 kPa at maximum. The primary beam passed through a tunnel of the doughnut-shaped gas cell without entering the gas cell to avoid the production of argon plasma in the gas cell. The beam was stopped at a water cooled beam dump, which placed $\sim$80 cm downstream of the gas cell and was made of a tungsten plate with a thickness of 6 mm and diameter of 50 mm. The beam dump was surrounded by the lead and paraffin blocks to prevent the radiations induced by the primary beam from damaging KISS control devices.

The doughnut-shaped gas cell [79] has a circular window with a diameter of 90 mm around the tunnel to implant the TLFs into the gas cell. The window was sealed by using a thin gold-coating Kapton foil with a thickness of 5 μm to increase the implantation fractions of the TLFs and to reduce a charge-up issue on the surface, respectively. The TLFs implanted into the gas cell were stopped and neutralized in the gas cell. A well designed laminar gas flow efficiently transported the TLFs to the gas cell exit. There was a pair of ion collection electrodes (ICEs) upstream of the gas cell exit to collect the survival ions coming from the stopping region.

The atoms were ionized element-selectively by two-color resonant laser irradiation at the laser ionization region where there was a pair of laser windows made of synthetic quarts for UV laser irradiation. The ions emitted from the gas cell together with argon gas were trapped in the radial direction by pseudo trapping potential in Multi-RF Ion Guides (MRFIG). The MRFIG, which consisted of one Octupole and two Sextupole ion guides (OPIG and SPIG1, 2, respectively) [80, 81] with different inner diameters, efficiently cooled the emittance of ions, and transported the ions from high pressure region to low pressure region for further acceleration. Then, ions were accelerated by an electric field of 20 kV potential difference between SPIG2 and an extraction electrode placed in the third (3rd) room. The electric potential of 20 kV was applied to the upstream parts indicated by zeroth (0th), first (1st) and second (2nd) rooms in the gas cell system in Fig 15. The 2nd and 3rd rooms were connected by an insulator flange.

The details of each component in the gas cell system are mentioned in the following subsections.

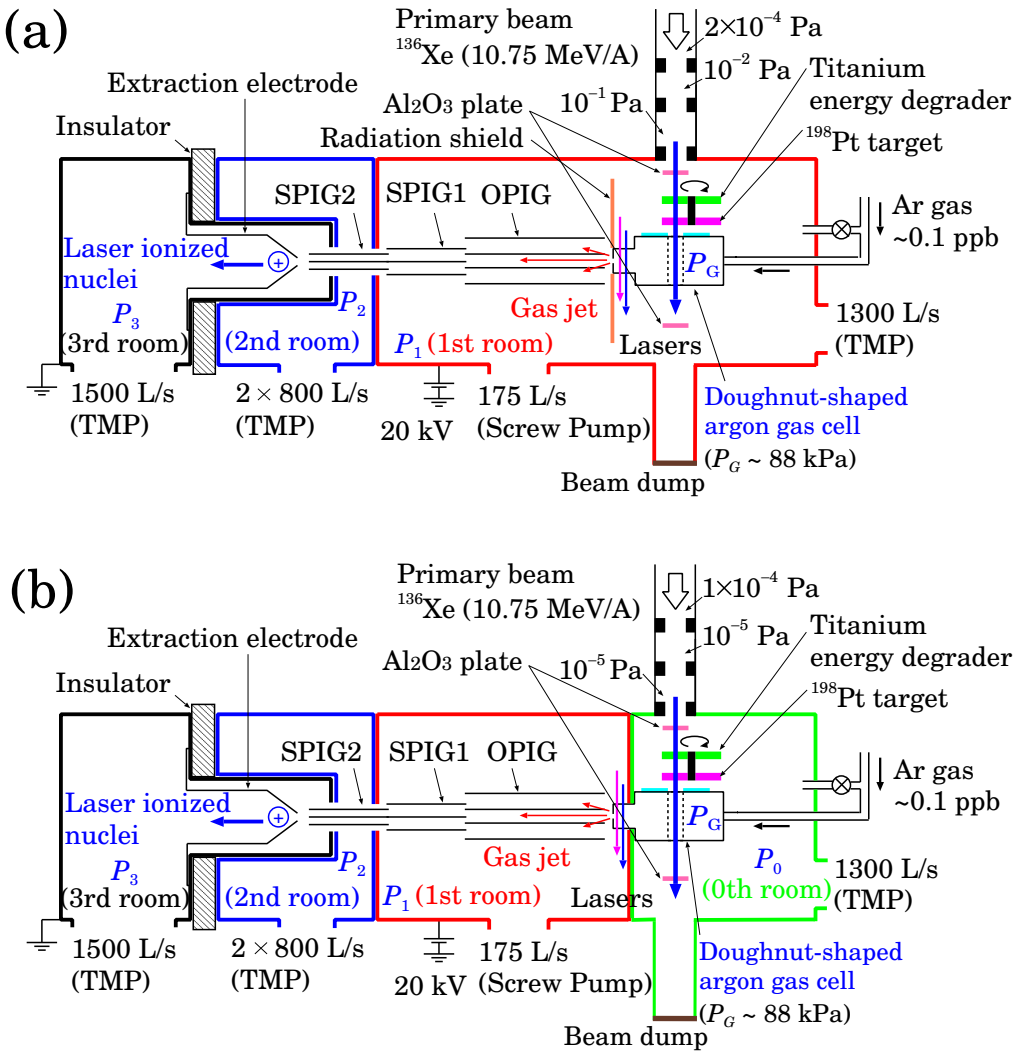

Figure 15: Schematic views of the two types of the gas cell system [79]. The boundaries of the zeroth, first, second and third rooms for a differential pumping are indicated by the thick green, red, blue, and black lines, respectively. (a) Doughnut-shaped gas cell with a radiation shield for suppression of the plasma effect induced by the primary beam, and the configuration of three rooms. (b) Doughnut-shaped gas cell and the configuration of four rooms, where the pressure of the zeroth room reaches to a high vacuum of 10^{-4} Pa to significantly suppress the plasma effect induced by the primary beam.

3.1.1 Primary beam transport

We applied a differential pumping system in the primary beamline, which consisted of three pumping sections, to keep the primary beamline with a pressure level of 10^{-4} Pa without the use of the partition foil between the primary beamline and the 1st (0th) room as shown in Fig. 15(a) (15(b)). The pressures of these rooms from the upstream were 2×10^{-4} (1×10^{-4}), 10^{-2} (10^{-5}), and 10^{-1} (10^{-5}) Pa, which sufficiently low to transport the primary beam, in the case of a gas cell pressure of 88 kPa in Fig. 15(a) (15(b)).

As shown in Fig. 15, two aluminum oxide (Al_2O_3) plates are placed at the upstream and downstream of the gas cell to check the spot size and position of the primary beam. The effective area of the Al_2O_3 plate is 20×20 mm^2 and thickness is 1 mm. These Al_2O_3 plates are graduated in 5 mm in the horizontal and vertical directions. The beam position and size are adjusted by monitoring the fluorescence emitted from the upstream Al_2O_3 plate by a camera with the primary beam intensity of less than 0.005 pnA. Then, the

beam transport passing through the doughnut-shaped gas cell is confirmed by using the downstream Al_2O_3 plate in the same manner as performed at the upstream Al_2O_3 plate.

3.1.2 Radiation shield

In the case of the setup shown in Fig. 15(a), the plasma produced by the irradiation of primary beam along the primary beam trajectory in the 1st room would neutralize the laser-ionized atoms during the transport in the MRFIG. We introduced the radiation shield around the gas cell exit as shown in Fig. 15(a) to suppress the plasma effect. The shield was made of a stainless steel with a thickness of 2 mm and drastically attenuated the UV radiation, low-energy characteristic X-rays (less than 5 keV), and electrons (less than a few MeV) arising from the argon atoms. The area of the shield approximately 30 cm in height and 40 cm in width was large enough to shadow the MRFIG.

After the confirmation of the increasing of ion yields by introducing the radiation shied as explained in later subsection 4.2.1, we separated the vacuum chamber to construct the 0th room newly as shown in Fig. 15(b). The pressures of the the 0th, 1st, 2nd, and 3rd rooms in the front ends in Fig. 15 were $P_0 = 10^{-4}$ Pa, $P_1 = 30$ Pa, $P_2 = 10^{-1}$ Pa, and $P_3 = 10^{-4}$ Pa, respectively.

3.1.3 Rotating energy-degrader and target

The energy-degrader (three Ti foils) and target were used in combination with rotating wheels as shown in Figs. 16(a), (b), and (c) to reduce the thermal damages on the foils. Fig. 16(a) shows the front view of the wheel. Center diameter of the foil area indicated by violet color was 60 mm, and the foil width was 10 mm. The area was segmented to eight foils by wheel spokes with 3 mm width, and the fraction of the foil area was 87%. Fig. 16(b) shows top view of the assembled wheels. The red arrow indicates the primary beam. Total 5 wheels were fixed to one rotating shaft. The maximum rotating speed of the motor was 2000 rpm in high vacuum conditions ($\sim 10^{-5}$ Pa). Typical rotating speed was 1000 rpm. The motor was cooled by a water cooled copper block, which played a role as a collimator with a diameter of 10 mm and length of 35 mm.

The spokes of the first wheel were covered by eight aluminum oxide (Al_2O_3) plates, and eight ID tags corresponding to the spoke positions, as shown in Fig. 16(a). A photo-sensor was installed to identify the ID tag position, i.e. the spoke positions, to ensure that chopping the primary beam did not irradiate the spokes. Full details of the operation can be found in Ref. [82]. The chopping timing and duration were adjusted by monitoring the fluorescence emitted from the Al_2O_3 plates on the spokes by a camera. The primary beam was chopped at a beam deflector at the downstream of a Xe-gas ion source synchronizing with the output signal from the photo-censor via a gate and delay generator (GDG) which adjusted the duration time and the delay of the photo-censor signal.

The energy deposit of $^{136}Xe^{20+}$ beam with a diameter of 6 mm in the Ti foils and ^{198}Pt target are shown in Table 4. The beam irradiated area was considered to calculate the energy deposit per unit area. The area of annulus with inner and outer diameters of 54 and 66 mm, respectively, was considered in the case of the rotating wheel. In a previous on-line experiment, the energy degrader made of Havar foil with 10 μm in thickness was broken by the irradiation of ^{136}Xe beam with 25 pnA and an energy of 10.75 MeV/nucleon. In that case, expected energy deposit in the foil was about 30 W/cm^2. An available maximum intensity of ^{136}Xe beam was estimated to be 250 pnA in the use of the rotating Ti foils with 3 μm in thickness and ^{198}Pt foil with 12.5 mg/cm^2 in thickness, because the energy

deposits in these foils are enough lower than that which induced the foil broken due to the thermal damage at the previous measurement.

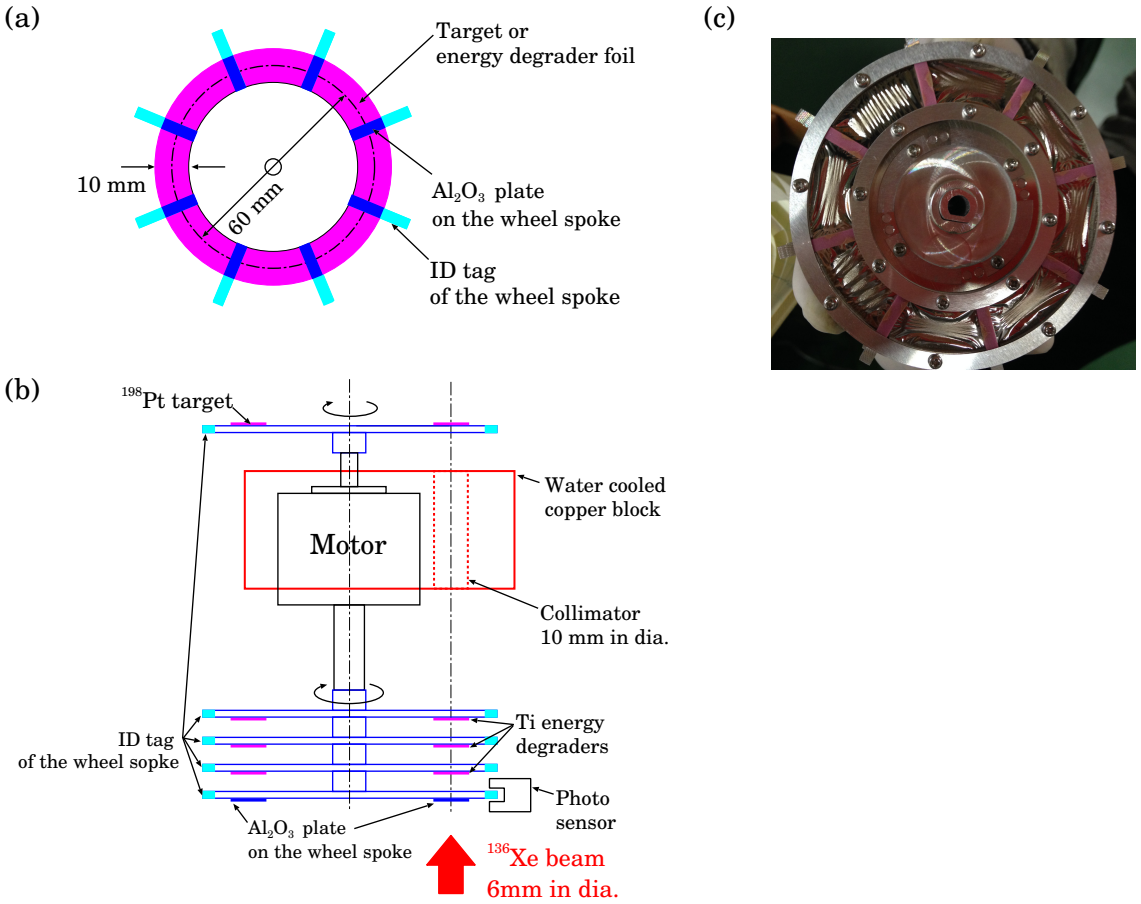

Figure 16: (a) Front view of the wheel. (b) Top view of the assembled wheels with a shaft, motor, water cooled copper collimator, and photo-censor. (c) Photo of the wheel with Al_2O_3 plates on the eight spokes (material color is pink) and eight Ti foils with 3 μm in thickness.

Table 4: Energy deposits of ^{136}Xe beam on the foils.

Foil	Thickness (μm)	Beam energy (MeV/nucleon)	Energy loss (MeV)	Energy deposit (W/pnA/cm^2)		(W/cm^2)
				fixed	rotating	rotating 250 pnA
1st layer Ti	3	10.75	60	0.21	0.0053	1.3
2nd layer Ti	3	10.31	61	0.21	0.0054	1.3
3rd layer Ti	3	9.86	61	0.22	0.0054	1.4
^{198}Pt	5.8	9.41	349	1.23	0.0309	7.7

3.1.4 Doughnut-shaped gas cell

The TLFs produced by the MNT reactions were stopped, neutralized, and laser-ionized in an argon gas cell. Figure 17 shows the three-dimensional views of the KISS gas cells [79, 83]. The size and components of the gas cell are represented in Fig. 17(a). The same components without Havar foil windows were used in the doughnut-shaped gas cell shown in Fig. 17(b).

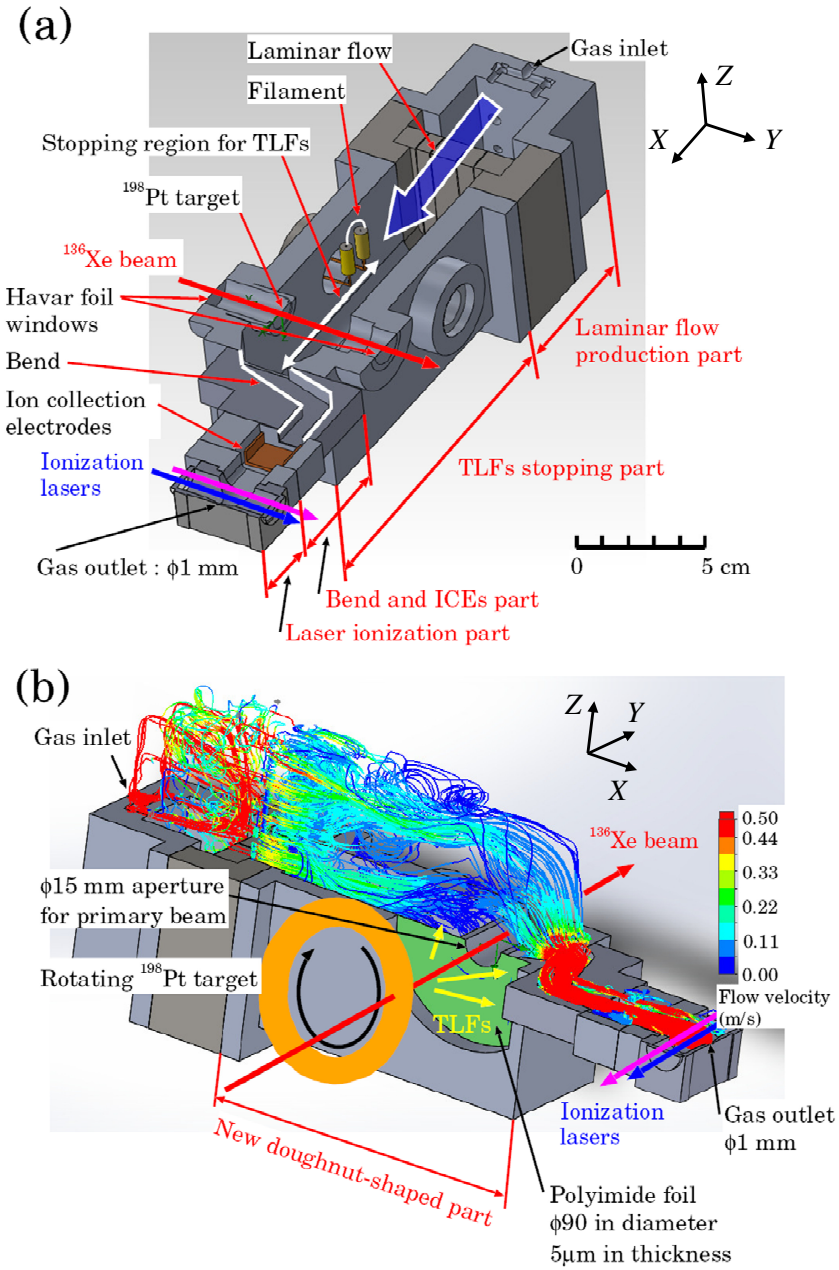

Figure 17: Schematic views of (a) the original KISS gas cell [83], and (b) the doughnut-shaped gas cell [79].

The KISS gas cell consisted of the following four parts: laminar flow production, TLFs stopping, bend and a pair of ion collection electrodes (ICEs), and laser ionization. The uniform laminar gas flow was generated at the laminar flow production part which consists of four slits and a gas buffer region between the slits and ten gas injection ports. The TLFs were stopped and neutralized at the stopping region, whose size is $90(Z) \times 120(X) \times 30(Y)$ mm^3. The bend part was applied for shielding the downstream region

of the gas cell from the plasma induced by the TLFs injection and for suppressing the reduction of the extraction efficiency and the selectivity by the plasma. The ICEs were introduced to absorb unwanted ions and increase the sensitivity. The suppression factor of the unwanted ions was measured to be more than 10^5 with ± 50 V for the respective electrodes. Just before the gas cell exit, a pair of synthetic quarts windows (10 mm in diameter) was installed for the laser irradiation. The length in X direction of laser ionization region was 10 mm and the previously measured evacuation time was ~ 10 ms [83]. This evacuation time is enough shorter than the atomic reaction time of 5.6 s for the molecular ion formation between the ionized TLFs and impurities considering the typical reaction rate of 1×10^{-10} cm^3/s and an impurity level of 0.1 ppb at argon gas pressure of 74 kPa. The size of the gas cell exit hole was 1 mm in diameter.

The doughnut-shaped gas cell [79] shown in Fig. 17(b) had aperture of 15 mm in diameter along the primary beam axis. The primary beam passes through the aperture without entering the gas cell. The TLFs and the elastic nuclei were implanted in the gas cell by penetrating a thin polyimide foil 90 mm in diameter and 5 μm thick. The angular acceptance of the window was designed to be 48°–79°, which enabled full coverage of the TLF emission angles of $65° \pm 10°$ in the laboratory frame. Both sides of the polyimide foil were coated with a 10 nm layer of gold to avoid charge-up issues on the surfaces. A stainless-steel honeycomb grid [84], with 92.5% transparency and a thickness of 0.5 mm, covered the polyimide foil to maintain the argon-gas pressure at 88 kPa with the polyimide foil. The maximum pressure of 88 kPa was determined by the maximum conductance of the gas flow value at KISS. The evaluated implantation efficiency $\varepsilon_{\mathrm{implant}}$ and stopping efficiency $\varepsilon_{\mathrm{stopping}}$ were 0.71 (including the 92.5% transparency of the honeycomb grid) and 0.82, respectively. The stopping power was calculated by the SRIM2008 code [85].

The colored lines in Fig. 17(b) indicate the calculated argon gas flow trajectories. The gas flow trajectories toward the gas cell exit smoothly. The previously measured mean transport-time of the TLFs from the stopping region to the gas cell exit was 455 ms. This is faster than typical half-life $T_{1/2} = 1$ s of $A \sim 200$ nuclei and the decay loss probability was estimated to be $< 13\%$. The estimated transport efficiency $\varepsilon_{\mathrm{transport}}$ considering the diffusion loss of TLFs at the gas cell wall was 0.36. Finally, the extraction efficiency of the TLFs from the doughnut-shaped gas cell was estimated to be $\varepsilon_{\mathrm{extraction}} = \varepsilon_{\mathrm{implant}} \times \varepsilon_{\mathrm{stopping}} \times \varepsilon_{\mathrm{transport}} = 0.21$.

3.1.5 Laser ionization

The neutralized TLFs are laser-ionized element-selectively at the laser ionization region located near the gas cell exit. Figure 18 shows the schematic view of the two-color two-step laser resonance ionization schemes used in KISS. The atoms are excited element-selectively by the photo-absorption of a wavelength λ_1. The atomic continuum above an ionization potential is populated by the photon-absorption of the following ionization laser with a wavelength λ_2. The atomic excited states have been studied for many elements and the properties of the atomic states are available from [86, 87, 88]. We selected the transition to the excited state which has the Einstein coefficient A with a order of 10^{7-8} s^{-1}, and less transition probability to intermediate states (indicated by the violet arrow) than that to the ground state. The required photo-absorption cross-sections to obtain the ionization efficiency of several ten % in the KISS gas cell (in-gas-cell, laser spot size 10 mm in diameter) are a order of $10^{-14\ \mathrm{to}\ -13}$ cm^2 for the λ_1 laser and $10^{-15\ \mathrm{to}\ -14}$ cm^2 for the λ_2 laser. The photo-absorption cross-sections of Ta, W, Re, Os, and Ir were studied in Refs. [74, 89, 90].

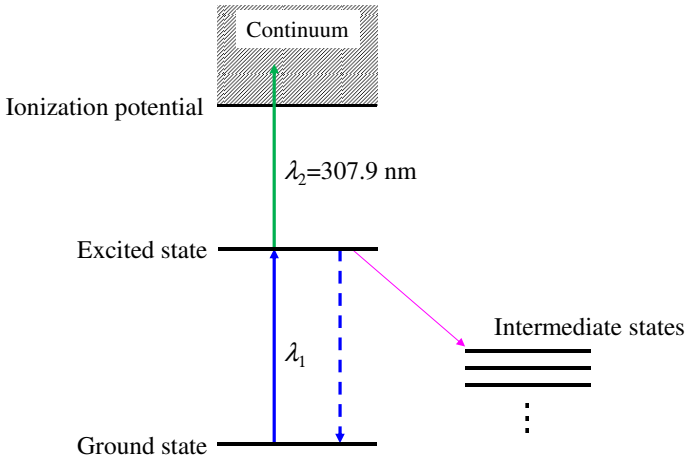

Figure 18: Schematic view of the two-color two-step laser resonance ionization scheme indicated by blue and green lines. The blue broken line indicates the transition from the excited state to the ground state. The violet line indicates the transitions from the excited state to the intermediate states.

The ionization potentials of the elements with $Z = 55$–78 are < 8.97 eV. The intense excimer laser (XeCl, $\lambda_2 = 307.9$ nm, 4.03 eV, and about 5 W) was used as the λ_2 laser. Therefore, the required wavelength for the λ_1 laser was ultraviolet (UV) region with $\lambda_1 < 256$ nm. The laser wavelength λ_1 was obtained from the wavelength tunable dye laser combined with a second harmonic generator (SHG). Figure 19 shows the schematic view of the KISS laser system.

The laser paths of the λ_1 and λ_2 lasers are indicated by the blue and green lines, respectively. The dye laser (Radiant Dyes, NarrowScan) pumped by the excimer laser (XeCl, Lambda Physik, LPX240i) generates a fundamental wavelength of $2\lambda_1 \sim 500$ nm

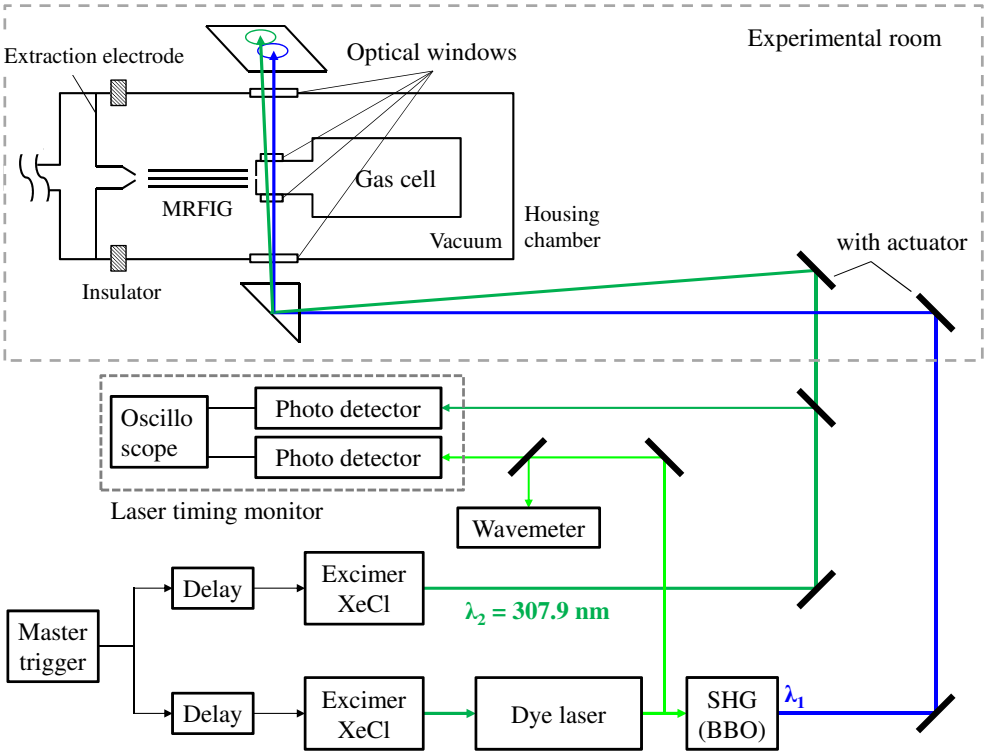

Figure 19: Schematic view of the KISS laser system.

by using the dye Coumarin 500 (C500). The laser with $2\lambda_1$ from the dye laser was frequency doubled by using a barium borate (BBO) crystal placed in a second-harmonic generator (SHG). Conversion efficiency of the dye laser and SHG are about 13 % and 10 %, respectively. Typical laser powers of the λ_1 and λ_2 lasers were 500 μJ/pulse at the exit of the SHG and 50 mJ/pulse, respectively. The measured laser pulse width was $\sim$ 15 ns in FWHM. The measured line width of the λ_1 laser was 3.4 GHz in FWHM. The repetition rate of the lasers was variable from 1 to 200 Hz. The external trigger signals for the two excimer lasers were provided by a function generator (Tektronix, Inc., AFG1022) and through the cable delay modules. A part of $2\lambda_1$ and λ_2 lasers were incident in photo diodes (Electro-Optics Technology Inc., ET3020) to monitor the timing between those lasers with an oscilloscope. The timing between the two lasers were monitored during the experiments and the delay time was adjusted with 1 ns step as to keep the maximum ion yield. The wavelength $2\lambda_1$ was monitored by sampling about 1% fraction of the laser power at a wavemeter WS6 (HighFinesse) during the measurements. The transmissions of the lasers with λ_1 and λ_2 between the exit of the laser and the laser ionization region in the gas cell were measured to be about 50% and 25%, respectively. The spacial overlap of two lasers at the gas cell were optimized before the experiment. The laser positions on a paper through the vacuum chamber were adjusted by using mirrors with actuators to maximize the ionization efficiency during the experiment.

The excitation transitions used in the present experiments were $5d_76s_2\ ^4F_{9/2} \rightarrow 5d_66s_26p\ ^6F_{9/2}$ (λ_1 = 247.587 nm, 40390 cm^{-1}) for iridium and $5d_96s\ ^3D_3 \rightarrow\ 5d_86s6p\ ^5F_4^0$ (λ_1 = 248.792 nm, 40194 cm^{-1}) for platinum. The Einstein coefficients of these transitions are 2.073×10^7 s^{-1} for iridium and 6.284×10^7 s^{-1} for platinum [88]. The measured laser power dependences of the number of the laser-ionized stable $^{191}Ir^+$ are shown in Fig. 20. The horizontal axis indicates the laser power at the gas cell. The saturation were achieved with a λ_1 laser power of about 40 μJ/pulse and λ_2 laser power of about 12 mJ/pulse.

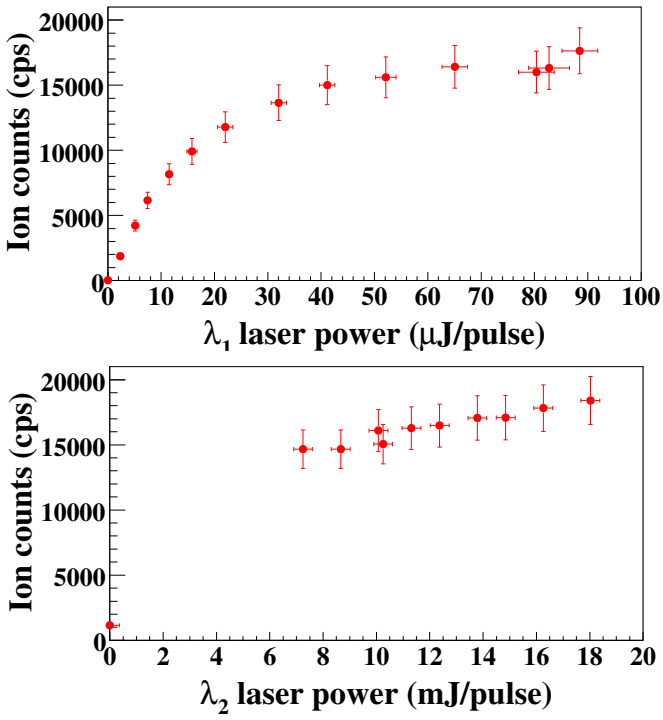

Figure 20: λ_1 laser (upper) and λ_2 laser (lower) power dependences of the number of the laser-ionized stable $^{191}Ir^+$.

3.1.6 Gas purification system

The TLFs stopped in the gas cell would form molecules or molecular ions combined with impurities, such as H_2, H_2O and $(C_nH_m)_x$, in argon gas. These molecules cannot be ionized resonantly and high-efficiently by irradiation of the ionization lasers, and also the molecular ions would be formed in the gas cell after the laser-ionization of TLF atoms. As the result, the extraction yield of the TLF ions from KISS are decreased due to the impurities in argon gas and the gas cell. Therefore, to achieve high extraction efficiency of singly-charged radioactive ions produced by the laser resonance ionization, it is essential to reduce the amount of impurities to a level of around 1 ppb [63] by using a gas cell whose evacuation time and pressure are about several hundreds ms and several tens kPa, respectively.

Figure 21 shows a schematic view of the argon gas feeding line [83]. The line consists of a 1/4-inch electro-polished stainless steel tube, metal-sealed valves, and the devices shown in Fig. 21. It can be baked up to 390 K and can be pumped using an oil-free pump. We purchased a high-purity argon gas cylinder with the purity of $> 99.9999\%$. The impurities in the argon gas, based on a list for the cylinder provided by the company, are O_2 (< 0.1 ppm), N_2 (< 0.3 ppm), H_2 (< 0.1 ppm), CO (< 0.1 ppm), CO_2 (< 0.1 ppm), total hydro carbon (THC, < 0.1 ppm), and H_2O (< 0.2 ppm). These impurities are reduced the levels to < 1 ppb by using a getter-based purifier (MonoTorr Phase II 3000, SAES Pure Gas, Inc.). The argon gas flow rate is monitored by a mass flow meter (SEF-8450F, HORIBA STEC, Co.,Ltd). Argon gas with a pressure of 200 kPa is supplied through a quartz tube (inner diameter 4 mm, length 500 mm) to the gas cell system placed on a high voltage platform in order to avoid electric discharge. The argon gas is additionally purified to < 0.1 ppb, except for N_2, through a getter-stabilized zeolite filter (MC1-903F Micro Torr, SAES Pure Gas, Inc.), which can provide the purification under the pressure of 200 kPa in the system. The pressure of the argon gas is reduced to the required gas cell pressure of several ten kPa, which depends on the experimental conditions, by using a piezo valve in the mass-flow controller (SEC-8450LS, HORIBA STEC, Co., Ltd.) with a flow range of 0.1–6.0 standard liters per minute (slm). The gas cell pressure is monitored in the range 10^{-2} Pa–100 kPa by a cold-cathode type pressure-gauge (M-320XG, Canon Anelva, Co., Ltd.).

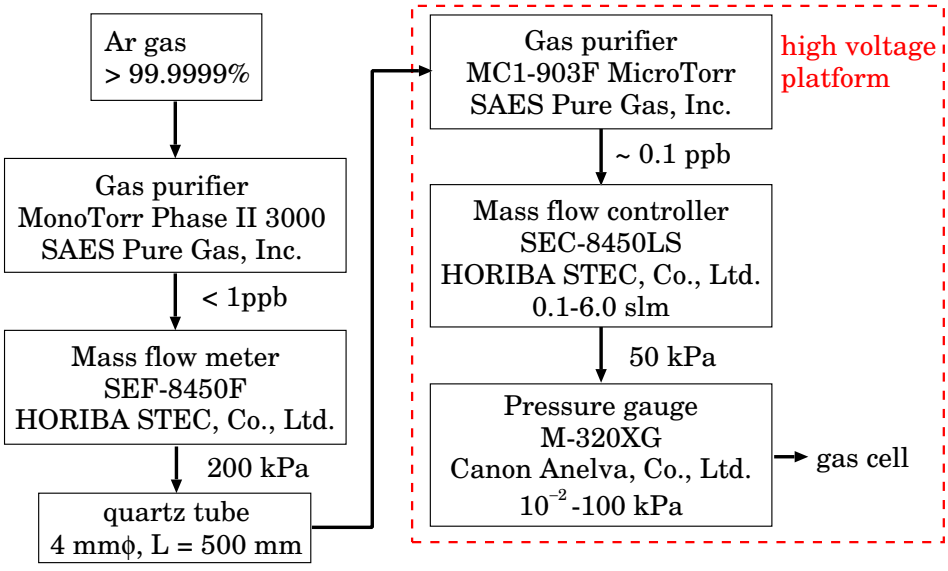

Figure 21: Schematic view of the argon gas feeding line.

The effect of each purification stage (getter-based purifier, baking, and zeolite filter) was confirmed by measuring the mass distribution of the extracted ions from the KISS gas cell system as shown in Fig. 22. Here, we used the original gas cell in Fig. 17(a). The ions were produced by the irradiation of α-particles from a standard Am-α source (40 kBq) which was placed at the front of the Havar window of the gas cell. The mass spectrum in Fig. 22(a) was obtained with the only use of the getter-baser purifier. Most of argon ions induced by the α-particles formed hydrate molecules such as $ArH(H_2O)^+$, $ArH(H_2O)_2^+$, and $Ar_2H(H_2O)_2^+$. Other peaks seen in the spectrum would be originated from the compounds of argon ions and hydrocarbons such as $Ar_x(C_nH_m)_y^+$. The mass spectrum in Fig. 22(b) was obtained after the baking of the gas cell and gas lines at 390 K with argon gas flow of 0.3 slm during more than two days. The most of $Ar_x(C_nH_m)_y^+$ were disappeared but still argon hydrate ions were observed. The mass spectrum in Fig. 22(c) was obtained after a half-day of the gas flow through the additional zeolite filter. The argon hydrate ions were disappeared and argon dimer ions were appeared. The hydride ions of argon dimer were also observed but the yield of them was 5 times lower than that of $^{40}Ar_2^+$. In this way, most of impurity was removed by the filters and baking of the gas cell and gas lines.

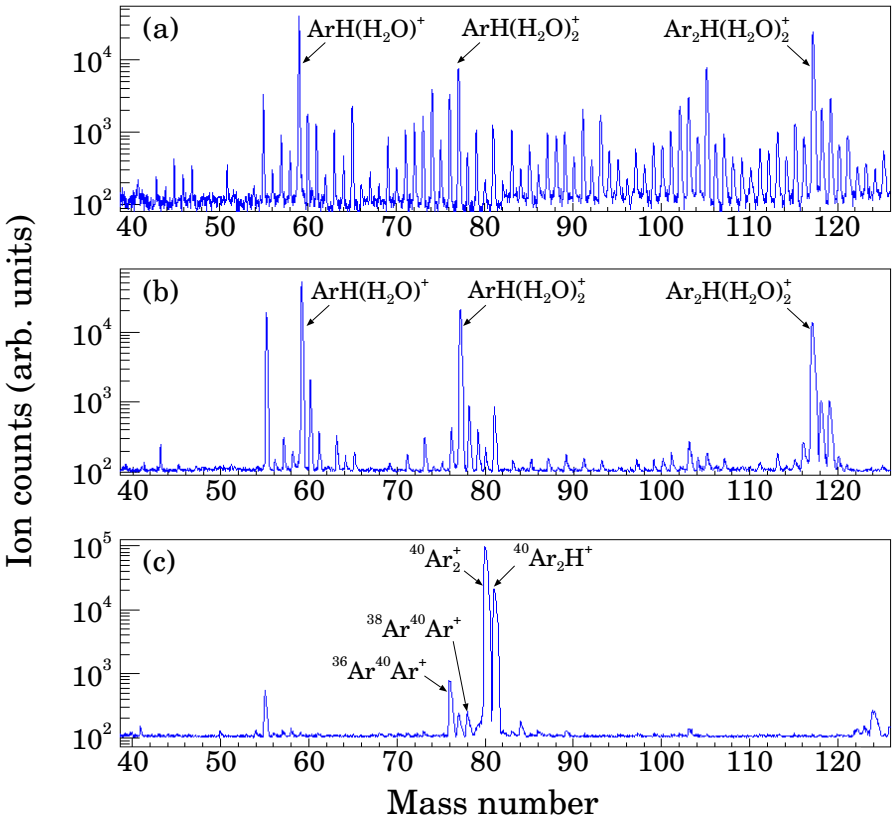

Figure 22: Measured mass distribution with three purification condition: (a) with getter-base purifier, (b) after the gas cell baking with 390 K, and (c) with additional zeolite filter.

3.1.7 Multi-RF ion guide (MRFIG)

The ions ejected from the gas cell exit were transported to the higher vacuum region through a Multi-RF ion guide (MRFIG) for the acceleration with 20 kV. MRFIG consists of three kinds of multi-pole RF ion guides [80, 81]. The cross-sectional view of a

sextupole ion guide with cylindrical electrodes is shown in Fig. 23(a). The poles with the number of $N_{\rm p}$ are positioned with equally space and a radius of inscribed circle of r_0. The ions are confined in the electric potential produced by RF voltage of $\pm V_{\rm RF}\cos(\omega t)$ and $\pm V_{\rm RF}\cos(\omega t+\pi)$ applied to the multi-poles alternatively in opposite phase, where $V_{\rm RF}$, ω, and t are the amplitude of RF voltage, angular frequency, and time. The potential (U) around a central axis is expressed by

$$U = \left(\frac{r}{r_0}\right)^{N_{\rm p}/2} \cdot V_{\rm RF} \cdot \cos\left(\frac{N_{\rm p}}{2}\theta\right) \cdot \cos(\omega t). \tag{67}$$

Here, r and θ are the position in cylindrical coordinates. The potential does not affect to the axial motion of ions. The ion motion can be expressed by the sum of two motions: one is slow average motion and another one is fast oscillation motion around the slow average trajectory with high enough ω. The average trajectory is described by a periodic motion in the effective potential ($U_{\rm eff}$) which is given by

$$U_{\rm eff} = \frac{\left(\frac{N_{\rm p}}{2}qV_{\rm RF}\right)^2}{4m(r_0\omega)^2}\left(\frac{r}{r_0}\right)^{N_{\rm p}-2}. \tag{68}$$

Here, m and q are the particle mass and ionic charge, respectively. For the confinement of ions with heavier mass, the lower frequency or higher RF amplitude is required. The transportation efficiency of ions through the multi-pole RF ion guides becomes almost 100% by applying suitable RF voltage and frequency.

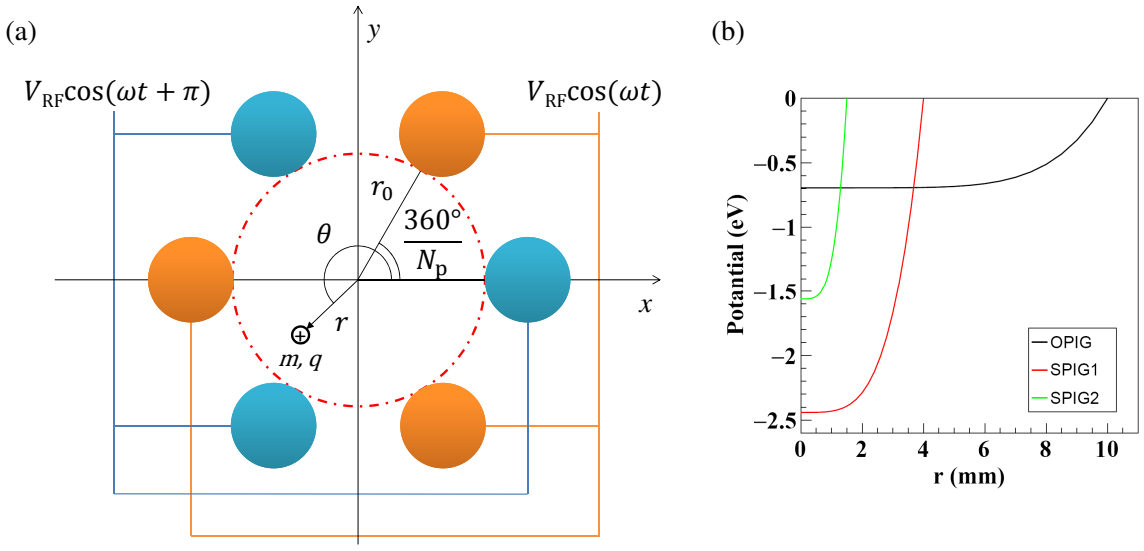

Figure 23: (a) Cross-sectional view of a multi-pole RF ion guide with $N_{\rm p} = 6$. (b) Pseudo-potentials produced by the three multi-pole RF ion guides which are used at KISS with the voltage settings shown in Table 5. The axial symmetry potential lines for the singly-charged ion with a mass number of $A = 198$ are plotted and the surface of the electrode is set to 0 V.

Figure 24 shows the MRFIG setup used in the combination with both KISS gas cell systems in Figs. 15(a) and (b). Three multi-pole RF ion guides were used for efficient trapping of laser-ionized atoms using the first ion guide, differential pumping with small inscribed diameter of the third ion guide, and molecular dissociation with DC voltages between the ion guides. The first ion guide has octupole configuration ($N_{\rm p} = 8$, OPIG), second and third ion guides have sextupole configuration ($N_{\rm p} = 6$, SPIG1, 2). The

geometry of the OPIG was 20 mm in diameter and 155 mm in length; that of SPIG1 after the OPIG was 8 mm in diameter and 71 mm in length; and that of SPIG2 after SPIG1 was 3 mm in diameter and 200 mm in length. The position of OPIG was 20 mm from the gas cell exit. The rod diameters of the OPIG, SPIG1, and SPIG2 were 8, 4, and 1.5 mm, respectively. The OPIG-SPIG1 and SPIG1-SPIG2 configured to overlap to each other with a length of 0.5 mm at both ends, respectively. The pseudo-potential distribution produced by each RF ion guide in Fig. 23(b) are calculated by using Eq. (68). The three potential distributions are deep enough to trap the singly-charged ion, which has a mass number of $A = 198$ and kinetic energy of 0.1 eV, which corresponds to the typical gas-jet velocity of ~ 550 m/s [72].

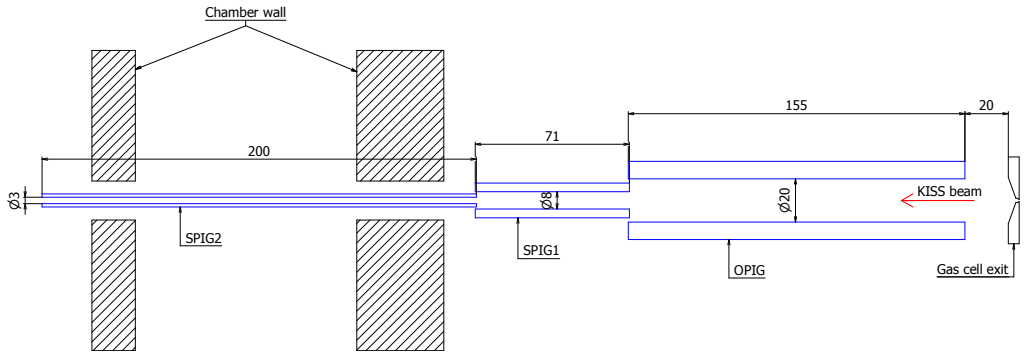

Figure 24: Setup of the MRFIG. The unit of dimension is mm.

The RF circuit for the multi-pole RF ion guides is shown in Fig. 25. The sine wave was generated by using a waveform generator (Hioki E.E. Corp., 7075 Waveform generator) and RF amplifier (OPIG: Thamway Co., Ltd., T145-5516A, SPIG1: Thamway Co., Ltd., T145-4716A, SPIG2: RF Power Labs, Inc., Wideband RF Amplifier M102L). The sine wave was divided into two signals by using a Ferrite core with 3 turns for input and 19 turns for output. The resonance of the LC circuit was obtained adjusting variable condensers (Comet PCT, CVUN-1000AC/5-BAJA). DC voltage for the molecular dissociation was applied to the LC circuit through the low-pass filter in Fig. 25. The output of the LC circuit was monitored by using a voltage probe (Iwatsu electric Co., Ltd., SS-0014) and oscilloscope (Tektronix, Inc., TDS 2024B). The outputs are introduced to the electrodes in the vacuum chamber through feedthroughs.

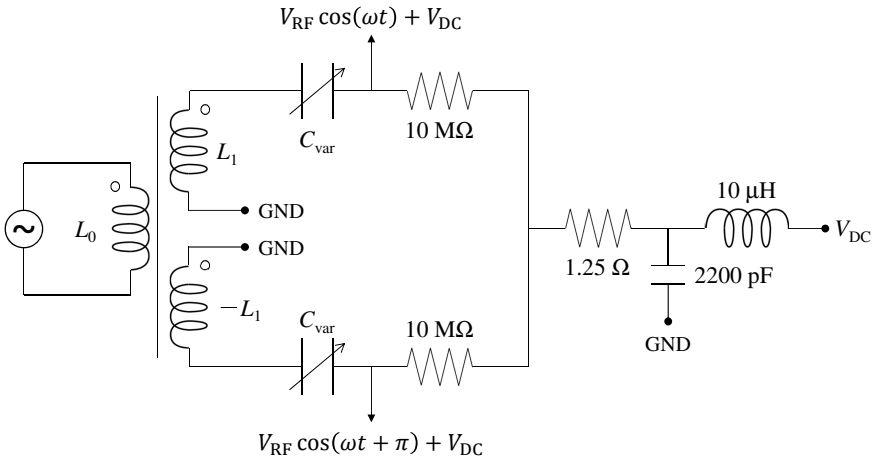

Figure 25: RF circuit for the multi-pole RF ion guides. The $L_{0,1}$, C_{var}, and V_{DC} are the inductances of trans coils, capacitance of the variable condenser, and DC voltage.

The OPIG was installed to increase the trap efficiency of laser-ionized atoms emitted with a large diameter gas-jet [79]. The typical operation parameters of the MRFIG are summarized in Table 5. The RF amplitudes and DC voltages are adjusted at every KISS experiment to maximize the KISS beam transportation.

DC voltages were applied independently to the OPIG, SPIG1, and SPIG2 to dissociate molecular ions around the overlapped positions. Typical DC voltages for the dissociation are listed in Table 5. The acceleration energy of molecular ions ($\sim$ 1.7 eV) between SPIG1 and SPIG2 using the voltage settings for molecular dissociation exceeds the binding energy of hydrate molecular ions of transition metal ($\leq$ 1.7 eV) [79]. Therefore, more than 90% of the molecular ions was recovered as singly-charged ions of our interest element.

Table 5: Typical operation parameters of the MRFIG with molecular dissociation mode.

	RF frequency $\omega/2\pi$ (MHz)	RF amplitude V_{RF} (peak-to-peak V)	DC voltage V_{DC} (V)
OPIG	2	150	0
SPIG1	2	150	-10
SPIG2	4	90	-29

3.2 KISS beam transport

The Z-selected ion beam with an energy of 20 keV is analyzed with mass number of each beam particle by a dipole magnetic field and then transported to the detector station. Figure 26 shows the ion-optical components on the KISS beamline. The ion-optical configuration in KISS is EQD-MD-MQD-F1-EQT-F2, where EQD, MD, MQD, and EQT are electric quadrupole doublet, magnetic dipole, magnetic quadrupole doublet, and electric quadrupole triplet, respectively. F1 and F2 indicate two focusing planes. The size and distance of each ion-optical component are summarized in Table 6.

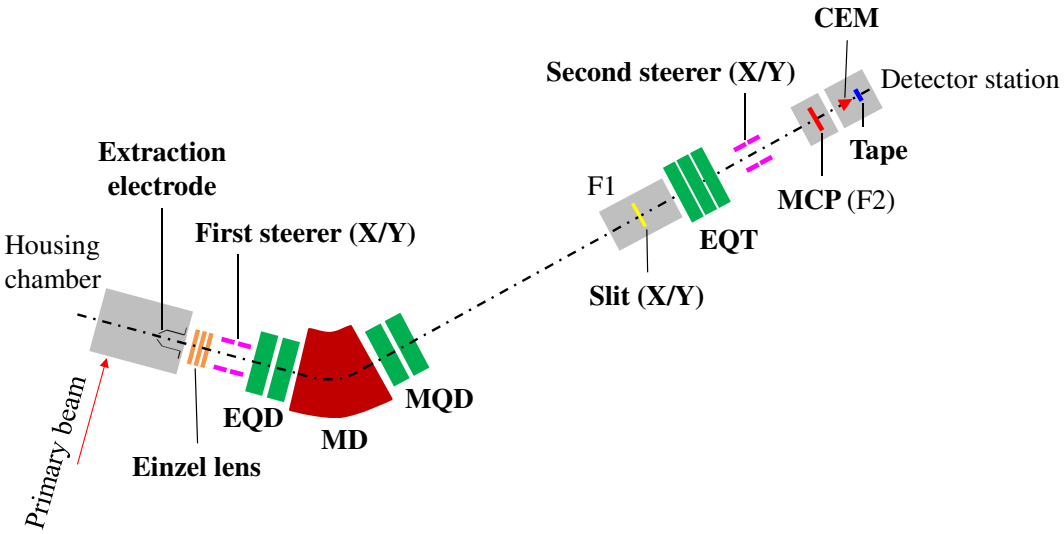

Figure 26: Schematic view of the KISS beamline.

The accelerated KISS beam at the extraction electrode passes through an einzel lens and steerer. The einzel lens is a beam focusing component. The steerer consists of two

Table 6: Basic parameters for the ion-optical components and beam diagnostics at the KISS beamline. Drift length is the length from the exit of each component to the entrance of next component.

Optics component	Size	Drift length (cm)
From extraction electrode	-	83
EQ01	Electrode length = 10 cm, Diameter = 6 cm	10
EQ02	Electrode length = 10 cm, Diameter = 6 cm	30
MD	bending radius $\rho = 133$ cm, deflection angle = 45°	30
MQ03	Field length = 20 cm, Bohr diameter = 13 cm	20
MQ04	Field length = 20 cm, Bohr diameter = 13 cm	403
F1 X slit	-	54.3
EQ05	Electrode length =10 cm, Diameter = 6 cm	5
EQ06	Electrode length =10 cm, Diameter = 6 cm	5
EQ07	Electrode length =10 cm, Diameter = 6 cm	114
MCP	-	40.8
CEM	-	10.2 (to Tape)

sets of parallel planar electrodes (size= 25×25 mm^2, gap= 30 mm) for horizontal (X) and vertical (Y) directions with a spacing of 150 mm along the beam direction. The steerer is used to adjust the beam position at X and Y direction. Mass numbers of extracted ions are selected by a dipole magnetic field in the MD. The relation between the magnetic rigidity $B\rho$ of the MD and mass number A of a singly charged ion is expressed as

$$B\rho = \sqrt{2Am_uE}, \tag{69}$$

where E is an energy of extracted ion and m_u is the atomic mass unit, namely, m_u = 931.494013(37) MeV/c^2. Measured mass resolving power was about 900 for the ions with $A \sim 190$. The mass distribution after the MD was restricted by using the slit system for the X and Y directions placed at F1 to suppress the contaminations with mass numbers $A \pm 1$. The second steerer placed at the F2 consists of two sets of parallel planar electrodes (size= 60×60 mm^2, gap= 60 mm) for X and Y directions with a spacing of 200 mm along the beam direction. A two-dimensional beam profile monitor was also installed at the F2.

The beam profile monitor at F2 was a multi-channel plate detector (Photonis USA Inc., hereafter termed as MCP) with a delay-line anode (RoentDek Handels GmbH, DLD40). The MCP has an active area of 40 mm in diameter, micro-channels of 25 μm in diameter, and the plate of 1.5 mm in thickness with Chevron configuration. The operating voltages applied to the front and back side of the MCP stack are -1900 V and +50 V, respectively. The multiplied electrons in the MCP are collected by delay-line anodes applied a voltage of +300 V which consist of a wire strained to each X and Y directions with 1 mm pitch (isolated two layers). The beam profile is obtained from the collected signals of the delay-line anode readouts with a typical resolution of 0.1 mm. The operating pressure of the

MCP is less than 2×10^{-4} Pa. Typical size of the KISS beam at the MCP is 2 mm in FWHM.

The transport of the KISS beam was measured at the final plane located at 40.8 cm downstream from the MCP and 10.2 cm upstream from the tape which passes through the center of the detector station. The final beam monitor was a channel electron multiplier (Photonis USA Inc., MAGNUM^{TM} electron multiplier 5901, hereafter termed as CEM) which has beam irradiation part of $\sim$ 8 mm in diameter. The operating pressure of the CEM is recommended to be less than 0.1 Pa. The operating voltage of the CEM was -1850 V. The transport of the KISS beam was optimized by adjusting the second steerer to maximize the ion counts at the CEM.

3.3 Detection system

The detection system was consisted of a tape transport system, β-ray and γ-ray detectors, veto counters for cosmic-ray, and lead shield for environmental background γ-rays. Figure 27 shows the photo of detector station without γ-ray detectors and lead shield.

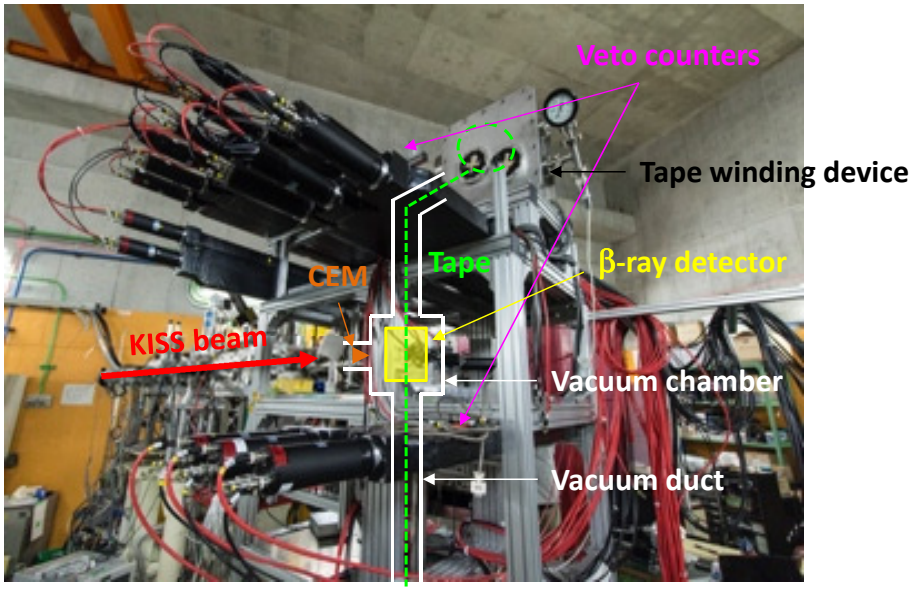

Figure 27: Photo of the KISS detector station.

Tape transport system

The extracted ions with an energy of 20 keV from KISS were implanted on the tape which was placed in a vacuum chamber and at the final focus point of the detector system. The tape was made of an aluminized Mylar with a thickness of 12.5 μm and width of 12.5 mm. The tape was driven upward by using two tape winding devices placed at the top and bottom sides of the detection system. The tape moves about 30 cm at every starting time of time sequence for activity measurements to removing out the residual activities just after every measurements for precise decay spectroscopy.

β-ray and γ-ray detectors

For β-ray detection, we used plastic scintillator telescopes at the first experiment and newly developed gas counters at the second one. The β-ray detectors in a vacuum chamber

cover the implantation point on the Mylar tape to achieve large solid angle $> 75\%$ of 4π, and have an aperture for KISS beam transport. For γ-ray detection, we used two coaxial-type germanium detectors and four clover-type germanium detectors at the first and second experiments, respectively. These were placed just outside of the vacuum chamber to achieve the large solid angle. The details of two detector setups for the first and second experiments are shown in following subsections.

Veto counters for cosmic-ray

Plastic scintillators were used as the veto counters for cosmic-ray to reject the cosmic-ray events which fired the β-ray detectors. The veto counters used at the first (second) experiment consisted of 13(10) wide plastic scintillator bars (BICRON BC408, size: $5\times15\times135$ cm^3) and 4(4) narrow plastic scintillator bars (BC408, size: $5\times5\times135$ cm^3) with photomultiplier tubes (Hamamatsu Photonics K.K., H7195, hereafter marked as PMT), and surrounded the β-ray detectors to reject the background events with $> 90\%$ efficiency as shown by black long bars in Fig. 27. Coincidence events between two PMTs were recognized as true background events, whose rate was typically 20 kHz. The expected counting rate of muons induced by cosmic-rays was about 380 cps by accounting for the typical intensity 1 cm$^{-2}\cdot$min^{-1} of muons [91] and the area of the veto counters (~ 23000 cm^2). Main component of the measured background events was originated from the environmental background γ-rays emitted from the wall of the experimental room. Although the counting rate stemming from the environment was dominant, we could reject the background events of the β-ray detectors originating from cosmic-ray events by using the veto counters. The veto duration time was set to be 2 μs for each event. The veto efficiency of the veto counters was estimated to be $\sim 93\%$ for 1 GeV muons obeying the typical zenith angle distribution ($\cos^2\theta$) according to GEANT4 simulations [92].

Lead shield

About 100 lead blocks (typical size of $20\times10\times5$ cm^3) composed the lead shield, which surrounded the vacuum chamber for the β-ray detectors and the Ge detectors as much as possible to reduce the environmental background events induced by Compton scatterings of background γ-rays.

Ion counter for KISS beam tuning

Stable ion beam was used to optimize the KISS beam transport. The beam optics parameters can be applied to radioactive ions extracted from the KISS gas cell. At the optimization of the beamline optics by counting the number of ions, the CEM was placed at 10 cm upstream of the tape in the both experiment. The CEM was used to maximize KISS beam transport efficiency at the focal plane, and was then moved to a non-obstructive position to allow for implanting the radioactive ions on the tape.

3.3.1 Detector setup in the first experiment

In the first experiment, we used the plastic scintillator telescopes [93] and two coaxial-type germanium detectors. The cross-sectional view of the detector setup and details of the plastic scintillator telescopes are shown in Figs. 28(a) and (b), respectively.

The β-ray telescopes were composed of three double-layered thin plastic scintillators (Eljen Technology, EJ204), whose thicknesses of the first and second layers are 1 mm and

2 mm, respectively. The solid angle of the β-ray telescopes was 75% of 4π. All plastic scintillators of the β-ray telescopes were connected to photomultiplier tubes (Hamamatsu Photonics K.K., H3178-51) installed outside of the vacuum chamber and coupled via light guides. All plastic scintillators and light guides were wrapped by reflection sheets (Reiko Co., Ltd., LUIREMIRROR) with a reflectance of 97.5% and thickness of 37 μm, which were used to increase the detection efficiency of the thin plastic scintillators by suppressing the scintillation-light attenuation.

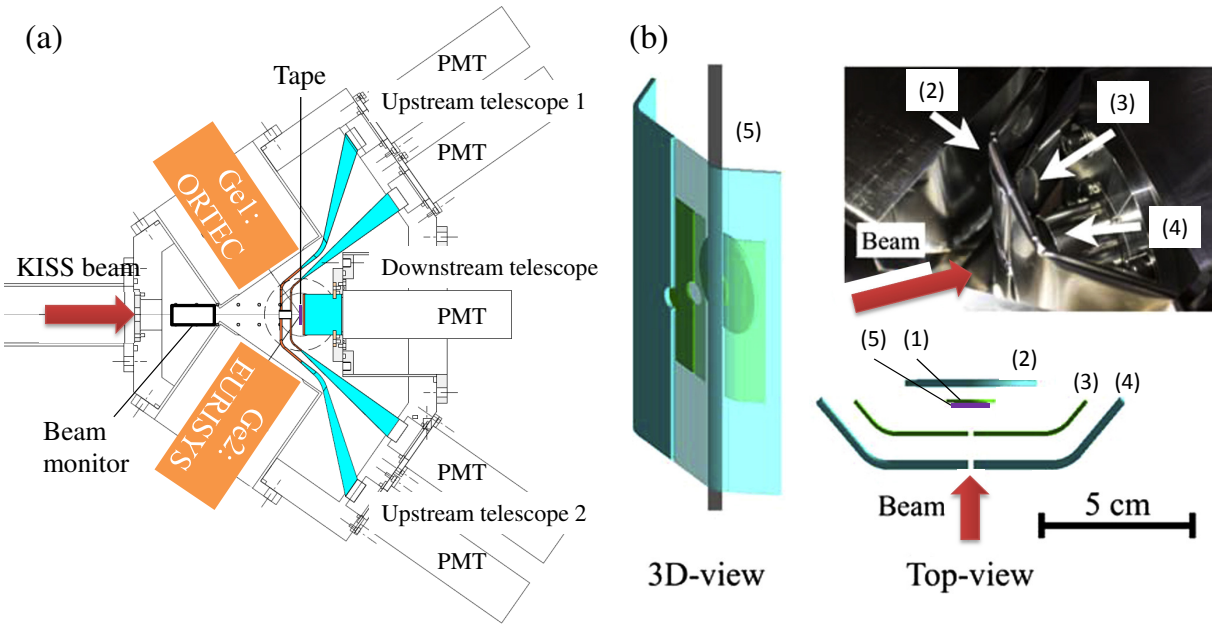

Figure 28: (a) Cross-sectional view of the detector setup with three plastic scintillator telescopes and two germanium detectors. Red arrow indicates the KISS beam. The tape (violet line) and beam monitor (black open box, CEM), and five light guides (blue-colored parts) and PMTs for upstream and downstream counters are also shown. (b) Configuration of the β-ray telescopes: (1) downstream ΔE_1 counter, (2) downstream ΔE_2 counter, (3) upstream ΔE_1 counters, (4) upstream ΔE_2 counters, and (5) tape. All components indicated in (b) are installed in the vacuum chamber and are operated under vacuum. The PMT for downstream ΔE_1 counter was attached on top of the flange of the vacuum chamber and not shown in (a).

The minimum ionization peak energies in the first and second scintillators were estimated to be 190 keV and 380 keV, respectively The energy thresholds of the first and second layers of the β-ray telescopes were set to be around 20 keV and 30 keV, respectively. Absolute detection efficiency was simulated by using GEANT4 to be almost zero at $Q_\beta < 0.7$ MeV because most of the β-rays can not reach the second layer due to the energy losses in the first layer and reflection sheets. The absolute detection efficiency at the energy of $Q_\beta = 2.28$ MeV emitted from ^{90}Sr/^{90}Y source was measured to be 50%, which was consistent with the GEANT4 simulation result. The simulated detection efficiencies at the energy of $Q_\beta = 1$ and 4 MeV were 14% and 75%, respectively, and the efficiency was saturated at $Q_\beta > 4$ MeV. The measured background rate of the β-ray telescopes with veto counters and lead shield was 0.09 cps.

The two coaxial-type germanium detectors of GMX40P4-ST (ORTEC) and EGC45-210-R (EURISYS MESURES) were used for γ-ray detection which are indicated as Ge 1 and 2, respectively, in Fig. 28(a). These germanium detectors were placed at the outside of the vacuum chamber with a distance of 55 mm from the tape center to increase the

detection efficiency by using an aluminum silk-hat-type flange with a window thickness of 1 mm. The measured absolute detection efficiency and full width at half maximum (FWHM) of a photo-peak for both germanium detectors are summarized in Table 7.

Table 7: Settings and specifications of the germanium detectors.

	First experiment		Second experiment
	GMX40P4-ST	EGC45-210-R	SCGe×4
High voltage	-4400 V	-4000 V	+3500 V
Shaping time	10 μs	3 μs	4.4 μs
Efficiency @121 keV	1.0%	1.3%	16%
FWHM @121 keV	3.3 keV	2.3 keV	2.3–2.5 keV
Efficiency @1406 keV	0.16%	0.23%	7.5%
FWHM @1406 keV	4.2 keV	3.0 keV	2.5 keV
Dynamic energy range	0.03–3.1 MeV		0.02–8 MeV

3.3.2 Detector setup in the second experiment

In the second experiment, we used the gas counter and four clover-type germanium detectors. The cross-sectional views of the detector setup are shown in Figs. 29(a) and (b).

The multi-segmented proportional gas counter (MSPGC) was newly developed for precise β-decay spectroscopy at KISS [94]. The MSPGC consisted of 32 narrow and long proportional gas counters. β-ray events were distinguished from background event originated from cosmic-rays and Compton scatterings of environmental background γ-rays by analyzing the hit pattern of the counters. The gas-filled area of the MSPGC is indicated by the blue colored mesh in Fig. 29(b). The detector gas was Ar (90%) + CH_4 (10%) (hereafter referred to as P10) of 1 atm which is generally used for proportional gas counters. The thick blue lines in Fig. 29(b) indicate the trapezoidal-shaped cathode foils of 32 gas counters. Sixteen pairs of counters were arranged cylindrically around the tape in two layers. The cathode was made of an aluminized Mylar foil with a thickness of 25 μm and anode was made of a Be-Cu wire with a diameter of 100 μm. The cathode of gas counters had an active length of 200 mm. The total solid angle of the 32 counters was 80% of 4π. The orange-colored parts in Fig. 29(b) indicate the partition foil between gas region and vacuum region. The partition foil was made of an aluminized Mylar foil with a thickness of 25 μm and supported by honeycomb grid which was made of stainless steel. The much less material density comparing with a plastic scintillator allows a lower threshold energy of β-ray around 100 keV. Therefore, the absolute detection efficiency at low-Q_β was expected to be improved.

Figure 29(c) shows typical hit patterns identified as the β-ray events. We termed an event as "$M = 2$" when only one telescope was fired, and an event as "$M = 3$" when one telescope ($M = 2$) and an adjacent outer counter were fired. Absolute detection efficiency at $Q_\beta = 1$ MeV was simulated to be 45% by using GEANT4, and the measured background rate of the MSPGC with the veto counters and lead shield was 0.1 cps by applying the hit patterns of $M = 2$ or 3. The details of development of the MSPGC were explained in Appendix C.

The MSPGC was installed in an aluminum cylindrical vacuum chamber with an outer diameter of 96 mm and thickness of 1 mm. The four super clover germanium detectors (Canberra, 4-fold 32 segmented super clover HPGe, relative efficiency ≈ 38% at 1.332 MeV, hereafter marked as SCGe) were placed at a distance of 4.8 cm from the MSPGC center. The typical measured absolute detection efficiency and FWHM of a photo-peak are summarized in Table 7.

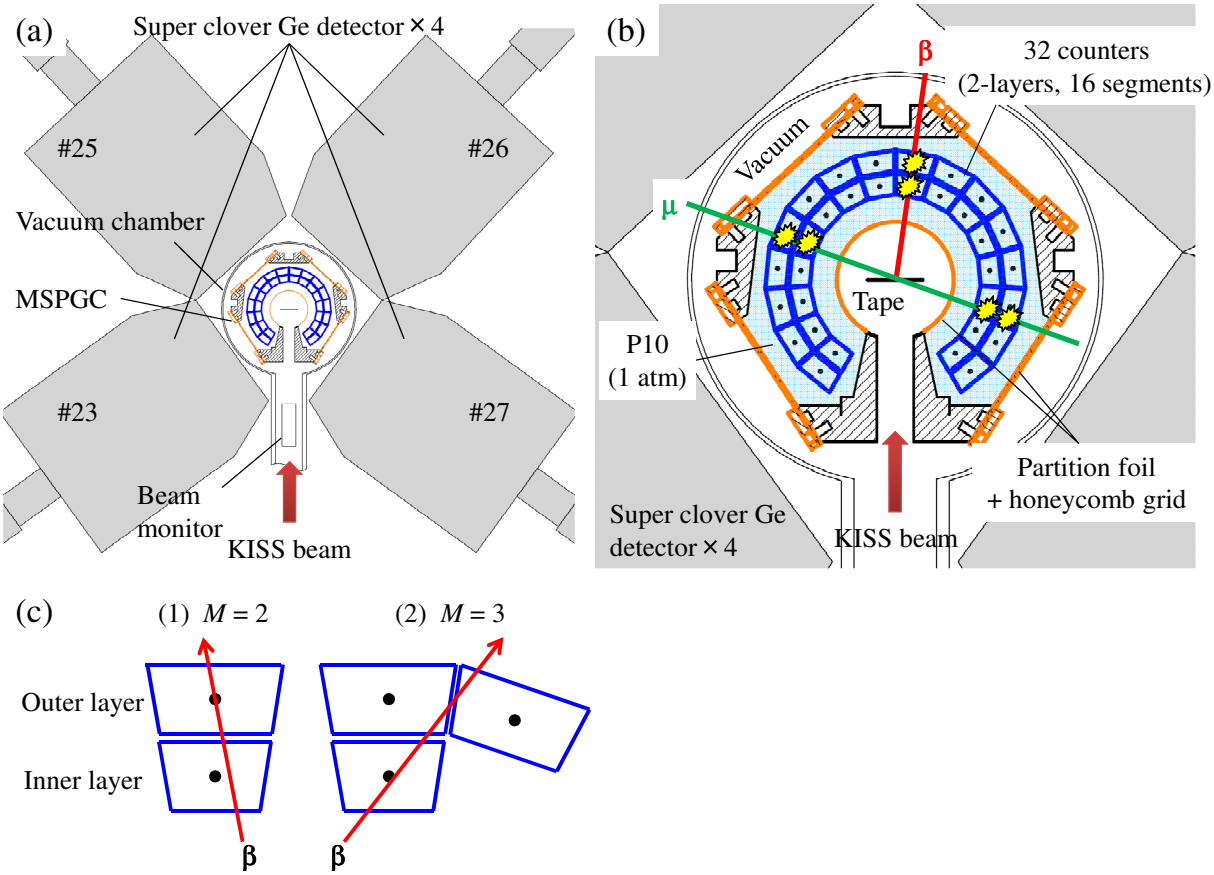

Figure 29: (a) Cross-sectional view of the detector setup with gas counter, four germanium detectors, vacuum chamber and beam monitor. (b) Cross-sectional view of the MSPGC in the vacuum chamber. The red and green lines indicate the β-ray from the implanted radioactive nuclei on the tape and muon from secondary cosmic-ray, respectively. (c) Schematic view of the hit patterns of (1) $M = 2$ and (2) $M = 3$.

4 Experiments

We performed two on-line experiments to measure the HFS of neutron-rich iridium isotopes. The HFS measurements of ^{196,197}Ir in the first experiment and ^{197,198}Ir in the second experiment were performed by using the gas cell system in Figs. 15(a) and (b) and the detector system in Figs. 28 and 29, respectively.

In both experiments, the primary beam of $^{136}Xe^{+20}$ with an energy of 10.75 MeV/nucleon and the rotating target of ^{198}Pt with a thickness of 12.5 mg/cm^2 were used. The rotating energy degrader mentioned in subsection 3.1.3 was used to reduce the primary beam energy down to $\sim$ 9.4 MeV/nucleon which is optimal energy for the MNT reactions.

The experiments were proceeded as follows: (1) ^{136}Xe beam tuning, (2) optimization of the gas cell pressure for extracting $^{199}Pt^+$, (3) the primary beam intensity dependence measurement of the extraction yield of $^{199}Pt^+$, (4) the β-decay half-life measurements of iridium isotopes, and (5) the HFS measurements of iridium isotopes. We show the results of (1)–(5) in the following subsections.

4.1 Primary beam tuning

At the beginning of the experiments, we tuned the spot size of the primary beam and confirmed the beam transport with a primary beam intensity of less than 0.005 pnA. As mentioned in subsection 3.1.1, the primary beam was tuned to be about 6 mm in diameter and centralized at the upstream beam monitor Al_2O_3. After the evacuation of the upstream Al_2O_3 from the beam axis, we confirmed the transportation of the primary beam passing through the doughnut-shaped gas cell by using the downstream Al_2O_3.

The time sequence of the primary beam chopping mentioned in subsection 3.1.3 were optimized after the primary beam transportation. The rotating speed of rotating wheels were 1000 rpm and passage time per one separated area by 1/8 was 7.5 ms. The fluorescence materials of ZnS and Al_2O_3 were used in the first and second experiment on the spokes of the first wheel, respectively. In the first experiment, the fluorescence of ZnS was disappeared immediately by the irradiation of primary beam with a intensity of less than 0.005 pnA. Therefore, we could not optimized the time sequence, and the beam-on duty was 87%. In the second experiment, we could optimize the time sequence with a primary beam intensity of 10 pnA. The time delay from the photo sensor signal to beam-off signal was optimized to be 1.10–1.14 ms on the oscilloscope in the KISS experimental hall, although the actual time delay was not known due to the time delay in the signal cables to the ^{136}Xe ion source. The duration of beam-on and -off were 4.13 and 3.37 ms, respectively, and corresponding beam-on duty was 55.1% in the second experiment.

4.2 Extraction of $^{198,199}Pt^+$ for system optimization

The system optimization were performed using the $^{198,199}Pt^+$ beams. During the system optimization, the laser wavelength for the excitation transition was fixed at λ_1 = 248.791 nm, and the laser repetition rate was 50 Hz. The typical laser powers of 680 μJ/pulse for λ_1 and 58 mJ/pulse for λ_2, which are enough high for the saturation of ionization efficiency, were used. In order to subtract background contaminations such as survived (non-laser ionized) ions and laser-ionized ions by only the ionization laser with λ_2, we measured the extraction yields in both λ_1 ON and OFF conditions, and evaluated the ion yields by the laser resonance ionization technique.

$^{198}Pt^+$ beam with the optimal gas cell pressure and primary beam intensity for the TLFs as shown in the following subsection 4.2.1 was used for the optimization of the

KISS beam transport. The MRFIG and KISS beamline optics were tuned as to fulfill the criteria: the maximum yield of $^{198}Pt^{+}$, beam spot size of $\sim$ 2 mm in diameter at the MCP, and transportation of the $^{198}Pt^{+}$ beam from F1 to F2 without tilting angled for X and Y axes. Then, we transported the $^{198}Pt^{+}$ beam to the CEM. We tuned the electric potential of the second X/Y steerer slightly to maximize the KISS beam transport efficiency at the CEM. Then, we moved the CEM to a non-obstructive position to allow for implanting the radioactive ions on the tape.

4.2.1 Extraction of $^{199}Pt^{+}$

We measured the gas cell pressure and the primary beam intensity dependences of the extraction yields of the ^{199}Pt ($T_{1/2}$ = 30.8(2) min) to confirm the optimal condition for the MNT reaction products. The $^{199}Pt^{+}$ ions were implanted during $T_{\rm on} = 0.5T_{1/2}$ and β-rays were measured by using the β-ray detectors. The yield of $^{199}Pt^{+}$ was obtained from the fitting of the measured growth curve and corrected by detection efficiency of the β-ray detectors. The measurement results of the extraction yield of $^{199}Pt^{+}$ as a function of gas cell pressure is shown in Fig. 30. Here, each extraction yield was normalized to the value obtained at the primary beam intensity of 25 pnA by using the measured primary beam dose. This measurement was done in the first experiment. Finally, we adjusted the gas cell pressure to 74 kPa where the measured extraction yield was maximum.

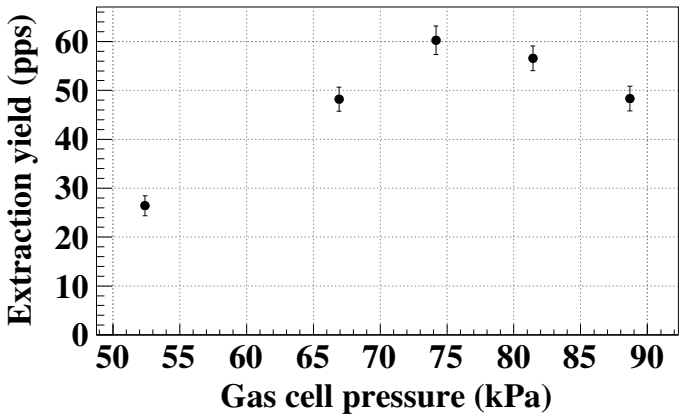

Figure 30: Measured extraction yield of $^{199}Pt^{+}$ as a function of gas cell pressure measured with a primary beam intensity of 25 pnA in the first experiment.

The measurement results of the extraction yield of $^{199}Pt^{+}$ as a function of the primary beam intensity is shown in Fig. 31. The blue triangles and red circles in Fig. 31 indicate the measured extraction yields with the use of the two KISS front ends in Figs. 15(a) and (b), respectively. The black square indicates the measured extraction yield with the use of previous KISS front end in which we used a traditional gas cell (no doughnut aperture) and a non-rotating target placed in the gas cell without radiation shield (the previous KISS front end is shown in Fig. 1(a) of Ref. [83]). The extraction yield obtained at the primary beam intensity of 20 pnA were increased from $\sim$ 20 pps using the previous KISS front end [83] to 100 pps using the KISS front end in Fig. 15(a) The extraction efficiency from the gas cell was improved from approximately 0.01% to 0.1% by accounting for the ejection rate 3.2×10^{5} pps of ^{199}Pt from the target, beam-on duty of primary beam, and the implantation efficiency $\varepsilon_{\rm implant}$ = 0.71 (1.0) and stopping efficiency $\varepsilon_{\rm stopping}$ = 0.82 (0.86) of TLFs for the present (previous) gas cell as mentioned in subsection 3.1.4. In this way, we successfully increased the extraction yield by more than one order of magnitude. This

enhancement was attributed to suppression of the plasma induced in the gas cell and along the primary beam trajectory owing to the installations of the doughnut-shaped gas cell and the radiation shield together with the separate vacuum room, respectively. However, we observed a decrease of the extraction yield at the primary beam intensity $\geq$ 60 pnA. This result indicates that we could not completely suppress the plasma effect and further improvements are required to the front end. We used the primary beam intensity of 50 pnA in following measurements.

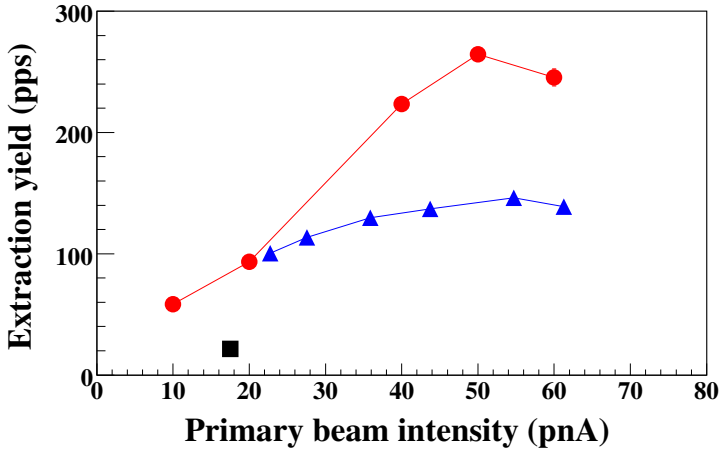

Figure 31: Measured extraction yield of $^{199}Pt^{+}$ as a function of primary beam intensity with a gas cell pressure of 74 kPa. The results with the use of the previous KISS front end [83] (black square) and present KISS front ends shown in Figs. 15(a) (blue triangles) and (b) (red circles) are shown. Statistical error bars are smaller than the symbols.

4.3 β-decay half-life measurements of iridium isotopes

The extraction of iridium isotopes were confirmed from the measurements of β-decay half-lives. The half-lives of ^{196,197}Ir were measured using the plastic scintillator telescopes and half-life of ^{198}Ir was measured using the MSPGC. The radioactive nuclei purified by KISS were implanted into the tape during $T_{\rm on} = 1.5 \times T_{1/2}$. The implantation of the radioactive nuclei was suspended during $T_{\rm off} = 4 \times T_{1/2}$ to measure the decay curves of the radioactive nuclei implanted on the tape. Just before every $T_{\rm on}$ timing, the tape was moved around 30 cm during $T_{\rm move} = 1$ s to remove unwanted activities for the half-life measurements.

The measured growth and decay time spectra were shown in Fig. 32. The deduced half-lives from the fitting of measured time spectra were summarized in Table 8. In the fitting, the half-life of a parent nucleus, background rate of the detector, and implantation intensity of the parent nucleus were considered as free parameter. The reported half-life of the daughter nucleus [95, 96] was treated as fixed parameter, and no contamination for each implantation was assumed. The evaluated half-lives of all iridium isotopes were in good agreement with the previously reported values. The evaluated extraction yields were normalized at the conditions of a primary beam intensity of 50 pnA, laser repetition rate of 100 Hz, and beam-on duty of 100%. Here, to evaluate the extraction yields (or upper limit for ^{197,198}Ir) in Table 8, we used the weighted-averaged detection efficiency of each β-ray detector by accounting for the β-decay transition strengths and energies Q_β (or maximum Q_β with 100% probability) [95, 96]. The evaluated yields were high enough to perform the HFS measurements for these isotopes.

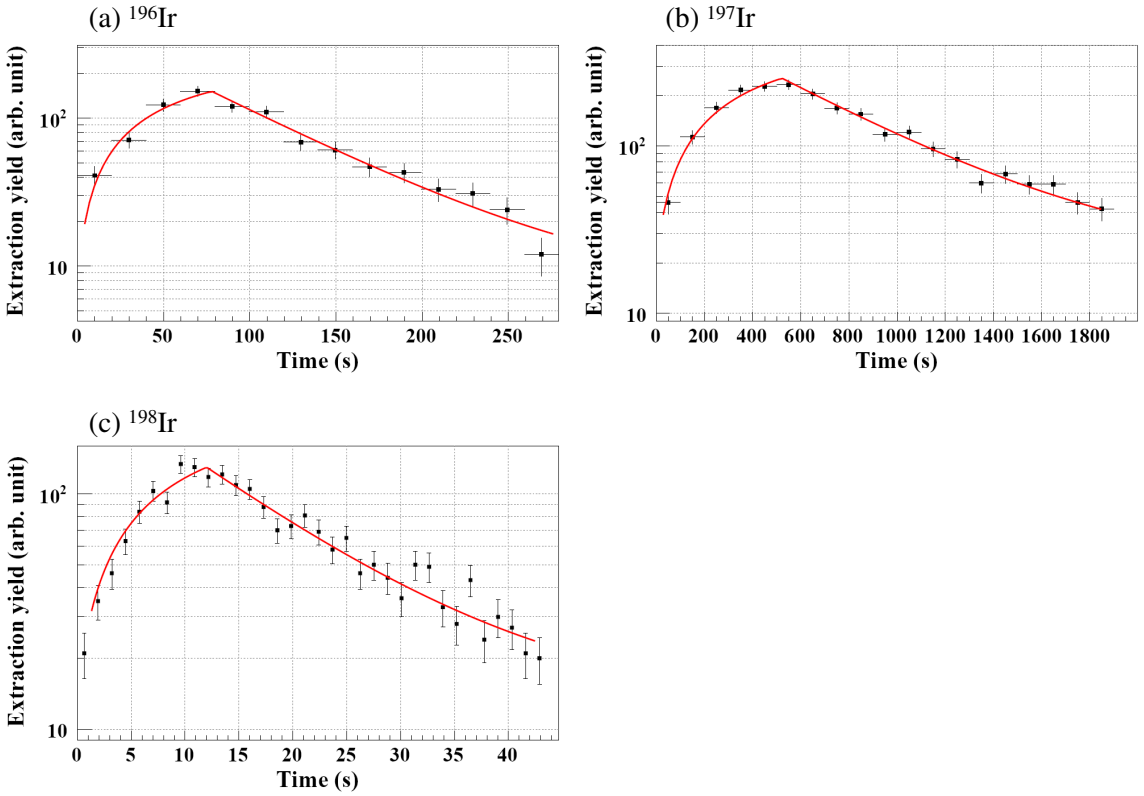

Figure 32: Measured growth and decay time spectra for (a) ^{196}Ir, (b) ^{197}Ir, and (c) ^{198}Ir. The solid line indicates the best fitting curve to the experimental data.

Table 8: Fitting results of growth and decay time spectra for ^{196,197,198}Ir shown in Fig. 32. The extraction yields are normalized for the condition of a primary beam intensity of 50 pnA, laser repetition rate of 100 Hz, and beam-on duty of 100%.

Nuclide	Reduced χ^2	Measured half-life	Reported half-life	Extraction yield (pps)
^{196}Ir	0.99	51(4) s	52(1) s [95]	~ 11
^{197}Ir	0.63	6.1(4) min	5.8(5) min [96]	< 9
^{198}Ir	0.94	8.9(4) s	8(1) s [97]	< 4.6

4.4 HFS measurements of iridium isotopes

The HFS measurements by laser ionization spectroscopy were done for unstable iridium isotopes ^{196,197,198}Ir and stable isotopes ^{191,193}Ir. The HFS of stable isotopes were measured to determine the response function for the experiential condition in the first and second experiments. We used the atomic excitation transition of $5d_7 6s_2\ ^4F_{9/2} \rightarrow 5d_6 6s_2 6p\ ^6F_{9/2}$ corresponding to $\lambda_1 = 247.587$ nm.

Neutral atoms of the stable isotopes were obtained by the resistive heating of a iridium filament (ϕ0.5 mm with heating current of 21.5 A) installed in the KISS gas cell. The numbers of laser-ionized atoms were counted by using the MCP at F2.

The implantation yields of unstable iridium isotopes were evaluated from the fittings of the measured growth time spectra as shown in Fig. 33. The implantation yield ($I_{\rm imp}$) including the detection efficiency and background rate ($R_{\rm BG}$) were treated as free param-

eter, and the half-lives were fixed to the reported values [21] in the fittings. The fitting results of the free parameters are shown on each spectrum. The evaluated R_{BG} values were consistent with each measurement and the off-line test mentioned in subsection 3.3. This result indicates that there was no additional background originated from the accumulated radioactivity. The yield at on-resonance frequency was more than ten times larger than that at off-resonance frequency. The fluctuation of primary beam intensity during T_{on} was reflected to the fitting error of evaluated implantation yield. The fluctuation of primary beam intensity between the HFS measurements during the scan of the wavelength λ_1 was corrected by accounting for the primary beam dose.

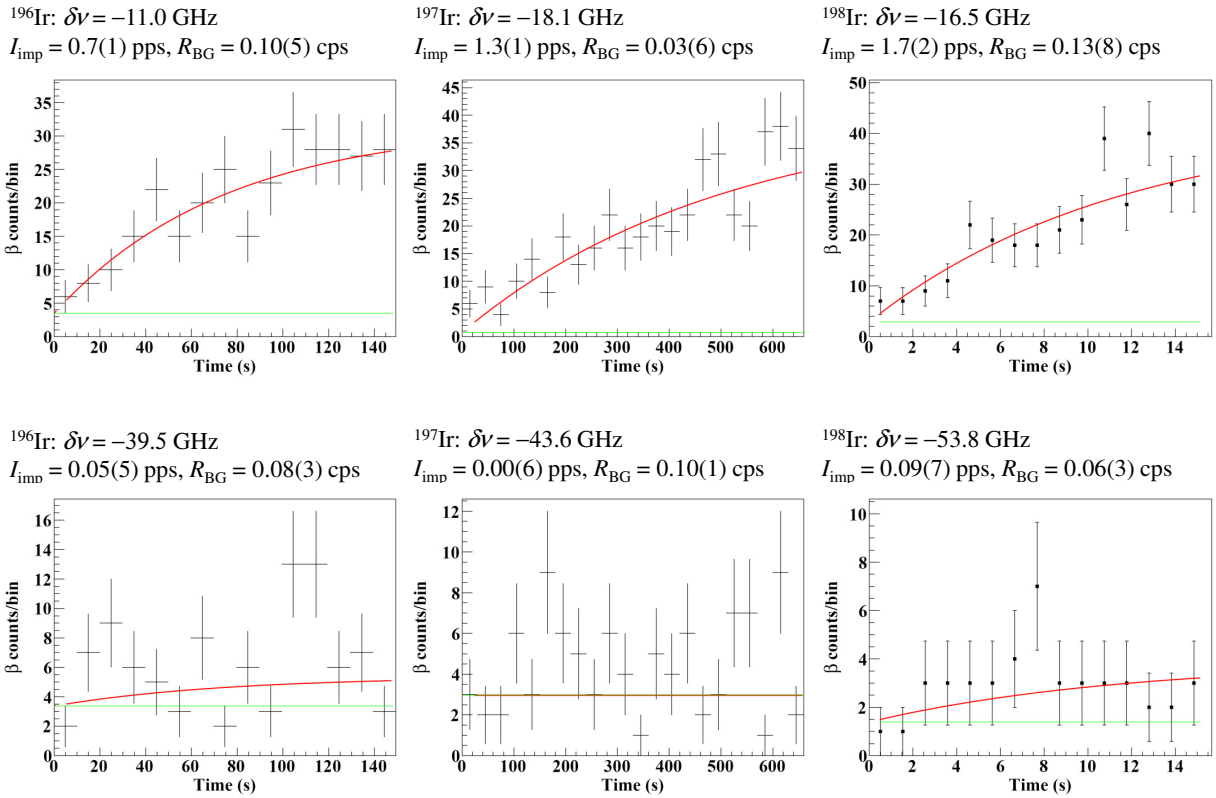

Figure 33: Typical growth time spectra of ^{196,197,198}Ir measured during $T_{\mathrm{on}} = 3T_{1/2}$ for ^{196}Ir and $2T_{1/2}$ for ^{197,198}Ir. The spectra at on- and off-resonance frequencies are shown in the upper and lower panels, respectively. The green and red lines indicate the evaluated background level and the fitting curve (the growth curve and background level), respectively. The fitting results for the implantation yield (I_{imp}) including the detection efficiency and background rate (R_{BG}) are shown on each spectrum.

4.5 Analyses of measured HFS spectra

We discuss the details of the HFS analysis procedure and the results in this subsection. From this section, the parameters A_i and B_i ($i = \mathrm{gs}, \mathrm{ex}$) mean the hyperfine coupling constants A_{HF} and B_{HF} of ground or excited state defined in subsection 2.3, respectively. At first, we show the physical quantities investigated from the fittings of the measured HFS spectra in Table 9. The μ, Q, A_{gs}, and B_{gs} of ^{191,193}Ir were precisely measured by atomic beam magnetic resonance (ABMR) method [98] and muonic X-ray measurement [99]. The parameters indicated by the red and blue colors in Table 9 were deduced in the present work from the fittings of the HFS spectra of ^{191}Ir and the other isotopes, respectively.

Table 9: Summary of the HFS parameters of iridium isotopes. The μ, Q, $A_{\rm gs}$, and $B_{\rm gs}$ of stable isotopes ^{191,193}Ir were precisely measured in Refs. [98, 99]. The parameters indicated by the red and blue colors were unknown values, and deduced from the fittings of the HFS spectra of ^{191}Ir and the other isotopes, respectively.

	Mass number				
	191	193	196	197	198
I^π	$3/2^+$	$3/2^+$	$(0,1)^-$	$3/2^+$	unknown
μ ($\mu_{\rm N}$)	+0.1507(6)	+0.1636(6)	μ^A		
Q (b)	+0.816(9)	+0.751(9)	Q^A		
$A_{\rm gs}$ (MHz)	+57.52128(3)	+62.65537(2)	$A^A_{\rm gs}(A^{191}_{\rm gs},I^{191},\mu^{191},I^A,\mu^A)$		
$B_{\rm gs}$ (MHz)	+471.2045(3)	+426.2355(2)	$B^A_{\rm gs}(B^{191}_{\rm gs},Q^{191},Q^A)$		
$A_{\rm ex}$ (MHz)	$A^{191}_{\rm ex}$	$A^{193}_{\rm ex}(A^{191}_{\rm ex},I^{191},\mu^{191},I^{193},\mu^{193})$	$A^A_{\rm ex}(A^{191}_{\rm ex},I^{191},\mu^{191},I^A,\mu^A)$		
$B_{\rm ex}$ (MHz)	$B^{191}_{\rm ex}$	$B^{193}_{\rm ex}(B^{191}_{\rm ex},Q^{191},Q^{193})$	$B^A_{\rm ex}(B^{191}_{\rm ex},Q^{191},Q^A)$		
$\delta\nu^{191,A}_{\rm IS}$	0	$\delta\nu^{191,A}_{\rm IS}$			

Evaluation of $A^{191}_{\rm ex}$, $B^{191}_{\rm ex}$, and Lorentz width

The energy shifts of the hyperfine levels are the function of the $A_{\rm HF}$, $B_{\rm HF}$, and I as shown in Eqs. (7) and (11). In the case of the ^{191}Ir, the $A_{\rm gs}$, $B_{\rm gs}$, and I values are known. Therefore, the unknown HFS parameters $A^{191}_{\rm ex}$ and $B^{191}_{\rm ex}$ were deduced from the analyses of the HFS spectra of the ^{191}Ir.

The HFS spectra of ^{191}Ir were measured at the three gas cell pressures of 12, 45, and 74 kPa. The measurements with lower gas cell pressures were to determine the $A^{191}_{\rm ex}$ and $B^{191}_{\rm ex}$ more precisely by reducing the effect of the pressure broadening.

As mentioned in subsection 2.6.3, the pressure width ($\delta\nu_{\rm pressure}$) and power width ($\delta\nu_{\rm power}$), which are common for the HFS spectra of all the isotopes measured by using the same gas cell pressure and laser power, are unknown. The Lorentz width without the natural width ($\delta\nu_{\rm L} = \delta\nu_{\rm pressure} + \delta\nu_{\rm power}$) was determined from the fitting of the HFS spectrum of ^{191}Ir for each gas cell pressure. The obtained $\delta\nu_{\rm L}$ values were applied to the fittings of the HFS spectra of the other isotopes. Moreover, we checked the linearity of the pressure widths and shifts as a function of gas cell pressure to confirm the validity of the fitting results.

I, μ, and Q of the unstable isotopes

The A_i and B_i ($i = {\rm gs}, {\rm ex}$) values of the unstable isotope with a mass number A are calculated by using modified Eqs. (52) and (53) as

$$A^A_i = A^{191}_i \frac{I^{191}}{\mu^{191}} \frac{\mu^A}{I^A}, \tag{70}$$

$$B^A_i = B^{191}_i Q^{191} \frac{1}{Q^A}, \tag{71}$$

$$(i = {\rm gs}, {\rm ex}). \tag{72}$$

The μ^A and Q^A values of the unstable isotopes were deduced from the analyses of the HFS spectra of the unstable isotopes.

In the case of ^{196,198}Ir, the I values are also unknown. We performed the fittings of the HFS spectra of them by assuming the spin values of I = 0, 1, 2, and 3. The most probable I values for them were suggested from the reduced χ^2 values of the fittings.

Evaluation of the electronic factor F_{247}

The HFS measurement of ^{193}Ir was performed to deduce the electronic factor F_{247} for our transition which is used to calculate the nuclear parameter $\lambda^{AA'}$, namely, the variation of nuclear mean-square charge radius $\delta\langle r_c^2\rangle^{AA'}$ as mentioned in subsections 2.4.2 and 2.5. By modifying the Eq. (45), we deduced the F_{247} by using the theoretical electronic factor $F_{351} = -30.94$ GHz·fm^{-2} for the transition $\lambda = 351.5$ nm [26] as

$$F_{247} = \frac{\delta\nu_{\mathrm{FS},247}^{191,193}}{\delta\nu_{\mathrm{FS},351}^{191,193}} F_{351}. \tag{73}$$

The HFS spectrum of ^{193}Ir was measured at the gas cell pressure of 12 kPa to determine the isotope shift $\delta\nu_{\mathrm{IS}}^{191,193}$ more precisely by reducing the effect of the pressure broadening. The unknown A_{ex} and B_{ex} values of the ^{193}Ir were determined in the same manner for the unstable isotopes using Eqs. (70) and (71).

4.5.1 Fitting method

We fitted the HFS spectra of ^{191}Ir (12, 45, and 74 kPa), ^{193}Ir, and an unstable isotope simultaneously for proper error propagation from the parameters for the stable isotopes. Figure 34 shows the schematic HFS spectra of ^{191}Ir and ^{A}Ir where the fitting parameters for the HFS spectra of ^{191}Ir and ^{A}Ir are indicated by red characters. In addition to the parameters shown in Table 9, following three values were considered in each HFS spectrum: the peak shift $\delta\nu_{\mathrm{shift}}^{191}$, the amplitude coefficient f_{amp}, and background level f_{BG}. Here, the peak shift is the deviation between the center of gravity for the frequency of the ^{191}Ir and the reference frequency 1210862 GHz, and was determined for each gas cell pressure. The f_{amp} was multiplied to the relative transition probabilities explained in subsection 2.6.3 to reproduce the height of each measured HFS spectrum. Linear background equation $f_{\mathrm{BG}} = a(\mathrm{offset})+b(\mathrm{slope})\times\nu(= c/\lambda_1$: frequency) was used in the HFS spectra for the stable isotopes to consider the temporal change of the yield of impurities from the iridium filament and the gas cell. Constant background in the HFS spectra for the unstable isotopes was assumed by accounting for the constant extraction yield of survived and laser-ionized impurities which are independent of the laser frequency λ_1.

Constraints for the fitting parameters

The A_{ex}^{191}, B_{ex}^{191}, $\delta\nu_{\mathrm{L}}$, $\delta\nu_{\mathrm{shift}}^{191}$, $\delta\nu_{\mathrm{IS}}^{191,A}$, and slope of the background function were treated as free parameters. The f_{amp} and offset of the background function were constrained as positive values. The μ^A and Q^A were constrained in the reasonable values estimated from the systematic trends of the μ^A and Q^A listed in Table 10. From the Table 10, the μ values of the iridium and gold isotopes falls in the range from -0.0107 to $+0.64$ μ_{N} except for the $+1.924$ μ_{N} of the ^{192}Ir with high spin value of $I^\pi = 4^-$. The Q values falls in the range from -0.24 to $+2.87$ b. We set the constraints for μ and Q as $-0.7 \le \mu \le +0.7$ μ_{N} and $-5 \le Q \le +5$ b, respectively, for all the unstable isotopes. In the case of simultaneous fitting including the HFS spectrum of the unstable isotope, we performed the fittings with three initial μ values, $\mu_{\mathrm{initial}} = -0.7$, 0, and $+0.7$ μ_{N}, to check the convergence of the fitting at local χ^2 minimization point.

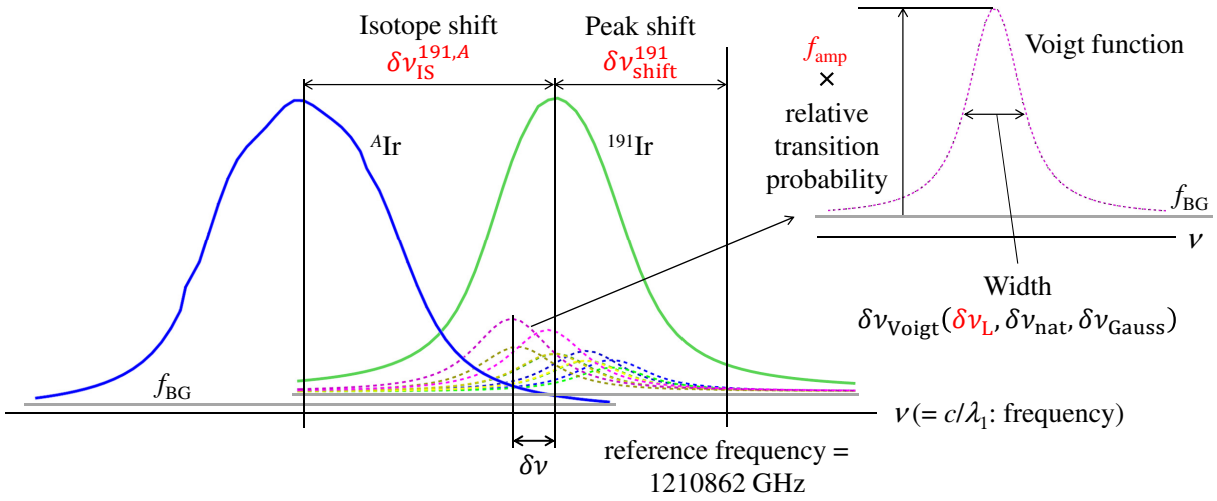

^{191}Ir: $\delta\nu\left(I^{191}, J_{\mathrm{gs}}, J_{\mathrm{ex}}, A_{\mathrm{gs}}^{191}, B_{\mathrm{gs}}^{191}, A_{\mathrm{ex}}^{191}, B_{\mathrm{ex}}^{191}\right)$, $f_{\mathrm{BG}} = a(\mathrm{offset}) + b(\mathrm{slope}) \times \nu$

^{193}Ir: $\delta\nu\left(I^{193}, J_{\mathrm{gs}}, J_{\mathrm{ex}}, A_{\mathrm{gs}}^{193}, B_{\mathrm{gs}}^{193}, A_{\mathrm{ex}}^{191}, B_{\mathrm{ex}}^{191}, \mu^{193}, Q^{193}\right)$, $f_{\mathrm{BG}} = a(\mathrm{offset}) + b(\mathrm{slope}) \times \nu$

$^{196-198}$Ir: $\delta\nu\left(I^{A}, J_{\mathrm{gs}}, J_{\mathrm{ex}}, A_{\mathrm{gs}}^{191}, B_{\mathrm{gs}}^{191}, A_{\mathrm{ex}}^{191}, B_{\mathrm{ex}}^{191}, \mu^{A}, Q^{A}\right)$, $f_{\mathrm{BG}} = a(\mathrm{constant})$

Figure 34: Schematic view of the HFS spectra of ^{191}Ir (green line) and ^{A}Ir (blue line) and, the related fitting parameters for the HFS spectra. The fitting parameters are indicated by the red letters. The broken lines indicate the peaks corresponding to the transitions between hyperfine levels of ^{191}Ir. The gray lines indicate the background level of each HFS spectrum.

Table 10: The μ and Q values of iridium and gold isotopes [24]. Upper part of the table shows the values for odd-even isotopes with $I^{\pi} = 3/2^{+}$. Lower part of the table shows the values for odd-odd isotopes.

Element	N	I^{π}	μ (μ_{N})	Q (b)
Ir ($Z = 77$)	112	$3/2^{+}$	+0.147(7)	+0.82(8)
Ir	114	$3/2^{+}$	+0.1507(6)	+0.816(9)
Ir	116	$3/2^{+}$	+0.1636(6)	+0.751(9)
Au ($Z = 79$)	112	$3/2^{+}$	+0.1369(9)	+0.72(2)
Au	114	$3/2^{+}$	+0.1396(6)	+0.66(2)
Au	116	$3/2^{+}$	+0.145(5)	+0.607(18)
Au	118	$3/2^{+}$	+0.145746(9)	+0.59(3)
Au	120	$3/2^{+}$	+0.261(2)	+0.510(16)
Ir	113	$(4)^{+}$	0.04(1)	+2.87(16)
Ir	115	4^{-}	+1.924(10)	+2.15(6)
Ir	117	1^{-}	+0.39(1)	+0.339(12)
Au	113	1^{-}	−0.0107(15)	−0.228(8)
Au	115	1^{-}	+0.0763(13)	−0.240(9)
Au	117	2^{-}	+0.580(15)	0.81(7)
Au	119	2^{-}	+0.64(2)	+0.640(19)

Fitting tools

The fitting was performed by using the ROOT [100] with the MINUIT [101] library for function minimization and error analysis. For the error analysis, MINOS option was used to calculate asymmetric parameter errors taking into account both parameter correlations and non-linearities. The applied response function as the lineshape was the Voigt function provided in the mathematical library of ROOT. The errors of fitting parameters shown in later subsections are enlarged by considering the square root of the obtained reduced χ^2.

4.5.2 Energy shifts by the hyperfine coupling constants A_{HF} and B_{HF}

Typically, the contribution from B_{HF} to the energy shift of hyperfine levels is much smaller than that by A_{HF}. Figures 35(a) and (b) show the energy shift of hyperfine levels with $I = 3/2$ and $J = 9/2$ induced by A_{HF} and B_{HF} from -1000 to $+1000$ MHz, respectively. The energy shift by B_{HF} is an order of hundreds MHz, and is more than one order of magnitude smaller than the spectral linewidth of several GHz in the present work and the energy shift induced by A_{HF}. Therefore, the obtained B_{ex}^{191} and Q^A from the fittings of the HFS spectra had a minimal influence on the spectrum as shown in following subsections.

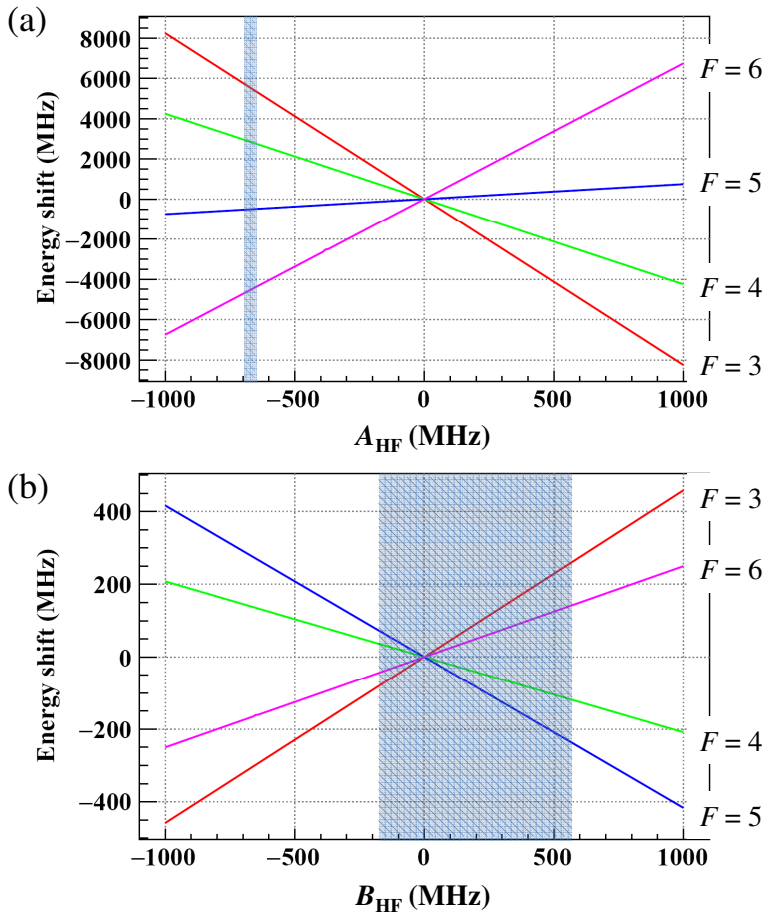

Figure 35: The energy shift of hyperfine levels with $I^\pi = 3/2^+$ and $J = 9/2$ as a function of A_{HF} and B_{HF}. The hatched regions indicate the fitting results of $A_{\mathrm{ex}}^{191} = -674^{+19}_{-19}$ MHz and $B_{\mathrm{ex}}^{191} = 201^{+369}_{-376}$ MHz shown in subsection 4.5.3

4.5.3 Fitting results of the HFS spectra of stable isotopes

The simultaneous fitting results of the five HFS spectra for the stable isotopes are discussed to evaluate the parameter values of $A_{\rm ex}^{191}$, $B_{\rm ex}^{191}$, $\delta\nu_{\rm L}$ for each gas cell pressure, and $\delta\nu_{\rm IS}^{191,193}$. These values are the reference values to check the validity of the simultaneous fitting with the HFS spectrum of an unstable isotope. The measured HFS spectra with the best fitting curves are shown in Fig. 36. The obtained fitting parameter values and reduced χ^2 from the best fittings are summarized in Table 11. The systematic error stemmed from the fluctuation of the KISS beam extraction was evaluated to be ±10% of the measured extraction yield. The worse S/N ratio in Fig. 36(e) comparing with Fig. 36(d) might be due to the measurement before the yield of impurities from the iridium filament and the gas cell was almost saturated.

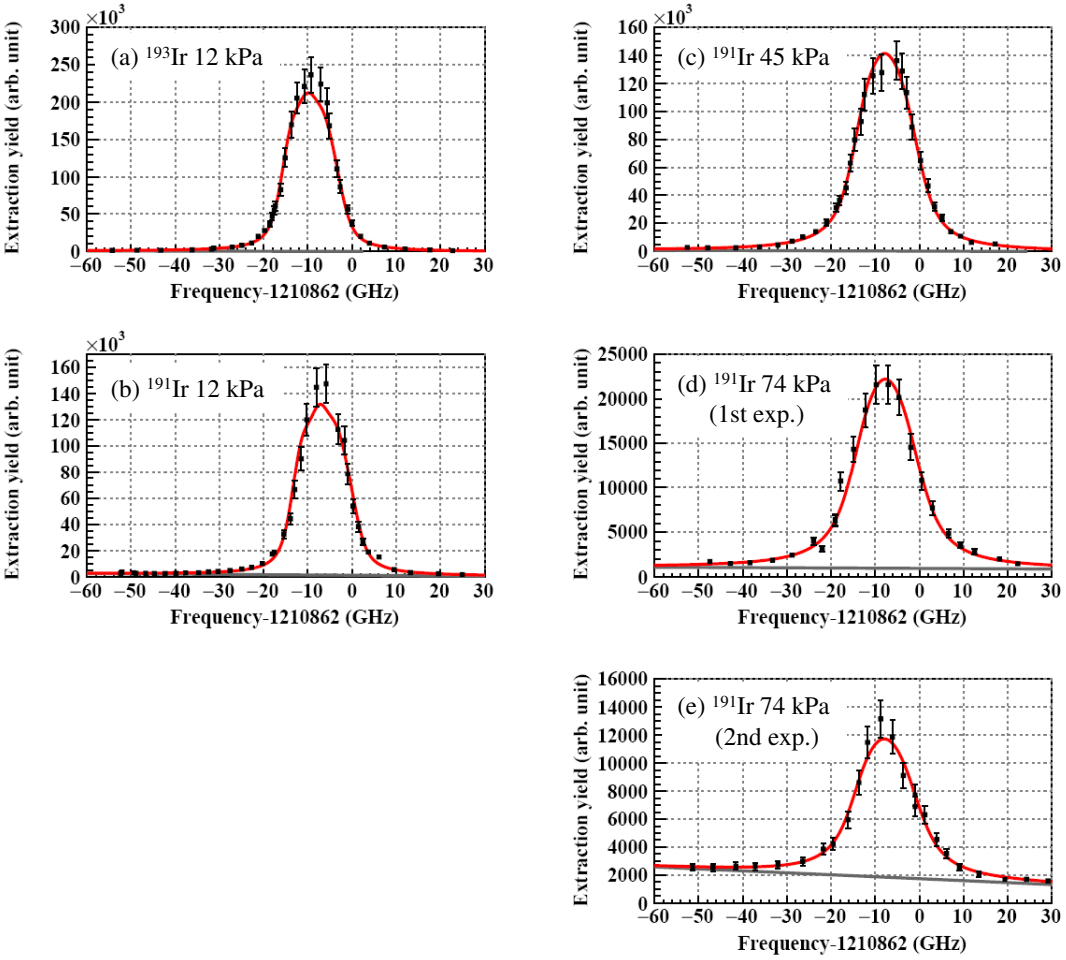

Figure 36: Measured HFS spectra of (a) ^{193}Ir with a gas cell pressure $P_{\text{gas-cell}} = 12$ kPa, (b) ^{191}Ir with $P_{\text{gas-cell}} = 12$ kPa, (c) ^{191}Ir with $P_{\text{gas-cell}} = 45$ kPa, (d) ^{191}Ir with $P_{\text{gas-cell}} = 74$ kPa in the first experiment, and (e) ^{191}Ir with $P_{\text{gas-cell}} = 74$ kPa in the second experiment. The red lines indicate the best fitting curves to the experimental data. The gray lines indicate the background components in the best fitting curves.

Figure 37 shows the enlarged spectrum of Fig. 36(b). The ten peaks corresponding to the transitions from $F_{\rm gs} = 3,\ 4,\ 5,$ and 6 to each $F_{\rm ex}$ are indicated by blue, green, orange, and magenta lines, respectively. The energy shifts of hyperfine levels with obtained $A_{\rm ex}^{191}$ and $B_{\rm ex}^{191}$ are from about −5600 to +4600 MHz by $A_{\rm ex}^{191}$ and from about −240 to +260 MHz by $B_{\rm ex}^{191}$ as shown by the hatched regions in Figs. 35(a) and (b). The position of each peak is mainly determined by $A_{\rm HF}$ constants. This means that we can deduce

Table 11: Evaluated parameters from the best fittings to the HFS spectra of ^{191,193}Ir.

Parameter	Value
$A_{\rm ex}^{191}$ (MHz)	-674^{+19}_{-19}
$B_{\rm ex}^{191}$ (MHz)	201^{+369}_{-376}
$\delta\nu_{\rm L}^{\rm 12kPa}$ (GHz)	$3.1^{+0.1}_{-0.1}$
$\delta\nu_{\rm L}^{\rm 45kPa}$ (GHz)	$6.5^{+0.3}_{-0.3}$
$\delta\nu_{\rm L}^{\rm 74kPa,1st}$ (GHz)	$8.5^{+0.8}_{-0.8}$
$\delta\nu_{\rm L}^{\rm 74kPa,2nd}$ (GHz)	$8.4^{+1.2}_{-1.1}$
$\delta\nu_{\rm shift}^{\rm 191,12kPa}$ (GHz)	$-6.7^{+0.1}_{-0.1}$
$\delta\nu_{\rm shift}^{\rm 191,45kPa}$ (GHz)	$-7.6^{+0.2}_{-0.2}$
$\delta\nu_{\rm shift}^{\rm 191,74kPa,1st}$ (GHz)	$-7.6^{+0.3}_{-0.3}$
$\delta\nu_{\rm shift}^{\rm 191,74kPa,2nd}$ (GHz)	$-7.7^{+0.4}_{-0.4}$
$\delta\nu_{\rm IS}^{193}$ (GHz)	$-2.8^{+0.2}_{-0.2}$
$f_{\rm amp}^{\rm 191,12kPa}$	48657^{+1735}_{-1719}
$a^{\rm 191,12kPa}$	1322^{+135}_{-135}
$b^{\rm 191,12kPa}$	-21^{+3}_{-3}
$f_{\rm amp}^{\rm 191,45kPa}$	65310^{+1848}_{-1844}
$a^{\rm 191,45kPa}$	0^{+254}_{-0}
$b^{\rm 191,45kPa}$	-16^{+5}_{-4}
$f_{\rm amp}^{\rm 191,74kPa,1st}$	11042^{+482}_{-481}
$a^{\rm 191,74kPa,1st}$	957^{+148}_{-152}
$b^{\rm 191,74kPa,1st}$	-2^{+3}_{-3}
$f_{\rm amp}^{\rm 193,12kPa}$	75660^{+2338}_{-2320}
$a^{\rm 193,12kPa}$	0^{+13}_{-0}
$b^{\rm 193,12kPa}$	-12^{+2}_{-2}
$f_{\rm amp}^{\rm 191,74kPa,2nd}$	5115^{+322}_{-317}
$a^{\rm 191,74kPa,2nd}$	1741^{+104}_{-106}
$b^{\rm 191,74kPa,2nd}$	-14^{+2}_{-2}
reduced χ^2 (all)	1.5
reduced χ^2 (191, 12 kPa)	2.0
reduced χ^2 (191, 45 kPa)	1.5
reduced χ^2 (191, 74 kPa, 1st)	2.0
reduced χ^2 (193, 12 kPa)	1.6
reduced χ^2 (191, 74 kPa, 2nd)	0.6

the μ values of the unstable isotopes because the entire widths in the HFS spectra of the unstable isotopes can be explained mainly by μ values under the reasonable constraints for Q as $-5 \leq Q \leq +5$ b as mentioned in subsection 4.5.1.

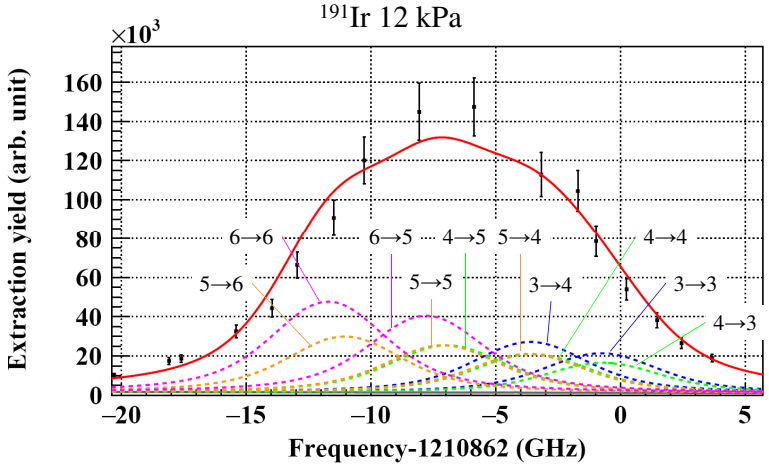

Figure 37: The enlarged spectrum of Fig. 36(b) with the ten peaks corresponding to each hyperfine transition. The $i \rightarrow j$ labels indicate the transitions between $F_{\rm gs} \rightarrow F_{\rm ex}$.

Pressure broadening and pressure shift

Figures 38(a) and (b) show the pressure dependence of Lorentz width $\delta\nu_{\rm L}$ and peak shift $\delta\nu^{191}_{\rm shift}$, respectively, which are listed in Table 11. The best fitting lines, which are linear functions, are indicated by the red lines. The reduced χ^2 of the fittings are 0.95 and 2.58 for the plots in Figs. 38(a) and (b), respectively. The deduced pressure broadening coefficient is $\Gamma_{\rm pressure} = 95(8)$ MHz/kPa and pressure shift coefficient is $\Gamma_{\rm shift} = -19(7)$ MHz/kPa. The data points lie on the linear functions, and the order of $\Gamma_{\rm pressure}$ and $\Gamma_{\rm shift}$ are consistent with the previous studies using an argon gas cell as listed in Table 3. Therefore, we conclude that the fitting results of the HFS spectra for the stable isotopes are reasonable. Note that the consistent values within the error margin of one sigma for the parameters listed in Table 11 were obtained even in the simultaneous fitting including the HFS spectrum of the unstable isotope, which are shown in later subsections. It indicates that most of the fittings were preformed properly.

The intercept of the linear function in Fig. 38(a) corresponds to the component of the power broadened width. The deduced power broadened width is 2.1(2) GHz. The value is smaller than the estimated value of 4.5 GHz due to the shorter laser pulse width compare to the lifetime of the atomic excited state as mentioned in subsection 2.6.3.

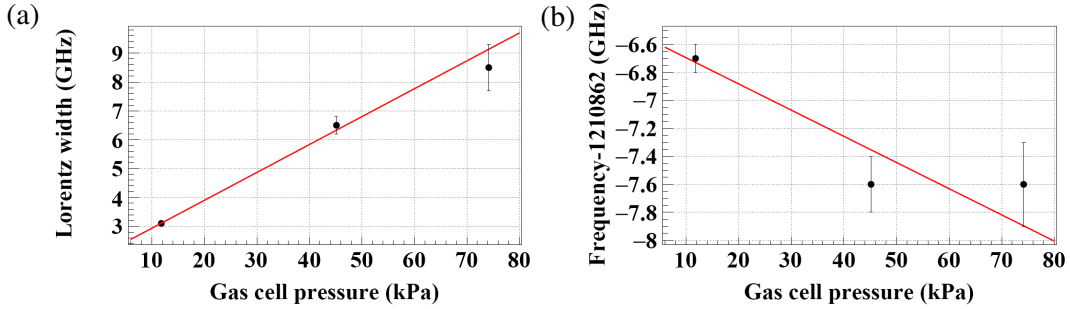

Figure 38: Measured pressure broadening and shift of iridium in argon gas. Pressure dependence of (a) Lorentz width $\delta\nu_{\rm L}$ and (b) peak shift $\delta\nu^{191}_{\rm shift}$ which values are shown in Table 11. The red lines indicate the best fitting results by linear functions.

4.5.4 Results of the simultaneous fittings including the HFS spectra of ^{197}Ir

In the case of ^{197}Ir, there is an isomeric state at the excitation energy of $E_{\rm ex} = 115$ keV [96] which has similar half-life ($T_{1/2} = 8.9(3)$ min) with the ground state and spin-parity $I^{\pi} = 11/2^{-}$ as shown in Fig. 39(a). Dominant decay type of the isomeric state is β-decay (99.75%). The isomer could be produced by the MNT reaction of ^{136}Xe + ^{198}Pt and extracted from KISS [102]. The expected HFS spectrum of isomeric state is shown in Fig. 39(b) with assumptions of $\mu = +6\ \mu_N$ and $Q = 1.7$ b from the systematics of $I^{\pi} = 11/2^{-}$ isomeric state shown in Table 12. The peaks are distributed in a wide frequency range ($\sim$ 400 GHz). The HFS spectra of the ground and isomeric states were measured in the first and second experiments with a narrow ($\sim$ 50 GHz) and wide ($\sim$ 200 GHz) frequency ranges, respectively. In the second experiment, we measured the data at the frequencies corresponding to each HFS peak position. If the isomeric yield was 5 cps as same as that of the ground state, we can observe about 0.5 cps at the peak position, which deviate with five sigma from the background level of 0.1 cps.

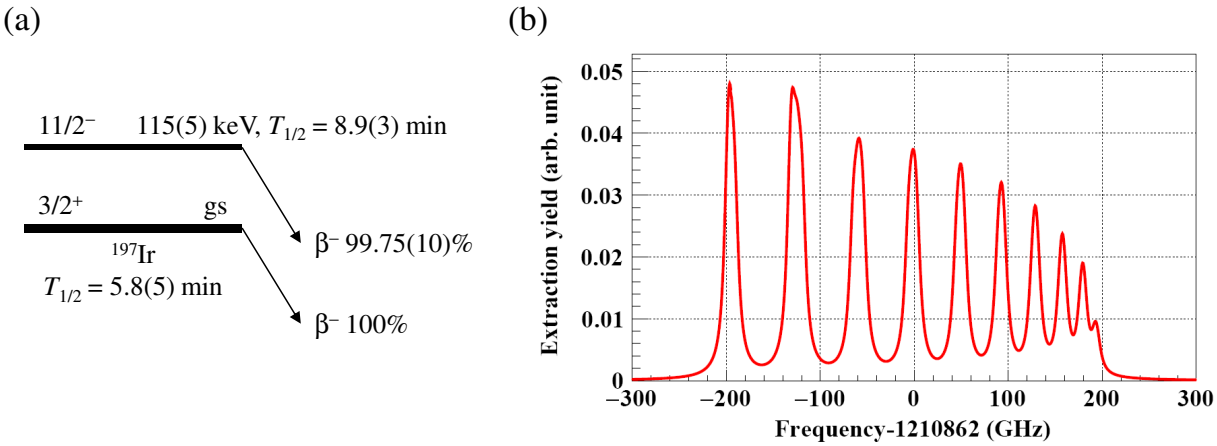

Figure 39: (a) The ground state and $I^{\pi} = 11/2^{-}$ isomeric state at 115 keV of ^{197}Ir. (b) Expected HFS spectrum of the isomeric state with assumptions of $\mu = +6\ \mu_{\rm N}$ and $Q = +1.7$ b from the systematics of $11/2^{-}$ isomeric state, and $\delta\nu_{\rm IS}^{191,197{\rm m}} = 10$ GHz which is similar value with the isotope shift of the ground state.

The following four parameters for the HFS of the isomeric state were additionally included in the fitting of ^{197}Ir HFS spectrum: $\mu^{197{\rm m}}$, $Q^{197{\rm m}}$, $\delta\nu_{\rm IS}^{191,197{\rm m}}$, and a relative amplitude coefficient $f_{\text{rel-amp}}$ of the HFS of the isomeric state to the one of the ground state. The height of the peak for each hyperfine transition in the isomeric state was expressed as $f_{\text{rel-amp}} \times f_{\text{amp}} \times$ (relative transition probability). The $\mu^{197{\rm m}}$ value was constraint in the range from +5 to +7 $\mu_{\rm N}$ from the systematics of known μ values of $I^{\pi} = 11/2^{-}$ isomeric state of iridium and gold isotopes as shown in Table 12. The same constraint for the $Q^{197{\rm g}}$ value was applied to the $Q^{197{\rm m}}$ value. The isotope shift of the isomeric state $\delta\nu_{\rm IS}^{191,197{\rm m}}$ was treated as free parameter. The relative amplitude coefficient $f_{\text{rel-amp}}$ was constrained as positive value.

The five HFS spectra for the stable isotopes and two HFS spectra for ^{197}Ir were fitted simultaneously. The obtained fitting parameter values for ^{197}Ir and $^{197{\rm m}}$Ir are summarized in Table 13. The measured HFS spectra of ^{197}Ir with the fitting results are shown in Fig. 40. The evaluated parameters of $A_{\rm ex}^{191}$, $B_{\rm ex}^{191}$, and $\delta\nu_{\rm L}$ in the ^{197}Ir fitting are consistent with those evaluated in the ^{191}Ir fittings listed in Table 11. The three fittings with $\mu_{\rm initial}^{197} = -0.7$, 0, and +0.7 $\mu_{\rm N}$ were converged to the two results labeled as (a) and (b) in Table 13 with similar reduced χ^2 values for the HFS spectra of ^{197}Ir. The result (a)

Table 12: μ and Q values [24] of $I^\pi = 11/2^-$ isomeric states of iridium and gold isotopes.

Element	N	Energy (keV)	μ (μ_N)	Q (b)
^{187m}Ir	110	433.75(6)	+6.21(5)	3.1(3)
^{189m}Ir	112	372.17(4)	unknown	unknown
^{191m}Ir	114	171.29(4)	+6.03(4)	unknown
^{193m}Ir	116	80.239(6)	unknown	unknown
^{195m}Ir	118	100(5)	unknown	unknown
^{197m}Ir	120	115(5)	unknown	unknown
^{189m}Au	110	247.23(16)	+6.19(2)	unknown
^{191m}Au	112	266.2(7)	6.6(6)	unknown
^{193m}Au	114	290.19(3)	6.18(9)	+1.98(6)
^{195m}Au	116	318.58(4)	+6.17(9)	+1.41(10)
^{197m}Au	118	409.15(8)	(+)5.98(9)	+1.68(5)

was obtained with $\mu^{197}_{\rm initial} = +0.7$ μ_N, and result (b) was obtained with $\mu^{197}_{\rm initial} = 0$ and -0.7 μ_N. The similar μ^{197} values with opposite sign were obtained in the results (a) $\mu^{197} = +0.25^{+0.03}_{-0.03}$ μ_N and (b) $\mu^{197} = -0.23^{+0.03}_{-0.03}$ μ_N. The obtained error ranges for the Q^{197}, μ^{197m}, and Q^{197m} are the limit of the constraint for each parameter. The measured HFS spectra are not sensitive to these parameters.

The isomer production ratio deduced by calculating the area of the HFS distribution for ^{197}Ir and ^{197m}Ir with obtained parameter values are also shown in Table 13. The error of the isomer ratio stemmed from the error of $f_{\rm rel\text{-}amp}$. The obtained isomer ratios $0.5^{+0.6}_{-0.5}$ and $0.2^{+0.1}_{-0.1}$ for the results (a) and (b), respectively, are similar with the previously studied isomer ratio of 0.40(5) for ^{199m}Pt ($E_{\rm ex} = 424$ keV, $I^\pi = (13/2)^+$) [102] produced by the same MNT reaction system. The isomer ratios are also in agreement with that obtained from the fitting of β-decay time spectrum. The β-decay time spectrum in Fig. 32(b) was measured with the excitation laser wavelength $\lambda_1 = 247.5877$ nm. The isomer ratio of 0.1(2) was obtained from the fitting of β-decay time spectrum with fixing the half-lives of ground and isomer states. The isomer ratio at $\lambda_1 = 247.5877$ nm in the HFS spectrum is deduced to be $0.05^{+0.06}_{-0.05}$ from the value of $0.5^{+0.6}_{-0.5}$ in the HFS fitting result (a). These two isomer ratios evaluated independently are consistent within the error margin. The presence of isomer with such small fraction does not affect to the absolute value of μ for the ground state.

The magnetic moments of the ground states with $I^\pi = 3/2^+$ for the iridium and gold isotopes with $N = 112$, 114, and 116 are similar values as shown in Table 10. Moreover, the magnetic moment of ^{199}Au ($\mu = +0.261(2)$ μ_N [31]), which has the same neutron number $N = 120$ and spin-parity $I^\pi = 3/2^+$ with those of ^{197}Ir, is very close to $\mu^{197} = +0.25$ μ_N of the fitting result (a). Finally, we concluded that μ^{197} and $\delta\nu^{191,197}_{\rm IS}$ are evaluated to be $\mu^{197} = +0.25^{+0.03}_{-0.03}$ μ_N and $\delta\nu^{191,197}_{\rm IS} = -10.3^{+0.7}_{-0.7}$ GHz from the fitting result (a), accounting for the systematic values of μ.

Table 13: Fitting results of the HFS spectra of ^{197}Ir with three initial μ^{197} values.

Parameter	Fitting result (a)	Fitting result (b)
$\mu^{197}_{\mathrm{initial}}$ (μ_{N})	+0.7	0, -0.7
A^{191}_{ex} (MHz)	-675^{+19}_{-19}	-676^{+19}_{-18}
B^{191}_{ex} (MHz)	192^{+370}_{-247}	246^{+272}_{-232}
μ^{197} (μ_{N})	$0.25^{+0.03}_{-0.03}$	$-0.23^{+0.03}_{-0.03}$
Q^{197} (b)	5^{+0}_{-10}	5^{+0}_{-10}
$\mu^{197\mathrm{m}}$ (μ_{N})	$6.7^{+0.3}_{-1.7}$	$5.3^{+1.1}_{-0.3}$
$Q^{197\mathrm{m}}$ (b)	5^{+0}_{-10}	5^{+0}_{-10}
$\delta\nu^{12\mathrm{kPa}}_{\mathrm{L}}$ (GHz)	$3.1^{+0.1}_{-0.1}$	$3.1^{+0.1}_{-0.1}$
$\delta\nu^{45\mathrm{kPa}}_{\mathrm{L}}$ (GHz)	$6.5^{+0.3}_{-0.3}$	$6.5^{+0.3}_{-0.3}$
$\delta\nu^{74\mathrm{kPa,1st}}_{\mathrm{L}}$ (GHz)	$8.4^{+0.8}_{-0.7}$	$8.3^{+0.8}_{-0.7}$
$\delta\nu^{74\mathrm{kPa,2nd}}_{\mathrm{L}}$ (GHz)	$8.3^{+1.1}_{-1.0}$	$8.1^{+1.1}_{-1.0}$
$\delta\nu^{191,12\mathrm{kPa}}_{\mathrm{shift}}$ (GHz)	$-6.7^{+0.1}_{-0.1}$	$-6.7^{+0.1}_{-0.1}$
$\delta\nu^{191,45\mathrm{kPa}}_{\mathrm{shift}}$ (GHz)	$-7.6^{+0.2}_{-0.2}$	$-7.6^{+0.2}_{-0.2}$
$\delta\nu^{191,74\mathrm{kPa,1st}}_{\mathrm{shift}}$ (GHz)	$-7.6^{+0.3}_{-0.3}$	$-7.6^{+0.3}_{-0.3}$
$\delta\nu^{191,74\mathrm{kPa,2nd}}_{\mathrm{shift}}$ (GHz)	$-7.7^{+0.4}_{-0.3}$	$-7.7^{+0.3}_{-0.3}$
$\delta\nu^{193}_{\mathrm{IS}}$ (GHz)	$-2.8^{+0.2}_{-0.2}$	$-2.8^{+0.2}_{-0.2}$
$\delta\nu^{197}_{\mathrm{IS}}$ (GHz)	$-10.3^{+0.7}_{-0.7}$	$-10.3^{+0.6}_{-0.6}$
$\delta\nu^{197\mathrm{m}}_{\mathrm{IS}}$ (GHz)	-29^{+3}_{-20}	-43^{+4}_{-3}
$f^{191,12\mathrm{kPa}}_{\mathrm{amp}}$	48628^{+1739}_{-1723}	48574^{+1728}_{-1713}
$a^{191,12\mathrm{kPa}}$	1323^{+135}_{-136}	1326^{+134}_{-135}
$b^{191,12\mathrm{kPa}}$	-21^{+3}_{-3}	-21^{+3}_{-3}
$f^{191,45\mathrm{kPa}}_{\mathrm{amp}}$	65302^{+1854}_{-1850}	65289^{+1845}_{-1841}
$a^{191,45\mathrm{kPa}}$	0^{+256}_{-0}	0^{+257}_{-0}
$b^{191,45\mathrm{kPa}}$	-16^{+5}_{-4}	-16^{+5}_{-4}
$f^{191,74\mathrm{kPa,1st}}_{\mathrm{amp}}$	11025^{+482}_{-481}	11013^{+479}_{-478}
$a^{191,74\mathrm{kPa,1st}}$	970^{+145}_{-148}	982^{+143}_{-147}
$b^{191,74\mathrm{kPa,1st}}$	-2^{+3}_{-3}	-2^{+3}_{-3}
$f^{193,12\mathrm{kPa}}_{\mathrm{amp}}$	75637^{+2342}_{-2326}	75628^{+2330}_{-2315}
$a^{193,12\mathrm{kPa}}$	0^{+14}_{-0}	0^{+14}_{-0}
$b^{193,12\mathrm{kPa}}$	-12^{+2}_{-2}	-12^{+2}_{-2}
$f^{191,74\mathrm{kPa,2nd}}_{\mathrm{amp}}$	5095^{+317}_{-312}	5068^{+313}_{-309}
$a^{191,74\mathrm{kPa,2nd}}$	1747^{+101}_{-103}	1760^{+100}_{-102}
$b^{191,74\mathrm{kPa,2nd}}$	-14^{+2}_{-2}	-14^{+2}_{-2}
$f^{197,1\mathrm{st}}_{\mathrm{amp}}$	$0.54^{+0.05}_{-0.05}$	$0.57^{+0.03}_{-0.03}$
$a^{197,1\mathrm{st}}$	$0.00^{+0.02}_{-0.00}$	$0.00^{+0.01}_{-0.00}$
$f^{197,2\mathrm{nd}}_{\mathrm{amp}}$	$2.9^{+0.3}_{-0.3}$	$2.89^{+0.25}_{-0.25}$
$a^{197,2\mathrm{nd}}$	$0.32^{+0.09}_{-0.09}$	$0.32^{+0.07}_{-0.07}$
$f_{\mathrm{rel\text{-}amp}}$	$0.2^{+0.2}_{-0.2}$	$0.07^{+0.05}_{-0.05}$

Table 13: (continued)

Parameter	Fitting result (a)	Fitting result (b)
reduced χ^2 (all)	1.5	1.5
reduced χ^2 (^{191}Ir, 12 kPa)	2.0	2.0
reduced χ^2 (^{191}Ir, 45 kPa)	1.5	1.5
reduced χ^2 (^{191}Ir, 74 kPa, 1st)	2.0	2.0
reduced χ^2 (^{193}Ir, 12 kPa)	1.6	1.6
reduced χ^2 (^{191}Ir, 74 kPa, 2nd)	0.6	0.6
reduced χ^2 (^{197}Ir, 74 kPa, 1st+2nd)	2.3	2.1
isomer ratio	$0.5^{+0.6}_{-0.5}$	$0.2^{+0.1}_{-0.1}$

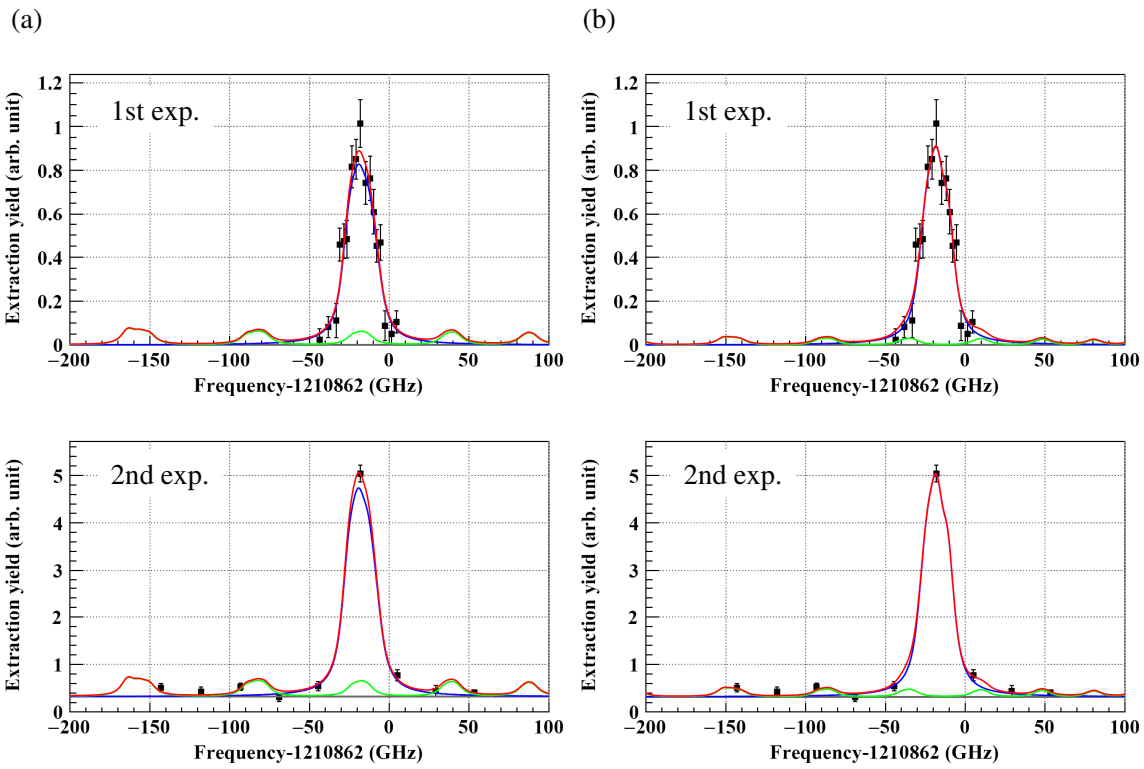

Figure 40: Measured HFS spectra of ^{197}Ir with the fitting curves obtained in the fitting results (a) and (b) (see the text). The blue and green lines indicate the evaluated HFS spectra of the ground and isomeric states, respectively. The gray and red lines indicate the background levels and the sum of three components, respectively. The top and bottom spectra were measured in the first and second experiments, respectively.

4.5.5 Results of the simultaneous fittings including the HFS spectrum of ^{196}Ir

The spin-parity value of ^{196}Ir is suggested to be $I^\pi = (0, 1)^-$ from the measured log ft values > 5.1 and 5.75 for β-decays ^{196}Os ($Z = 76$, $I^\pi = 0^+$) $\rightarrow$ ^{196}Ir [103] and ^{196}Ir $\rightarrow$ ^{196}Pt ($Z = 78$, $I^\pi = 0^+$) [104], respectively, as shown in Fig. 41. These measured log ft values suggested the first-forbidden transition ($\Delta\pi = 1$, $\Delta I = 0, \pm1, \pm2$), and thus spin-parity value of ^{196}Ir was suggested to be $I^\pi = (0, 1)^-$. There is an isomeric state at

$E_{\rm ex} = 410(11)$ keV with $I^\pi = (10, 11)^-$ and half-life $T_{1/2} = 1.40(2)$ h studied by ^{198}Pt(d,α) reaction [104]. The half-life is rather longer than the duration time $T_{\rm on} = 156$ s ($3 \times T_{1/2}$) of KISS beam on for the β-decay growth curve measurement of ^{196}Ir ($T_{1/2} = 52(1)$ s). The expected isomer contamination ratio in the growth curve is negligibly small $< 0.1\%$ if the extraction yield of the isomer is the same with that of the ground state.

The five HFS spectra for the stable isotopes and one HFS spectrum for ^{196}Ir were fitted simultaneously. The fittings were performed with the ten fitting conditions: the spin assumption of $I = 0$ and three initial μ^{196} values of $\mu^{196}_{\rm initial} = -0.7$, 0, and $+0.7$ $\mu_{\rm N}$ for each spin assumption of $I = 1$, 2, and 3. The obtained fitting parameter values for ^{196}Ir are summarized in Table 14 for the fitting with $I = 0$ and Table 15 for the fitting with $I \geq 1$. The measured hyperfine spectra of ^{196}Ir with the fitting results are shown in Fig. 42. The evaluated parameters of $A^{191}_{\rm ex}$, $B^{191}_{\rm ex}$, and $\delta\nu_{\rm L}$ in the ^{196}Ir fitting are consistent with those evaluated in the ^{191}Ir fittings listed in Table 11, . The three fittings with $\mu^{196}_{\rm initial} = -0.7$, 0, and $+0.7$ $\mu_{\rm N}$ were converged to the two results, which the sign of μ^{196} were positive and negative, for each spin assumption of $I = 1$, 2, and 3.

In the case of $I = 0$, the obtained $\delta\nu_{\rm L} = 9.4^{+1.0}_{-0.9}$ GHz is in agreement with $\delta\nu_{\rm L} = 8.5^{+0.8}_{-0.8}$ GHz at a gas cell pressure of 74 kPa in the first experiment. However, the obtained reduced $\chi^2 = 3.6$ for the HFS spectrum of ^{196}Ir with $I = 0$ is more than two times larger than those with other spin assumptions (reduced $\chi^2 = 1.6$–2.3). Therefore, the spin value of ^{196}Ir is suggested to be larger than zero. The smallest reduced $\chi^2 = 1.6$ was obtained with $I = 1$ and $\mu^{196} = +0.23^{+0.03}_{-0.03}$ $\mu_{\rm N}$. This result is consistent with previously measured log ft values.

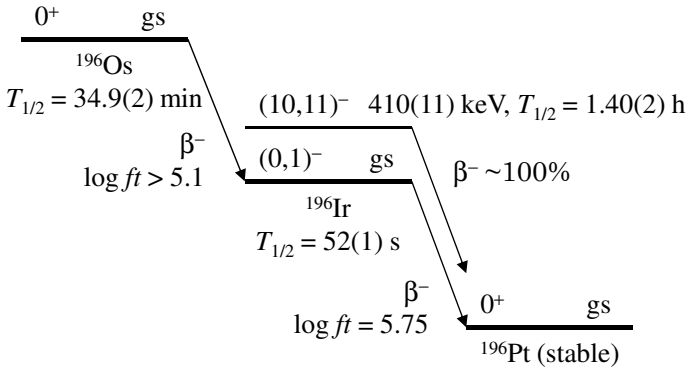

Figure 41: The β-decay scheme between ground states of ^{196}Os, ^{196}Ir, and ^{196}Pt. The β-decays of ^{196}Os and ^{196}Ir were measured in Refs. [103] and [104], respectively.

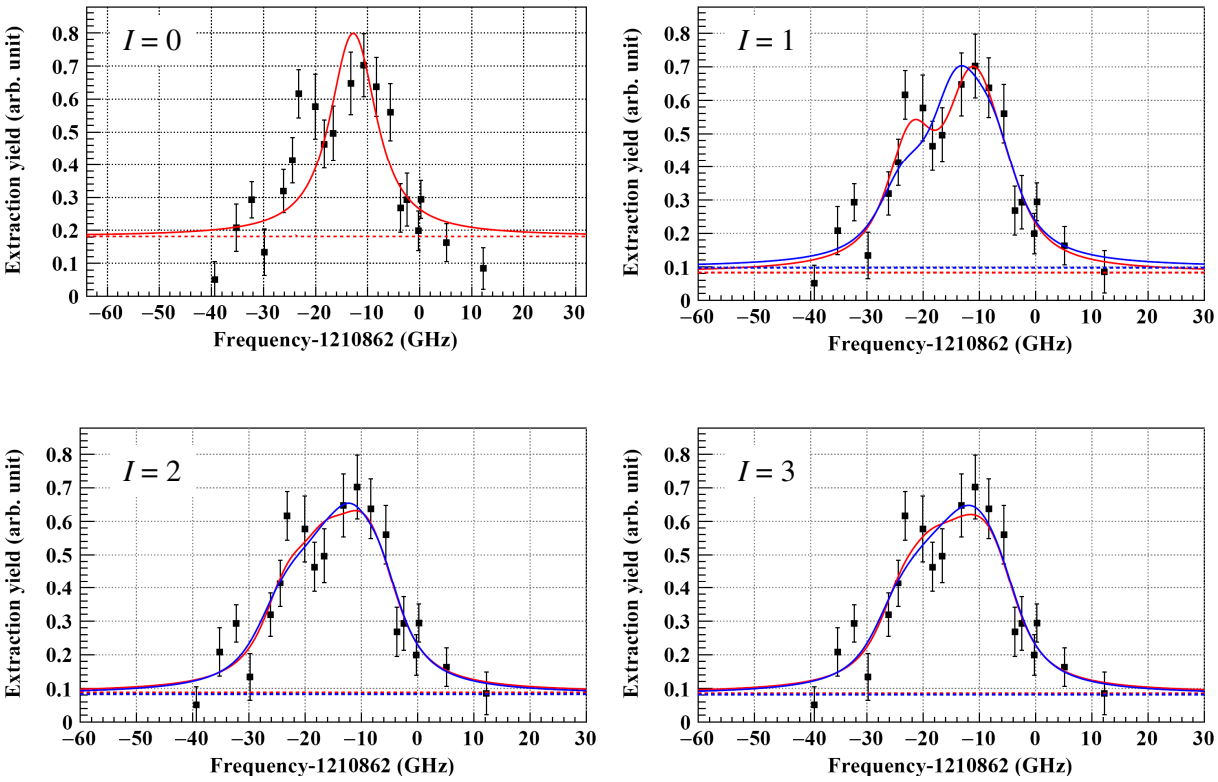

Figure 42: Measured HFS spectra of ^{196}Ir and the fitting curves with the spin assumptions of $I = 0$, 1, 2, and 3. The broken lines indicate the evaluated background levels. The red line in the spectrum with $I = 0$ shows the sum of the evaluated Voigt function and background level. The red and blue lines in the spectra with $I \geq 1$ show the sum of the evaluated HFS spectra and background levels with positive and negative μ^{196} values, respectively.

Table 14: Fitting results of the HFS spectrum of ^{196}Ir with $I = 0$.

Parameter	Value
A_{ex}^{191} (MHz)	-672^{+22}_{-21}
B_{ex}^{191} (MHz)	101^{+425}_{-435}
$\delta\nu_{\mathrm{L}}^{12\mathrm{kPa}}$ (GHz)	$3.2^{+0.1}_{-0.1}$
$\delta\nu_{\mathrm{L}}^{45\mathrm{kPa}}$ (GHz)	$6.5^{+0.3}_{-0.3}$
$\delta\nu_{\mathrm{L}}^{74\mathrm{kPa,1st}}$ (GHz)	$9.4^{+1.0}_{-0.9}$
$\delta\nu_{\mathrm{shift}}^{191,12\mathrm{kPa}}$ (GHz)	$-6.7^{+0.1}_{-0.1}$
$\delta\nu_{\mathrm{shift}}^{191,45\mathrm{kPa}}$ (GHz)	$-7.6^{+0.2}_{-0.2}$
$\delta\nu_{\mathrm{shift}}^{191,74\mathrm{kPa,1st}}$ (GHz)	$-7.4^{+0.3}_{-0.3}$
$\delta\nu_{\mathrm{IS}}^{193}$ (GHz)	$-2.8^{+0.2}_{-0.2}$
$\delta\nu_{\mathrm{IS}}^{196}$ (GHz)	$-5.3^{+1.0}_{-1.0}$
$f_{\mathrm{amp}}^{191,12\mathrm{kPa}}$	48774^{+1968}_{-1949}
$a^{191,12\mathrm{kPa}}$	1317^{+152}_{-153}
$b^{191,12\mathrm{kPa}}$	-21^{+3}_{-3}
$f_{\mathrm{amp}}^{191,45\mathrm{kPa}}$	65338^{+2092}_{-2086}
$a^{191,45\mathrm{kPa}}$	0^{+282}_{-0}
$b^{191,45\mathrm{kPa}}$	-16^{+6}_{-5}
$f_{\mathrm{amp}}^{191,74\mathrm{kPa,1st}}$	11146^{+547}_{-545}
$a^{191,74\mathrm{kPa,1st}}$	846^{+172}_{-176}
$b^{191,74\mathrm{kPa,1st}}$	-3^{+3}_{-3}
$f_{\mathrm{amp}}^{193,12\mathrm{kPa}}$	75685^{+2646}_{-2628}
$a^{193,12\mathrm{kPa}}$	0^{+15}_{-0}
$b^{193,12\mathrm{kPa}}$	-12^{+2}_{-2}
f_{amp}^{196}	$1.0^{+0.2}_{-0.2}$
a^{196}	$0.18^{+0.03}_{-0.03}$
reduced χ^2 (all)	1.9
reduced χ^2 (191, 12 kPa)	2.0
reduced χ^2 (191, 45 kPa)	1.5
reduced χ^2 (191, 74 kPa, 1st)	2.1
reduced χ^2 (193, 12 kPa)	1.7
reduced χ^2 (196)	3.6

Table 15: Fitting results of the HFS spectrum of ^{196}Ir with $I = 1$, 2, and 3 and three initial μ^{196} values.

Parameter	Value					
	$I = 1$		$I = 2$		$I = 3$	
$\mu^{196}_{\rm initial}$ ($\mu_{\rm N}$)	0, +0.7	-0.7	+0.7	0, -0.7	+0.7	0, -0.7
$A^{191}_{\rm ex}$ (MHz)	-677^{+20}_{-19}	-676^{+20}_{-20}	-673^{+20}_{-20}	-674^{+20}_{-20}	-674^{+20}_{-20}	-674^{+20}_{-20}
$B^{191}_{\rm ex}$ (MHz)	324^{+279}_{-234}	281^{+304}_{-228}	-197^{+333}_{-331}	-113^{+841}_{-322}	-114^{+338}_{-342}	-55^{+403}_{-341}
μ^{196} ($\mu_{\rm N}$)	$0.23^{+0.03}_{-0.03}$	$-0.23^{+0.03}_{-0.03}$	$0.27^{+0.03}_{-0.03}$	$-0.28^{+0.04}_{-0.04}$	$0.29^{+0.04}_{-0.03}$	$-0.29^{+0.04}_{-0.05}$
Q^{196} (b)	-5^{+10}_{-0}	-5^{+3}_{-0}	5^{+0}_{-2}	5^{+0}_{-10}	5^{+0}_{-2}	5^{+0}_{-9}
$\delta\nu_{\rm L}^{\rm 12kPa}$ (GHz)	$3.1^{+0.1}_{-0.1}$	$3.1^{+0.1}_{-0.1}$	$3.2^{+0.1}_{-0.1}$	$3.2^{+0.1}_{-0.1}$	$3.2^{+0.1}_{-0.1}$	$3.2^{+0.1}_{-0.1}$
$\delta\nu_{\rm L}^{\rm 45kPa}$ (GHz)	$6.5^{+0.3}_{-0.3}$	$6.5^{+0.3}_{-0.3}$	$6.5^{+0.3}_{-0.3}$	$6.5^{+0.3}_{-0.3}$	$6.5^{+0.3}_{-0.3}$	$6.5^{+0.3}_{-0.3}$
$\delta\nu_{\rm L}^{\rm 74kPa,1st}$ (GHz)	$8.3^{+0.8}_{-0.8}$	$8.5^{+0.9}_{-0.8}$	$8.4^{+0.9}_{-0.8}$	$8.5^{+0.9}_{-0.8}$	$8.4^{+0.9}_{-0.8}$	$8.4^{+0.9}_{-0.8}$
$\delta\nu_{\rm shift}^{\rm 191,12kPa}$ (GHz)	$-6.7^{+0.1}_{-0.1}$	$-6.7^{+0.1}_{-0.1}$	$-6.7^{+0.1}_{-0.1}$	$-6.7^{+0.1}_{-0.1}$	$-6.7^{+0.1}_{-0.1}$	$-6.7^{+0.1}_{-0.1}$
$\delta\nu_{\rm shift}^{\rm 191,45kPa}$ (GHz)	$-7.6^{+0.2}_{-0.2}$	$-7.6^{+0.2}_{-0.2}$	$-7.6^{+0.2}_{-0.2}$	$-7.6^{+0.2}_{-0.2}$	$-7.6^{+0.2}_{-0.2}$	$-7.6^{+0.2}_{-0.2}$
$\delta\nu_{\rm shift}^{\rm 191,74kPa,1st}$ (GHz)	$-7.6^{+0.3}_{-0.3}$	$-7.6^{+0.3}_{-0.3}$	$-7.6^{+0.3}_{-0.3}$	$-7.6^{+0.3}_{-0.3}$	$-7.6^{+0.3}_{-0.3}$	$-7.6^{+0.3}_{-0.3}$
$\delta\nu_{\rm IS}^{193}$ (GHz)	$-2.8^{+0.2}_{-0.2}$	$-2.8^{+0.2}_{-0.2}$	$-2.8^{+0.2}_{-0.2}$	$-2.8^{+0.2}_{-0.2}$	$-2.8^{+0.2}_{-0.2}$	$-2.8^{+0.2}_{-0.2}$
$\delta\nu_{\rm IS}^{196}$ (GHz)	$-7.1^{+0.7}_{-0.7}$	$-6.8^{+0.8}_{-0.8}$	$-7.0^{+0.8}_{-0.8}$	$-7.1^{+0.8}_{-0.9}$	$-7.1^{+0.8}_{-0.8}$	$-7.1^{+0.8}_{-0.9}$
$f_{\rm amp}^{\rm 191,12kPa}$	48526^{+1808}_{-1791}	48569^{+1846}_{-1829}	48613^{+1837}_{-1820}	48614^{+1837}_{-1820}	48607^{+1836}_{-1819}	48605^{+1835}_{-1818}
$a^{\rm 191,12kPa}$	1328^{+140}_{-141}	1326^{+143}_{-144}	1317^{+142}_{-143}	1319^{+142}_{-143}	1319^{+142}_{-143}	1320^{+142}_{-143}
$b^{\rm 191,12kPa}$	-21^{+3}_{-3}	-21^{+3}_{-3}	-21^{+3}_{-3}	-21^{+3}_{-3}	-21^{+3}_{-3}	-21^{+3}_{-3}
$f_{\rm amp}^{\rm 191,45kPa}$	65278^{+1926}_{-1921}	65289^{+1965}_{-1960}	65276^{+1949}_{-1945}	65283^{+1951}_{-1946}	65281^{+1949}_{-1945}	65284^{+1949}_{-1944}
$a^{\rm 191,45kPa}$	0^{+269}_{-0}	0^{+273}_{-0}	0^{+273}_{-0}	0^{+273}_{-0}	0^{+273}_{-0}	0^{+273}_{-0}
$b^{\rm 191,45kPa}$	-16^{+6}_{-4}	-16^{+6}_{-4}	-16^{+6}_{-4}	-16^{+6}_{-4}	-16^{+6}_{-4}	-16^{+6}_{-4}
$f_{\rm amp}^{\rm 191,74kPa,1st}$	11021^{+501}_{-500}	11041^{+512}_{-511}	11013^{+509}_{-507}	11020^{+509}_{-507}	11017^{+508}_{-507}	11022^{+508}_{-507}
$a^{\rm 191,74kPa,1st}$	976^{+153}_{-156}	958^{+158}_{-162}	970^{+156}_{-160}	966^{+156}_{-160}	968^{+156}_{-160}	966^{+156}_{-160}
$b^{\rm 191,74kPa,1st}$	-2^{+3}_{-3}	-2^{+3}_{-3}	-2^{+3}_{-3}	-2^{+3}_{-3}	-2^{+3}_{-3}	-2^{+3}_{-3}
$f_{\rm amp}^{\rm 193,12kPa}$	75631^{+2434}_{-2417}	75641^{+2483}_{-2466}	75379^{+2472}_{-2455}	75440^{+2471}_{-2454}	75435^{+2471}_{-2453}	75473^{+2469}_{-2452}
$a^{\rm 193,12kPa}$	0^{+14}_{-0}	0^{+14}_{-0}	0^{+14}_{-0}	0^{+14}_{-0}	0^{+14}_{-0}	0^{+14}_{-0}
$b^{\rm 193,12kPa}$	-12^{+2}_{-2}	-12^{+2}_{-2}	-12^{+2}_{-2}	-12^{+2}_{-2}	-12^{+2}_{-2}	-12^{+2}_{-2}
$f_{\rm amp}^{196}$	$0.51^{+0.07}_{-0.07}$	$0.48^{+0.07}_{-0.07}$	$0.30^{+0.04}_{-0.04}$	$0.30^{+0.05}_{-0.04}$	$0.21^{+0.03}_{-0.03}$	$0.22^{+0.03}_{-0.03}$
a^{196}	$0.08^{+0.04}_{-0.04}$	$0.10^{+0.04}_{-0.04}$	$0.09^{+0.04}_{-0.04}$	$0.08^{+0.04}_{-0.04}$	$0.09^{+0.04}_{-0.04}$	$0.08^{+0.04}_{-0.04}$
reduced χ^2 (all)	1.6	1.7	1.6	1.6	1.6	1.6
reduced χ^2	2.0	2.0	2.0	2.0	2.0	2.0
(191, 12 kPa)						
reduced χ^2	1.5	1.5	1.5	1.5	1.5	1.5
(191, 45 kPa)						
reduced χ^2	2.0	2.0	2.1	2.1	2.1	2.1
(191, 74 kPa, 1st)						
reduced χ^2	1.6	1.6	1.7	1.7	1.7	1.7
(193, 12 kPa)						
reduced χ^2 (196)	1.6	2.3	2.1	2.1	2.1	2.1

4.5.6 Results of the simultaneous fittings including the HFS spectrum of ^{198}Ir

The half-life of ^{198}Ir was measured by the fragmentation reaction of ^{208}Pb beam with ^{9}Be target [97]. However, I^{π} of the ground state has not been assigned yet. There is no isomeric state with half-life longer than 0.5 s, which can be extracted from the KISS gas cell. Therefore, we can neglect the contamination of any isomeric states on ^{198}Ir.

The five HFS spectra for the stable isotopes and one HFS spectrum for ^{198}Ir were fitted simultaneously. The fittings were performed with the ten fitting conditions: the spin assumption of $I = 0$ and three initial μ^{198} values of $\mu^{198}_{\rm initial} = -0.7$, 0, and $+0.7$ $\mu_{\rm N}$ for each spin assumption of $I = 1$, 2, and 3. The obtained fitting parameter values for ^{198}Ir are summarized in Table 16 for the fitting with $I = 0$ and Table 17 for the fitting with $I \geq 1$. The measured hyperfine spectra of ^{198}Ir with the fitting results are shown in Fig. 43. The evaluated parameters of $A^{191}_{\rm ex}$, $B^{191}_{\rm ex}$, and $\delta\nu_{\rm L}$ in the ^{198}Ir fitting except for $\delta\nu_{\rm L}^{191,198}$ value in the case of $I = 0$ are consistent with those evaluated in the ^{191}Ir fittings listed in Table 11. In the case of $I = 1$, the three fittings with $\mu^{198}_{\rm initial} = -0.7$, 0, and $+0.7$ $\mu_{\rm N}$ were converged the one result with $\mu^{198} = +0.15^{+0.02}_{-0.03}$ $\mu_{\rm N}$. In the case of $I = 2$ and 3, the three fittings with $\mu^{198}_{\rm initial} = -0.7$, 0, and $+0.7$ $\mu_{\rm N}$ were converged to the two results, which the sign of μ^{198} were positive and negative.

In the case of $I = 0$, the obtained $\delta\nu_{\rm L} = 12^{+1}_{-1}$ GHz is deviated more than three sigma from $\delta\nu_{\rm L} = 8^{+1}_{-1}$ GHz at a gas cell pressure of 74 kPa in the second experiment. Moreover, the obtained reduced $\chi^2 = 2.4$ for the HFS spectrum of ^{198}Ir with $I = 0$ is about two times larger than those with other spin assumptions (reduced $\chi^2 = 1.3$–1.7). Therefore, the spin value of ^{198}Ir is strongly suggested to be larger than zero. The smallest reduced $\chi^2 = 1.3$ was obtained with $I = 1$ and $\mu^{198} = +0.15^{+0.02}_{-0.03}$ $\mu_{\rm N}$.

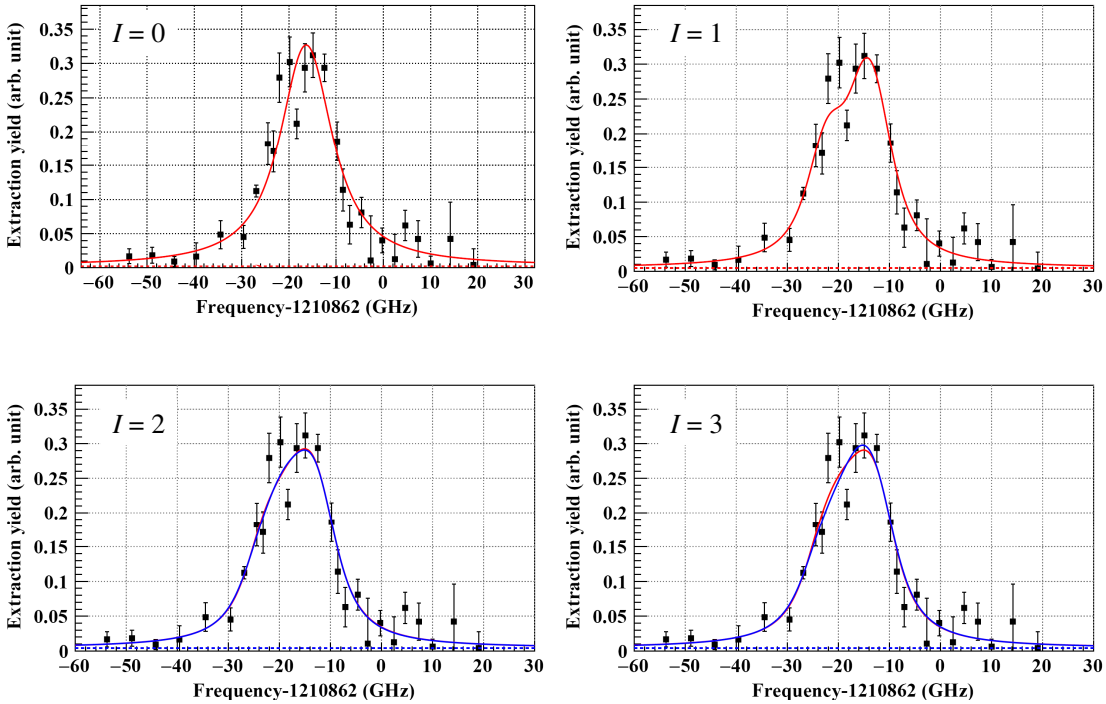

Figure 43: Measured HFS spectra of ^{198}Ir and the fitting curves with the spin assumptions of $I = 0$, 1, 2, and 3. The broken lines indicate the evaluated background levels. The red line in the spectrum with $I = 0$ shows the sum of the evaluated Voigt function and background level. The red and blue lines in the spectra with $I \geq 1$ show the sum of the evaluated HFS spectra and background levels with positive and negative μ^{198} values, respectively.

Table 16: Fitting results of the HFS spectrum of ^{198}Ir with $I = 0$.

Parameter	Value
A_{ex}^{191} (MHz)	-669^{+20}_{-20}
B_{ex}^{191} (MHz)	123^{+398}_{-407}
$\delta\nu_{\mathrm{L}}^{12\mathrm{kPa}}$ (GHz)	$3.2^{+0.1}_{-0.1}$
$\delta\nu_{\mathrm{L}}^{45\mathrm{kPa}}$ (GHz)	$6.5^{+0.3}_{-0.3}$
$\delta\nu_{\mathrm{L}}^{74\mathrm{kPa,1st}}$ (GHz)	$8.5^{+0.9}_{-0.8}$
$\delta\nu_{\mathrm{L}}^{74\mathrm{kPa,2nd}}$ (GHz)	$12.3^{+1.0}_{-1.0}$
$\delta\nu_{\mathrm{shift}}^{191,12\mathrm{kPa}}$ (GHz)	$-6.7^{+0.1}_{-0.1}$
$\delta\nu_{\mathrm{shift}}^{191,45\mathrm{kPa}}$ (GHz)	$-7.6^{+0.2}_{-0.2}$
$\delta\nu_{\mathrm{shift}}^{191,74\mathrm{kPa,1st}}$ (GHz)	$-7.6^{+0.3}_{-0.3}$
$\delta\nu_{\mathrm{shift}}^{191,74\mathrm{kPa,2nd}}$ (GHz)	$-7.8^{+0.4}_{-0.4}$
$\delta\nu_{\mathrm{IS}}^{193}$ (GHz)	$-2.8^{+0.2}_{-0.2}$
$\delta\nu_{\mathrm{IS}}^{198}$ (GHz)	$-8.6^{+0.6}_{-0.6}$
$f_{\mathrm{amp}}^{191,12\mathrm{kPa}}$	48900^{+1852}_{-1836}
$a^{191,12\mathrm{kPa}}$	1314^{+144}_{-144}
$b^{191,12\mathrm{kPa}}$	-21^{+3}_{-3}
$f_{\mathrm{amp}}^{191,45\mathrm{kPa}}$	65372^{+1971}_{-1967}
$a^{191,45\mathrm{kPa}}$	0^{+260}_{-0}
$b^{191,45\mathrm{kPa}}$	-16^{+6}_{-5}
$f_{\mathrm{amp}}^{191,74\mathrm{kPa,1st}}$	11052^{+514}_{-513}
$a^{191,74\mathrm{kPa,1st}}$	953^{+158}_{-162}
$b^{191,74\mathrm{kPa,1st}}$	-2^{+3}_{-3}
$f_{\mathrm{amp}}^{193,12\mathrm{kPa}}$	75781^{+2491}_{-2475}
$a^{193,12\mathrm{kPa}}$	0^{+14}_{-0}
$b^{193,12\mathrm{kPa}}$	-12^{+2}_{-2}
$f_{\mathrm{amp}}^{191,74\mathrm{kPa,2nd}}$	5590^{+341}_{-338}
$a^{191,74\mathrm{kPa,2nd}}$	1524^{+104}_{-106}
$b^{191,74\mathrm{kPa,2nd}}$	-13^{+3}_{-3}
f_{amp}^{198}	$0.66^{+0.05}_{-0.05}$
a^{198}	$0.002^{+0.007}_{-0.000}$
reduced χ^2 (all)	1.7
reduced χ^2 (191, 12 kPa)	2.0
reduced χ^2 (191, 45 kPa)	1.5
reduced χ^2 (191, 74 kPa, 1st)	2.0
reduced χ^2 (193, 12 kPa)	1.7
reduced χ^2 (191, 74 kPa, 2nd)	1.3
reduced χ^2 (198)	2.4

Table 17: Fitting results of the HFS spectrum of ^{198}Ir with $I = 1$, 2, and 3 and three initial μ^{198} values.

Parameter	Value				
	$I = 1$	$I = 2$		$I = 3$	
$\mu^{196}_{\mathrm{initial}}$ (μ_{N})	0, ±0.7	+0.7	0, -0.7	+0.7	0, -0.7
A^{191}_{ex} (MHz)	-678^{+18}_{-18}	-672^{+19}_{-19}	-677^{+19}_{-19}	-673^{+19}_{-19}	-673^{+19}_{-19}
B^{191}_{ex} (MHz)	477^{+265}_{-224}	-215^{+249}_{-255}	523^{+259}_{-240}	-166^{+266}_{-270}	-91^{+259}_{-269}
μ^{196} (μ_{N})	$0.15^{+0.02}_{-0.03}$	$0.19^{+0.02}_{-0.02}$	$-0.19^{+0.02}_{-0.02}$	$0.20^{+0.02}_{-0.02}$	$-0.19^{+0.02}_{-0.02}$
Q^{196} (b)	-4^{+2}_{-1}	5^{+0}_{-1}	-5^{+10}_{-0}	5^{+0}_{-1}	5^{+0}_{-10}
$\delta\nu_{\mathrm{L}}^{12\mathrm{kPa}}$ (GHz)	$3.1^{+0.1}_{-0.1}$	$3.2^{+0.1}_{-0.1}$	$3.1^{+0.1}_{-0.1}$	$3.2^{+0.1}_{-0.1}$	$3.2^{+0.1}_{-0.1}$
$\delta\nu_{\mathrm{L}}^{45\mathrm{kPa}}$ (GHz)	$6.5^{+0.3}_{-0.3}$	$6.5^{+0.3}_{-0.3}$	$6.5^{+0.3}_{-0.3}$	$6.5^{+0.3}_{-0.3}$	$6.5^{+0.3}_{-0.3}$
$\delta\nu_{\mathrm{L}}^{74\mathrm{kPa,1st}}$ (GHz)	$8.5^{+0.8}_{-0.8}$	$8.5^{+0.8}_{-0.8}$	$8.5^{+0.8}_{-0.8}$	$8.5^{+0.8}_{-0.8}$	$8.5^{+0.8}_{-0.8}$
$\delta\nu_{\mathrm{L}}^{74\mathrm{kPa,2nd}}$ (GHz)	$7.5^{+0.9}_{-0.9}$	$7.8^{+1.1}_{-1.0}$	$7.5^{+1.1}_{-1.0}$	$7.7^{+1.1}_{-1.0}$	$7.8^{+1.1}_{-1.0}$
$\delta\nu_{\mathrm{shift}}^{191,12\mathrm{kPa}}$ (GHz)	$-6.7^{+0.1}_{-0.1}$	$-6.7^{+0.1}_{-0.1}$	$-6.7^{+0.1}_{-0.1}$	$-6.7^{+0.1}_{-0.1}$	$-6.7^{+0.1}_{-0.1}$
$\delta\nu_{\mathrm{shift}}^{191,45\mathrm{kPa}}$ (GHz)	$-7.6^{+0.2}_{-0.2}$	$-7.6^{+0.2}_{-0.2}$	$-7.6^{+0.2}_{-0.2}$	$-7.6^{+0.2}_{-0.2}$	$-7.6^{+0.2}_{-0.2}$
$\delta\nu_{\mathrm{shift}}^{191,74\mathrm{kPa,1st}}$ (GHz)	$-7.5^{+0.3}_{-0.3}$	$-7.6^{+0.3}_{-0.3}$	$-7.5^{+0.3}_{-0.3}$	$-7.6^{+0.3}_{-0.3}$	$-7.6^{+0.3}_{-0.3}$
$\delta\nu_{\mathrm{shift}}^{191,74\mathrm{kPa,2nd}}$ (GHz)	$-7.7^{+0.3}_{-0.3}$	$-7.8^{+0.3}_{-0.3}$	$-7.7^{+0.3}_{-0.3}$	$-7.8^{+0.3}_{-0.3}$	$-7.8^{+0.3}_{-0.3}$
$\delta\nu_{\mathrm{IS}}^{193}$ (GHz)	$-2.8^{+0.1}_{-0.1}$	$-2.8^{+0.2}_{-0.2}$	$-2.8^{+0.2}_{-0.2}$	$-2.8^{+0.2}_{-0.2}$	$-2.8^{+0.2}_{-0.2}$
$\delta\nu_{\mathrm{IS}}^{198}$ (GHz)	$-9.4^{+0.5}_{-0.5}$	$-9.1^{+0.5}_{-0.5}$	$-9.3^{+0.5}_{-0.5}$	$-9.1^{+0.5}_{-0.5}$	$-9.0^{+0.5}_{-0.5}$
$f_{\mathrm{amp}}^{191,12\mathrm{kPa}}$	48513^{+1701}_{-1684}	48658^{+1729}_{-1713}	48512^{+1726}_{-1711}	48644^{+1727}_{-1711}	48647^{+1729}_{-1714}
$a^{191,12\mathrm{kPa}}$	1330^{+132}_{-133}	1315^{+134}_{-135}	1330^{+134}_{-135}	1317^{+134}_{-135}	1318^{+134}_{-135}
$b^{191,12\mathrm{kPa}}$	-21^{+3}_{-3}	-21^{+3}_{-3}	-21^{+3}_{-3}	-21^{+3}_{-3}	-21^{+3}_{-3}
$f_{\mathrm{amp}}^{191,45\mathrm{kPa}}$	65276^{+1817}_{-1813}	65287^{+1838}_{-1834}	65276^{+1844}_{-1840}	65287^{+1836}_{-1832}	65293^{+1840}_{-1836}
$a^{191,45\mathrm{kPa}}$	0^{+251}_{-0}	0^{+256}_{-0}	0^{+254}_{-0}	0^{+256}_{-0}	0^{+256}_{-0}
$b^{191,45\mathrm{kPa}}$	-16^{+5}_{-4}	-16^{+5}_{-4}	-16^{+5}_{-4}	-16^{+5}_{-4}	-16^{+5}_{-4}
$f_{\mathrm{amp}}^{191,74\mathrm{kPa,1st}}$	11048^{+473}_{-472}	11024^{+480}_{-478}	11050^{+480}_{-479}	11025^{+479}_{-478}	11028^{+480}_{-479}
$a^{191,74\mathrm{kPa,1st}}$	956^{+146}_{-149}	960^{+148}_{-152}	955^{+148}_{-151}	960^{+148}_{-151}	960^{+148}_{-152}
$b^{191,74\mathrm{kPa,1st}}$	-2^{+3}_{-3}	-2^{+3}_{-3}	-2^{+3}_{-3}	-2^{+3}_{-3}	-2^{+3}_{-3}
$f_{\mathrm{amp}}^{193,12\mathrm{kPa}}$	75684^{+2294}_{-2278}	75398^{+2326}_{-2309}	75698^{+2327}_{-2312}	75424^{+2324}_{-2307}	75478^{+2327}_{-2311}
$a^{193,12\mathrm{kPa}}$	0^{+14}_{-0}	0^{+13}_{-0}	0^{+14}_{-0}	0^{+13}_{-0}	0^{+13}_{-0}
$b^{193,12\mathrm{kPa}}$	-12^{+2}_{-2}	-12^{+2}_{-2}	-12^{+2}_{-2}	-12^{+2}_{-2}	-12^{+2}_{-2}
$f_{\mathrm{amp}}^{191,74\mathrm{kPa,2nd}}$	4987^{+300}_{-295}	5011^{+314}_{-309}	4996^{+314}_{-310}	5003^{+314}_{-310}	5020^{+315}_{-311}
$a^{191,74\mathrm{kPa,2nd}}$	1795^{+94}_{-96}	1781^{+99}_{-102}	1791^{+100}_{-102}	1785^{+100}_{-102}	1778^{+100}_{-102}
$b^{191,74\mathrm{kPa,2nd}}$	-14^{+2}_{-2}	-14^{+2}_{-2}	-14^{+2}_{-2}	-14^{+2}_{-2}	-14^{+2}_{-2}
f_{amp}^{198}	$0.20^{+0.01}_{-0.01}$	$0.121^{+0.008}_{-0.008}$	$0.120^{+0.008}_{-0.008}$	$0.086^{+0.006}_{-0.006}$	$0.086^{+0.006}_{-0.006}$
a^{198}	$0.005^{+0.006}_{-0.000}$	$0.004^{+0.006}_{-0.000}$	$0.004^{+0.006}_{-0.000}$	$0.004^{+0.006}_{-0.000}$	$0.004^{+0.006}_{-0.000}$
reduced χ^2 (all)	1.4	1.5	1.5	1.5	1.5
reduced χ^2 (191, 12 kPa)	2.0	2.0	2.0	2.0	2.0
reduced χ^2 (191, 45 kPa)	1.5	1.5	1.6	1.5	1.5
reduced χ^2 (191, 74 kPa, 1st)	2.0	2.1	2.0	2.1	2.1
reduced χ^2 (193, 12 kPa)	1.6	1.7	1.6	1.7	1.7
reduced χ^2 (191, 74 kPa, 2nd)	0.6	0.7	0.6	0.7	0.6
reduced χ^2 (198)	1.3	1.6	1.6	1.6	1.7

5 Discussion

We deduced the difference of charge radii and nuclear deformation parameters from the evaluated isotope shifts of iridium isotopes. The magnetic moments, difference of nuclear charge radii, and deformation parameters were compared with those by theoretical calculations. The evaluated magnetic moments of ^{196}Ir and ^{198}Ir were compared with semi-empirical magnetic moments to estimate the most probable spin-parity and wave-functions of odd-proton and -neutron.

5.1 Charge radii and deformation parameters

The variations of nuclear mean-square charge radius were deduced from measured isotope shifts by using Eq. (42). The unknown electronic factor F_{247} in the present transition was deduced by using Eq. (73) with $\delta\nu^{191,193}_{\mathrm{FS},351} = -2.03(2)$ GHz and $F_{351} = -30.94$ GHz·fm^{-2} which were reported in the previous laser spectroscopy experiment by Verney *et al.* [26]. The field shift $\delta\nu^{191,193}_{\mathrm{FS}}$ was calculated by using Eq. (18). There are no experimental and theoretical informations for the specific mass shift for nd $\rightarrow$ $(n+1)$p transition of iridium atom. Therefore, we included the contribution of unknown specific mass shift as the systematic error of the mass shift. The error of ± 60 MHz/ΔA was evaluated from the theoretical specific mass shift for nd $\rightarrow$ $(n+1)$p transition of osmium atom as mentioned in subsection 2.4.1. We evaluated $F_{247} = -43(4)$ GHz·fm^{-2} from the mass shift $\delta\nu^{191,193}_{\mathrm{MS}} = 0.03(12)$ GHz and $\delta\nu^{191,193}_{\mathrm{FS},247} = -2.8(2)$ GHz. The calculated $\lambda^{AA'}$ values of iridium isotopes are listed in Table 18.

The variation of the nuclear mean-square charge radius $\delta\langle r_{\mathrm{c}}^2\rangle^{191,A}$ and quadrupole deformation parameter $\delta\langle\beta_2^2\rangle^{191,A}$ for each iridium isotope were calculated according to subsection 2.5. We used the Seltzer coefficients C_1, C_2, and C_3 revised by Torbohm *et al.* [56], according to the previous study [26]. The reference isotope of the variations is ^{191}Ir. The absolute value of β_2 was calculated as

$$\left|\langle\beta_2^2\rangle\right|^{1/2} = \sqrt{\beta_2^2(191) + \delta\langle\beta_2^2\rangle^{191,A}}, \tag{74}$$

where $\beta_2(191) = +0.155$ was taken from the FRDM model [105]. The calculation results are listed in Table 18 and plotted in Figs. 44(a) and (b). The $\delta\langle r_c^2\rangle$ values up to $A = 198$ gradually increase with increasing of neutron number. The blue boxes in Fig. 44(b) show the values calculated by the FRDM model [105]. The trend of evaluated $|\beta_2|$ is consistent with that calculated by the FRDM model which suggests the prolate shape ($\beta_2 > 0$) for $A \leq 196$ isotopes and oblate shape ($\beta_2 < 0$) for $A \geq 197$ isotopes. To clarify the shape transition in iridium isotopes, it is necessary to measure the sign of β_2. This can be deduced from the intrinsic quadrapole moment. The relation between the electric quadrupole moment Q, which can be obtained from a HFS measurement, and intrinsic quadrupole moment Q_0 is given as Eq. (4-69) in Ref. [106]

$$Q = \frac{3K^2 - I(I+1)}{(I+1)(2I+3)} Q_0. \tag{75}$$

The Q_0 is given using β_2 as Eq. (4-191) in Ref. [106]

$$Q_0 = \frac{3}{\sqrt{5\pi}} Z R_0^2 \beta_2 \left(1 + \frac{2}{7}\sqrt{\frac{5}{\pi}}\beta_2 + \frac{1}{14\pi}\beta_2^2 - \cdots\right), \tag{76}$$

where R_0 is the nuclear radius defined as $R_0 = 1.1 \sim 1.2A^{1/3}$ fm. The Q will be measured at KISS with in-gas-jet laser ionization spectroscopy.

Table 18: The evaluated $\delta\langle r_c^2\rangle^{191,A}$ and $|\langle\beta_2^2\rangle|^{1/2}$ values of ^{193}Ir and $^{196-198}$Ir from Eqs. (46), (47), and (74). The reference isotope of the variations is ^{191}Ir with $\beta_2 = +0.155$ calculated by the FRDM model [105].

A	$\delta\nu_{\rm IS}^{191,A}$ (GHz)	$\delta\nu_{\rm FS}^{191,A}$ (GHz)	$\lambda^{191,A}$	$\delta\langle r_c^2\rangle^{191,A}$	$\delta\langle\beta_2^2\rangle^{191,A}$	$\|\langle\beta_2^2\rangle\|^{1/2}$
191	0	0	0	0	0	0.155
193	$-2.8^{+0.2}_{-0.2}$	$-2.8^{+0.2}_{-0.2}$	$+0.066^{+0.008}_{-0.008}$	$+0.070^{+0.009}_{-0.009}$	$-0.0030^{+0.0008}_{-0.0008}$	$0.145^{+0.003}_{-0.003}$
196	$-7.1^{+0.7}_{-0.7}$	$-7.2^{+0.8}_{-0.8}$	$+0.17^{+0.02}_{-0.02}$	$+0.18^{+0.03}_{-0.03}$	$-0.007^{+0.002}_{-0.002}$	$0.129^{+0.009}_{-0.009}$
197	$-10.3^{+0.7}_{-0.7}$	$-10.4^{+0.8}_{-0.8}$	$+0.24^{+0.03}_{-0.03}$	$+0.26^{+0.03}_{-0.03}$	$-0.005^{+0.003}_{-0.003}$	$0.14^{+0.01}_{-0.01}$
198	$-9.4^{+0.5}_{-0.5}$	$-9.5^{+0.7}_{-0.7}$	$+0.22^{+0.03}_{-0.03}$	$+0.23^{+0.03}_{-0.03}$	$-0.012^{+0.002}_{-0.002}$	$0.11^{+0.01}_{-0.01}$

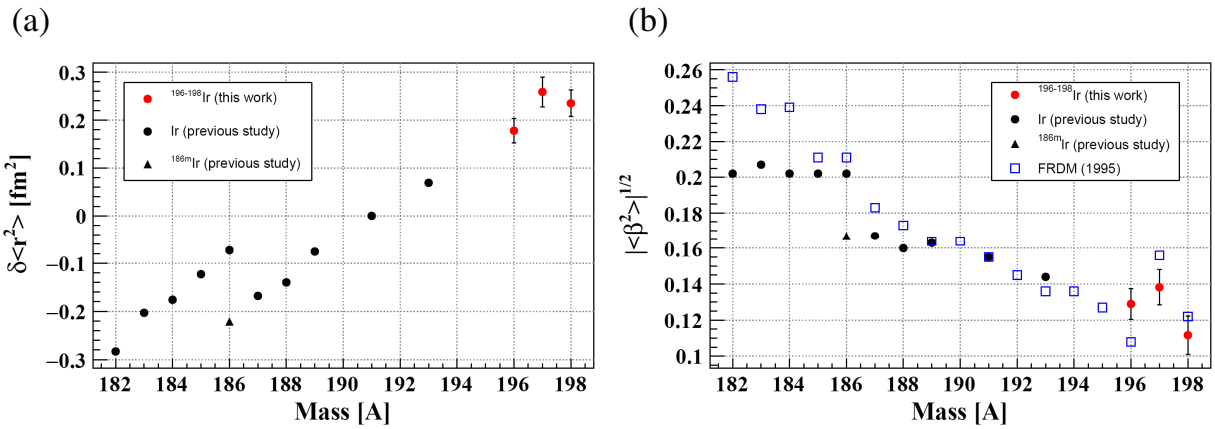

Figure 44: (a) Variation of mean-square charge radius and (b) absolute value of quadrupole deformation parameter on the iridium isotopic series. The black and red dots indicate the values reported in the previous study [26] and the evaluated values in the present work, respectively. The blue boxes indicate the values calculated by the FRDM model [105]. The values for the isomeric state of ^{186}Ir are represented by black triangles.

5.2 Theoretical calculation

Experimental results were compared with two theoretical calculations: Hartree-Fock-Bogoliubov (HFB) calculation with SkM* interaction and shell model calculations with modified Kuo-Herling (KHHE) interaction. We discuss the comparison between the experimental and theoretical values in the following subsections.

5.2.1 Self-consistent HFB calculation with SkM* interaction

The magnetic moments, variations of mean-square charge radii, and quadrupole deformation parameters of ^{191,193,196,197}Ir were calculated by the self-consistent HFB calculation with SkM* interaction [107]. The SkM* interaction is a parameter set which gives the reasonable agreement between experimental and theoretical binding energies and charge radii of the doubly magic nuclei from O to Pb [108]. The SkM* interaction also well reproduces the fission barrier of deformed ^{240}Pu, and, therefore, the interaction could be applied for the estimation of these values for a deformed nucleus. Firstly, the self-consistent HFB

calculation was performed for even-even core nucleus, such as ^{196}Os ($Z = 76$, $N = 120$) core of ^{197}Ir ($Z = 77$, $N = 120$), to determine the lowest energy state with deformation of the core nucleus. Then, one nucleon was added to one single particle state around Fermi energy with a occupation of 100%. The effects of the core polarization induced by added nucleon are treated self-consistently. The β_2 and charge radius were deduced from the nuclear density which was obtained by the HFB calculation. Experimental and theoretical results are summarized in Table 19. Theoretical results for the low-lying states of ^{197}Ir and ^{196}Ir are summarized in Tables 20 and 21, respectively.

The $I^\pi = 3/2^+$ states for ^{191,193,197}Ir were obtained by occupying the Nilsson level of $\pi 3/2^+[402]$. In the cases of ^{191}Ir and ^{193}Ir, the lowest $I^\pi = 3/2^+$ state appeared as the ground state and at the excitation energy of $E_{\rm ex,th} = 0.017$ MeV, respectively. Theoretical μ ($\mu_{\rm th}$) values of those states are more than four times larger than the experimental μ ($\mu_{\rm exp}$) values, and the sign of μ values are opposite. In the case of ^{197}Ir, the lowest $I^\pi = 3/2^+$ state appeared at $E_{\rm ex,th} = 0.20$ MeV, and the $\mu_{\rm th}$ value is nine times larger than the $\mu_{\rm exp}$ value. As shown in Table 20, all predicted low-lying states of ^{197}Ir were suggested to be the oblate deformation with the theoretical β_2 ($\beta_{2,\rm th}$) values of $\beta_{2,\rm th} = -0.12$ to -0.13. Even though the good agreement between the experimental and theoretical μ values was obtained from the calculated state with $E_{\rm ex,th} = 2.15$ MeV, the $\beta_{2,\rm th}$ value was required to become smaller by a factor of ~ 2 than the experimental one.

In the case of ^{196}Ir, the calculations were performed by occupying the $\pi 1/2^+$, $3/2^+$ and $\nu 1/2^-$, $3/2^-$ states for odd-proton and -neutron, respectively. The results for the lowest $I^\pi = 1^-$ state with the occupation of the $\pi 1/2^+[411]$ and $\nu 1/2^-[521]$ are shown in Table 19. The theoretical $\mu_{\rm th} = +0.423\ \mu_{\rm N}$ is about two times larger than the experimental $\mu_{\rm exp} = +0.23 \pm 0.03\ \mu_{\rm N}$. As shown in Table 21, all the states, except for the state at the last column, were suggested the oblate deformation with $\beta_{2,\rm th} = -0.153$ to -0.125.

The calculated $\delta\langle r_{\rm c}^2\rangle$ and $|\beta_2|$ were in good agreement with the experimental ones, except for the second results for ^{197}Ir. The disagreements between experimental and theoretical μ values were also reported in Refs. [26, 31, 102]. We need more experimental investigations for electromagnetic moments in the heavy neutron-rich nuclear region to construct the proper theoretical models or interactions in this nuclear region.

Table 19: Comparison of experimental and theoretical results by the HFB + SkM* calculations. The experimental values of ^{191,193}Ir were reported in Refs. [26, 98]. The reference isotope for the variations is ^{191}Ir with $\beta_2 = +0.155$ from the FRDM model [105]. The following Nilsson levels were occupied by valence nucleons: $\pi 3/2^+[402]$ for ^{191,193,197}Ir, and $\pi 1/2^+[411]$ and $\nu 1/2^-[521]$ for ^{196}Ir. The theoretical results with different $\beta_{2,\rm th}$ for ^{197}Ir is shown in the last column. In the case of ^{196}Ir, the energy of the state is the lowest within the calculated configurations and, however, it is not clear weather the state is a ground state or not.

A	I^π	$\mu_{\rm exp}$ ($\mu_{\rm N}$)	$\mu_{\rm th}$ ($\mu_{\rm N}$)	$\delta\langle r_{\rm c}^2\rangle_{\rm exp}$ (fm^2)	$\delta\langle r_{\rm c}^2\rangle_{\rm th}$ (fm^2)	$\lvert\langle\beta_2^2\rangle\rvert^{1/2}_{\rm exp}$	$\beta_{2,\rm th}$	$E_{\rm ex,th}$ (MeV)
191	$3/2^+$	+0.1507(6)	−1.073	0	0	+0.155	+0.174	0
193	$3/2^+$	+0.1636(6)	−0.7381	+0.0691(8)	+0.076	+0.144(1)	+0.156	0.017
196	1^-	+0.23(3)	+0.423	+0.18(3)	+0.194	0.129(9)	−0.138	-
197	$3/2^+$	+0.25(3)	+2.143 +0.261	+0.26(3)	+0.228 -	0.14(1)	−0.13 +0.06	0.20 2.15

Table 20: Theoretical results for low-lying states of ^{197}Ir by the HFB + SkM* calculations.

$E_{\mathrm{ex,th}}$ (MeV)	I^π	μ_{th} (μ_{N})	$\beta_{2,\mathrm{th}}$	Blocked level
0	$1/2^+$	-0.058	-0.13	$1/2^+[411]$
0.05	$1/2^-$	$+7.120$	-0.13	$1/2^-[550]$
0.20	$3/2^+$	$+2.143$	-0.13	$3/2^+[402]$
0.32	$5/2^-$	$+2.968$	-0.12	$5/2^-[532]$

Table 21: Theoretical results for low-lying states of ^{196}Ir by the HFB + SkM* calculations. These states were calculated with the combinations of the blocked proton orbit of $\pi 1/2^+$ or $\pi 3/2^+$, and neutron orbit of $\nu 1/2^-$ or $\nu 3/2^-$. The ground state is not identified in each calculation because only the state with the blocked level was calculated to evaluate the μ_{th} and $\beta_{2,\mathrm{th}}$. Therefore, the calculated energy of the states are shown in the table.

Energy (MeV)	I^π	μ_{th} (μ_{N})	$\beta_{2,\mathrm{th}}$	Blocked level
-1547.442	1^-	$+0.423$	-0.138	$\pi 1/2^+[411]$, $\nu 1/2^-[521]$
-1547.259	2^-	$+2.761$	-0.138	$\pi 3/2^+[402]$, $\nu 1/2^-[521]$
-1547.227	1^-	$+1.674$	-0.138	$\pi 3/2^+[402]$, $\nu 1/2^-[521]$
-1547.199	2^-	$+0.927$	-0.125	$\pi 1/2^+[411]$, $\nu 3/2^-[501]$
-1547.047	3^-	-0.071	-0.132	$\pi 3/2^+[402]$, $\nu 3/2^-[501]$
-1547.030	2^-	$+1.784$	-0.138	$\pi 3/2^+[402]$, $\nu 1/2^-[510]$
-1546.898	2^-	-0.622	-0.138	$\pi 1/2^+[411]$, $\nu 3/2^-[512]$
-1546.804	1^-	$+1.772$	-0.153	$\pi 3/2^+[402]$, $\nu 1/2^-[510]$
-1546.692	3^-	$+1.743$	-0.138	$\pi 3/2^+[402]$, $\nu 3/2^-[512]$
-1546.235	2^-	$+0.694$	$+0.097$	$\pi 1/2^+[400]$, $\nu 3/2^-[501]$

5.2.2 Shell model calculation

The μ and β_2 values of ^{196,197,198}Ir were calculated by using the shell model [109]. The KHHE interaction was used to calculate the neutron and proton hole interactions in the ^{208}Pb core [110]. The KHHE interaction well reproduces the properties, such as order and energy of levels, spectroscopic factors, and E2 transition rates, of nuclei with a few proton and/or neutron holes from the ^{208}Pb core. The full model space ($50 \leq Z \leq 82$ and $82 \leq N \leq 126$) calculation can be performed only for ^{198}Ir (5 proton- and 5 neutron-holes). Because huge computer power for the calculation is required for the full space calculations of ^{196,197}Ir due to many number of holes. Therefore, the truncated model space calculations were performed for ^{196,197}Ir.

The magnetic moment of a state by the shell model calculation (μ_{th}) is given as

$$\mu_{\mathrm{th}} = \sum_{i=0}^{n} a_i \langle \phi_i \left| (g_{\mathrm{s}} \boldsymbol{s}_{\mathrm{z}} + g_{\mathrm{l}} \boldsymbol{l}_{\mathrm{z}}) \right| \phi_i \rangle, \tag{77}$$

where ϕ_i is the linear combination of the nuclear wave-functions, and $\boldsymbol{s}_z$ and $\boldsymbol{l}_z$ are the projection operators of the nucleon spin and angular momentum, respectively. The $\mu_{\rm th}$ is deduced from the summation of the individual magnetic dipole moment for ϕ_i with the probability a_i. The $g_{\rm s}$ is the spin g-factor of nucleon: $g_{\rm s} = 5.586$ for proton and $g_{\rm s} = -3.826$ for neutron. The effective spin g-factor $g_{\rm s}^{\rm eff} = 0.6 g_{\rm s}$ was used considering the core-polarization. The $g_{\rm l}$ is the orbital g-factor of nucleon and the values $g_{\rm l} = 1.003$ for proton and $g_{\rm l} = -0.003$ for neutron were used.

Experimental and theoretical results are summarized in Table 22. In the case of the full model space calculation for ^{198}Ir, the $I^\pi = 1^-$ state became the ground state but the $\mu_{\rm th}$ value is six times higher than the $\mu_{\rm exp}$ value. The results of the second $I^\pi = 1^-$ state represent the reasonable $\beta_{2,\rm th}$, but the obtained $\mu_{\rm th}$ value was four times higher than the $\mu_{\rm exp}$ value. In the case of the truncated model space calculation for ^{198}Ir, the first $I^\pi = 1^-$ state became the ground state and the $\mu_{\rm th}$ and $\beta_{2,\rm th}$ values are not deviated from the experimental values, significantly.

In the case of ^{196}Ir, a better agreement of μ for the $I^\pi = 1^-$ state at $E_{\rm ex,th} = 0.204$ MeV is obtained and the $\beta_{2,\rm th}$ value indicates the oblate shape. In the case of ^{197}Ir, the $\mu_{\rm th}$ values of three $I^\pi = 3/2^+$ states are more than two times larger than the $\mu_{\rm exp}$ value, and the obtained $\beta_{2,\rm th}$ values are more than four times smaller than the experimental ones.

A part of the configuration of the nuclear wave-function obtained from the shell model calculation with a truncated model space for ^{198}Ir are listed in Table 23. As shown in the table, many configurations with small fractions were obtained due to the strong configuration mixing with many proton- and neutron-hole states. The same situations were obtained for other cases.

We need to compare the nuclear properties in this nuclear region more and the modification of nucleon-nucleon interaction parameter for neutron-rich nuclei far from ^{208}Pb. The agreements for the μ or $|\beta_2|$ within the margin of two-sigma error were obtained in a few cases as shown in Table 22, but we don't know weather the used truncations of the model space were proper to calculate the nuclear properties or not. Because $\mu_{\rm th}$ drastically changes by using a different truncation in the model space.

Table 22: Comparison of experimental and theoretical results by the shell model calculations.

A	I^π	Experimental results		Theoretical results			
		$\mu_{\rm exp}$ ($\mu_{\rm N}$)	$\lvert\langle\beta_2^2\rangle\rvert^{1/2}_{\rm exp}$	$\mu_{\rm th}$ ($\mu_{\rm N}$)	$\beta_{2,\rm th}$	$E_{\rm ex,th}$ (MeV)	Model space
196	1^-	$+0.23^{+0.03}_{-0.03}$	$0.129^{+0.009}_{-0.009}$	-2.474	$+0.120$	0	Truncated
				$+0.301$	-0.251	0.204	
197	$3/2^+$	$+0.25^{+0.03}_{-0.03}$	$0.14^{+0.01}_{-0.01}$	$+0.635$	-0.036	0	
				$+0.596$	-0.021	0.203	
				$+0.495$	-0.029	0.223	
198	1^-	$+0.15^{+0.02}_{-0.03}$	$0.11^{+0.01}_{-0.01}$	$+0.301$	-0.160	0	
				-0.291	$+0.132$	0.050	
				-1.333	$+0.197$	0	Full
				$+0.825$	-0.134	0.102	

Table 23: A part of configuration obtained from the truncated shell model calculation for ^{198}Ir with $I^\pi = 1^-$ and $E_{\rm ex,th} = 0$ keV. $\pi 0g_{7/2}$ and $\nu 0h_{9/2}$ orbits were fully occupied in all the configurations.

Proton orbit				Neutron orbit					Fraction
$1d_{5/2}$ (6)	$1d_{3/2}$ (4)	$2s_{1/2}$ (2)	$0h_{11/2}$ (12)	$1f_{7/2}$ (8)	$1f_{5/2}$ (6)	$2p_{3/2}$ (4)	$2p_{1/2}$ (2)	$0i_{13/2}$ (14)	
5	2	0	12	8	5	2	0	14	0.1386
5	2	0	12	8	5	1	1	14	0.0376
5	2	0	12	6	5	4	0	14	0.034
5	2	0	12	8	5	0	2	14	0.0333
5	2	0	12	8	3	4	0	14	0.0304
5	2	0	12	8	3	2	2	14	0.0244
5	2	0	12	8	5	4	0	12	0.0216
5	2	0	12	6	5	2	2	14	0.0212
5	2	0	12	8	4	2	1	14	0.0208
4	3	0	12	8	5	2	0	14	0.0187
4	2	1	12	8	5	2	0	14	0.0174
5	1	1	12	8	5	2	0	14	0.0153
5	2	0	12	8	5	2	2	12	0.0149
5	2	0	12	7	5	3	0	14	0.0117
4	2	1	12	7	5	3	0	14	0.0109
5	2	1	11	8	5	3	0	13	0.0095
4	2	1	12	8	4	2	1	14	0.0092
5	2	0	12	6	5	3	1	14	0.0087
5	2	0	12	8	3	3	1	14	0.0087
5	2	0	12	7	6	2	0	14	0.0084
⋮	⋮	⋮	⋮	⋮	⋮	⋮	⋮	⋮	⋮

5.3 Systematics of nuclear structure in odd-A iridium isotopes

The nuclear structure of odd-A iridium isotopes were well studied by the reactions: ^{191,193}Ir populated by the (^{3}He,d) and (α,t) reactions [111], ^{193,195}Ir populated by the (t,α) reaction [112], ^{193,195,197}Ir populated by the ($\vec{\rm t}$,α) reaction [113]. There are many radioactive decay ($A \leq 197$) studies such as ^{187}Ir in Ref. [114], ^{191}Ir in Ref. [115], and ^{193}Ir in Ref. [116], and electromagnetic moments studies ($A \leq 194$) compiled in Ref. [24].

Odd-A iridium isotopes from $A = 187$–197 has the ground state with $I^\pi = 3/2^+$, first excited state with $I^\pi = 1/2^+$, and isomeric state with $I^\pi = 11/2^-$ as summarized in Fig. 45. Suggested proton orbit for these three states are $3/2^+[402]$ for the ground state, $1/2^+[400]$ and admixture of γ-vibration couped to the $3/2^+[402]$ ground state for the first $1/2^+$ state, and $11/2^-[505]$ for the $11/2^-$ isomeric state [26, 111, 112, 114, 116]. The Nilsson diagram for single-proton levels in ^{197}Ir is shown in Fig. 46 calculated by HFB + SkM* model explained in subsection 5.2.1. The $11/2^-[505]$ state locates higher energy

than $1/2^+[400]$ with $\beta_2 > +0.1$. The order of $3/2^+$, $1/2^+$, and $11/2^-$ states is interpreted from prolate deformation with $\beta_2 > 0.1$, which were consistent with the previous studies for ^{189,191,193}Ir [26, 114].

The lowest state with $I^\pi = 3/2^+$ is predicted to be oblate shape as shown in Table 20. The FRDM model also predicts the oblate shape for ^{197}Ir as mentioned in subsection 5.1.

The shape transition in neutron-rich iridium isotopes cannot be concluded from the present experimental result of $|\beta_2| = 0.14 \pm 0.01$. As mentioned in subsection 5.1, it is necessary to measure the sign of β_2 to clarify the shape transition.

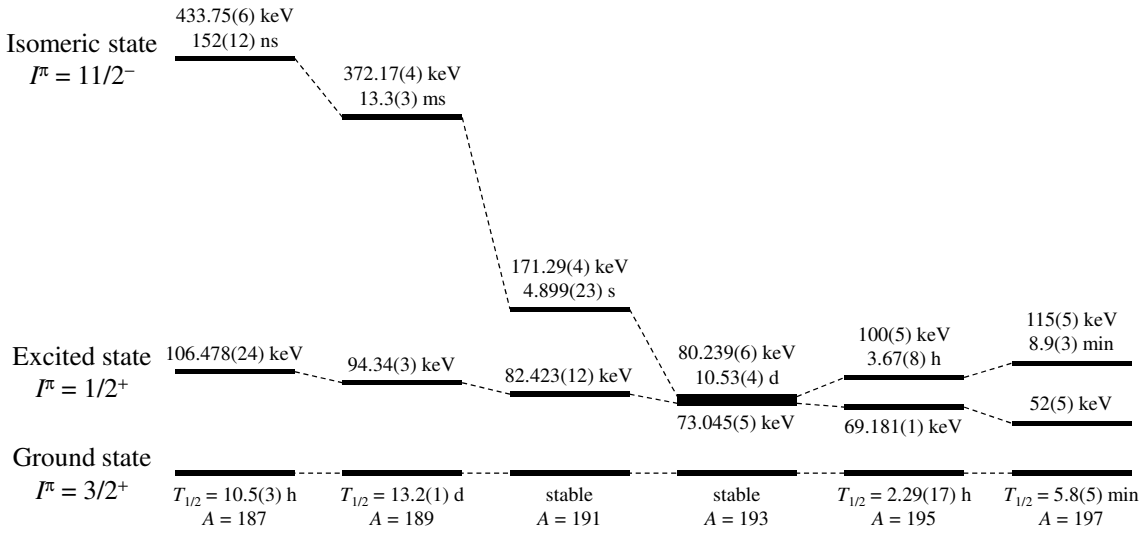

Figure 45: Systematics of the low-lying states in odd-A iridium isotopes from A = 187–197. The values of I^π, level energies, and half-lives from NNDC [21] are shown.

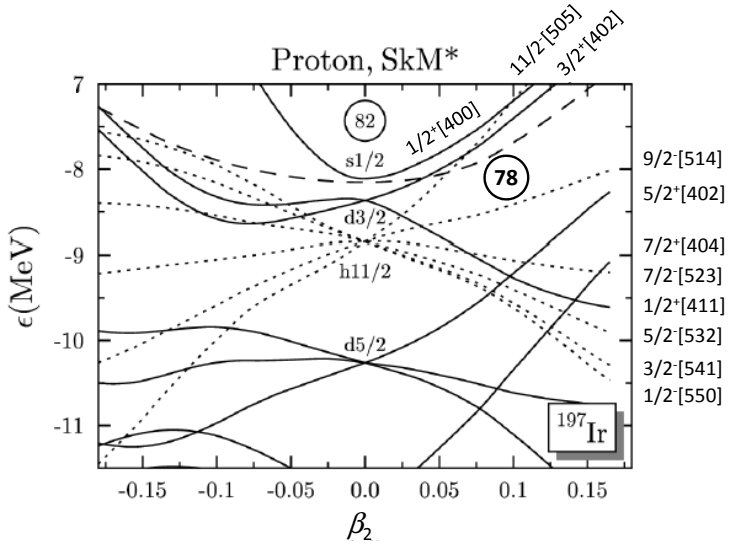

Figure 46: Nilsson diagram for single-proton levels of ^{197}Ir calculated by HFB + SkM* model explained in subsection 5.2.1. The broken line indicates the Fermi-level of ^{197}Ir.

The μ values of odd-A Ir and Au ($Z = 79$) isotopes of $I^\pi = 3/2^+$ are shown in Fig. 47. The evaluated μ value of ^{197}Ir shows the similar systematic trend in gold isotopes. These μ values at $N = 120$ are about two times larger than the values of the lighter odd-A isotopes which are close to the Schmidt value of of $\pi d_{3/2}$ orbit, $\mu = 0.124\ \mu_N$. The larger μ suggests the larger deformation of ^{197}Ir and ^{199}Au.

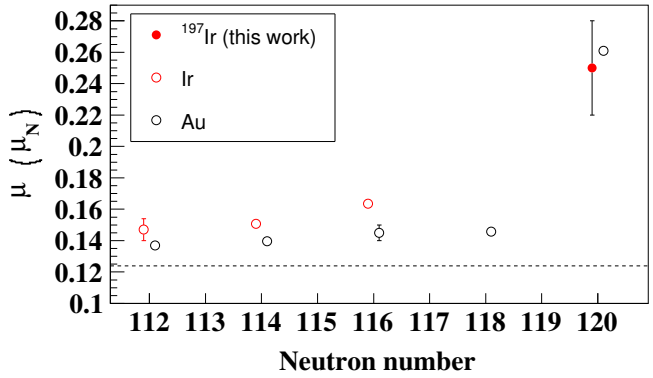

Figure 47: The μ values of iridium and gold isotopes with $N = 112$–120. Plotted μ values are the same with those in Table 10. The dashed line indicates the Schmidt value of $\pi d_{3/2}$ orbit, $\mu = 0.124\ \mu_N$.

5.4 Semi-empirical magnetic moments of ^{196}Ir and ^{198}Ir

The magnetic dipole moment of odd-odd nucleus is expressed by the linear combination of wave-functions of the valence proton and neutron as [117]

$$\mu = \frac{1}{2}\left[(g_p + g_n)I + (g_p - g_n)\frac{j_p(j_p+1) - j_n(j_n+1)}{I+1}\right], \tag{78}$$

where $g_{p,n}$ and $j_{p,n}$ are g-factor and angular momentum of the valence proton and neutron. The derivation of above equation is described in Appendix D. Semi-empirical magnetic moment is calculated by using the experimental g-factors of the nuclei with the same odd-proton or -neutron number. The experimental μ (μ_{exp}) values and semi-empirical μ (μ_{emp}) values were compared in Refs. [117, 118] to show the validity of μ_{emp}. In these references, the μ_{emp} values were in agreement with μ_{exp} values within the margin of 45%.

For ^{196}Ir and ^{198}Ir, $\pi h_{11/2}$ and $\pi d_{3/2}$ orbits for valence proton and $\nu i_{13/2}$, $\nu p_{3/2}$, $\nu f_{5/2}$, and $\nu p_{1/2}$ orbits for valence neutron were considered to calculate the μ_{emp} from the assumption of a single-particle orbit of the shell model as shown in Fig. 48.

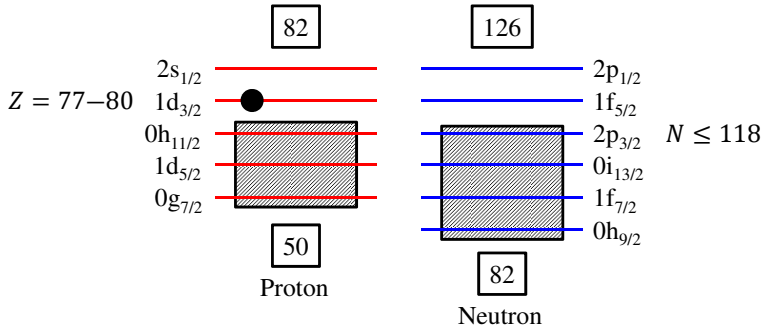

Figure 48: Single-particle orbits with the shell model description in the region of $50 \leq Z \leq 82$ and $82 \leq N \leq 126$.

The neighboring nuclei of ^{196}Ir ($Z = 77$, $N = 119$) and ^{198}Ir ($N = 121$) are ^{195}Ir ($N = 118$), ^{197}Ir ($N = 120$), ^{195}Os ($Z = 76$, $N = 119$), and ^{197}Os ($N = 121$). However, the μ_{exp} values of these isotopes have not been measured previously. Instead of these nuclei, the μ_{exp} values listed in Table 24 of ^{191m}Ir ($N = 114$, $I^\pi = 11/2^-$, $E_{ex} = 171$ keV), ^{193}Ir ($N = 116$, $I^\pi = 3/2^+$), ^{195m}Pt ($Z = 78$, $N = 117$, $I^\pi = 13/2^+$, $E_{ex} = 259$ keV), ^{193}Os ($N = 117$, $I^\pi = 3/2^-$), ^{195}Pt ($N = 117$, $I^\pi = 1/2^-$), and ^{199}Pt ($N = 121$, $I^\pi = 5/2^-$) were applied for the semi-empirical calculations.

Table 24: The $\mu_{\rm exp}$ values of ^{191m}Ir, ^{193}Ir, ^{193}Os, ^{195m}Pt, ^{195}Pt, and ^{199}Pt.

Nuclide	Z	N	I^π	$\mu_{\rm exp}$ ($\mu_{\rm N}$)	Corresponding single-particle orbit	Ref.
^{191m}Ir ($E_{\rm ex}$ = 171 keV)	77	114	$11/2^-$	+6.03(4)	$\pi h_{11/2}$	[24]
^{193}Ir	77	116	$3/2^+$	+0.1636(6)	$\pi d_{3/2}$	[98]
^{195m}Pt ($E_{\rm ex}$ = 259 keV)	78	117	$13/2^+$	−0.606(15)	$\nu i_{13/2}$	[24]
^{193}Os	76	117	$3/2^-$	+0.730(2)	$\nu p_{3/2}$	[119]
^{199}Pt	78	121	$5/2^-$	+0.75(8)	$\nu f_{5/2}$	[102]
^{195}Pt	78	119	$1/2^-$	+0.60952(6)	$\nu p_{1/2}$	[120]

The μ values of iridium isotopes with $I^\pi = 3/2^+$ are gradually increasing from μ = +0.147(7) $\mu_{\rm N}$ with $N = 112$ to μ = +0.1636(6) $\mu_{\rm N}$ with $N = 116$. The trend is the similar to from μ = +0.1369(9) $\mu_{\rm N}$ with $N = 112$ to μ = +0.145746(9) $\mu_{\rm N}$ with $N = 118$ for the gold isotopes. The μ values do not change drastically in this neutron number range of iridium and gold isotopes. Thus, it is expected that the μ value of ^{195}Ir is similar to that of ^{193}Ir. Namely, the experimental g-factor of ^{193}Ir can be used as $g_{\rm p}$ instead of that of ^{195}Ir.

5.4.1 Check the validity of the semi-empirical calculations for gold isotopes

The comparisons between the $\mu_{\rm exp}$ and $\mu_{\rm emp}$ were performed for ^{194}Au, ^{196}Au, and ^{198}Au. The results are summarized in Table 25. The most proper $\mu_{\rm emp}$ is obtained from the comparison with the $\mu_{\rm exp}$ by assuming the proton and neutron orbits listed in Table 25. The $\mu_{\rm emp}$ values are in good agreement with the $\mu_{\rm exp}$ values within the margin of 25%.

5.4.2 Estimations of spin values and wave-functions for ^{196,198}Ir

We calculated the $\mu_{\rm emp}$ values of odd-odd ^{194}Ir and ^{196,198}Ir whose $\mu_{\rm exp}$ values were measured in previous study [124] and in the present experiments, respectively. The $\mu_{\rm emp}$ values were calculated by using the $\mu_{\rm exp}$ values listed in Table 24, and are listed in Table 26. The $\mu_{\rm emp}$ value of ^{194}Ir calculated with the assumptions of $I^\pi = 1^-$ and neutron orbit $\nu p_{3/2}$ or $\nu f_{5/2}$ is in agreement with the $\mu_{\rm exp}$ = +0.39(1) $\mu_{\rm N}$. This result indicates that the semi-empirical model can predict the most proper I^π and wave-function from the comparison between the $\mu_{\rm exp}$ and $\mu_{\rm emp}$ for ^{194}Ir. In the cases of ^{196,198}Ir, the agreements of $\mu_{\rm emp}$ and $\mu_{\rm exp}$ within the margin of factor two of $\mu_{\rm exp}$ are found with the following configurations for each isotopes: $I^\pi = 1^-[\pi d_{3/2} \otimes \nu p_{3/2}]$, $I^\pi = 1^-[\pi d_{3/2} \otimes \nu f_{5/2}]$, $I^\pi = 2^-[\pi d_{3/2} \otimes \nu p_{3/2}]$, $I^\pi = 2^-[\pi d_{3/2} \otimes \nu f_{5/2}]$, and $I^\pi = 3^-[\pi h_{11/2} \otimes \nu i_{13/2}]$ for ^{196}Ir, and $I^\pi = 1^-[\pi d_{3/2} \otimes \nu p_{3/2}]$ for ^{198}Ir. There are many candidates for the configuration of ^{196}Ir from the comparison of $\mu_{\rm emp}$ and $\mu_{\rm exp}$. But, the configurations of ^{196}Ir are restricted to $I^\pi = 1^-[\pi d_{3/2} \otimes \nu p_{3/2}]$ and $I^\pi = 1^-[\pi d_{3/2} \otimes \nu f_{5/2}]$ by accounting for the suggested first-forbidden decay in the previous β-decay studies [103, 104], and the χ^2 analysis of the HFS spectrum in the present study.

When the experimental $g_{\rm p}$ of ^{197}Ir was used instead of ^{193}Ir, the values of $\mu_{\rm emp}$ changed about ±10%. This variation doesn't change the above conclusion about the most probable spin and configurations.

Table 25: The $\mu_{\rm exp}$ and $\mu_{\rm emp}$ values of ^{194}Au, ^{196}Au, and ^{198}Au ($Z = 79$).

Nuclide	^{194}Au	^{196}Au	^{198}Au
N	115	117	119
I^π	1^-	2^-	2^-
orbit	$\pi d_{3/2}$ $\nu p_{3/2}$	$\pi d_{3/2}$ $\nu p_{1/2}$	$\pi d_{3/2}$ $\nu p_{1/2}$
Neighboring nuclei and its $\mu_{\rm exp}$ ($\mu_{\rm N}$)	^{193}Au $I^\pi = 3/2^+$ +0.1396(5) [32]	^{195}Au $I^\pi = 3/2^+$ +0.145(5) [31]	^{197}Au $I^\pi = 3/2^+$ +0.145746(9) [121]
	^{195}Pt $Z = 78$, $N = 117$ $I^\pi = 3/2^-$, $E_{\rm ex} = 211$ keV +0.16(3) [122]	^{197}Hg $Z = 80$, $N = 117$ $I^\pi = 1/2^-$ +0.5273744(9) [123]	^{199}Hg $Z = 80$, $N = 119$ $I^\pi = 1/2^-$ +0.5058855(9) [24]
$\mu_{\rm emp}$ ($\mu_{\rm N}$)	+0.10	+0.72	+0.65
$\mu_{\rm exp}$ ($\mu_{\rm N}$)	+0.0763(13) [32]	+0.580(15) [31]	+0.64(2) [31]

Table 26: The $\mu_{\rm exp}$ and $\mu_{\rm emp}$ values of ^{194}Ir, ^{196}Ir, and ^{198}Ir. The $\mu_{\rm exp}^{196}$ and $\mu_{\rm exp}^{198}$ values were taken from Tables 15 and 17, respectively. The $\mu_{\rm exp}^{194}$ value was taken from Ref. [24]. The positive $\mu_{\rm exp}^{196}$ and $\mu_{\rm exp}^{198}$ values with $I^\pi = 1^-$ are listed as the most probable candidates from the reduced χ^2 fitting results.

I^π	Orbit	$\mu_{\rm emp}$ ($\mu_{\rm N}$)	$\mu_{\rm exp}^{194}$ ($\mu_{\rm N}$)	$\mu_{\rm exp}^{196}$ ($\mu_{\rm N}$)	$\mu_{\rm exp}^{198}$ ($\mu_{\rm N}$)
1^-	$\pi h_{11/2}$, $\nu i_{13/2}$	-3.36	+0.39(1)	$+0.23 \pm 0.03$	$+0.15^{+0.02}_{-0.03}$
	$\pi d_{3/2}$, $\nu p_{3/2}$	+0.30			
	$\pi d_{3/2}$, $\nu f_{5/2}$	+0.44			
	$\pi d_{3/2}$, $\nu p_{1/2}$	-0.17			
2^-	$\pi h_{11/2}$, $\nu i_{13/2}$	-1.57	-	$+0.27 \pm 0.03$ -0.28 ± 0.04	$\pm 0.19 \pm 0.02$
	$\pi d_{3/2}$, $\nu p_{3/2}$	+0.60			
	$\pi d_{3/2}$, $\nu f_{5/2}$	+0.57			
	$\pi d_{3/2}$, $\nu p_{1/2}$	+0.77			
3^-	$\pi h_{11/2}$, $\nu i_{13/2}$	-0.43	-	$+0.29^{+0.04}_{-0.03}$ $-0.29^{+0.04}_{-0.05}$	$+0.20 \pm 0.02$ -0.19 ± 0.02
	$\pi d_{3/2}$, $\nu p_{3/2}$	+0.89			
	$\pi d_{3/2}$, $\nu f_{5/2}$	+0.74			

5.5 Summary of the discussions

We evaluated the absolute values of β_2 from the measured isotope shifts by assuming the quadrupole-deformed nucleus. The shape transition from the prolate shape for ^{196}Ir to the oblate shape for ^{197}Ir is suggested from the comparison of $|\beta_2|$ values evaluated in the present work and calculated ones by the FRDM model. On the other hand, the

prolate shape is suggested for ^{197}Ir from the systematic level orders of low-lying states. To craftily the shape transition, we need to determine the sign of β_2. The sign of β_2 will be determined in the further measurement of the electric quadrupole moment Q by laser spectroscopy with high resolution.

The evaluated μ and $|\beta_2|$ were compared with the theoretical results by the HFB + SkM* calculation and shell model calculation. No theoretical results which reproduces the both of μ and $|\beta_2|$ were obtained. It would be due to the unsuitable interactions for the neutron-rich iridium isotopes.

From the comparison of experimental and empirical μ values for ^{196,198}Ir, the most probable spin values and configurations are suggested to be $I^\pi = 1^-[\pi \mathrm{d}_{3/2} \otimes \nu \mathrm{p}_{3/2}$ or $\nu \mathrm{f}_{5/2}]$ for ^{196}Ir and $I^\pi = 1^-[\pi \mathrm{d}_{3/2} \otimes \nu \mathrm{p}_{3/2}]$ for ^{198}Ir. The obtained most probable spin values from the comparison are in agreement with those suggested from the analyses of the measured HFS spectra.

6 Summary and outlook

6.1 Summary

More than half of the elements heavier than iron are originated from the rapid neutron capture process (r-process) in the explosive astrophysical phenomena such as core-collapse supernovae and neutron star merger. The waiting point nuclei with proton number $Z \sim 70$ and neutron magic number $N = 126$ are considered to be the origin of the third peak in the observed solar r-abundance pattern. The nuclear properties such as β-decay half-lives, masses, and β-delayed neutron emission probabilities of the waiting point nuclei are essential to understand the astrophysical environment of the r-process. However, it is difficult to produce them at the present facilities in the world because these nuclei are located far from the stability line ($\Delta N \sim +20$). Therefore, the reliable theoretical models to predict the nuclear properties of them are required. The predicted half-lives for the $N = 126$ nuclei by various theoretical models deviate more than one order of magnitude due to the competition of FF and GT β-decays. The systematic experimental studies of nuclear structure even for heavier nuclei than waiting point nuclei are important to improve the accuracies of the theoretical predictions.

The nuclear wave-function determines the dominant β-decay mode. The nuclear wave-function can be estimated from the nuclear electromagnetic (EM) moments. The EM moments are directly deduced from the hyperfine structures (HFS) measured by laser spectroscopy. In laser spectroscopy, the variation of the center of gravity frequency of HFS between different isotopes (isotope shift) is also deduced. From the isotope shift, the variation of the nuclear mean-square charge radius and quadrapole deformation parameter between different isotopes can be deduced. The deformation parameter is important parameter to estimate a deformed nuclear wave-function.

The measurement of EM moments for the neutron-deficient isotopes with $Z = 77, 78, 79$ by laser spectroscopy were performed at ISOLDE/CERN and ISOCELE/IPN. These isotopes were produced from the β^+/EC- or α-decay of the mercury ($Z = 80$) isotopes. On the other hand, there are almost no measurements for the neutron-rich isotopes, which can be produced by the nuclear reactions at in-flight facilities, due to the difficulties of the low-energy beam production for the laser spectroscopy. It is also difficult to extract the refractory elements from an ion source using thermal diffusion of reaction products from a production target. Therefore, we performed the HFS measurement of $^{196-198}$Ir ($Z = 77$, $N = 119$–121) by in-gas-cell laser ionization spectroscopy as the first step of systematic nuclear structure study for neutron-rich nuclei with $Z \sim 77$ at KEK isotope separation system (KISS).

The neutron-rich nuclei with $Z \sim 77$ can be produced by the multi-nucleon transfer (MNT) reactions of ^{136}Xe beam ($Z = 54$, $N = 82$, 9.4 MeV/nucleon) and ^{198}Pt target ($Z = 78$, $N = 120$, 12.5 mg/cm^2). KISS is the only experimental device that can extract the neutron-rich nuclei of refractory elements produced by the MNT reactions. KISS consists of a laser ion source combined with an argon gas cell to thermalize the target-like fragments (TLF) of the MNT product and an on-line isotope separator (ISOL). The TLFs are ionized in the gas cell element-selectively by the laser resonance ionization, and mass number A of the ions are separated by the ISOL system. The extracted ions of single nuclide are transported to a detector system for β-γ spectroscopy. The HFS measurement of unstable nuclei can be performed at KISS by counting the β-rays emitted from the laser-ionized nuclei as a function of excitation laser wavelength. The HFS spectrum is observed as one broad peak mainly due to the large pressure broadening by high gas cell pressure. Even though it is feasible to deduce the nuclear magnetic dipole moment and isotopes

shift which determine the peak width and position of the HFS spectrum, respectively.

The nuclear magnetic dipole moments (μ) and isotope shifts of $^{196-198}$Ir were evaluated from the analyses of the measured HFS spectra. The evaluated magnetic moment of ^{197}Ir ($N = 120$ and spin-parity value $I^\pi = 3/2^+$), $\mu = +0.25 \pm 0.03$ μ_N, is in good agreement with the previous studied $\mu = +0.261(2)$ μ_N of ^{199}Au ($Z = 79$, $N = 120$, and $I^\pi = 3/2^+$), which has the same proton orbit and the number of neutron. This result is consistent with the systematic trend of μ between the iridium and gold isotopes in the lighter odd-A. In the cases of ^{196}Ir ($N = 119$ and $I^\pi = (0, 1)^-$) and ^{198}Ir ($N = 121$ and $I^\pi =$ unknown), it is strongly suggested to be $I^\pi \geq 1$ from the smaller reduced χ^2 values for the fittings in the measured HFS spectra than that obtained with the assumption of $I = 0$. The μ values of $+0.23 \pm 0.03$ μ_N for ^{196}Ir and $+0.15^{+0.02}_{-0.03}$ μ_N for ^{198}Ir were obtained with the spin assumption of $I = 1$ as the best fitting results.

The variation of the nuclear mean-square charge radius $\delta\langle r_c^2\rangle^{AA'}$ and absolute value of the quadrapole deformation parameter $|\beta_2|$ were deduced from the evaluated isotope shift. The $\delta\langle r_c^2\rangle^{AA'}$ values based on ^{191}Ir were evaluated to be $\delta\langle r_c^2\rangle^{191,A'} = +0.18 \pm 0.03$, $+0.26 \pm 0.03$, and $+0.23 \pm 0.03$ fm^2 for ^{196,197,198}Ir, respectively. In the same way with the previous studies, the $|\beta_2|$ values were calculated by using the $\beta_2 = +0.155$ of ^{191}Ir predicted by the FRDM model as $|\beta_2| = 0.129 \pm 0.009$, 0.14 ± 0.01, and 0.11 ± 0.01 fm^2 for ^{196,197,198}Ir, respectively. The trend of evaluated $|\beta_2|$ is consistent with that predicted by the FRDM model which suggests the prolate shape ($\beta_2 > 0$) for $A \leq 196$ isotopes and oblate shape ($\beta_2 < 0$) for $A \geq 197$ isotopes.

The evaluated μ, $|\beta_2|$, and $\delta\langle r_c^2\rangle$ values were compared with the theoretical results by HFB + SKM* calculation and shell model calculation with KHHE interaction. In the HFB + SkM* calculation, the $|\beta_2|$ and $\delta\langle r_c^2\rangle$ values agree with the experimental values within a factor of 1.2. However, the theoretical μ values are more than two times larger than the experimental values. For the improvement of the accuracy of μ prediction, which strongly depends on the spin-isospin interaction, it would be required to develop the interaction as to reproduce physical parameters relevant to the spin-isospin interaction. In the shell model calculation, the theoretical values for $^{196-198}$Ir were calculated as the hole state from ^{208}Pb with the KHHE interaction. Due to the huge number of holes, the calculation were performed with a restricted model space for ^{196,197}Ir. The reliability of the restriction is not sure. Also in the shell model calculation, there were not found the agreements about the μ and $|\beta_2|$ simultaneously between the experimental and theoretical results for all isotopes.

The oblate shape for ^{197}Ir is suggested by the FRDM model, HFB + SkM* calculation, and shell model calculation. The odd-A iridium isotopes with $A = 187$–197 have the similar structure of the three low-lying excited states: the ground state of $3/2^+[402]$, low-lying excited state of $I^\pi = 1/2^+$ which is considered as the mixture state of $1/2^+[400]$ and γ-vibration of the ground state, and isomeric state of $11/2^-[505]$. From the systematics of these states, odd-A iridium isotopes with $A = 187$–197 are considered to be prolate shape. Also in the previous laser spectroscopy, prolate shape was suggested for the odd-A iridium isotopes with $A = 187$–193. The precise HFS measurement with high resolution laser spectroscopy makes possible to deduce a nuclear electric quadrupole moment which is needed to identify the sign of β_2. Then, the shape transition in iridium isotopes will be revealed.

To estimate the most probable I^π values and valence nucleon orbits of ^{196,198}Ir, the evaluated μ values were compared with the semi-empirical μ values calculated by using the experimental g-factors of the neighboring nuclei, whose valence nucleons would have the same neutron or proton orbit with ^{196,198}Ir. The experimental μ values are reproduced

with the assumption of $I^\pi = 1^-$ for both isotopes. The configurations of nuclear wave-functions are suggested to be $I^\pi = 1^-$ [πd3/2 $\otimes$ νp3/2 or νf5/2] for ^{196}Ir and $I^\pi = 1^-$ [πd3/2 $\otimes$ νp3/2] for ^{198}Ir.

6.2 Outlook

From the in-gas-cell laser resonance ionization spectroscopy, we deduced the μ and $|\beta_2|$ values with a precision of 10% for $^{196-198}$Ir, and obtained the most probable $I^\pi = 1^-$ for ^{196,198}Ir. It is essential to determine the sign of β_2 from the measurement of nuclear electric quadrupole moment to reveal the shape transition in iridium isotopes. For this precise measurements, there are three requirements as follows: HFS measurement by laser spectroscopy with high resolution , low-background β-ray detector, and multi-reflection time-of-flight mass spectrograph (MR-TOF) for high-precision mass separation as to separate the ground and isomer states.

In-gas-jet laser ionization spectroscopy

Electric quadrupole moment Q of a nucleus with $I > 1/2$ causes energy shift of about 200 MHz in addition to the energy shift (hundreds MHz to a few GHz) of HFS by nuclear magnetic dipole moment. The HFS measurement with a resolution of 300 MHz is required to determine the Q with a precision of 10%. In the present in-gas-cell laser ionization spectroscopy, the resolution was about 11 GHz due to the Doppler broadening (300 K), pressure broadening (74 kPa), and the linewidth of the dye laser (3.4 GHz). In-gas-jet laser ionization spectroscopy is effective to suppress the Doppler and pressure broadening [72]. The laser ionization is performed in the gas-jet, which has uniform velocity along the beam axis, formed by the Laval nozzle as shown in Fig. 49. In KISS, the gas temperature and pressure in the gas-jet are estimated to be about 12 K and 20 Pa, respectively, as shown in Table 27. The Doppler and pressure broadening are reduced by a factor of $\sim$1/5 and $\sim$1/100, respectively. Moreover, we have plan to construct the new excitation laser system consists of a narrow-band CW diode laser as a seed laser for a dye amplifier pumped by an intense Nd:YAG laser with 10 kHz repetition rate for high-efficiency in-gas-jet laser ionization spectroscopy. The typical linewidth of the new laser system is 90 MHz [72]. We plan to perform the laser spectroscopy with a resolution of 300 MHz in the near future.

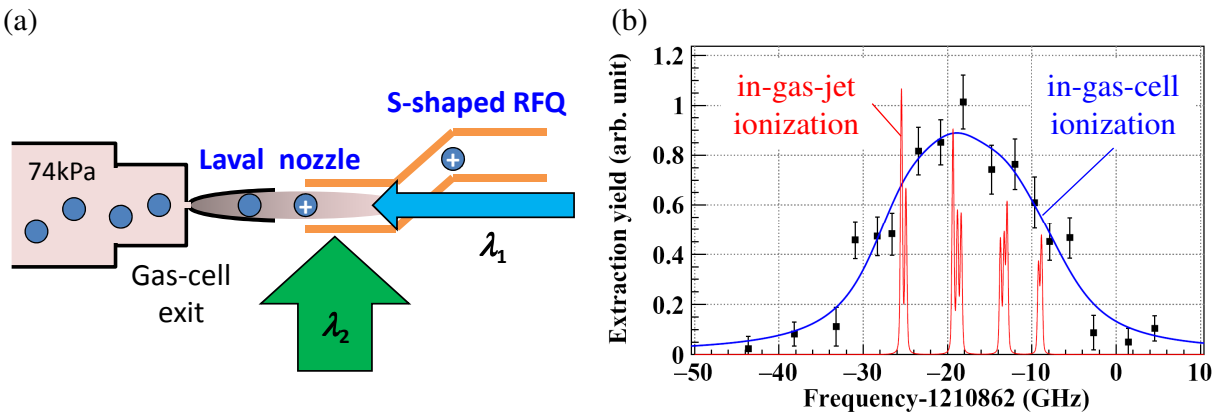

Figure 49: Schematic view of in-gas-jet laser ionization spectroscopy at KISS (a) and the expected HFS spectrum of ^{197}Ir (b).

Table 27: Comparison of the parameters and widths in FWHM between in-gas-cell and -jet laser ionization spectroscopy. The laser linewidth of 90 MHz, which is shown in the table, will be achieved by using a newly installed dye amplifier seeded by the narrow-band CW diode laser.

Parameter	in-gas-cell	in-gas-jet
Temperature (K)	300	12
Doppler width (MHz)	941	213
Laser linewidth (MHz)	90	90
Gas pressure (kPa)	74	0.022
Pressure broadening (MHz)	8034	62
Natural width (MHz)	16	16
Lorentz width (MHz)	8050	78
Total width (MHz)	8168	276

Low-background gas counter

To perform β-decay spectroscopy and a HFS measurement for more neutron-rich and lower yield nuclei, it is essential to reduce the background rate of the β-ray detector. In the present β-ray detector, approximately two-dimensional position detection are achieved by the multi-segmented proportional gas counter. The three dimensional position detection can be achieved by identifying the longitudinal hit position of β-ray, which is realized by replacing the material of anode wire from Be-Cu to resistive carbon. We expects that the carbon wire of 10 μm in diameter makes possible the longitudinal position resolution of 2 mm in FWHM [125], and, therefore, the background rate can be suppressed down to 0.01 cps. The laser ionization spectroscopy of ^{199}Ir ($N = 122$) and ^{198}Os ($Z = 76, N = 122$) produced by the MNT reaction of ^{136}Xe + ^{198}Pt system can be performed.

Installation of the MR-TOF

In general, an isomeric state is reported to exist at the excitation energy of a few hundreds keV in the nuclei of Hf–Pt region. Therefore, the measured HFS spectrum would include the HFS of ground and isomeric states because these states cannot be separated by the KISS mass separator (dipole magnet) with a mass resolving power of $M/\Delta M = 900$. Two HFS should be considered in the analysis, and, therefore, this causes the large uncertainties for the deduced magnetic moments and isotope shifts. We have plan to install the MR-TOF [126] to perform the direct mass measurement for the neutron-rich nuclei of Hf–Pt region. The MR-TOF, which is applicable to short-lived nuclei, can measure the nuclear mass with high-precision (typically a order of 10^{-6}). We can select the ground or isomeric state by using the MR-TOF. Then, the HFS measurement by counting the number of laser-ionized and mass-selected nuclei as a function of laser wavelength of λ_1 is performed by using an ion detector placed at downstream of the MR-TOF. Therefore, the HFS measurement can be done efficiently without waiting of β-decays of unstable nuclei.

References

[1] E.M. Burbidge et al., Rev. of Mod. Phys. 29 (1957) 547.

[2] H. Grawe et al., Rep. Prog. Phys. 70 (2007) 1525.

[3] L. R. Buchmann et al., Nucl. Phys. A 777 (2006) 254.

[4] F. Käppeler et al., Nucl. Phys. A 777 (2006) 291.

[5] E.M. Burbidge et al., Rev. Mod. Phys. 29 (1957) 547.

[6] C. Freiburghaus et al., Astrophys. Jour. 525 (1999) L121.

[7] K.L. Kratz et al., Astrophys. Jour. 403 (1993) 216.

[8] B.P. Abbott et al., Phys. Rev. Lett. 119 (2017) 161101.

[9] E. Pian et al., Nature 551 (2017) 67.

[10] M.R. Drout et al., Science 358 (2017) 1570.

[11] J.M. Pearson, et al., S Phys. Lett. B 387 (1996) 455.

[12] P. Möller, At. Data and Nucl. Data Tables 109-110 (2016) 1.

[13] G. Lorusso et al., Phys. Rev. Lett. 114 (2015) 192501.

[14] H. Kura et al., Pog. thor. Phys. 113 (2005) 305.

[15] http://wwwndc.jaea.go.jp/CN14/index.html.

[16] P. Möller, Phys. Rev. C 67 (2003) 055802.

[17] http://t2.lanl.gov/nis/molleretal/publications/rspeed2002.html.

[18] T. Suzuki et al., Phys. Rev. C 85 (2012) 015802.

[19] I.N. Borzov, Nucl. Phys. A 777 (2006) 645.

[20] I.N. Borzov, Phys. At. Nucl. 74 (2011) 1435.

[21] http://www.nndc.bnl.gov.

[22] M. Mumpower et al., AIP ADVANCES 4 (1024) 041009.

[23] S. Chiba, private communication (2009).

[24] N.J. Stone, IAEA Vienna Report No. INDC(NDS)-0658 (2014).

[25] S.A. Ahmad et al., Nucl. Phys. A 483 (1988) 244.

[26] D. Verney et al., Eur. Phys. J. A 30 (2006) 489.

[27] Th. Hilberath et al., Z. Phys. A - Hadron and Nuclei 342 (1992) 15.

[28] U. Krönert et al., Z. Phys. A - Atomic Nuclei 331 (1988) 521.

[29] F. Le Blanc et al., Phys. Rev. Lett. 79 (1997) 2213.

[30] K. Wallmeroth et al., Nucl. Phys. A 493 (1989) 224.

[31] G. Savard et al., Nucl. Phys. A 512 (1990) 241.

[32] G. Passler et al., Nucl. Phys. A 580 (1994) 173.

[33] G. Ulm et al., Z. Phys. A - Atomic Nuclei 325 (1986) 247.

[34] S. Frauendorf et al., Phys. Lett. 55B (1975) 365.

[35] Zs. Podolyák et al., J. Phys. Conf. Ser. 381 (2012) 012052.

[36] T. Kubo et al., Nucl. Instrum. and Meth. B 204 (2003) 97.

[37] H. Geissel et al., Nucl. Instrum. and Meth. B 70 (1992) 286.

[38] A. Gottberg, Nucl. Instrum. and Meth. B 376 (2016) 8.

[39] P. Bricault, Eur. Phys. J. Special Topics 150 (2007) 227.

[40] C.H. Dasso et al., Phys. Rev. Lett. 74 (1994) 1907.

[41] Y.X. Watanabe et al., Phys. Rev. Lett. 115 (2016) 172503.

[42] V. Zagrebaev et al., Phys. Rev. Lett. 101 (2008) 122701.

[43] T. Kurtukian-Nieto et al., Phys. Rev. C 89 (2014) 024616.

[44] E. Kugler et al., Nucl. Instrum. and Meth. B 70 (1992) 41.

[45] P.G. Bricault et al., Nucl. Instrum. and Meth. B 126 (1997) 231.

[46] J. Kurcewicz et al., Phys. Lett. B 717 (2012) 371.

[47] http://www.nishina.riken.jp/RIBF/BigRIPS/intensity.html.

[48] G.W.F. Drake, Springer Handbook of Atomic, Molecular, and optical Physics (Springer-Verlag New York, 2006).

[49] W.R. Johnson, Atomic Structure Theory, lectures on Atomic Physics (Springer-Verlag Berlin Heidelberg, 2007).

[50] N. Yamanaka, Phys. Lett. A 243 (1998) 132.

[51] K. Heilig et al., At. data Nucl. Data Tables 14 (1974) 613.

[52] C.F. Fischer and L. Smentek-Mielczarek, J. Phys. B: At. Mol. Phys. 16 (1983) 3479.

[53] L.A. Bloomfield et al, Phys. Rev. A 27 (1983) 2261.

[54] J. Bauche, LE JOURNAL DE PHYSIQUE. 35 (1974) 19.

[55] P. Palmeri et al., J. Quant. Spectros. Radia. Transfer 185 (2016) 70.

[56] G. Torbohm, B. Fricke and A. Rósen, Phys. Rev. A 31 (1985) 2038.

[57] E.C. Seltzer, Phys. Rev. 188 (1969) 1916.

[58] P. Aufmuth and E. Wöbker, Z. Phys. A - Atoms and Nuclei 321 (1985) 65.

[59] W.H. King, Isotope Shifts in Atomic Spectra (Plenum, London, 1984).

[60] W.D. Myers et al., Nucl. Phys. A 410 (1983) 61.

[61] Yu. Kudryavtsev et al., Nucl. Instrum. and Meth. B 204 (2003) 336.

[62] Yu. Kudryavtsev et al., Nucl. Instrum. and Meth. B 114 (1996) 350.

[63] Yu. Kudryavtsev et al., Nucl. Instrum. and Meth. B 179 (2001) 412.

[64] Yu. Kudryavtsev et al., Nucl. Instrum. and Meth. B 267 (2009) 2908.

[65] L. Weissman et al., Nucl. Instrum. and Meth. A 423 (1999) 328.

[66] R. Ferrer et al., Phys. Lett. B 728 (2014) 191.

[67] T.E. Cocolios et al., Phys. Rev. C 81 (2010) 014314.

[68] C. Granados et al., Phys. Rev. C 96 (2017) 054331.

[69] Ingolf V. Hertel and Claus-Peter Schulz, Atoms, Molecules and Optical Physics 1: Atoms and Spectroscopy (Springer-Verlag Berlin Heidelberg, 2015)

[70] J.J. Olivero et al., JQSRT 17 (1977) 233.

[71] T. Sonoda et al., Nucl. Instrum. and Meth. B 267 (2009) 2918.

[72] Yu. Kudryavtsev et al., Nucl. Instrum. and Meth. B 297 (2013) 7.

[73] R. Ferrer et al., Nucl. Instrum. and Meth. B 317 (2013) 317.

[74] Y. Hirayama et al., J. Phys. B: At. Mol. Opt. Phys. 50 (2017) 215203.

[75] M.L. Citron et al., Phys. Rev. A 16 (1977) 1507.

[76] U. Köster et al., Phys. Rev. C 84 (2011) 034320.

[77] L. Weissman et al., Phys Rev. C 65 (2002) 024315.

[78] N.J. Stone et al., Phys. Rev. C 77 (2008) 067302.

[79] Y. Hirayama et al., Nucl. Instrum. and Meth. B 412 (2017) 11.

[80] K. Okuno, J. Phys. Soc. Jpn. 55 (1986) 1504.

[81] H.J. Xu et al., Nucl. Instrum. and Meth. A 333 (1993) 274.

[82] D. Kaji and K. Morimoto, Nucl. Phys. A 792 (2015) 11.

[83] Y. Hirayama et al., Nucl. Instrum. and Meth. B 353 (2015) 4.

[84] H. Haba et al., J. Nucl. Radiochem. Sci. 8 (2007) 55.

[85] J.F. Ziegler, http://www.srim.org/.

[86] https://www.nist.gov/pml/atomic-spectra-database.

[87] http://www.pmp.uni-hannover.de/cgi-bin/ssi/test/kurucz/sekur.html.

[88] C.H. Corliss et al., NBS Monograph 53 (1962).

[89] Y. Hirayama et al., J. Phys. B: At. Mol. Opt. Phys. 47 (2014) 075201.

[90] M. Mukai et al., JPS Conf. Proc. 6 (2015) 030127.

[91] G. Hausser, Annu. Rev. Nucl. Part. Sci. 45 (1995) 543.

[92] S. Agostinelli et al., Nucl. Instrum. and Meth. A 506 (2003) 250.

[93] S. Kimura et al., Nucl. Instrum. and Meth. B 376 (2016) 338.

[94] M. Mukai et al., Nucl. Instum. and Meth. A 884 (2018) 1.

[95] H. Xiaolong, Nuclear Data Sheets 108 (2007) 1093.

[96] H. Xiaolong, Nuclear Data Sheets 104 (2005) 283.

[97] T. Kurtukian-Nieto et al., Eur. Phys J. A 50 (2014) 135.

[98] K.H. Bürger et al., Phys. Lett. B 140 (1984) 17.

[99] Y. Tanaka et al., Phys. Rev. C 29 (1984) 1830.

[100] https://root.cern.ch.

[101] CERN Program Library entry D506.

[102] Y. Hirayama et al., Phys. Rev. C 96 (2017) 014307.

[103] P.E. Haustein et al., Phys. Rev. C 16 (1977) 1559.

[104] J.F.W. Jansen et al., Nucl. Phys. A 115 (1968) 321.

[105] P. Möller, At. Data and Nucl. Data Tables 59 (1995) 185.

[106] A. Bohr and B.R. Mottelson, Nuclear structure Volume II: Nuclear deformations (World Scientific Publishing Co. Pte. Ltd., 1998)

[107] K. Washiyama, private communication (2017).

[108] J. Bartel et al., Nucl. Phys A 386 (1982) 79.

[109] C. Yuan, private communication (2017).

[110] L. Rydstrom et al., Nucl. Phys. A 512 (1990) 217.

[111] R.H. Price et al., Nucl. Phys. A 176 (1971) 338.

[112] Y. Yamazaki et al., Z. Phys. A 285 (1978) 191.

[113] J.A. Cizewski et al., Phys. Rev. C 27 (1983) 1040.

[114] C. Sébille-Schück et al., Nucl. Phys. A 212 (1973) 45.

[115] R.H. Price et al., Nucl. Phys. A 174 (1971) 497.

[116] R.H. Price et al., Nucl. Phys. A 187 (1972) 641.

[117] R.J. Blin-Stoyle, Rev. Mod. Phys 28 (1956) 75.

[118] S.A. Ahmad et al., Z. Phys. A - Atoms and Nuclei 321 (1985) 35.

[119] R. Eder et al., Phys. Rev. C 40 (1989) 2246.

[120] W.G. Proctor et al., Phys. Rev. 81 (1951) 20.

[121] H. Dahmen et al., Z. Phys. A 200 (1967) 456.

[122] L. Varga et al., Phys. Rev. C 6 (1972) 388.

[123] R.J. Reimann et al., Phys. Rev. C 7 (1973) 2965.

[124] E. Hagn et al., Z. Phys. A - Atoms and Nuclei 306 (1982) 73.

[125] T. Mihara et al., Publ. Astron. Soc. Japan 63 (2011) S623.

[126] P. Schury et al., Nucl. Instrum. and Meth. B 317 (2013) 537.

[127] I. Angeli, At. Data and Nucl. Data Tables 87 (2004) 185.

[128] R. Veenhof, Nucl. Instrum. and Meth. A 419 (1998) 726.

[129] B. Singh, Nuclear Data Sheets 108 (2007) 79.

[130] S. Singh et al., Nucl. Instrum. and Meth. B 51 (1990) 5.

[131] https://physics.nist.gov/cuu/index.html.

Appendix

A King plot

The isotope shift of Eq. (18) is rewritten as

$$\delta\nu_{\rm IS}^{AA'} = \frac{A'-A}{AA'}K_{\rm MS} + F\lambda^{AA'}, \tag{A.1}$$

where

$$\begin{aligned} K_{\rm MS} &= K_{\rm NMS} + K_{\rm SMS}, \\ K_{\rm NMS} &= m_{\rm e}\nu_0, \\ K_{\rm SMS} &= \frac{\delta K_{\rm MP}}{h}. \end{aligned}$$

Here, the parameter F means an electronic factor defined as $F_{\rm e}$ in subsection 2.4.2. The King plot is used to deduce the $K_{\rm MS}$ and F values, and to check the validity of isotope shift measurement. The two types of King plots are shown in Figs. A.1(a) and (b).

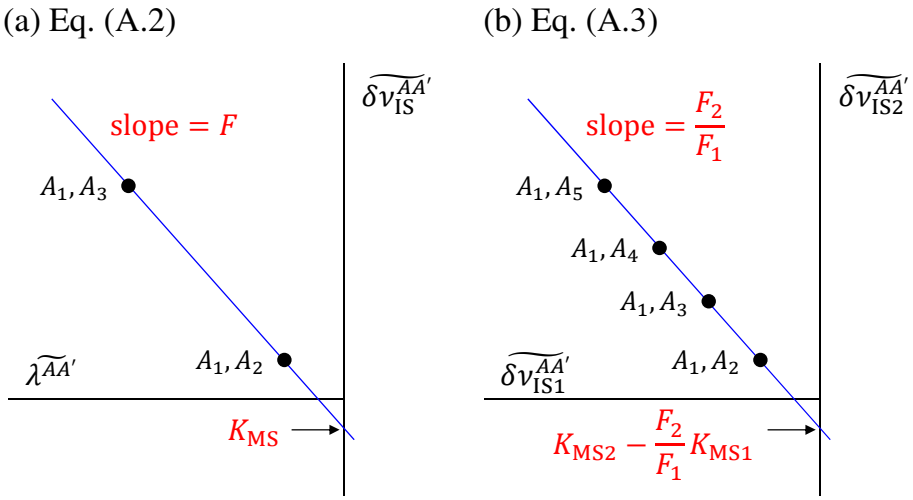

Figure A.1: Two types of King plots. The blue lines in (a) and (b) are expressed by Eq. (A.2) and Eq. (A.3), respectively.

Eq. (A.1) is rewritten as

$$\widetilde{\delta\nu_{\rm IS}^{AA'}} = K_{\rm MS} + F\widetilde{\lambda^{AA'}}, \tag{A.2}$$

where

$$\begin{aligned} \widetilde{\delta\nu_{\rm IS}^{AA'}} &= \frac{AA'}{A-A'}\delta\nu_{\rm IS}^{AA'}, \\ \widetilde{\lambda^{AA'}} &= \frac{AA'}{A'-A}\lambda^{AA'}. \end{aligned}$$

The two-dimensional plot of $\widetilde{\delta\nu_{\rm IS}^{AA'}}$ and $\widetilde{\lambda^{AA'}}$ indicates linear relation as shown in Fig. A.1(a). The $K_{\rm MS}$ and F values are deduced as an intercept and slope, respectively, from the King

plot by using the $\delta\nu_{\rm IS}$ and $\lambda^{AA'}$ values evaluated from the known informations of the stable (or unstable) isotopes. This method is available if at least two isotopes shifts ($\delta\nu_{\rm IS}^{A_1A_2}$ and $\delta\nu_{\rm IS}^{A_1A_3}$) and two nuclear parameters ($\lambda^{A_1A_2}$ and $\lambda^{A_1A_3}$) are known for stable or long-lived isotopes. Here, the measured variation of mean-square charge radius $\delta\langle r_{\rm c}^2\rangle^{AA'}$ by muonic X-ray and elastic electron scattering measurements are used to deduce the $\lambda^{AA'}$ values. The resulting $\delta\langle r_{\rm c}^2\rangle^{AA'}$ values for various isotopes by muonic X-ray, elastic electron scattering, and optical isotope shift measurements are summarized in Ref. [127]. Then, the $\lambda^{AA'}$ values for unstable isotopes are deduced from Eq. (A.2) by applying the deduced $K_{\rm MS}$ and F values and measured $\delta\nu_{\rm IS}^{AA'}$ values.

The $K_{\rm MS}$ and F values can be deduced without using $\lambda^{AA'}$ as follows. When the isotope shifts of a certain AA' pairs for two atomic transitions are known, $\widetilde{\lambda^{AA'}}$ can be deleted as follows:

$$\begin{aligned}
\text{Transition 1} : \widetilde{\delta\nu_{\rm IS1}^{\rm AA'}} &= K_{\rm MS1} + F_1\widetilde{\lambda^{AA'}}, \\
\text{Transition 2} : \widetilde{\delta\nu_{\rm IS2}^{\rm AA'}} &= K_{\rm MS2} + F_2\widetilde{\lambda^{AA'}}, \\
\widetilde{\lambda^{AA'}} &= \frac{1}{F_1}(\widetilde{\delta\nu_{\rm IS1}^{AA'}} - K_{\rm MS1}), \\
\widetilde{\delta\nu_{\rm IS2}^{AA'}} &= \left(K_{\rm MS2} - \frac{F_2}{F_1}K_{\rm MS1}\right) + \frac{F_2}{F_1}\widetilde{\delta\nu_{\rm IS1}^{AA'}}.
\end{aligned} \tag{A.3}$$

There are four unknown parameters F_1, F_2, $K_{\rm MS1}$, and $K_{\rm MS2}$ in Eq. (A.3). From the King plot, the values of $K_{\rm MS2} - \frac{F_2}{F_1}K_{\rm MS1}$ and $\frac{F_2}{F_1}$ are deduced as an intercept and slope of fitted linear function, respectively. If the isotope shifts of four different AA' pairs for the two transitions are available, these unknown parameters can be deduced. When the F_1 and $K_{\rm MS1}$ values for one transition are known, the F_2 and $K_{\rm MS2}$ values can be deduced by using two data points. The linear relation between $\widetilde{\delta\nu_{\rm IS1}^{AA'}}$ and $\widetilde{\delta\nu_{\rm IS2}^{AA'}}$ in Eq. (A.3) and Fig. A.1(b) is applicable to check the consistency of measured isotope shifts by using different transitions.

In the case of iridium, the $\lambda^{AA'}$ values of the isotopes with $A = 191, 193, 196, 197$, and 198 have not been studied previously through the muonic X-ray or elastic electron scattering measurements. Therefore, we cannot deduce the F and $K_{\rm SMS}$ values by using the King plot in Fig. A.1(a). Moreover, the King plot in Fig. A.1(b) is not applicable because the values of four isotopes shifts $\delta\nu_{\rm IS}^{191,193}$, $\delta\nu_{\rm IS}^{191,196}$, $\delta\nu_{\rm IS}^{191,197}$, and $\delta\nu_{\rm IS}^{191,198}$ have not been measured by using the different two excitation transitions. Therefore, we deduced the F value for our transition by using Eq. (45) in subsection 2.4.2.

B Evaluation of nuclear spin value I from the number of hyperfine transitions

The value of nuclear spin I can be determined from the number of hyperfine transitions when the I value is smaller than the initial and final atomic spin J_1 and J_2, namely, $I \leq J_i$ ($i = 1,\ 2$). The number of transitions with the combination of I and $\Delta J = J_2 - J_1$ are summarized in Tables B.1 and B.2 in the cases of $I \leq J_i$ ($i = 1$ and 2) and $I \leq J_i$ ($i = 1$ or 2), respectively.

Table B.1: The number of transitions between HFS of two atomic states with $I \leq J_1$ and J_2. In the case of $|\Delta J| = 0$ with $J_1 = J_2 = I$, the number of transitions is the same as that in the case of $|\Delta J| = 1$ because one forbidden transition with $F_1 = F_2 = 0$ is removed.

$\|\Delta J\|$	Nuclear spin I					
	1/2	1	3/2	2	5/2	3
0	4	7	10	13	16	19
1	3	6	9	12	15	18

Table B.2: The number of transitions between HFS of two atomic states with $I \leq J_1$ and $I > J_2$.

I	J_1	J_2	Number of transitions
1/2	1	0	2
1	1	0	3
1	3/2	1/2	5
3/2	3/2	1/2	6
3/2	2	1	8
2	2	1	9
2	5/2	3/2	11
5/2	5/2	3/2	12
5/2	3	2	14
3	3	2	15
3	7/2	5/2	17

We use the transition with known J_1 and J_2. If the hyperfine peaks are apparently separated in a measured HFS spectrum, the spin value is determined by referring to the above tables. In the case of the broad HFS spectrum, the spin value is suggested from the minimum reduced χ^2 value evaluated from the fitting analysis with the parameter of the nuclear spin value as we performed in subsections 4.5.5 and 4.5.6.

C Multi-segmented proportional gas counter

We developed a high-efficiency and low-background multi-segmented proportional gas counter (MSPGC) [94] for β-decay spectroscopy.

A radioactive ion beam (purity > 99.7%) with an energy of 20 keV is obtained from the KISS facility by applying element-selective laser resonance ionization and a dipole magnetic field for the selection of atomic and mass numbers, respectively. The radioactive ions extracted from the KISS gas cell [79] are implanted on the aluminized Mylar tape which passes through the center of the detector station. β-decay spectroscopy is performed by using β-ray detectors and γ-ray detectors, which surround the tape. The implantation rate of the neutron-rich nuclei is typically less than 10 particles per second (pps). For the precise β-decay spectroscopy, a low-background event rate of 0.01–0.1 counts per second (cps) and high detection efficiency, even for β-rays from low-Q_β emitters at around 1 MeV, are essential for the β-ray detector.

The background events in the signals from the β-ray detector consist of two major parts. First are the electrons produced by Compton scatterings of environmental background γ-rays. The major sources of Compton scatterings are the materials around the detector. The second are muons from secondary cosmic-rays and induced particles by the muons such as electrons and photons. Therefore, the use of low-density materials for the detector would reduce the background events. Tracking of the detected particle enables discrimination of the background events and identification of the β-rays emitted from the implanted tape. The MSPGC has been developed to fulfill the above requirements. The low-density material is also important for keeping high detection efficiency by reducing the energy loss of β-rays in each counter. We report the details of the design work of the MSPGC in section C.1, the performances of the developed MSPGC in section C.2, and a summary in section C.3.

C.1 Details of the MSPGC

A cross-sectional overview of the KISS decay station is shown in Fig. C.1, while a more detailed view of the MSPGC is provided in Fig. C.2. The decay station consisted of the MSPGC, an aluminum vacuum chamber, four super clover germanium detectors, and a beam monitor as shown in Fig. C.1. An aluminized Mylar tape with a width of 12.5 mm and thickness of 12.5 μm passed through the center of the MSPGC. The KISS beam (indicated by a red arrow in Figs. C.1 and C.2) typically had a circular profile with 2 mm diameter in full width at half maximum (FWHM). The radioactive ions extracted from KISS were implanted on the tape.

The MSPGC was installed in an aluminum cylindrical vacuum chamber with an outer diameter of 96 mm and thickness of 1 mm. The four super clover germanium detectors (Canberra, 4-fold 32 segmented super clover HPGe, relative efficiency $\approx$ 38% at 1.332 MeV, hereafter marked as SCGe) were placed at a distance of 4.8 cm from the MSPGC center. The beam monitor (Channeltron for ion counting, hereafter marked as CEM) was placed 10 cm before the tape. The CEM was used to maximize KISS beam transport efficiency at the focal plane, and was then moved to a non-obstructive position to allow for implanting the radioactive ions on the tape.

C.1.1 Design of the MSPGC

The gas-filled area of the MSPGC is indicated by the thick black line in Fig. C.2. The detector gas was Ar (90%) + CH_4 (10%) (hereafter referred to as P10) which is gen-

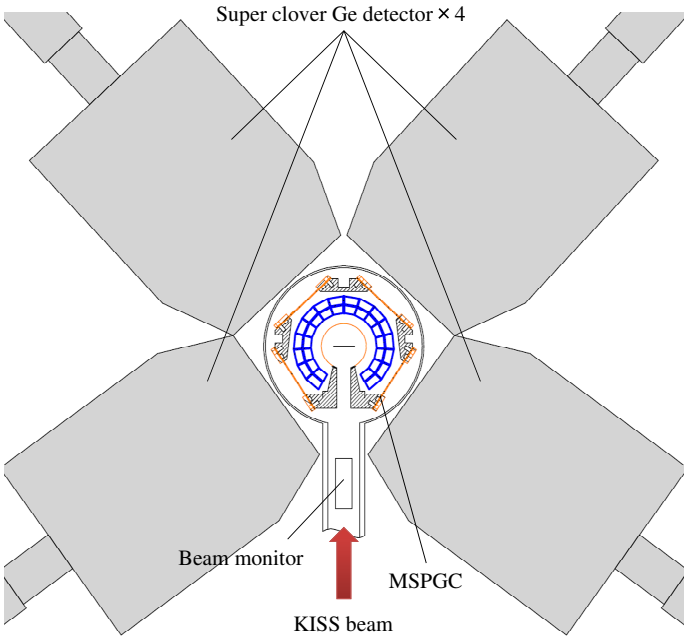

Figure C.1: Cross-sectional view of the detector setup for β-γ spectroscopy at the KISS detector station.

erally used for proportional gas counters. The thick blue lines in Fig. C.2 indicate the trapezoidal-shaped cathode foils of 32 gas counters. Sixteen pairs of counters were arranged cylindrically around the tape in two layers. Hereafter, we refer to the gas counters of the inner (outer) layer as inner (outer) counters. The detailed geometry of one pair is shown in Fig. C.3(a). The cathode of gas counters had a trapezoidal cross-section with approximately 34 or 41 mm^2, respectively, for the inner and outer counters, and an active length of 200 mm. The large length of the counter and its small trapezoidal cross-section allow for the realization of a large solid angle with a distance of 19.5 mm between the MSPGC center and cathode surface of the inner counter. The total solid angle of the 32 counters was 80% of 4π.

The cathode was made of an aluminized Mylar foil with a thickness of 25 μm. The cathode shape was realized by wrapping a flat foil around an aluminum trapezoidal bar, and then using a heat gun to set the creases made along the four edges. At one end of the cathode, a 10 mm long, trapezoidal aluminum support was inserted as shown in Fig. C.3(b). The aluminum supports had a 2.5 mm diameter hole for gas flow and insertion of the anode wire inside an insulating pipe. The inner surface of each cathode foil was glued to an aluminum support using a conductive epoxy. Finally, each support with its cathode foil was affixed to the detector. The anode wire was a 100 μm diameter Be-Cu wire.

The frame of the MSPGC was made of stainless steel. The frame had four large windows (size: 24.3×200 mm^2) to minimize the attenuation of the γ-rays emitted from the implanted radioactive nuclei. The orange-colored parts in Fig. C.2 and Fig. C.3(c) indicate the windows between the gas region and vacuum region. The window foil was an aluminized Mylar foil with a thickness of 25 μm. This was covered by a 0.5 mm thick, 92.5% transmission, stainless steel honeycomb grid [84] to maintain the P10 pressure in the MSPGC on the level of 100 kPa without distorting the shape. The grid was fixed by small screws to the stainless steel frame. The entrance aperture for the KISS beam was 8.5 mm in diameter as shown in Fig. C.2 and Fig. C.3(c). This was sufficiently large to transport the KISS beam.

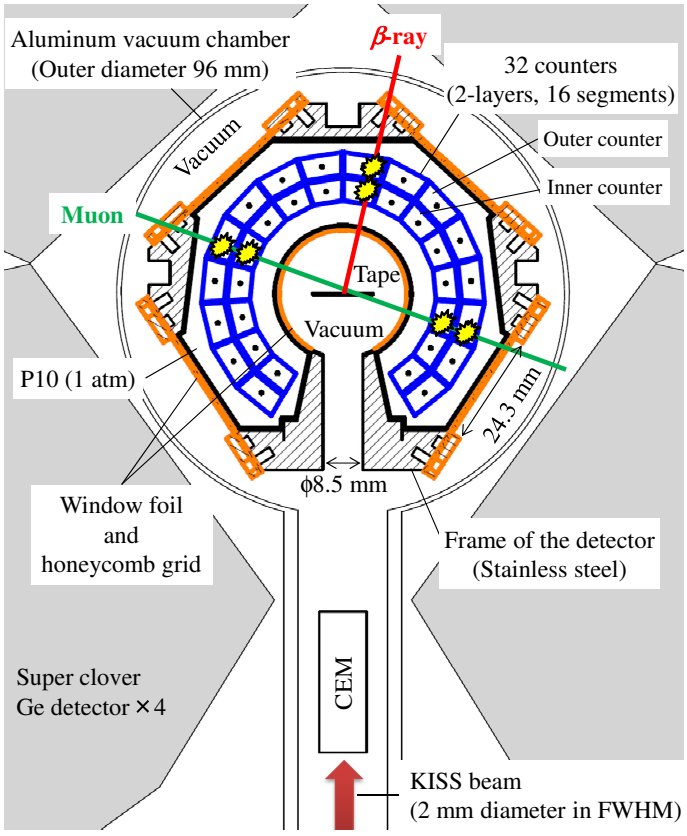

Figure C.2: Cross-sectional view of the MSPGC with the vacuum chamber, SCGe detectors, and CEM. The red and green lines indicate the β-ray from the implanted radioactive nuclei and muon from secondary cosmic-ray, respectively.

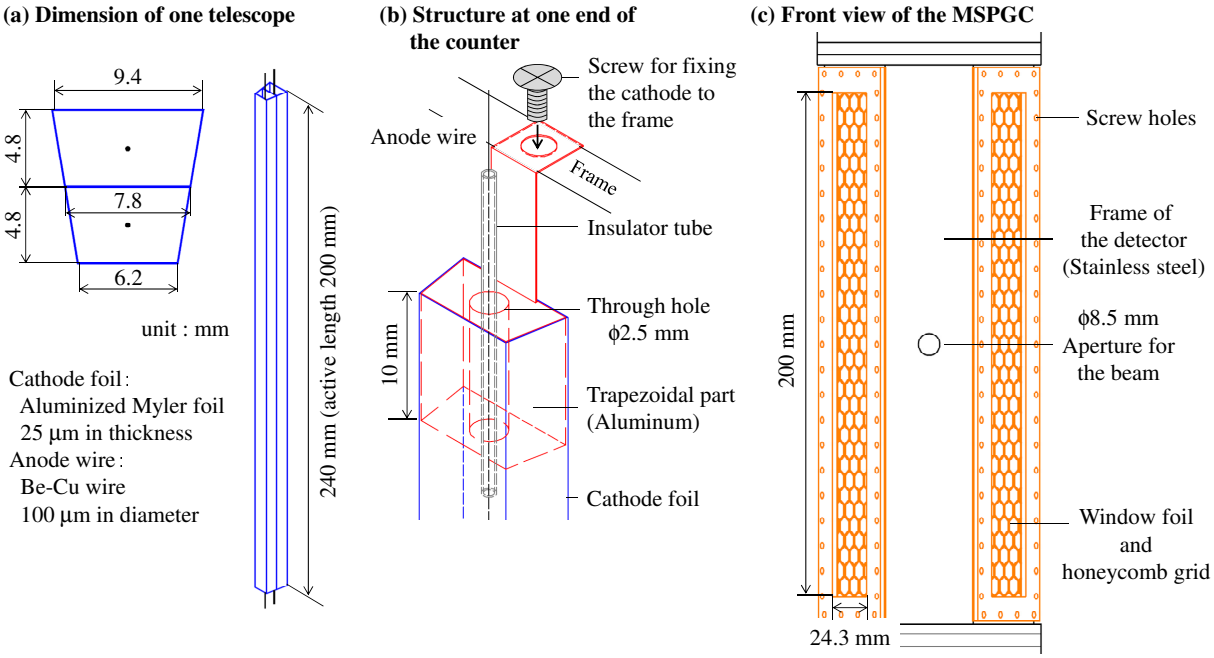

Figure C.3: Schematic view of (a) one telescope (a pair of the inner and outer counter), (b) the aluminum part at one end of the counter, and (c) the front view of the MSPGC frame.

C.1.2 Operation of the MSPGC

The typical gas flow rate was 18 cm^3/min while maintaining the P10 gas in the counter at atmospheric pressure. The pressure in the vacuum chamber during the gas flow was lower than 2×10^{-2} Pa, which was sufficiently low for operation of the CEM. The corresponding gas leak rate from the MSPGC into the vacuum chamber could be deduced to be less than 6×10^{-3} Pa·m^3/s, which was sufficiently small for the stable operation of the MSPGC. It takes approximately 1.5 hours to refresh the gas in the MSPGC.

Figure C.4 shows the schematic view of the high voltage connection and signal amplifications for a gas counter. An array of 16 parallel 1 MΩ resistors is used to simultaneously bias all counters in a layer from a single channel of a high-voltage power supply (iseg, NHQ-205M). Each gas counter was connected to a preamplifier through a coupling capacitance of 1 nF. The preamplifier contained a charge sensitive preamplifier (Hoshin, N012-1, 1 V/pC) and an amplifier circuit using an operational amplifier (Burr-Brown, OPA685U, gain: 4). We used an additional amplifier module (Clear-Pulse, 4018A, gain: ∼2.25) for discriminating noise signals. The total voltage gain factor of the electronic circuit was approximately 9. The pulse height of the counter output signals was converted to a digital signal by using a peak hold analog-to-digital converter (ADC, Hoshin, C008). The present voltage gain of 9 enables to distinguish a minimum-ionization energy-loss distribution from electric noise in a ADC spectrum for the background-event suppression. The time duration between the event trigger for data acquisition (DAQ) and delayed logic signal from each counter was recorded by using a time-to-digital converter (TDC, Hoshin, C021).

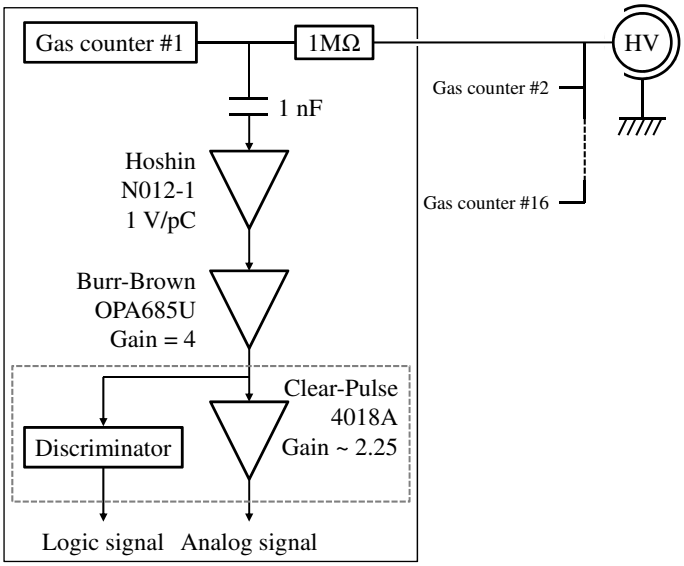

Figure C.4: Schematic view of the high voltage connection and signal amplifications for the gas counter.

Figure C.5 shows the diagrams for data flows and the DAQ triggers in present measurements. Figure C.5(a) shows the data flow including all the detector signals during a KISS on-line experiment, where there are three independent triggers as follows: the "OR" signal of the 16 inner counters in the MSPGC, the "OR" signal of the four SCGe detectors, and a KISS beam-on signal. These three triggers were handled by a trigger handling module. When one of the triggers is accepted, the module attached a common time stamp to synchronize each data set relevant to each trigger, and transferred the data to an acquisition computer (PC) through each data bus (CAMAC or VME). In MSPGC

performance tests without the signals of the SCGe detectors and KISS beam-on, there are three kinds of the data flow relevant to the following trigger signals: (b) the inner counter signal, (c) the outer counter signal, and (d) the coincidence signal of the plastic scintillator telescope (details given in subsection C.2.1).

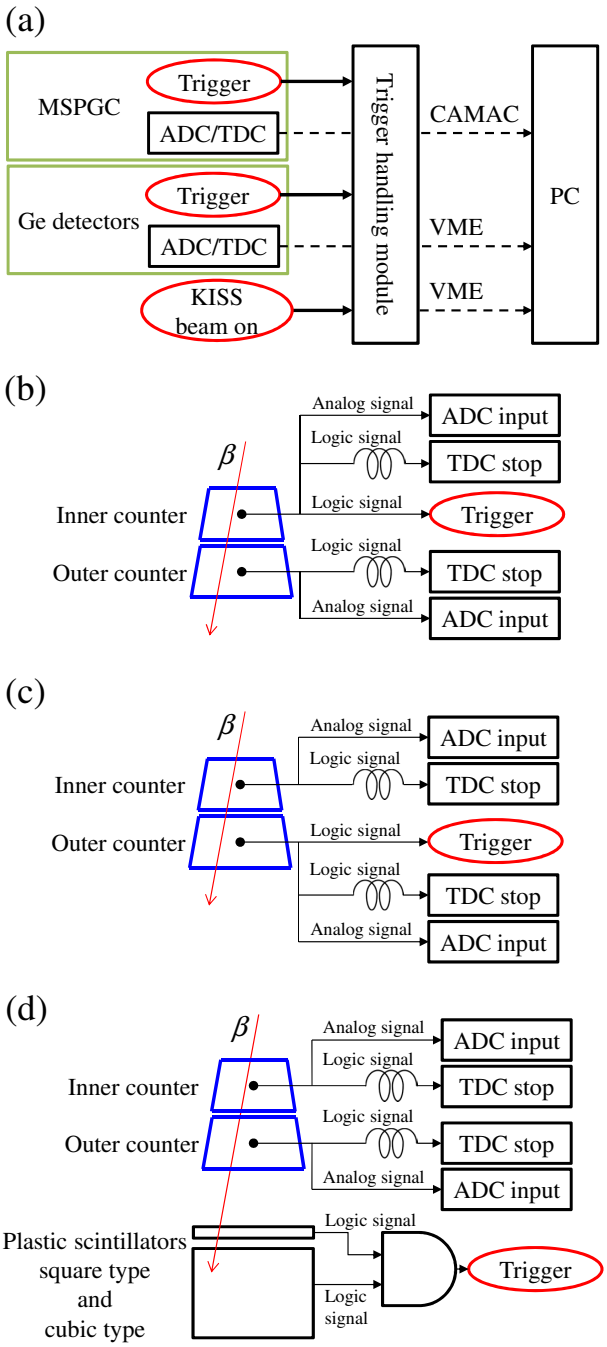

Figure C.5: Schematic diagram of the data flow with four trigger conditions.

Each adjacent inner and outer counter pair worked as a telescope counter in a coincidence measurement for identifying β-ray events. As shown in Fig. C.2, the β-ray (red line, fired one telescope) that comes from the implanted radioactive nuclei on the tape in the center of the MSPGC can be distinguished from the background event (green line, fired 4 counters) by analyzing the hit patterns of the gas counters. Thus, we can suppress most background events. Figures C.6(a) and (b) show typical hit patterns which are identified as the β-ray events. We termed the event where only one telescope was fired

as "$M = 2$", the event where one telescope ($M = 2$) and an adjacent outer counter were fired as "$M = 3$", and the event where one or more counter was fired as "$M \geq 1$". We will show results in the case of $M \geq 1$ in later sections.

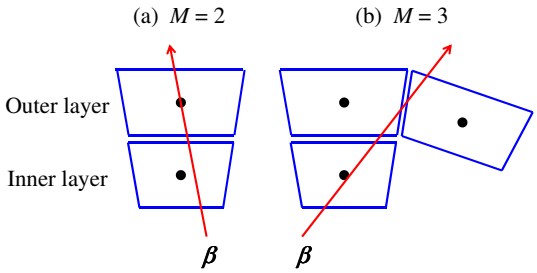

Figure C.6: Schematic view of the hit patterns of (a) $M = 2$ and (b) $M = 3$.

C.2 Performance tests of the MSPGC

At first, by using one telescope consisting of an inner and outer counter of the MSPGC, placed in a small chamber with gas flow, we searched for the optimal anode voltage for the operation of the counters in the proportional regime with atmospheric gas pressure, no discharge, and high gas gain. Then, the intrinsic detection efficiencies of the inner and outer counter together with one telescope were measured under the optimized working conditions as a function of β-ray source position x and y which are coordinates along the axial and horizontal direction of the telescope, respectively. After the performance test of the one telescope in the small chamber, we assembled the full counter set in the vacuum chamber as shown in Fig. C.2. The performance, in terms of the peak height (ADC), timing (TDC), and coincidence rate (proportional to absolute detection efficiency) were studied for each MSPGC counter as functions of gas flow rate. Then, the intrinsic detection efficiencies of some counters as a function of β-ray source position x along the axial direction of the counter and the coincidence rate in each telescope were measured by using the optimal gas flow rate. Next, the background event rate in the MSPGC was measured at the actual detector position on the KISS beamline. Finally, we demonstrated the MSPGC performance in half-life measurements of neutron-rich heavy radioactive nuclei.

C.2.1 Performance test of one telescope in a small chamber with gas flow

The optimization of anode voltages and measurement of intrinsic detection efficiencies were performed for one telescope in the small chamber in Fig. C.7 with gas flow (18 cm^3/min). Figure C.7 shows the cross-sectional view of the measurement setup. The gas-filled area of the small chamber is indicated by the thick black line in Fig. C.7. The top and bottom of the chamber (see Fig. C.7) were sealed by a 25 μm aluminized Mylar foil for β-ray transmission. The trajectories of the β-rays from a ^{90}Sr/^{90}Y source were restricted by the two collimators set at the top and bottom of the chamber. A plastic scintillator telescope was installed after the bottom collimator to identify β-ray events. The telescope comprised a thin sheet (size: 26 mm×30 mm, 1 mm thick) and a thick cube (size: 20 mm×20 mm×20 mm). The source with the collimators and the plastic scintillator telescope were movable along the axial (x) and horizontal (y) directions of the counter in the range of ±93 mm and ±12 mm from the counter center, respectively. The collimated trajectories of the β-ray with the source at center and shifted 1 mm horizontally off-center are indicated by the solid and dashed green lines, respectively, in Fig. C.7.

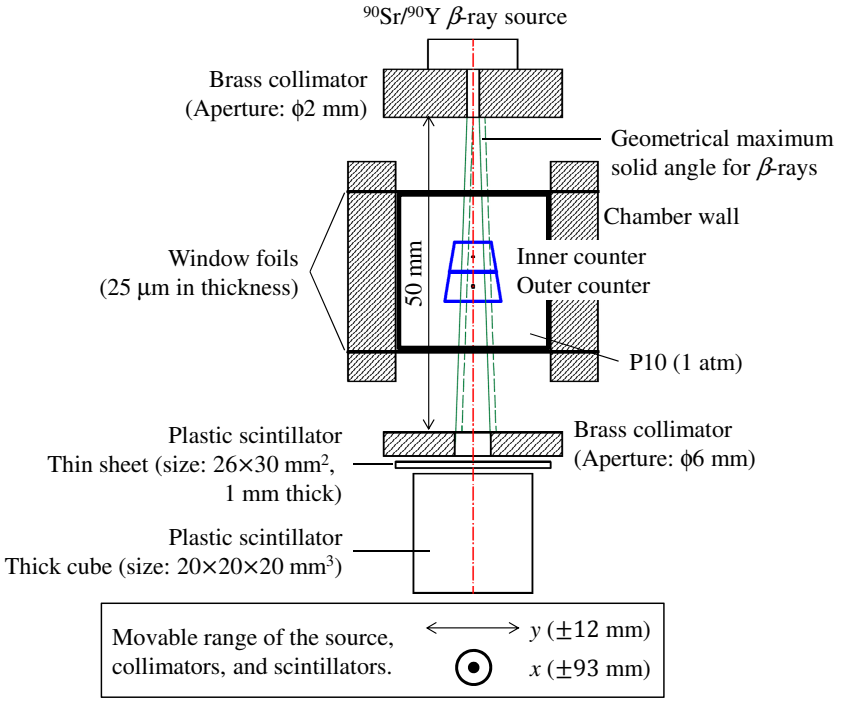

Figure C.7: Schematic view of the performance test setup using the small chamber with gas flow. The solid and dashed green lines indicate the collimated trajectories of the β-ray with the source at center and shifted 1 mm horizontally off-center, respectively.

C.2.1.1 Optimization of the anode voltages We determined the optimal anode voltages based on the following five criteria: (1) the coincidence rate between the inner and outer counter should be saturated to achieve maximum detection efficiency (good accumulation field), (2) the minimum-ionization peak position in the ADC spectrum should be high enough to distinguish a β-ray event signal from electronic noise and (3) to apply a low threshold value at the ADC channel of 10% peak height in further off-line analysis, (4) the proportional counters should work stable for at durations of at least one week (typical beam time period) without significant discharge between the anode and cathode which would cause significant damage on the cathode foil, (5) a fast accumulation time (narrow distribution in TDC spectrum) should be achieved in order to reject any accidental background events as much as possible in further off-line analysis.

At first, we scanned the anode voltages roughly and found that the coincidence rates were saturated at the anode voltages of +1800 V and +1820 V in the inner and outer counter, respectively. Then, we investigated the anode voltage dependences of the coincidence rate between the inner and outer counter precisely by changing the anode voltage of one counter (called the test counter) with the use of optimal anode voltage for the other counter which generates the DAQ trigger signal. The DAQ triggers and data flows for studying the anode voltage dependencies of the inner and outer counter are shown in Figs. C.5(c) and (b), respectively. The anode voltage dependencies of the coincidence rate are shown in Fig. C.8(a). The measured rate in the inner counter (black colored dots) was similar to the saturated value (∼20 cps) within the range of +1600 V to +1860 V, while the rate in the outer counter (red colored triangles) was slowly increased with increasing the voltage and became saturated at around +1720 V. The saturation voltage +1720 V was higher than +1600 V for the inner counter. The relatively low gain of the outer counter could originate from the longer distance between the cathode foil and anode wire than that in the case of the inner counter. This is supported by the results of GARFIELD

[128] simulations in which the simulated gas gains were 9000 and 8000 for the inner and outer counter, respectively, by considering realistic geometries under the anode voltage of +1800 V for both counters.

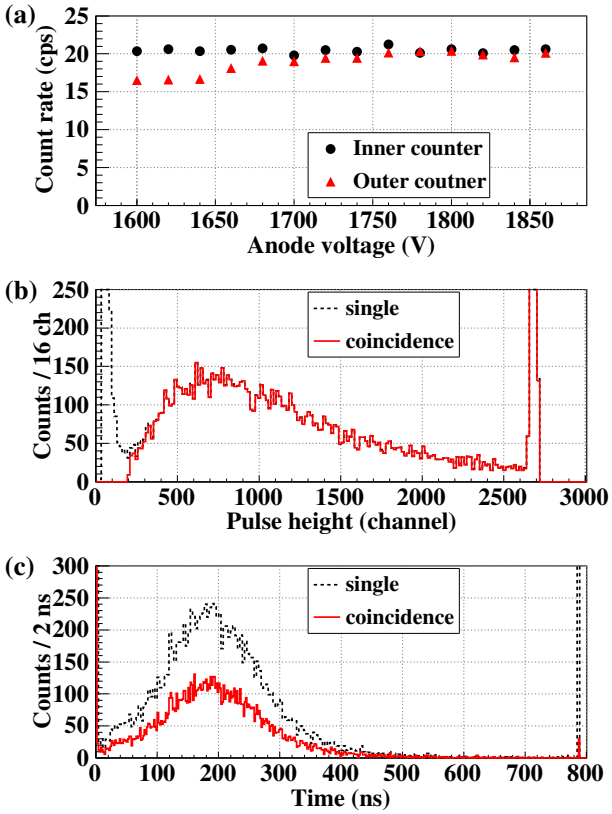

Figure C.8: (a) The anode voltage dependence of the coincidence rates in the inner and outer counter. (b) Typical pulse height distribution and (c) time duration distribution. The dotted and solid lines indicate the single and coincidence spectra, respectively.

In further measurements, we applied the anode voltage of +1800 V for both counters by taking account of the criteria. Although the anode voltage of the outer counter was decreased from +1820 V to +1800 V to avoid discharge, all the above mentioned criteria were fulfilled. Figures C.8(b) and (c) show the typical pulse height and time duration spectra of the output signals from the test counter with the anode voltage of +1800 V, respectively. Typical single and coincidence spectra are shown by the dotted and solid lines, respectively. The minimum-ionization peak was observed around channel 700 in Fig. C.8(b). We applied the software threshold at channel 200 to suppress the accidental coincidence with noise signals. The minimum-ionization energy was evaluated to be 600 eV from GEANT4 [92] simulations. Therefore, channel 200 in this spectrum corresponded to around 140 eV by taking into account the pedestal at channel 50. Here, the hardware threshold was below channel 150 in the DAQ system. This was lower than the software threshold. Charge collection time was measured to be approximately 200 ns in FWHM as shown in Fig. C.8(c). This was consistent with the simulated drift time profile of the induced electrons in the counter by using the GARFIELD code. Hence, the distribution of the electric field in the counters would be as expected.

C.2.1.2 Intrinsic detection efficiency The intrinsic detection efficiencies were investigated for the inner and outer counter, and one telescope. The DAQ trigger was the

coincidence signal from the plastic scintillator telescope. The DAQ trigger and data flows for this measurement are shown in Fig. C.5(d).

The intrinsic detection efficiency of the inner (outer) counter is evaluated from Eqs. (A.2)–(A.4) as follows

$$\varepsilon_{\mathrm{IN(OUT)}} = N_{\mathrm{GCtelescope}}/N_{\mathrm{OUT(IN)}}, \tag{C.1}$$

where $N_{\mathrm{GCtelescope}}$ is the number of coincidence events between the two gas counters and $N_{\mathrm{IN(OUT)}}$ is the number of events in the inner (outer) counter. $N_{\mathrm{GCtelescope}}$ and $N_{\mathrm{IN(OUT)}}$ are written as

$$\begin{aligned} N_{\mathrm{GCtelescope}} &= \varepsilon_{\mathrm{IN}} \times \varepsilon_{\mathrm{OUT}} \times N_0, & \text{(C.2)} \\ N_{\mathrm{IN}} &= \varepsilon_{\mathrm{IN}} \times N_0, & \text{(C.3)} \\ N_{\mathrm{OUT}} &= \varepsilon_{\mathrm{OUT}} \times N_0, & \text{(C.4)} \end{aligned}$$

where N_0 is the number of β-ray events which pass through the gas counter telescope. The measurements were performed as a function of axial position x of the ^{90}Sr/^{90}Y source assembly to investigate the efficiency at each axial point of the counter. Figure C.9 shows the measured intrinsic detection efficiencies of the inner (red colored dots) and outer (blue colored triangles) counter, and one telescope ($\varepsilon_{\mathrm{IN}} \times \varepsilon_{\mathrm{OUT}}$, black colored open squares). The measured intrinsic detection efficiencies were almost unity in the range of $x = -93$ to $+93$ mm. The intrinsic detection efficiencies were 97(1)%, 98(1)%, and 95(1)% for the inner counter, outer counter, and telescope, respectively.

We also measured the efficiency at 1 mm shifted source position from the center of the counter in the horizontal (y) direction as shown in Fig. C.7. The collimated β-ray trajectories with this source position are indicated by the green dashed lines in Fig. C.7. Although the β-rays pass near the edge of the inner counter, the intrinsic detection efficiency was not decreased.

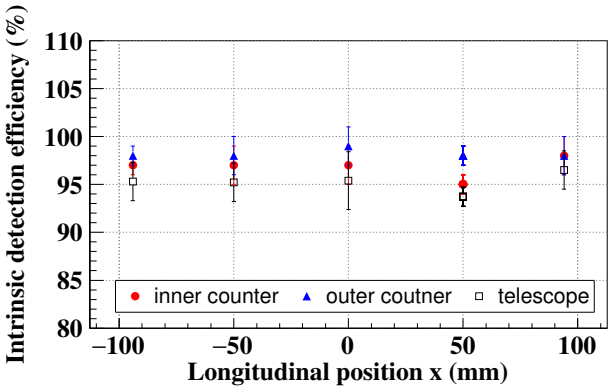

Figure C.9: Measured intrinsic detection efficiencies for inner (red colored dots) and outer (blue colored triangles) counter, and one telescope (black colored open squares) as a function of β-ray source position x along the axial direction of the telescope.

C.2.2 Performance test of the fully assembled MSPGC

The gas flow rate dependence of the gas gain and intrinsic detection efficiency of the fully assembled MSPGC and the uniformity of coincidence rate in all the telescopes were investigated by using the setup shown in Fig. C.10, under atmospheric pressure. A point-like β-ray source of ^{90}Sr/^{90}Y (3.7 kBq) was manufactured to place at a distance of 2.5 mm from the MSPGC center. The same plastic scintillator telescope and collimator as shown

in Fig. C.7 were installed at the outside of the MSPGC to identify the β-ray events which penetrate a pair of the inner and outer counter. The surfaces of the source and scintillators were aligned to the radial direction of each gas counter. Moreover, the background event rate was measured at the actual detector position in the vacuum chamber as shown in Fig. C.2.

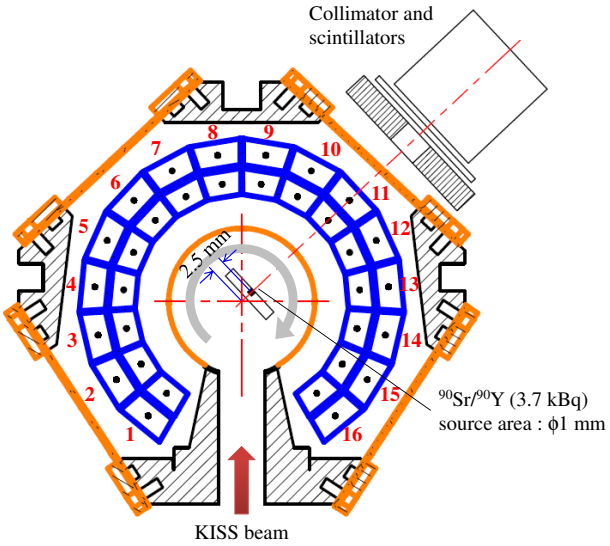

Figure C.10: Schematic view of the performance test setup of the MSPGC. The same plastic scintillator telescope and the collimator as shown in Fig. C.7 were used. The labels from 1 to 16 indicate the different sets of telescopes. The source was set 2.5 mm from the MSPGC center.

C.2.2.1 MSPGC performance as a function of gas flow rate We investigated the coincidence rate and pulse height distribution as a function of gas flow rate. We used the measurement setup displayed in Fig. C.10 without the scintillators and a coincidence rate of 150 cps, which is more than 10 times larger than the typical implantation rate of radioactive nuclei in a KISS experiment. In the measurement, the β-rays hit the entire region of one telescope where the edges of the counters were included. The DAQ trigger and data flows for this measurement are shown in Fig. C.5(b) (the "OR" signal of the 16 inner counters). The observed coincidence rate and the peak position of minimum-ionization in the pulse height distribution of each telescope were independent of the gas flow rate in the range of 18–45 cm^3/min. The results indicated that the gas flow close to the edge of the counter would be sufficient. To minimize the gas consumption rate, we set the gas flow rate to be 18 cm^3/min. This gas flow rate was high enough for the stable operation of the MSPGC in the on-line measurements because the β-ray yield is quite low compared with that in the performance test.

C.2.2.2 Confirmation of intrinsic detection efficiency The intrinsic detection efficiency was measured again for confirmation of MSPGC performances by using the point source of ^{90}Sr/^{90}Y with the setup as shown in Fig. C.10. The DAQ trigger and data flows for this measurement are shown in Fig. C.5(d). The measurements were performed for telescopes #2, #6, #11, and #15, where the β-rays from the source were not blocked by the stainless steel frame, as a function of axial position x of the ^{90}Sr/^{90}Y source assembly in the same way that explained in subsection C.2.1.2. The measured intrinsic detection efficiencies for these telescopes were in good agreement with those measured in the small chamber as reported in subsection C.2.1.2.

C.2.2.3 Coincidence rate in all the telescopes We measured the $M = 2$ coincidence rate in all the telescopes by using the point source of ^{90}Sr/^{90}Y. The DAQ trigger was the logical "OR" of the signals from all the inner counters. The DAQ trigger and data flows for this measurement are shown in Fig. C.5(b). Figure C.11 shows the measured coincidence rate in each telescope. The error was governed by the systematic error which stemmed from the uncertainty of the source position (5%). The counting rates in telescopes #2 to #15 were almost uniform. Based on the measurement results, we confirmed that the absolute detection efficiency of each telescope was uniform, except for #1 and #16.

The reduction of the counting rates in telescopes #1 and #16 arose from the blocking of β-rays by the sealing materials, which were added around the connection area of the inner window foil to the detector frame to avoid any gas leak. The sum of the counting rates in telescopes #1 and #16 was almost the same as the counting rate in the other telescopes. This means that the absolute detection efficiency of the MSPGC was reduced by a factor of 0.94(5) ($\simeq 15/16$, hereafter referred to as reduction factor). This value was calculated by using the averaged counting rate in telescopes #2 to #15 and the summed counting rates in telescopes #1 and #16. The error of the reduction factor was 5% of the exact value by considering the uncertainty of the source position.

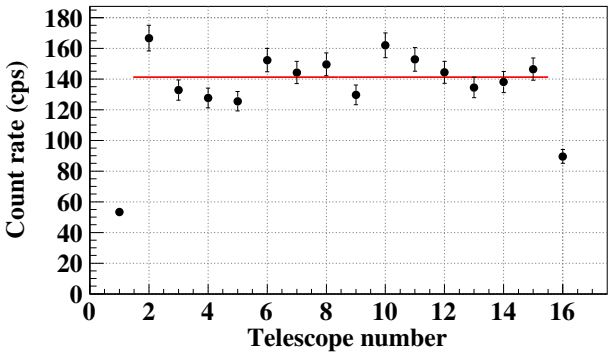

Figure C.11: Measured coincidence rate in each telescope ($M = 2$). The solid line indicates the averaged counting rate in telescopes #2 to #15.

C.2.3 Background event rate

The measurements of the background event rate in the MSPGC were performed with the following three conditions: 1. without veto counters for cosmic-rays and lead block shield (Pb shield) for environmental background γ-rays, which were surrounding the MSPGC and SCGe detectors, 2. with the veto counters and without the Pb shield, 3. with the veto counters and the Pb shield. In all the measurements, the four SCGe detectors were placed at a distance of 4.8 cm from the MSPGC center. The DAQ trigger and data flows for this measurement are shown in Fig. C.5(b) (the "OR" signal of the 16 inner counters).

The veto counters consisted of 10 plastic scintillator bars (BICRON BC408, size: $5 \times 15 \times 135$ cm^3 for each) and 4 bars (BC408, size: $5 \times 5 \times 135$ cm^3 for each) with photomultiplier tubes (HAMAMATSU H7195, hereafter marked as PMT) at both ends. Coincidence events between two PMTs were considered to be true background events, whose rate was typically 20 kHz. The expected counting rate of cosmic-rays was about 380 cps by accounting for the typical intensity 1 /cm^2/min of muons [91] and the area of the veto counters ($\sim$23000 cm^2). Most of the measured background rate is originated from the environmental background γ-rays emitted from the wall of the experimental room. Although the counting rate stemming from the environment was dominant, we

could reject the background events of the MSPGC originating from cosmic-ray events by using the veto counters. The veto duration time was set to be 2 μs for each event. The veto efficiency of the veto counters was estimated to be 0.93 for 1 GeV muons obeying the typical zenith angle distribution ($\cos^2\theta$) according to GEANT4 simulations.

The Pb shield mainly reduced background events induced by Compton scatterings of background γ-rays.

The measured background event rates under each of the three conditions are summarized in Table C.1 with the three hit patterns of the MSPGC: $M \geq 1$, $M = 2$, and $M = 2$ or $M = 3$. Accounting for the hit patterns of $M = 2$ or $M = 3$, the background event rate could be reduced by a factor of 1/5 from that of $M \geq 1$ in all three conditions. Finally, we achieved a background event rate of 0.11 cps for $M = 2$ or $M = 3$ with the use of the veto counters and Pb shield. This background event rate was sufficiently low to measure the half-lives of the nuclei which were extracted from KISS with intensities of a few pps. Figure C.12 shows the background event rate measured in each telescope. The background event rate clearly decreased in telescopes #4, #8, #9, and #13. This was because the environmental background radiation, mainly γ-rays, was suppressed by the stainless steel pillars located just outside of these telescopes as shown in Fig. C.10. However, the counting rates in telescopes #1 and #16 were slightly higher than those for the others. This can be understood as follows. Telescopes #2 to #15 have the neighboring telescopes. On the other hand, right (left) side of telescope #1 (#16) is the stainless steel wall, and therefore one adjacent telescope is absent for #1 and #16 telescopes. The absence of these adjacent telescopes causes the increasing of $M = 2$ events due to the mis-identification of some fraction of $M > 2$ events.

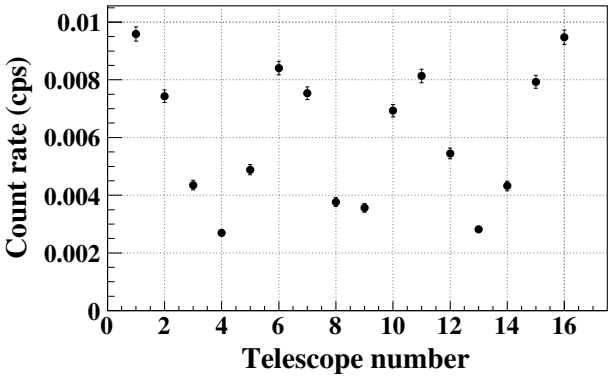

Figure C.12: Measured background event rate in each telescope with $M = 2$.

Table C.1: Measured background event rates in the MSPGC for three experimental setup conditions with three hit patterns.

Setup	Background event rate (cps)		
	$M \geq 1$	$M = 2$	$M = 2$ or $M = 3$
w/o veto, Pb	2.5	0.52	0.59
w/ veto	1.5	0.35	0.40
w/ veto, Pb	0.6	0.09	0.11

C.2.4 On-line experimental results obtained by using the MSPGC

We performed half-life measurements of the radioactive nuclei produced in the multi-nucleon transfer reaction of ^{136}Xe beam (50 pnA and 9.6 MeV/nucleon) and ^{198}Pt target (12.5 mg/cm^2) by using the MSPGC. We present the results for ^{198}Ir ($Z = 77$ and $N = 121$) as a typical case of the half-life measurements. We evaluated the absolute detection efficiency of the MSPGC for the β-rays from analyzing the β-delayed γ-ray energy spectra of ^{199}Pt ($Z = 78$ and $N = 121$) which were measured in single and in coincidence with the β-rays ($M \geq 1$ and $M = 2$). The MSPGC is sensitive to low energy photons such as X-rays with an energy of around 10 keV. We evaluated the detection efficiency for the X-rays by analyzing the decay curve obtained by using the MSPGC and the γ-ray energy spectra of ^{199m}Pt ($E_{ex} = 424$ keV) which were measured in single and in coincidence with the β-rays ($M \geq 1$).

The time sequence of the half-life measurement consisted of a tape moving time (T_{move}), KISS beam-on time (T_{on}) and KISS beam-off time (T_{off}). During T_{on}, the radioactive nuclei purified by KISS was implanted and its duration time was set to be 1.5 or 2 times the reported half-lives ($T_{on} = 1.5 \times T_{1/2}$ or $2 \times T_{1/2}$) of ^{198}Ir or ^{199m}Pt, respectively. The implantation of the radioactive nuclei was suspended during T_{off} to measure the decay curves of the radioactive nuclei implanted on the tape. The T_{off} was set to be $4 \times T_{1/2}$. Just before every T_{on} timing, the tape was moved around 30 cm during $T_{move} = 1$ s to avoid unwanted activities for the half-life measurements. The time sequence was repeated 56 times for ^{198}Ir and 21 times for ^{199m}Pt. The DAQ trigger and data flows for the on-line experiment are shown in Fig. C.5(a).

C.2.4.1 Half-life measurement for ^{198}Ir The growth and decay time spectrum measured by the MSPGC is shown in Fig. C.13. Here, we applied the hit patterns of $M = 2$ or $M = 3$. The evaluated half-life of 9.8(7) s was in good agreement with the previously reported value of 8(2) s [97].

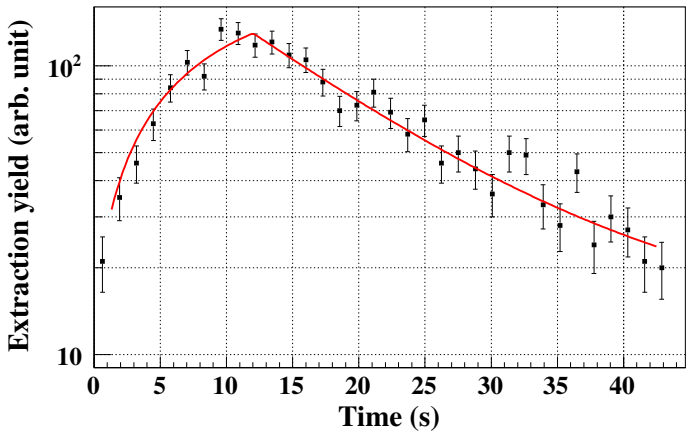

Figure C.13: Measured growth and decay time spectrum of β-rays for ^{198}Ir. The solid line indicates the best fitting curve to the experimental data.

C.2.4.2 Evaluation of the absolute detection efficiency for β-rays and X-rays The decay scheme of ^{199m}Pt and ^{199}Pt are shown in Fig. C.14(a). The isomeric state decays to the lower excited state at an energy of 32 keV by emitting a 392 keV γ-ray with a half-life of 13.6(4) s [129]. The γ-ray emission probability of the 392 keV transition is 84.9%. The lower excited state decays to the ground state by emitting the conversion electron with a 97% branching ratio. The ground state of ^{199}Pt decays to the excited

states or ground state of ^{199}Au. The absolute γ-ray intensity of the 543 keV transition is 11.74% and is the most intense γ-ray among the β-delayed γ-rays of ^{199}Pt.

We evaluated the absolute detection efficiency for the β-rays by using the 543 keV transition. We compared the yield of the photo-peak measured in the β-γ coincidence and γ-single energy spectra. Figures C.14(b) and (c) show the measured γ-ray energy spectra in coincidence with the MSPGC signals of the hit patterns of $M \geq 1$ and $M = 2$, respectively. The evaluated absolute detection efficiencies were 78(8)% ($M \geq 1$) and 39(4)% ($M = 2$) at $Q_\beta = 1.16$ MeV. They were consistent with the estimated value from GEANT4 simulations as shown in later subsection C.2.5.

We evaluated the absolute detection efficiency for X-rays from the β-γ spectroscopy of $^{199\mathrm{m}}$Pt. Characteristic X-rays with an energy of < 12 keV were emitted from the L-shell of platinum atoms in association with a conversion electron energy of 32 keV because the transition energy is lower than the binding energy of K-shell electrons (78.394 keV). The X-rays could be detected by the MSPGC through the photoelectric effect in one gas counter ($M = 1$), although the internal conversion electron with an energy of 32 keV is hard to detect even in the inner counter owing to the energy loss in the window foils. Hence, in the γ-ray energy spectrum in Fig. C.14(b) measured with $M \geq 1$, the photo-peak of 392 keV originating from the isomeric state was measured by detecting the characteristic X-rays from the platinum atom. However, in the γ-ray energy spectrum in Fig. C.14(c) measured with $M = 2$ (i.e., detection of the conversion electron originated from the 392 keV transition), the photo-peak of 392 keV disappeared.

We performed the fitting of the decay curve measured by using the MSPGC ($M \geq 1$) in Fig. C.14(d) to evaluate the non-corrected detection efficiency for X-rays which includes fluorescence probabilities of X-rays. In the fitting, we considered the decays of the isomeric and ground states. The implantation yields of the isomeric and ground states, evaluated from the γ-ray energy spectrum, were used as free parameters within the range of the measured one sigma error. The implantation yield of the isomer, which was deduced from the growth curve of the 392 keV photo-peak in the single γ-ray energy spectrum, was 51.6(27) pps with consideration of the photo-peak efficiency of the SCGe detectors and γ-ray emission probability. Then, implantation yield of the ground state was calculated using the production ratio of 40(5)% for the isomeric state to the ground state, as reported in Ref. [102]. The other free fitting parameters were the background event rate, half-life of the isomeric state, and detection efficiency which was consisted of the absolute detection efficiency for the conversion electrons originating from the 392 keV transition and non-corrected detection efficiency for the characteristic X-rays. The absolute detection efficiency for the β-rays from the β-decay of the ground state, which was a fixed parameter in the fitting, was evaluated using the estimated values from GEANT4 simulations considering the β-decay branching ratios and Q_β's [129]. The intrinsic detection efficiencies and reduction factor were also considered as described in subsection C.2.5.

The fitted half-life of 12.4(7) s was in agreement with the previously reported value of 13.6(4) s within the error margin of two sigma. The fitted detection efficiency for the conversion electron and X-rays was 12(2)%. The expected absolute detection efficiency for the conversion electron was 11.0(9)% considering the internal conversion probability (15.1(5)% [129]), solid angle of the MSPGC (80(4)%), intrinsic detection efficiency (97(1)%), and reduction factor (0.94(5)). Consequently, the non-corrected detection efficiency for the X-rays with $M = 1$ was 1^{+2}_{-1}%.

The non-corrected detection efficiency for the X-rays was also deduced by comparing the yields of the 392 keV photo-peak in the single spectrum and coincidence spectrum with the MSPGC signals. The 392 keV photo-peak in the coincidence spectrum with

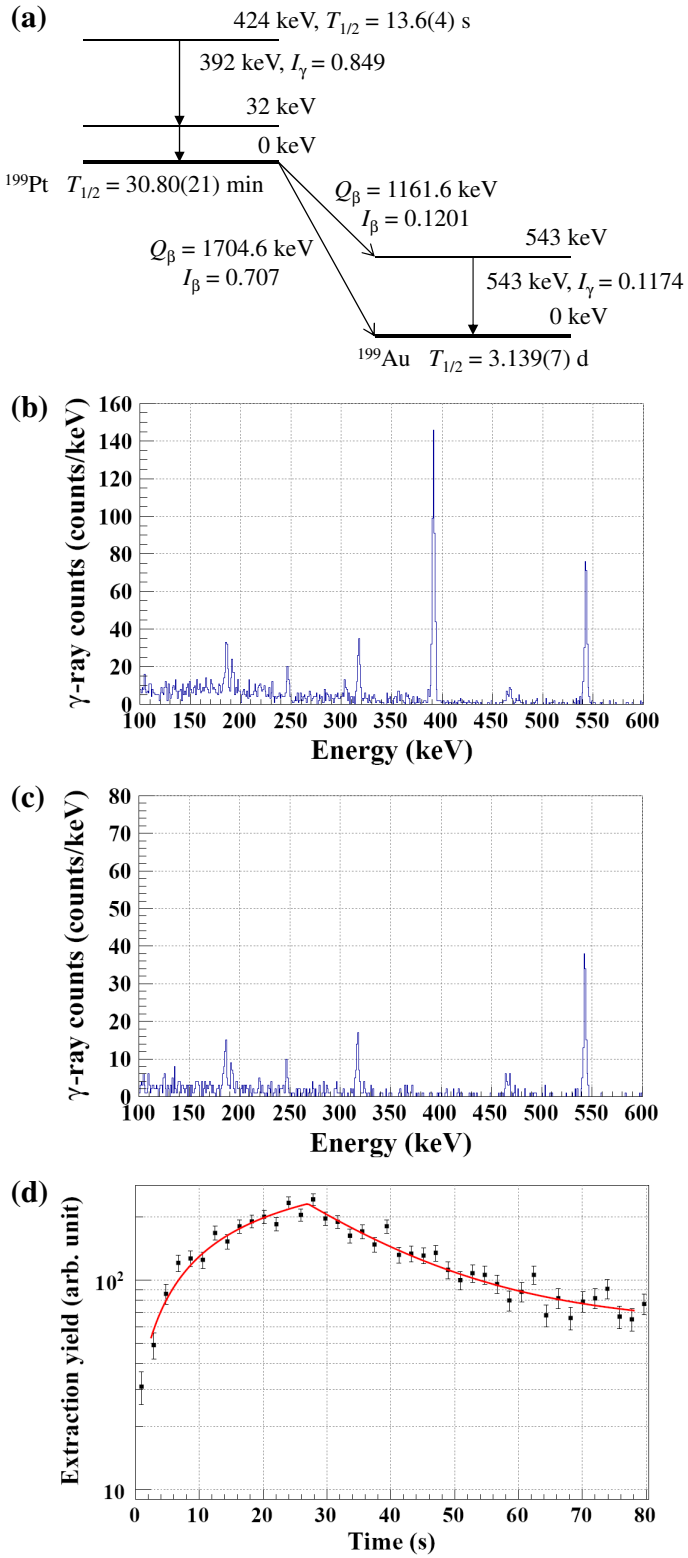

Figure C.14: (a) Decay scheme of the isomeric state (E_{ex} = 424 keV, $T_{1/2}$ = 13.6(4) s) and ground state of ^{199}Pt ($T_{1/2}$ = 30.80(21) min) [129]. Measured γ-ray energy spectra which coincide with the MSPGC hit patterns of (b) $M \geq 1$ and (c) $M = 2$. (d) Measured growth and decay time spectrum for ^{199m}Pt by using the MSPGC ($M \geq 1$). The solid line indicates the best fitting curve to the experimental data.

the MSPGC signals of $M \geq 1$ mode (coincidence window of 500 ns) would be triggered only by the X-rays originating from the 32 keV transition. The deduced non-corrected detection efficiency for the X-rays was 3.7(4)%.

These two non-corrected detection efficiencies for the X-rays of 1^{+2}_{-1}% and 3.7(4)% were corrected to 3^{+6}_{-3}% and 12(1)% as the absolute detection efficiency by accounting for the averaged L-shell fluorescence probability of 0.328 reported in Ref. [130]. These two values were consistent within the error margin of two sigma. The result indicates that the MSPGC is sensitive to X-rays. Thus, the sensitivity to X-rays of the MSPGC is a useful feature to search for an isomeric state. Because, in the case of a spin isomer which decays to the ground state via internal cascade transitions, there is a characteristic X-ray emission followed by the conversion electron emission from the lower excited state in the heavy nuclear region. Therefore, we can identify the γ-rays originating from an isomeric state as shown in Figs. C.14(b) and (c).

C.2.5 Absolute detection efficiency as a function of Q_β

The absolute detection efficiency of the MSPGC as a function of Q_β was simulated by using the GEANT4 simulation toolkit [92]. EM standard of option 4, which was designed for applications requiring higher accuracy of electrons, hadrons, and ion tracking by using the most accurate standard and low-energy models, was used in the simulation.

In the present simulation, all the materials composing the active volume of the MSPGC, except for the screw heads and grids, were taken into account. However, we confirmed that the effects of the non-included materials were negligible from the comparison between the simulated efficiency and measured efficiency by using ^{199}Pt β-delayed γ-rays as described in later.

The simulation results are shown in Fig. C.15. The vertical axis shows the absolute detection efficiencies estimated for the three hit patterns: $M \geq 1$ (red colored dots), $M = 2$ (blue colored triangles), and $M = 2$ or $M = 3$ (black colored squares). The absolute detection efficiencies in Fig. C.15 were normalized by accounting for the measured intrinsic detection efficiencies: 97(1)% (inner counter), 98(1)% (outer counter), and 95(1)% (telescope), and the reduction factor of 0.94(5) owing to the sealing materials of the MSPGC as mentioned in subsections C.2.1.2 and C.2.2.3 The normalization factors (f) for the corresponding hit patterns were as follows: $f = 0.97 \times 0.94$ for $M \geq 1$, $f = 0.95 \times 0.94$ for $M = 2$, and $f = 0.95 \times 0.98 \times 0.94$ for $M = 3$. The error bars shown in Fig. C.15 were approximately 7% of each simulated efficiency by considering the uncertainty of the solid angle in the assembled MSPGC (5%) and the error of the intrinsic detection efficiencies (1%) and reduction factor (5%).

The simulated absolute detection efficiency for the β-ray of $Q_\beta = 1$ MeV was 45(3)% with $M = 2$ or $M = 3$. This value was three times higher than that of the plastic scintillator telescopes previously used at KISS (three sets of ΔE-E counters, 1 and 2 mm in thickness, respectively, $\Delta\Omega = 75\%$) [93]. This result satisfies the initial requirement for designing the MSPGC. The simulated efficiency was saturated at approximately 60% for $Q_\beta > 4$ MeV with $M = 2$.

The absolute detection efficiencies evaluated from the β-γ spectroscopy of ^{199}Pt are shown by the red colored open dot for $M \geq 1$ and blue colored open triangle for $M = 2$. These measured efficiencies were in agreement with simulated efficiencies. The measured efficiencies include the responses near the edge and area close to the cathode foil, where the detection efficiency was not measured as part of the performance tests. The good agreement of the efficiency between the measurement and simulation indicates that the detection efficiency would not be reduced near the edges or area close to the cathode foil.

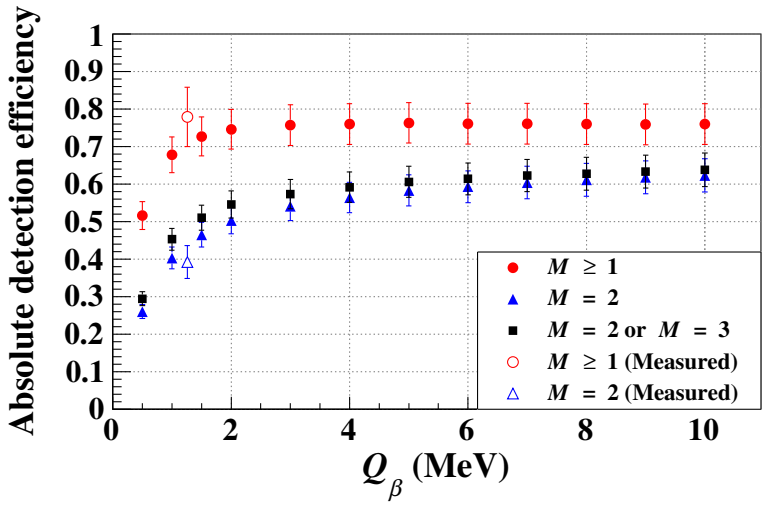

Figure C.15: Estimated absolute detection efficiency of the MSPGC as a function of Q_β from GEANT4 simulations. Here, the hit patterns of $M \geq 1$ (red colored dots), $M = 2$ (blue colored triangles), and $M = 2$ or $M = 3$ (black colored squares) were shown. The details of the experimental results (red colored open dot for $M \geq 1$ and blue colored open triangle for $M = 2$) are explained in subsection C.2.4.

C.3 Summary

A multi-segmented proportional gas counter (MSPGC) with high detection efficiency and low-background event rate has been developed for the β-decay spectroscopy of rare reaction products around $N = 126$. The MSPGC consists of two cylindrically aligned layers of 16 proportional gas counters (32 counters in total), each counter had a long active length and small trapezoidal cross-section. The total solid angle of the 32 counters was 80% of 4π. β-rays were distinguished from the background events including cosmic-rays by analyzing the hit patterns of independent counters.

Performance of the MSPGC was investigated by using a ^{90}Sr/^{90}Y source. Sufficiently high gas gains for the inner and outer counters were obtained by applying an anode voltage of +1800 V to each counter. The deduced intrinsic detection efficiencies were 97(1)% for the inner counter, 98(1)% for the outer counter, and 95(1)% for one telescope. The measured counting rate in all the telescopes (except for #1 and #16) indicated relatively uniform detection efficiency among telescopes. A background event rate of 0.11 cps ($M = 2$ or $M = 3$) was achieved using the combination of the veto counters and Pb shield for the suppression of the background events induced by cosmic-rays and background γ-rays, respectively. This background event rate was sufficiently low to measure the half-lives of the nuclei which were extracted from KISS with intensities of a few pps.

We could successfully measure the half-lives of the radioactive nuclei ^{198}Ir and ^{199m}Pt by using the MSPGC. The measured half-lives were consistent with previously reported values. From the analysis of the β-γ spectroscopy of ^{199m}Pt, we evaluated the absolute detection efficiency for the X-rays originating from the 32 keV transition followed by the internal decay of the isomeric state. The evaluated absolute detection efficiency for the X-rays with $M = 1$ was 3^{+6}_{-3}%.

The estimated absolute detection efficiency of the MSPGC from GEANT4 simulations was consistent with the evaluated efficiency from the analysis of the β-γ spectroscopy of ^{199}Pt, saturating at approximately 60% for $Q_\beta > 4$ MeV.

The MSPGC distinguished between the β-ray event and background event by using two-dimensional tracking. It will be possible to perform three-dimensional tracking by

adding the information of the detection position along the anode wire. We plan to develop three-dimensional tracking to suppress the background event rate down to the 0.01 cps level for the precise β-decay spectroscopy of more neutron-rich nuclei in the near future.

D Magnetic moments on the single-particle model

This section describes nuclear magnetic dipole moments and the moments of odd-odd nuclei on the single-particle model.

The nuclear magnetic dipole moment consists of the magnetic moments stemmed from the orbital motions and spins of the nucleons in a nucleus. The magnetic dipole moment operator $\boldsymbol{\mu}_{\rm op}$ is defined by [117]

$$\boldsymbol{\mu}_{\rm op} = \boldsymbol{\mu}_{\rm orbital} + \boldsymbol{\mu}_{\rm spin}, \tag{D.1}$$

where

$$\begin{aligned} \boldsymbol{\mu}_{\rm orbital} &= \mu_{\rm N} \sum_{i=1}^{A} g_{\rm l}^i \boldsymbol{l}^i, \\ \boldsymbol{\mu}_{\rm spin} &= \mu_{\rm N} \sum_{i=1}^{A} g_{\rm s}^i \boldsymbol{s}^i. \end{aligned}$$

The $\mu_{\rm N} = e\hbar/2m_{\rm p}c$ ($m_{\rm p}$ is the proton mass) is called the nuclear magneton, and is the unit for nuclear magnetic moment. The $\boldsymbol{l}$ and $\boldsymbol{s}$ are the orbital angular moment and spin of a nucleon, respectively. The $g_{\rm l}$ and $g_{\rm s}$ are the orbital and spin gyromagnetic ratios of the nucleons: $g_{\rm l} = 1$ and $g_{\rm s} = 5.585694702$ for a proton while $g_{\rm l} = 0$ and $g_{\rm s} = -3.826085456$ for a neutron [131]. The expected value of the z-component of $\boldsymbol{\mu}_{\rm op}$ is given by

$$\mu = \int \Psi_I^{I*} (\boldsymbol{\mu}_{\rm op})_{\rm z} \Psi_I^I dV = \langle \mu_{\rm z} \rangle_{m_{\rm s}=I}, \tag{D.2}$$

where $\Psi_I^{m_{\rm s}}$ is the wave-function for a nucleus with a nuclear spin I and magnetic substate $m_{\rm s}$. The magnetic moments of proton and neutron are $\mu(P) = 2.793\ \mu_{\rm N}$ and $\mu(N) = -1.913\ \mu_{\rm N}$, respectively.

On the single-particle model, an even number of protons and neutrons are considered to be coupling with spin-zero, and the valence proton or neutron with spin j governs the magnetic moment. Therefore, Eq. (D.2) is rewritten by using the orbital angular moment l and spin s of the valence nucleon as

$$\begin{aligned} \mu_{\rm sp} &= \int \Psi_I^{I*} (g_{\rm l} \boldsymbol{l} + g_{\rm s} \boldsymbol{s})_{\rm z} \Psi_I^I dV \\ &= j \left\langle \frac{g_{\rm l} \boldsymbol{l} \cdot \boldsymbol{j} + g_{\rm s} \boldsymbol{s} \cdot \boldsymbol{j}}{\boldsymbol{j} \cdot \boldsymbol{j}} \right\rangle \\ &= \frac{j}{2} \left\{ (g_{\rm l} + g_{\rm s}) + (g_{\rm l} - g_{\rm s}) \frac{l(l+1) - \frac{3}{4}}{j(j+1)} \right\}, \end{aligned} \tag{D.3}$$

where $j = l \pm 1/2$. The magnetic moments of the nucleus with odd-proton or -neutron are given from Eq. (D.3) as

$$\begin{aligned} \text{odd-proton} : j &= l + 1/2,\ \mu_{\rm sp} = \left(j - \frac{1}{2} \right) + \mu(P), \\ j &= l - 1/2,\ \mu_{\rm sp} = \frac{j}{j+1} \left[\left(j + \frac{3}{2} \right) - \mu(P) \right], \\ \text{odd-neutron} : j &= l + 1/2,\ \mu_{\rm sp} = \mu(N), \\ j &= l - 1/2,\ \mu_{\rm sp} = -\frac{j}{j+1} \mu(N). \end{aligned}$$

In the case that the valence proton and neutron of odd-odd nucleus occupy the appropriate shell model orbit, the operator $\boldsymbol{\mu}_{\rm op}$ for the odd-odd nucleus is given as

$$\begin{aligned}\boldsymbol{\mu}_{\rm op} &= \boldsymbol{\mu}^{\rm p}_{\rm orbital} + \boldsymbol{\mu}^{\rm p}_{\rm spin} + \boldsymbol{\mu}^{\rm n}_{\rm orbital} + \boldsymbol{\mu}^{\rm n}_{\rm spin} \\ &= \boldsymbol{\mu}^{\rm p}_{\rm sp} + \boldsymbol{\mu}^{\rm n}_{\rm sp} \\ &= g_{\rm p}\boldsymbol{j}_{\rm p} + g_{\rm n}\boldsymbol{j}_{\rm n}, \end{aligned} \tag{D.4}$$

where $\boldsymbol{j}_{\rm p}$ and $\boldsymbol{j}_{\rm n}$ are the total angular momentum of the valence proton and neutron, respectively. The $g_{\rm p}$ and $g_{\rm n}$ are calculated from Eq. (D.3). The nuclear wave-function, with a nuclear spin I and magnetic substates $m^{\rm p}_{\rm s}$ and $m^{\rm n}_{\rm s}$ for the protons and neutrons, can be written as

$$\Psi^{m_{\rm s}}_{I} = \sum_{m^{\rm p}_{\rm s}, m^{\rm n}_{\rm s}} C(I j_{\rm p} j_{\rm n}; m^{\rm p}_{\rm s} m^{\rm n}_{\rm s}) \psi^{m^{\rm p}_{\rm s}}_{n_{\rm p} l_{\rm p} j_{\rm p}} \psi^{m^{\rm n}_{\rm s}}_{n_{\rm n} l_{\rm n} j_{\rm n}}, \tag{D.5}$$

where $\psi^{m^k_{\rm s}}_{n_k l_k j_k}$ $(k = {\rm p}, {\rm n})$ is the wave function of a nucleon with a main quantum number n_k, orbital angular momentum l_k, total spin j_k, and magnetic substate $m^k_{\rm s}$. The excepted value of the magnetic moment for an odd-odd nucleus is given with replacements of $g_{\rm l} \to g_{\rm p},\ g_{\rm s} \to g_{\rm n},\ \boldsymbol{l} \to \boldsymbol{j}_{\rm p},\ \boldsymbol{s} \to \boldsymbol{j}_{\rm n}$, and $\boldsymbol{j} \to \boldsymbol{I}$ in Eq. (D.3) as

$$\mu_{\text{odd-odd}} = \frac{I}{2}\left\{(g_{\rm p} + g_{\rm n}) + (g_{\rm p} - g_{\rm n})\frac{j_{\rm p}(j_{\rm p}+1) - j_{\rm n}(j_{\rm n}+1)}{I(I+1)}\right\}. \tag{D.6}$$

The semi-empirical $\mu_{\text{odd-odd}}$ for a nucleus can be calculated from Eq. (D.6) by using experimental values of g-factors of the neighboring nuclei which have corresponding spin values to $j_{\rm p}$ and $j_{\rm n}$.

Acknowledgments

I received a lot of help to carry out the works for this thesis from people in Wako nuclear science center, RIKEN Nishina center, Univ. of Tsukuba, and collaborators of the experiments.

Firstly, I would like to show my greatest appreciation to Dr. Yoshikazu Hirayama and Prof. Hiroari Miyatake for the teaching of an innumerable amount of experimental techniques and physics, many kind advices for developing works, analyses, writings, and presentations, and encouragements with lots of patience, and the opportunity for me to join the KISS project. I would also like to express my gratitude to Dr. Yutaka Watanabe, Dr. Nobuaki Imai, Dr. Hironobu Ishiyama, Dr. Sun-Chan Jeong, and Prof. Michiharu Wada for a lot of help, teaching, and discussion. Special thanks to Dr. Peter Schury for the developing of the electric circuits for the gas counter and many help to write the paper in English. I would like to thank to Dr. Sota Kimura, Dr. Jinhyung Park, Mr. Murad Ahmed for the great efforts for the preparation and development of the detectors.

I am deeply grateful to Prof. Akira Ozawa for the advices to the research and thesis and teaching in the lab. seminar. I would like to thank to Dr. Kimikazu Sasa, especially for the cooperation to the target irradiation test. I would like to thank to past and present staffs and students belonging to the low-energy nuclear physics in Univ. of Tsukuba.

I would like to thank to Dr. Hiroshi Watanabe, Dr. Junyoung Moon, Dr. Akihiro Taniguchi, and members of Shimoda Lab. in Osaka Univ. to join and help the experiment.

I really appreciate to Dr. Toshiyuki Kubo for the employment as a Junior research assistant in RIKEN that was definitely necessary for me to go to doctoral degree. I also really appreciate to Dr. Hideki Ueno for the employment as a part time worker in RIKEN that was definitely necessary for me to continue the work for the last one year, and kind advices for the interviewing.